UNIVERSITY OF SOUTHAMPTON

FACULTY OF PHYSICAL SCIENCES AND ENGINEERING

School of Physics and Astronomy

Phenomenology of searches for new neutral resonances in top quark pair production at the LHC

by

Declan Andrew Millar

Thesis for the degree of Doctor of Philosophy

March 2018

UNIVERSITY OF SOUTHAMPTON

ABSTRACT

FACULTY OF PHYSICAL SCIENCES AND ENGINEERING

School of Physics and Astronomy

Thesis for the degree of Doctor of Philosophy

PHENOMENOLOGY OF SEARCHES FOR NEW NEUTRAL RESONANCES IN TOP QUARK PAIR PRODUCTION AT THE LHC

by Declan Andrew Millar

This report presents the research that I have done in conjunction with my supervisors Lucio Cerrito and Stefano Moretti, as well as in collaboration with Francesco Spanò, over the last three years of my studies. Chapter 6 presents work conducted as part of the e/γ signature trigger group within the ATLAS collaboration. Chapter 7 presents work released in a publicly available paper, while the study discussed in chapter 8 I hope to be the subject of an upcoming publication.

This thesis presents two studies considering new neutral resonances in top quark pair production at the Large Hadron Collider. Its focus is largely on charge and spin asymmetry observables sensitive to the chiral couplings of a Z' boson. Both analyses employ a $2 \to 6$ simulation accounting for all possible leading order topologies for both signal and (irreducible) top backgrounds including interference effects. The first is a parton-level analysis aimed at the lepton-plus-jets final state, using a reconstruction procedure of the (anti)top quark mass and momenta that closely mimics experimental conditions. Results show the potential of these observables to characterise the chiral couplings of the Z' boson and distinguish between different theoretical models, and to improve the discovery potential in combination with the $t\bar{t}$ differential cross section. The second study extends to an analysis using the dilepton final state in top pair production to observe a new resonance, accounting for parton-shower, hadronisation and simulated reconstruction with the ATLAS detector. Several approaches to top reconstruction and their relative observational power are explored. Finally a study of the sources for single electron trigger inefficiencies with the ATLAS detector is presented.

Table of Contents

Declaration of Authorship

I, Declan Andrew Millar, declare that the thesis entitled *Phenomenology of searches for new neutral resonances in top quark pair production at the LHC* and the work presented in the thesis are both my own, and have been generated by me as the result of my own original research. I confirm that:

- this work was done wholly or mainly while in candidature for a research degree at this University;
- where any part of this thesis has previously been submitted for a degree or any other qualification at this University or any other institution, this has been clearly stated;
- where I have consulted the published work of others, this is always clearly attributed;
- where I have quoted form the work of others, the source is always given. With the exception of such quotations, this thesis is entirely my own work;
- I have acknowledged all main sources of help;
- where the thesis is based on work done by myself jointly with others, I have made clear exactly what was done by others and what I have contributed myself;

Signed: .....

Date: .....

Acknowledgements

Where to start? It's been a long journey to here, so long that it would be impossible for me to sufficiently thank everyone across Southampton, Queen Mary and CERN; an exhaustive list would stretch many pages.

First and foremost, I would like to thank my supervisors Lucio and Stefano for their astute guidance, patience and expertise. It has been a pleasure to learn from them both and collaborate on projects that bring together phenomenology and experiment in high energy physics. I am immensely grateful for their boundless understanding and compassion. It stands to reason that if not for Stefano's choice to include me in the CERN-based Masters programme I'd have lived a very different and much less rich life. I'm also incredibly grateful to Francesco for his consistent guidance and advice over many years and Eram for his reliable and wise counsel. Additionally, I'm indebted to Peter Jenni, Fabiola Gianotti and the rest of the ATLAS PhD Grant selection committee and to Steve McMahon for his no-doubt influential recommendation.

Special thanks go to friends Ben, Dave, Lewis, Graham and Tamsin at QMUL and CERN for their company and bountiful help getting to grips with the tools of experimental physics. At Southampton I'm grateful to the whole 4119 crew, and in particular Fred, Juri, Miguel, Pete, Will and Zoë for theoretical and grounded discussions.

Last, but certainly not least, I'd like to thank my family: Pardis, Mum, Dad, Ryan, Nan, Granddad for their unwavering faith, pride and support in all areas of life.

CHAPTER 1

The Standard Model and beyond

1.1 Quantum Field Theory

1.1.1 Why Quantum Field Theory?

Special Relativity (SR) and Quantum Mechanics (QM) revolutionised human understanding of physics during the 20th century [1, 2, 3, 4]. Individually, their axioms and consequences defy natural instincts honed to understand observable forces around the metre scale, and which are encoded in the framework of Classical Mechanics (CM). Taken in combination, SR and QM necessitate the formulation of a locally acting framework that allows the creation and annihilation of identical, indistinguishable particles. Under this formulation, classical fields, physical quantities defined at every point in spacetime $\psi(\vec{x}, t)$, take centre stage, while particles emerge naturally following their quantisation.

To see why these fields are necessary, the principles of QM, which emerged due to the failure of CM to explain black-body radiation and the photoelectric effect, will be briefly outlined. The possible states of a system are encapsulated in a complete set of orthonormal basis vectors of a complex Hilbert space, $\langle j|i\rangle = \delta_{ij}$. Thus, any state can be written as a linear combination of these vectors, $|\psi\rangle = a_i |i\rangle$. Particle observables, such as momentum, take the form of Hermitian operators $A = A^\dagger$. This ensures that observed values, given by an eigenvalue of the operator $A|i\rangle = a_i |i\rangle$, are real-valued. The time evolution of this system, which must preserve the norm of the state vector over time, is governed

by the general Schrödinger equation,

$$H\left|\psi(t)\right\rangle = i\frac{\mathrm{d}}{\mathrm{d}t}\left|\psi(t)\right\rangle, \tag{1.1.1}$$

where the Hamiltonian H is an observable corresponding to the total energy of the system. Expanding the state in the basis of the position operator, we extract the wave function, $\langle\vec{x}|\psi(t)\rangle \equiv \psi(\vec{x},t)$, and interpret $|\psi(\vec{x},t)|^2$ as the probability density of the system. Schrödinger originally formulated QM in terms of wave mechanics, with a Hamiltonian based on the conservation of classical kinetic and potential energies, $H = \frac{p^2}{2m} + V(\vec{x})$. Inserting the corresponding operators, $P = i\vec{\nabla}$ and Eq. 1.1.1, we arrive at the wave schrödinger equation,

$$\left(-\frac{1}{2m}\nabla^2 + V(x)\right)\psi(\vec{x},t) = i\frac{\partial}{\partial t}\psi(\vec{x},t). \tag{1.1.2}$$

This equation best illustrates the revolutionary consequences of QM, such as wave-particle duality. Its solutions, for various free and constrained systems, illustrate that measurements made of a system are constrained to discrete quanta. Immediately though, we can see an issue: SR, which emerges due to the failure of CM to accommodate Maxwell's equations of electromagnetism, is not respected. By consequence of the postulates of SR, space and time are fused into a single four dimensional spacetime continuum, $x^\mu \equiv x$, yet Eq. 1.1.2 features a second-order derivative in space, and a first order derivative in time.

If instead a hamiltonian that is directly motivated by mass-energy conservation $E^2 = p^2 + m^2$ is substituted,

$$\left(\frac{\partial^2}{\partial t^2} - \nabla^2 + m^2\right)\phi(\vec{x},t) = \left(\partial^\mu\partial_\mu + m^2\right)\phi(x) = 0, \tag{1.1.3}$$

the result, the Klein-Gordon (KG) equation, clearly respects SR. However, we see this realisation is also unsatisfactory. Firstly, there are both positive and negative energy solutions. This is manifest in the square root of the mass-energy equation, but is problematic when interpreting ϕ as a wavefunction. Furthermore, $|\phi|^2$ can no longer be interpreted as a probability density, as it is Lorentz invariant, while a density should transform as the time-like component of a 4-vector. When an adequate interpretation for the probability density is derived, it is no longer positive definite.[1]

The Feynman-Stuekelberg interpretation can mollify these problems by constraining negative energy states to move backwards in time, such that the emission of a negative

[1] The following definitions of the probability density and current respect the conservation law $\partial_\mu J^\mu = 0$,

$$\rho = J^0 = i\left(\phi^*\frac{\partial\phi}{\partial t} - \phi\frac{\partial\phi^*}{\partial t}\right), \qquad \vec{J} = -i\left(\phi^*\vec{\nabla}\phi - \phi\vec{\nabla}\phi^*\right). \tag{1.1.4}$$

energy particle may be interpreted as the absorption of a positive energy antiparticle with equal and opposite four-momentum. Thus, antiparticles appear.

To avoid the negative roots of Eq. 1.1.3, we might propose an equation of motion with only linear spacetime derivatives,

$$(\gamma^\mu \partial_\mu - m)\,\psi = 0. \tag{1.1.5}$$

If we iterate Eq. 1.1.5, by applying the operator twice on the wavefunction, and demand equivalence with Eq. 1.1.3, the matrices γ^μ must satisfy the anti-commutation relation,

$$\{\gamma_\mu, \gamma_\nu\} = 2\eta_{\mu\nu}. \tag{1.1.6}$$

These are the Dirac γ-matrices, and Eq. 1.1.5 the Dirac equation. The fewest number of dimensions in which they may be constructed is four, and there are multiple equivalent representations. One choice, used throughout this thesis, is the Chiral representation,

$$\gamma^0 = \begin{pmatrix} 0 & 1 \\ 1 & 0 \end{pmatrix}, \qquad \vec{\gamma} = \begin{pmatrix} 0 & \vec{\sigma} \\ \bar{\sigma} & 0 \end{pmatrix}, \tag{1.1.7}$$

where $\sigma^\mu = (\mathbf{1}, \vec{\sigma})$, $\bar{\sigma}^\mu = (\mathbf{1}, -\vec{\sigma})$, and $\vec{\sigma}$ are the Pauli spin matrices,

$$\sigma^1 = \begin{pmatrix} 0 & 1 \\ 1 & 0 \end{pmatrix}, \qquad \sigma^2 = \begin{pmatrix} 0 & -i \\ i & 0 \end{pmatrix}, \qquad \sigma^3 = \begin{pmatrix} 1 & 0 \\ 0 & -1 \end{pmatrix}. \tag{1.1.8}$$

Additionally, we may define the chirality operator,

$$\gamma^5 \equiv i\gamma^0\gamma^1\gamma^2\gamma^3 = \begin{pmatrix} -1 & 0 \\ 0 & 1 \end{pmatrix}. \tag{1.1.9}$$

This can be used in projection operators,

$$P_{L,R} = \frac{1}{2}(1 \pm \gamma_5), \tag{1.1.10}$$

to single out the chiral components of the Dirac spinors.

When solved for a particle in its rest frame, Eq. 1.1.5 also presents negative energy solutions. However, defining $\rho = J^0 = \psi^\dagger\psi$ and $\vec{J} = \psi^\dagger\vec{\alpha}\psi$, satisfying $\partial_\mu j^\mu = 0$, we see that we can construct a positive definite probability density. Dirac interpreted negative energy states as holes in an infinite sea of energy states. This idea introduces the concept of pair production, but does not provide a framework for calculating the interactions that allow particle numbers to change. To describe this, an entirely new framework is required: Quantum Field Theory (QFT).

1.1.2 What is Quantum Field Theory?

QFT is a framework based on the quantisation of classical fields. In the previous section, the degrees of freedom in CM were promoted to operators acting on a Hilbert space; in QFT there are infinite degrees of freedom, defined at every point in space, $\phi(\vec{x},t)$. Here $\vec{x}$ is no longer a dynamic variable but merely a label. In this 2nd quantisation, Eqs. 1.1.3 and 1.1.5 remain, yet are reinterpreted to describe the dynamics of classical fields. Following canonical quantisation, $\phi(\vec{x},t)$ and $\psi(\vec{x},t)$ are no longer interpreted as wave functions, but operator-valued functions acting on a Fock space.[2] As in classical field theory, the dynamics of the field are described by an action,

$$S = \int \mathrm{d}t \int \mathrm{d}^3x\, \mathcal{L}(\phi, \dot{\phi}, \vec{\nabla}\phi) = \int \mathrm{d}^4x\, \mathcal{L}(\phi, \partial_\mu \phi). \tag{1.1.11}$$

In this thesis, three classes of field are considered, each with a unique Lagrangian (density). Massive complex scalar, massive spinor (fermionic, Dirac), and vector (bosonic) fields are described, respectively, by Lorentz-invariant Lagrangians,

$$\mathcal{L}_{scalar} = \partial^\mu \phi^\dagger \partial_\mu \phi - m^2 \phi^\dagger \phi, \tag{1.1.12}$$

$$\mathcal{L}_{spinor} = \bar{\psi}(\partial\!\!\!/ - m)\psi, \tag{1.1.13}$$

$$\mathcal{L}_{vector} = F^{\mu\nu} F_{\mu\nu}, \tag{1.1.14}$$

where $\partial\!\!\!/ \equiv \gamma^\mu \partial_\mu$ and $F_{\mu\nu} = \partial_\mu A_\nu - \partial_\nu A_\mu$. By minimising the corresponding actions, the equations of motion in Eqs. 1.1.3 and 1.1.5 are recovered.

Dirac fermion fields describe well particles such as electrons; however, they are not the building blocks of the Standard Model. A Dirac fermion carries a four-dimensional, reducible representation of $\mathrm{SO}^+(1,3)$, meaning fermions carry two inequivalent, irreducible two-dimensional representations.[3] This is clear when using the Chiral representation (Eq. 1.1.7), where we can write the four-component Dirac spinor as two two-component Weyl spinors of opposite Chirality (Eq. 1.1.9),

$$\psi = \begin{pmatrix} \chi \\ \eta \end{pmatrix} : \qquad \gamma_5 \begin{pmatrix} \chi \\ 0 \end{pmatrix} = - \begin{pmatrix} \chi \\ 0 \end{pmatrix}, \qquad \gamma_5 \begin{pmatrix} 0 \\ \eta \end{pmatrix} = + \begin{pmatrix} 0 \\ \eta \end{pmatrix}, \tag{1.1.15}$$

which transform independently under Lorentz transformations and are mixed in the Dirac Lagrangian only via mass terms,

$$\mathcal{L} = \chi^\dagger \bar{\sigma}^\mu i \partial_\mu \chi + \eta^\dagger \sigma^\mu i \partial_\mu \eta - m \chi^\dagger \eta - m \eta^\dagger \chi. \tag{1.1.16}$$

[2] The Fock space is the sum of the n-particle Hilbert spaces.

[3] $\mathrm{SO}^+(1,3)$ denotes the Lorentz group. This is the orthogonal (set of real matrices whose transpose are equal to their inverse) Lie group preserving the length, $t^2 - x^2 - y^2 - z^2$, and that preserves spatial orientation (special/proper) and the time direction (orthochronous).

Classical physics has always benefited from the recognition of symmetries in order to simplify systems by exploiting mathematical redundancies in their description. Noether's theorem states that the presence of a global symmetry in the action of a physical system is always associated with a conserved current.

A key principle in the formulation of QFT is gauge symmetry. Gauge, local or internal symmetries are properties of each point in spacetime, and to impose this symmetry on a Lagrangian new interactions must be introduced. Taking, for example, the Lagrangian of a massless fermion field (from Eq. 1.1.14),

$$i\bar{\psi}\gamma^{\mu}\partial_{\mu}\psi = 0, \tag{1.1.17}$$

observe it is trivially invariant under a global phase shift $\psi \to e^{iq\theta}\psi$, i.e. it is manifestly invariant under a global symmetry described by the U(1) Lie group. However, if the continuous parameter of the transformation is made local, $\theta \to \theta(x)$, an additional term $iq\partial_{\mu}\theta(x)$ is generated. Thus, to ensure the Lagrangian remains invariant under a U(1) gauge group a new vector field must be introduced with complementary transformation properties that exactly cancel those of the spinor field: $A_{\mu} \to A_{\mu} - \partial_{\mu}\theta(x)$ and that couples to the spinor field with strength q. Thus, an invariant Lagrangian is,

$$\mathcal{L} = \frac{1}{4}F^{\mu\nu}F_{\mu\nu} + i\bar{\psi}\not{\mathrm{D}}\psi, \tag{1.1.18}$$

where the minimal substitution $\mathrm{D}_{\mu} = \partial_{\mu} + iqA_{\mu}$ has been made, and a kinetic term for the newly introduced field has been added.

This simple interaction underpins all of electromagnetism, where the massless photon is identified with the A_{μ} gauge vector field, coupled to fermions via their electric charge q. The associated current $J_{\mu} = \bar{\psi}\gamma_{\mu}\psi$, conserved in accordance with Noether's theorem, is identified with the conservation of electric charge. The electric charge coupling is sufficiently small as to allow accurate treatment using perturbative QFT, and, upon quantisation, the rules of Quantum Electrodynamics (QED) are revealed. The resulting prediction for the anomalous magnetic dipole moment of the electron has been calculated to an order of α^5 and agrees with the experimentally determined value to within 10^{-8} [5, 6]. This makes it one of the most accurately verified predictions in physics, thus validating QED in particular, and the framework of QFT in general.

In the canonical quantisation classical fields are promoted to operator valued functions, obeying commutation relations,

$$[\phi_a(\vec{x}), \phi_b(\vec{y})] = \left[\pi^a(\vec{x}), \pi^b(\vec{y})\right] = 0, \tag{1.1.19}$$

$$\left[\phi_a(\vec{x}), \pi^b(\vec{y})\right] = i\delta^{(3)}(\vec{x}-\vec{y})\delta^b_a, \tag{1.1.20}$$

where $\pi_a(\vec{x}) = \partial\mathcal{L}/\partial\dot{\phi}_a$ is the momentum conjugate to the real scalar field $\phi_a(\vec{x})$. These field operators are then expanded as a sum of plane wave solutions for an infinite array of coupled quantum harmonic oscillators parameterised by creation and annihilation operators, $a^\dagger(\vec{p})$ and $a(\vec{p})$, respectively,

$$\phi(x) = \int \frac{\mathrm{d}^3p}{2E(2\pi)^3}\left[a(\vec{p})e^{-ipx} + a^\dagger(\vec{p})e^{ipx}\right], \tag{1.1.21}$$

$$\pi(x) = \int \frac{\mathrm{d}^3p}{2E(2\pi)^3}(-i)\left[a(\vec{p})e^{-ipx} - a^\dagger(\vec{p})e^{ipx}\right]. \tag{1.1.22}$$

Canonical quantisation proceeds via the Hamiltonian formulation where time evolution is carried by the states, which are a function of all possible field configurations. Manifest Lorentz invariance is lost, and must be restored later.[4]

In the interaction picture the Hamiltonian is split into free and interacting parts, $H = H_0 + H_{int}$. Here H_0 governs the time evolution of operators and H_{int} governs the evolution of states $|\psi\rangle_I$, $idU = H_I(t)Udt$. The solution to this is given by Dyson's formula,

$$U(t, t_0) = \mathrm{T}\exp\left(-i\int_{t_0}^{t}\mathrm{d}t'\, H_I(t')\right). \tag{1.1.23}$$

The power expansion of this formula demonstrates the perturbative nature of this approach. In scattering theory, we assume the initial and final states are eigenstates of the free theory, which allows us to define the scattering matrix,

$$\langle f|\, S\,|i\rangle \equiv \lim_{t\to\pm\infty(1-i\epsilon)} \langle f|\, U(t,-t)\,|i\rangle\,. \tag{1.1.24}$$

Then, by applying Wick's theorem, we may expand the terms in Eq. 1.1.23 to derive all possible normal-ordered contracted terms. Each of the terms arising in $\langle f|\, S-1\,|i\rangle$ may be represented schematically using Feynman Diagrams.

At leading order (LO), i.e. for terms proportional to $\alpha^{n=1}$, we may derive exact solutions. However, if we were to use them to naively calculate the correlation function for any process involving loops ($n > 1$), it would often yield infinity. We solve this problem using the process of renormalisation, a systematic way of removing infinities from physical observables, such as cross sections and decay widths.

We first identify that the 'bare' fields and coupling constants in our Lagrangian cannot be determined experimentally, they are just parameters in our Lagrangian. If we were to perform an experiment to measure the coupling constant for a certain interaction at a certain energy scale we would be trying to measure the physical or 'renormalised' coupling which is directly related to the cross section for this interaction [7]. Therefore, we introduce renormalised quantities for every bare quantity in our Lagrangian. We can

[4] An alternative quantisation formulation using path integrals maintains intrinsic Lorentz invariance.

then consider our bare quantities to be infinite in such a way that exactly cancels the infinities arising from our loop calculations. We achieve this systematic cancellation by rewriting the Lagrangian in terms of renormalised quantities and counter-terms. Clearly any finite term can be absorbed into an infinite one, so there are many different renormalisation schemes, which define how much of the finite parts we absorb. The minimal subtraction (MS) scheme is a commonly used example.

In order to manipulate the divergent integrals we must first regularise them by making the integral finite. We could do this by imposing a momentum cut-off scale. In the modern view this cut-off has physical significance, it determines the scale above which new physics becomes important, for which our current model is only an effective theory. The process of renormalisation ensures that when physical amplitudes are expressed in terms of renormalised parameters the cut-off dependence vanishes.

1.1.3 Beyond Quantum Field Theory

As stated above, the framework of QFT has been validated using extremely precise experiments. However, when applied to gravity any naive attempt to quantise the gravitational field, as described classically within the framework of General Relativity (GR), results in a non-renormalizable theory. Thus, while Quantised GR can describe an effective theory of gravity, QFT appears to fall short of a Theory of Everything (TOE). A satisfying unification of quantum mechanics and GR is arguably the most important goal in modern high-energy physics and many different approaches have been developed towards a solution.

One such approach is Asymptotic Safety, which retains the (non-perturbative) framework of QFT in a search for a consistent and predictive quantised gravitational field by finding a theory featuring a non-trivial fixed point in its renormalisation group flow [8, 9]. Such a solution would ensure that quantum gravity remains safe from ultraviolet divergences, in which cross sections go to infinity as distance scales become small.

Another famous approach is String Theory, where the point-like particles of quantum mechanics are extended to two-dimensional loops of 'string' [10]. On this foundation, GR, Yang-Mills Gauge theories and electromagnetism naturally emerge. While this is a tantalising feature, String Theories necessitate many additional elements, such as extra spatial dimensions. They have also been criticised for a lack of perceived predictivity, at least for observations at human-accessible energy scales. Nevertheless, String Theory, and its derivations and extensions, are still undoubtably the most popular candidates for a TOE.

As we will see in section 1.5, the theories explored in this thesis are largely ignorant of GR or Quantum Gravity, and are limited to attempts at unifying those theories well de-

Field	$\mathrm{SU}(3)_C$	$\mathrm{SU}(2)_L$	$\mathrm{U}(1)_Y$
q	3	2	$+\frac{1}{6}$
u^c	$\bar{3}$	1	$-\frac{2}{3}$
d^c	$\bar{3}$	1	$+\frac{1}{3}$
ℓ	1	2	$-\frac{1}{2}$
e^c	1	1	$+1$
H	1	2	$-\frac{1}{2}$

Table 1.2.1: The Standard Model matter fields and their G_{SM} representations.

scribed by QFT. Nevertheless, these theories may be inspired by/consistent with String Theory, and the unification of the Standard Model symmetry groups would surely bring us closer to an all-encompassing TOE.

1.2 Gauge structure and particle content

The Standard Model (SM) defines a renormalizable Quantum Field Theory encompassing fifteen Weyl fermions and one complex scalar, with gauge symmetry $\mathrm{G}_{SM} \equiv \mathrm{SU}(3) \times \mathrm{SU}(2) \times \mathrm{U}(1)$. The fermions comprise three generations of five fields, $\psi_i \in \{q, u^c, d^c, \ell, e^c\}$, that, along with the scalar field, H, carry irreducible representations of G_{SM}.[5] The irreducible representations carried by each field for each subgroup of the SM are listed in table 1.2.1.

This brief definition is sufficient to write down a complete, concise schematic Lagrangian for the SM,

$$\mathcal{L} = i\bar{\psi}_i \bar{\sigma}^\mu \mathrm{D}_\mu \psi_i - \frac{1}{4} F^a_{\mu\nu} F^{a\mu\nu} + \lambda^{ij} \psi_i \psi_j \Phi^{(c)} + \mathrm{h.c.} + |\mathrm{D}_\mu \Phi|^2 - V(\Phi)^2, \tag{1.2.1}$$

where i, j are generational indices, and a labels the different gauge fields. Beneath this elegant depiction lies a complex theoretical playground of interactions and mathematical miracles, revealing many testable predictions that uniquely result from this structure. This comprehensive theory required decades of theoretical and experimental endeavour unifying the strong, weak and electromagnetic forces.

The first two terms of Eq. 1.2.1 form the gauge sector. There are twelve gauge fields: eight gluons, three W-bosons and one B-boson in the adjoint representations of $\mathrm{SU}(3)_C$, $\mathrm{SU}(2)_L$ and $\mathrm{U}(1)_Y$, respectively. The covariant derivative D_μ contains the group generators in the designated representations, as well as the three gauge couplings g_s, g_2 and g_1.

[5] Here c denotes charge conjugation, the operation transforming a field between a particle and its antiparticle, $\psi^c \equiv \bar{\psi}$ [11].

The following two terms comprise the flavour sector, whose Lagrangian may be expanded,

$$L = \lambda^u q \Phi^c u^c + \lambda^d V q \Phi^c d^c + \lambda^e \ell \Phi^c e^c + \text{h. c.}, \tag{1.2.2}$$

where λ^i are three 3×3 complex matrices in generational space, which are diagonal in the appropriate basis. This basis is arrived at using the 3×3 unitary quark-mixing or Cabibbo–Kobayashi–Maskawa (CKM) matrix, V, the only source of flavour mixing in the SM. In addition to the six real parameters of the quark masses, the CKM matrix contains three real angles and one complex phase. This phase is a source of CP-violation.

The final two terms represent the Higgs sector, with potential,

$$V(\Phi) = -\mu^2 \Phi^\dagger \Phi - \lambda (\Phi^\dagger \Phi), \tag{1.2.3}$$

where $\mu, \lambda > 0$. This is a critical ingredient in Electroweak Symmetry Breaking (EWSB) (section 1.4.1).

1.3 Quantum Chromodynamics

The SU$(3)_C$ subgroup governs the interactions between the quarks living in its fundamental representation. This representation is three dimensional, therefore, unlike QED, whose charge all comes in one flavour, its charges come in three different 'colours', hence its name, Quantum Chromodynamics. This group has eight generators, T^a, parameterising the gauge transformation, U$(x) = e^{i\alpha(x)T^a}$, and are associated with the eight gluons of QCD, $A_\mu = T_a A^a_\mu$.[6] These generators form a non-trivial algebra under commutation,

$$[T_a, T_b] = f_{abc} T_c, \tag{1.3.1}$$

where $f_{abc} = -f_{bac}$. Consequently, this gives rise to a non-Abelian gauge theory with field strength tensor,

$$G^a_{\mu\nu} = \partial_\mu A^a_\nu - \partial_\nu A^a_\mu + g_s f_{abc} A^b_\mu A^c_\nu, \tag{1.3.2}$$

and Lagrangian,

$$\mathcal{L}_{QCD} = -\frac{1}{4} G^{\mu\nu}_a G^{\mu\nu}_a + i \bar{\psi}_i \not{D} \psi_i, \tag{1.3.3}$$

where D$_\mu = \partial_\mu + i g_s T^a A^a_\mu$. This interaction is vector-like, coupling equally to left and right-chiral components and manifests itself as the strong nuclear force, owing to its high coupling strength, g_s. Evaluation of the gluon kinetic terms in Eq. 1.3.3 and the final term in Eq. 1.3.2 exhibits the three and four-point self-interaction terms for gluons. These additional interactions lead to an interesting scale (μ) dependence for the QCD

[6] While the SU(n) Lie group features $n \times n$ dimensional unitary matrices. The additional requirement for determinant 1 (orientation preserving) leads to $N^2 - 1$ independent degree of freedom.

coupling, with a β-function at one-loop level of,

$$\beta(g_s) = \frac{\partial g_s}{\partial \log \mu} = -g_s^3 \frac{1}{(4\pi)^2}\left(11 - \frac{2}{3}n_f\right), \tag{1.3.4}$$

where n_f is the number of flavours [12]. With six flavours the beta function is negative such that the coupling strength decreases with increasing energy scale, resulting in asymptotic freedom. This suggests that, for the high-energy collisions at the LHC, QCD interactions may be treated in the perturbative limit. Conversely, at small distances, parton interactions are difficult to model mathematically, but are observed to be confined tightly inside composite hadrons. This phenomenon of quark confinement, whereby quarks may not be observed as free particles, appears to be related to, but is distinct from, asymptotic freedom. The consequence of this being that quarks and gluons produced in hard-scattering processes rapidly hadronise, forming showers of mesons and/or baryons. This can be modelled by introducing a potential between interacting coloured objects that grows linearly with increasing separation, such that it is 'cheaper' energetically for spontaneous pair creation to produce bound colour singlets.

1.4 Electroweak interaction

The electroweak interactions unify electromagnetism and the weak nuclear force. The Glashow-Weinberg-Salam (GWS) model provides a – now experimentally well-justified – description of this unified theory. We begin with an SU(2) gauge field coupled to a scalar field, Φ, that transforms in the fundamental (spinor) representation. We then assign this same scalar a charge of $Y = -\frac{1}{2}$ under an additional $\mathrm{U}(1)_Y$ symmetry.[7]

Therefore, we insist our Lagrangian is invariant under the gauge transformation,

$$\Phi \to e^{i\alpha^a T^a} e^{-\frac{i}{2}\beta}\Phi, \tag{1.4.1}$$

where $T^a = \sigma^a/2$. Operators σ^a with $a = 1, 2, 3$ are the Pauli matrices, and Φ is a complex doublet,

$$\Phi = \begin{pmatrix} \phi^+ \\ \phi^0 \end{pmatrix} = \frac{1}{\sqrt{2}}\begin{pmatrix} \phi_1 + i\phi_2 \\ \phi_3 + i\phi_4 \end{pmatrix}. \tag{1.4.2}$$

This necessitates a covariant derivative,

$$\mathrm{D}_\mu\Phi = \left(\partial_\mu + \frac{i}{2}g_2\sigma^a W_\mu^a + \frac{i}{2}g_1 B_\mu\right)\Phi, \tag{1.4.3}$$

where W_μ^a and B_μ are the SU(2) and $\mathrm{U}(1)_Y$ gauge bosons, respectively, with overall Lagrangian,

$$\mathcal{L}_{EW} = -\frac{1}{4}G_a^{\mu\nu}G^a_{\mu\nu} - \frac{1}{4}F^{\mu\nu}F_{\mu\nu} + i\bar{\psi}_i \not{D}\psi_i + |\mathrm{D}_\mu\Phi|^2 - V(\Phi). \tag{1.4.4}$$

[7] Without the additional $\mathrm{U}(1)_Y$ symmetry, no massless photon could be recovered.

The corresponding generators are mutually commutative; therefore, they may have independent gauge couplings, g_2 and g_1, respectively.

1.4.1 Electroweak symmetry breaking

At some scale, the field Φ acquires a vacuum expectation value (VEV), $v = \frac{\mu}{\sqrt{\lambda}}$, which is chosen to be real and in the $\sigma^3 = -1$ direction, i.e. expanding Φ about its VEV,

$$\Phi = \frac{1}{\sqrt{2}} \begin{pmatrix} \phi_1 + i\phi_2 \\ v + h + i\phi_4 \end{pmatrix}. \tag{1.4.5}$$

In the unitary gauge, $\phi_1 = \phi_2 = \phi_4 = 0$, this reduces to

$$\Phi = \frac{1}{\sqrt{2}} \begin{pmatrix} 0 \\ v + h \end{pmatrix}. \tag{1.4.6}$$

Inserting this into the covariant derivative and expressing the Pauli matrices in explicit form gives,

$$\begin{aligned} \mathrm{D}_\mu \Phi &= \frac{1}{\sqrt{2}} \left\{ \partial_\mu + i g_2 \begin{pmatrix} W_\mu^0 & \sqrt{2} W_\mu^+ \\ \sqrt{2} W_\mu^- & -W_\mu^0 \end{pmatrix} + i \frac{g_1}{2} B_\mu \right\} \begin{pmatrix} 0 \\ v + h \end{pmatrix} \\ &= \frac{1}{\sqrt{2}} \begin{pmatrix} i g_2 \sqrt{2} W_\mu^+ (v + h) \\ \left(\partial_\mu - i g_2 W_\mu^0 + i \frac{g_1}{2} B_\mu \right) (v + h) \end{pmatrix}, \end{aligned} \tag{1.4.7}$$

where we have defined $\sqrt{2} W_\mu^\pm \equiv W_\mu^1 \mp i W_\mu^2$ and $W_\mu^0 \equiv W_\mu^3$. By calculating $|\mathrm{D}_\mu \Phi|^2$ explicitly,

$$|\mathrm{D}_\mu \Phi|^2 = \frac{1}{2} (\partial_\mu h)^2 + \frac{g^2 v^2}{4} W^{+\mu} W_\mu^- + \frac{v^2}{8} \left(g_2 W_\mu^0 - g_1 B_\mu \right)^2 \tag{1.4.8}$$

$$+ \frac{g_2^2}{4} W^{+\mu} W_\mu^- \left(2vh + h^2 \right) + \frac{1}{8} \left(g W_\mu^0 - g_1 B_\mu \right)^2 \left(2vh + h^2 \right), \tag{1.4.9}$$

it is observed that certain fields have acquired self-interaction, i.e. mass, terms. However, these states differ from those of the interacting Lagrangian; they are given by a linear combination of the original fields. This may be formulated as a rotation,

$$A_\mu = \sin\theta_w W_\mu^0 + \cos\theta_w B_\mu, \tag{1.4.10}$$

$$Z_\mu = \cos\theta_w W_\mu^0 - \sin\theta_w B_\mu. \tag{1.4.11}$$

The weak mixing (Weinberg) angle, $\tan\theta_W = g_1/g_2$, parameterises the mixing between B and W^0 leading to the diagonalised mass eigenstates of the photon γ, and Z boson. Thus, three massive vectors, one massless vector and a massive Higgs.

It may be observed that a U(1) gauge symmetry has survived this breaking mechanism,

$$\left(Y + \frac{T_3}{2}\right) \begin{pmatrix} 0 \\ \frac{v}{\sqrt{2}} \end{pmatrix} = 0. \tag{1.4.12}$$

We identify this symmetry with $\mathrm{U}(1)_Q$ of electromagnetism. In terms of the diagonalised states, the covariant derivative

$$\mathrm{D}_\mu = \partial_\mu + ig_2 \sin\theta_w \left(Y + \frac{T_3}{2}\right) A_\mu + \frac{ig}{\cos\theta_w} \left(T_3 - \sin^2\theta_w \left(Y + \frac{T_3}{2}\right)\right) Z_\mu. \tag{1.4.13}$$

Thus, we can further identify the elementary charge, $e = g\sin\theta_w$, and A_μ with the photon.

The form of the covariant derivative will uniquely determine the couplings of the EW bosons to all fermions, according to Eq. 1.4.4. However, first we must determine which representations the fermions live in. Most generally, we know that the kinetic energy term for the Dirac fermions reduces to two separable pieces,

$$\bar{\psi}_L i\partial\!\!\!/ \psi_L + \bar{\psi}_R i\partial\!\!\!/ \psi_R, \tag{1.4.14}$$

implying that the Weyl fermions, ψ_L and ψ_R, are free to live in different representations of the gauge group. Indeed, from experimentation, we know that nature exploits this freedom; the $W^\pm$ bosons couple only to the left-chiral components of fermions,

$$\mathcal{L}^\pm_{int} = -g_2 W^-_\mu \bar{\psi}_i \gamma^\mu P_L \psi_j + \mathrm{h.\,c.}. \tag{1.4.15}$$

This implies that ψ_L lives in the fundamental representation of $\mathrm{SU}(2)_L$, while ψ_R lives only in its trivial representation. Of course, the coupling between fermions and Z bosons is given by

$$\frac{g_2}{\cos\theta_w}\left(T_3 - \sin^2\theta_w Q\right) = g_z Q_Z. \tag{1.4.16}$$

The form of this coupling is important to remember when considering Generalised Sequential Models in section 2.2.1.

Knowing the charge relation allows us to calculate the necessary hypercharges to reproduce the electromagnetic charge for each fermion. Hence, we may assign the quantum numbers specified in Tab. 1.2.1. This leads to two different sets of couplings for left and right chiral fermions.

In Summary, we have seen how the Higgs field acquires a non-zero vacuum expectation value, leading to electroweak symmetry breaking (EWSB),

$$\mathrm{SU}(3)_C \times \mathrm{SU}(2)_L \times \mathrm{U}(1)_Y \to \mathrm{SU}(3)_C \times \mathrm{U}(1)_Q. \tag{1.4.17}$$

Field	$SU(3)_C$	$U(1)_Q$
G^a	8	0
$W^\pm$	1	± 1
Z, A	1	0
(u_L, d_L)	3	$(+\frac{2}{3}, -\frac{1}{3})$
u_R	$\bar{3}$	$+\frac{2}{3}$
d_R	$\bar{3}$	$-\frac{1}{3}$
(ν_L, ℓ_L)	1	$(0, -1)$
ℓ_R	1	-1
h	1	0

Table 1.4.1: The Standard Model fields and representations after EWSB.

This mechanism results in three massive gauge bosons: W^+, W^- and Z, as well as the massless photon, and a massive scalar Higgs. Fermions also acquire a mass via a Yukawa coupling to the Higgs field. Therefore, at our low energy scale we may summarise the SM particle content in table 1.4.1.

1.5 Problems with the Standard Model

Despite its explanations for, and successful predictions of, numerous observations in data, and the delicate structure with which it does so, there are compelling reasons to consider scenarios beyond the SM. These reasons can be split, roughly, into observational and theoretical issues.

In particular, there are four experimental observations that have been clearly established and are unexplained in the SM. Foremost, neutrino oscillations necessitate neutrino masses that do not arise from the SM Lagrangian. In addition to this are three prominent cosmological requirements. Firstly, there is the requirement for neutral, massive dark matter to explain the observed galactic rotation curve, and no suitable candidate appearing in the SM particle content. Another demand is for an explanation to the apparent inflation in the early universe, suggested by density perturbations in the cosmic microwave background. Lastly, and perhaps most compellingly, there is the profusion of matter in the universe with comparatively little antimatter. The degree of charge parity (CP) violation required for sufficient Baryogenesis in the early universe appears to be greater than that obtainable from the sources of CP violation in the SM, however, experimental tests of the neutrino mixing matrix are continuing.

In addition to these observed conflicts with the SM are many unexplained, or disunited, features in nature. Chiefly, as explained in section 1.1.3, while is suitable as an Effective

Field Theory (EFT) of gravity for predictions at low energies, its failure at the Planck scale means it cannot be naively combined with the SM. There are also reasons to consider new models arising due to aesthetic, yet compelling, considerations; namely, the 19 free and independent parameters in the SM Lagrangian. Many physicists feel a truly fundamental theory should provide relationships that reduce these. Furthermore, the scales of these parameters are vastly disparate, with a six order-of-magnitude difference in the Yukawa couplings. If one naively adds the neutrino masses via the same mechanism in order to account for the recent experimental data, this hierarchy stretches to twelve orders of magnitude.

Another cause of wide concern arises for the scalar Higgs self-coupling parameter, λ, in Eq. 1.2.3. At LO, λ appears to essentially be a free parameter and can be chosen such that it remains negative ensuring the wine bottle-shaped potential required for a non-zero vacuum and EWSB. However, when considering higher-order diagrams, it is subject to corrections, meaning that, to retain the desired value for the Higgs mass, the bare mass must be corrected by a Δm_h^2 that depends on the scale, Λ, and the coupling to the fermion in the loop [11],

$$\Delta m_h^2 = -\frac{|\lambda_f|^2}{8\pi^2}\Lambda^2 + ... \tag{1.5.1}$$

Therefore, as Λ is increased to the Planck Scale, and the higher-order corrections increase accordingly, Δm_h^2 must be increased until ≈ 30 orders of magnitude higher than the observed Higgs mass. The dominant contributions come from top quark loops owing to its very large mass. This necessity of fine-tuning appears deeply unnatural. Spinor and vector couplings are protected from these corrections by gauge and chiral symmetries, respectively. While the sole scalar boson of the SM, the Higgs is responsible for setting all particle masses. Consequently, this issue permeates the whole SM. Thus, while the theory is technically fully renormalizable it fails to be satisfactory at all scales.

It is clear that the source of the problem is the vast difference in scale between the Planck-limit and the EW scale, called the hierarchy problem. If there appears some new cut-off not too far above the EW scale, the level of fine tuning can be vastly reduced. For example, one can postulate that the scalar field arises as a composite state in the form of a pseudo-Nambu-Goldstone boson due to a symmetry that is broken at a higher, but not too high, scale (section 2.3). Due to the intimate relationship between the top quark and the hierarchy problem, the top quark would be an invaluable probe of any such new mechanism. Additional motivation for higher scale mechanisms can be found in Grand Unified theories (GUTs). Calculating the higher-order corrections for gauge couplings, g_s, g_1 and g_2, and the resultant β functions suggests that, with increasing scale, they approach each other in value. This suggests that the SM gauge group could be embedded within a larger symmetry group. Further motivation for these scenarios can be found in the natural emergence of charge quantisation and solutions for the hierarchical structure of fermion masses and mixings. Residual U(1) symmetries are commonly

encountered in such theories, which introduce new vector fields: Z' bosons, and these form the benchmark models explored in this thesis.

CHAPTER 2

Z' bosons

2.1 Introduction

In its most general definition, a Z' boson labels any additional neutral resonance appearing in the invariant mass spectrum of a fermion–antifermion pair. More strictly it can be limited to the designation of any hypothesised spin-1 vector boson decaying to such a state. These appear ubiquitously in Beyond the Standard Model (BSM) theories.

The most obvious discovery channels for Z' are Drell-Yan (DY) processes, i.e. $pp \to \gamma Z Z' \to \{e^+e^-, \mu^+\mu^-\}$.[1] For models that are universal, with the same coupling strength to each generation of fermion, and that do not more strongly couple to the quark sector, the strongest exclusion limits are set by this channel. Analysing 20.3 fb^{-1} of proton-proton data at $\sqrt{s} = 8$ TeV delivered by the LHC, both the ATLAS experiment and CMS experiment exclude a Sequential SM (SSM) Z', at the 95% confidence level, for masses lower than 2.90 TeV, in the combined electron and muon channels [13, 14]. Using 3.2 fb^{-1} of $\sqrt{s} = 13$ TeV data, the ATLAS collaboration has published combined results in DY that place a lower limit on the mass of an SSM Z' at 3.36 TeV [15]. The latest results from both collaborations, with approximately 13 fb^{-1}, push this limit on narrow resonances to 4 TeV [16, 17].

The present limits coming from $t\bar{t}$ events are typically lower, with the most stringent limits on a narrow leptophobic Z' excluding masses only less than 2.4 TeV [18, 19]. Therefore,

[1] Generally $pp \to \gamma Z Z' \to \{\tau^+\tau^-, \mu^+\mu^-\}$ is also a valid channel, however, taus are unstable and appear as jets which complicates the event reconstruction and reduces the resolution.

if considering models featuring Z' bosons with large decay widths, leptophobic models with preferential couplings to the quark sector, or non-universally coupling models with enhanced third generation couplings, one may explore theories which embed one or more Z' with lower masses than generally prohibited by DY results.

New fundamental, heavy gauge bosons are encountered in many beyond the Standard Model (BSM) theories. Z' often arise due to residual $\mathrm{U}(1)$ symmetries resulting from the spontaneous symmetry breaking of a Grand Unified Theory (GUT), with the notable exception of $\mathrm{SU}(5)$. These residual symmetries result in a new electroweak (EW) scale gauge structure [20][21],

$$\mathrm{SU}(3)_C \times \mathrm{SU}(2)_L \times \mathrm{U}(1)_Y \times \mathrm{U}(1)_{Y'}. \tag{2.1.1}$$

These classes of model are primarily considered in this thesis, and discussed in more detail in section 2.2. Naturally, as with the photon and the Z boson in the SM case, neutral gauge bosons may also be embedded through non-Abelian gauge extensions of G_{SM} in association with the diagonal generators. In general these Z' will be accompanied by charged gauge bosons which may impose further model constrains in other channels.

Multiple new Z' bosons can also arise in extra-dimensional models, as Kaluza-Klein excitations of Standard Model (SM) gauge fields. These can lead to new, quasi-degenerate resonances in collider experiments [22].

Whatever the source of the newly embedded massive Z' boson(s), the structure of the theory leads to an additional interaction term with fermions in the low-energy Lagrangian that may be cast in the form,

$$\mathcal{L} \supset \sum_i g' Z'_\mu \bar{\psi}_i \gamma^\mu \left(g'^i_L P_L + g'^i_R P_R \right) \psi_i, \tag{2.1.2}$$

where $g'^i_{L(R)}$ are the left(right) couplings between the Z' and the fermion species i, while g' is an overall coupling strength. Projectors, $P_{L,R} = \frac{1}{2}(1 \pm \gamma_5)$, single out the chiral components of the Dirac spinors. Thus, an equivalent parameterisation is given by

$$\mathcal{L} \supset \sum_i g' Z'_\mu \bar{\psi}_i \gamma^\mu \left(g'^i_V - g'^i_A \gamma_5 \right) \psi_i, \tag{2.1.3}$$

where g'^i_V and g'^i_A are, respectively, the vector and axial-vector couplings between the Z' and the fermion species i. A demonstration of how this form may be arrived at for particular models is presented in the following section. It's apparent that the low-energy Lagrangian for a massive gauge boson in Eq. 2.1.3 is not gauge invariant. This is a result of the gauge symmetry undergoing spontaneous breaking at some higher energy scale, in a mechanism similar to that of SM electroweak symmetry breaking described in section 1.4.1. Thus, generally, a new scalar multiplet is required that will acquire a VEV at this

scale. This leads to a low-energy Lagrangian featuring a gauge boson that has acquired a mass through this mechanism and is no longer invariant under the gauge symmetry.

In section 1.4.1, we saw how the interacting fields W_μ^0 and B_μ of the electroweak bosons are mixed to form the mass eigenstates of A_μ and Z_μ. Adding new neutral vector bosons to the SM can, in general, introduce a different mass basis, i.e. the Z' field will have to mix in such a way as to re-introduce fields that may be identified with the photon, Z boson and the new vector boson.

The level of mixing depends on the charge of the Higgs doublet under the $\mathrm{U}(1)'$. If non-zero, its VEV will also contribute to the Z' mass. Likewise, any new scalar fields introduced to break the $\mathrm{U}(1)'$ may live in a non-trivial representation of the EW subgroup, leading to an admixture of states. It's important that the new scalar multiplet carry zero electric charge, as the original combination of Y and T_L^3 (Eq. 1.4.12), in order to ensure a massless photon. Furthermore, it is important to preserve the ratio between the W and Z boson masses, $m_W/m_Z = \cos\theta_w$, a key prediction, and test, of the SM. This is achieved most readily when new scalar multiplets live in the trivial or fundamental representation of $\mathrm{SU}(2)_L$ [23].

An additional mixing mechanism may occur between $\mathrm{U}(1)_Y$ and $\mathrm{U}(1)'$ owing to the independent gauge invariance of the abelian field strength tensor $F_{\mu\nu}$, allowing the existence of $F^{\mu\nu}F'_{\mu\nu}$ terms. This is known as gauge kinetic mixing [24]. These effects can also arise naturally due to higher order corrections, even if absent from the original Lagrangian. When multiple new Z' are introduced, non-trivial corrections may be induced, particularly when the mass gap between the new vectors is small. Potential $Z-Z'$ mass mixing, as well as gauge kinetic mixing with the hypercharge gauge boson, are assumed to be negligible in the following benchmark models.

2.2 Benchmark Models

There are several candidates for a GUT, a hypothetical enlarged gauge symmetry, motivated by approximate gauge coupling unification at around the 10^{13} TeV energy scale [25, 26, 27, 28]. At lower energies these may proceed through sequential spontaneous symmetry breaking mechanisms, often leaving residual $\mathrm{U}(1)$ gauge symmetries, until the familiar $\mathrm{SU}(3)\times\mathrm{SU}(2)\times\mathrm{U}(1)$ gauge structure of the SM is recovered. Examples of these cascade mechanisms are illustrated in Fig. 2.2.1 featuring $\mathrm{SO}(10)$ and E_6, which motivate a variety of models featuring a Z'.

In isolation there is no particular reason for these Z' to have masses as low as the TeV scale; however, for supersymmetric implementations of these unified models, the extra $\mathrm{U}(1)$ breaking scale is generally linked to the scale of soft supersymmetry breaking [30]. Hence, the motivations for a TeV scale Z' are the same as those for TeV scale supersym-

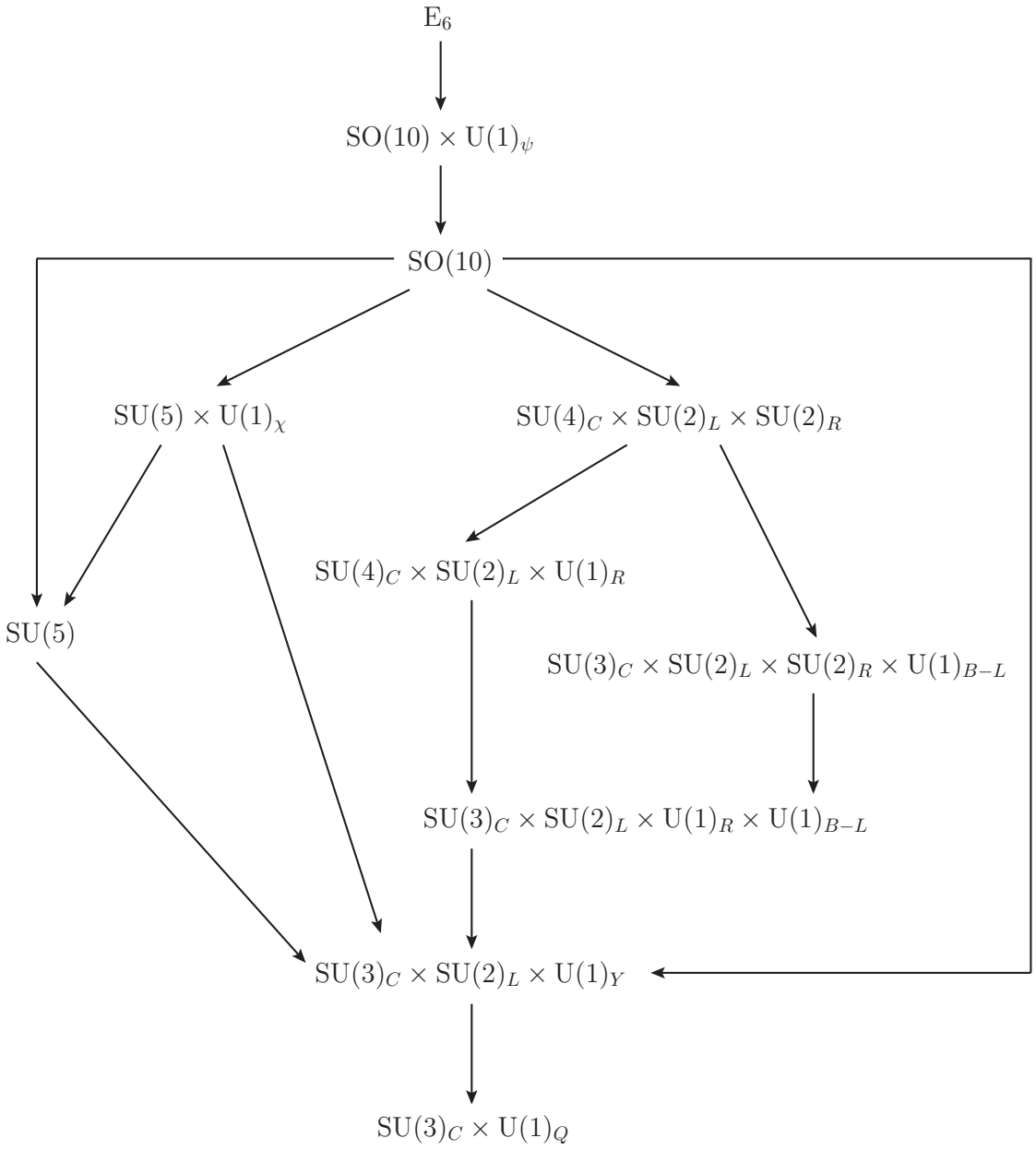

Figure 2.2.1: A chart of the possible spontaneous symmetry breaking chains featuring GUT candidates SU(5), SO(10) and E_6. The residual U(1) symmetries can lead to the Z' benchmark models explored in this study. The Diagram is based on an illustration in Ref. [29]. In general the U(1) symmetries can be broken at close to the GUT scale or remain unbroken until the TeV scale. Thus, while residual U(1) groups are not drawn in subsequent steps, they are not necessarily broken, i.e. $SO(10) \times U(1)_\psi \rightarrow SU(5) \times U(1)_\psi \times U(1)_\chi$.

metry, namely, a solution to the Hierarchy problem, and naturally occurring exact gauge coupling unification [31].

In each of the models, the residual U(1) gauge symmetry is assumed to be broken around the TeV scale, resulting in a massive Z' boson. This leads to an additional term in the low-energy neutral-current (NC) Lagrangian,

$$-\mathcal{L}'_{NC} = eJ^{\mu}_{e}A_{\mu} + g_{Z}J^{\mu}_{Z}Z_{\mu} + g'J'^{\mu}Z'_{\mu}, \tag{2.2.1}$$

for the electromagnetic coupling e to the photon field A^{μ}, g_Z coupling to the Z boson field Z^{μ}, and g' coupling to the Z' boson field Z'^{μ}. The later couples to a vector current,

$$J'^{\mu} = \sum_{f}\bar{\psi}_{f}\gamma^{\mu}Q'\psi_{f} = \sum_{f}\bar{\psi}_{f}\gamma^{\mu}\left[g'^{f}_{L}P_{L} - g'^{f}_{R}P_{R}\right]\psi_{f} = \sum_{f}\bar{\psi}_{f}\gamma^{\mu}\frac{1}{2}\left[g'^{f}_{V} - g'^{f}_{A}\gamma_{5}\right]\psi_{f}, \tag{2.2.2}$$

where $g'^{f}_{L(R)}$ are the chiral couplings to the left(right)-handed projections of a specific fermion field $P_L(P_R)\psi_f$, and $g'^{f}_{V,A}$ are the corresponding vector and axial couplings. These depend on the particular combination of generators in Q', which along with the overall coupling g', depend on the model. The charge generators of these couplings Q' for each model class correspond to those defined in Eqs. 2.2.5, 2.2.17 and 2.2.23. This term leads to a corresponding additional Feynman rule and diagram (Fig. 3.2.1c).

I study a number of benchmark examples of such models, particularly those found in Ref. [21], which may be classified into three types: General Sequential Models (GSM), Generalised Left-Right symmetric (GLR) models and E_6 inspired models. Below I give a brief overview of each classification, followed by a summary of the assumptions and parameters used.

2.2.1 Generalised Sequential Models

Above the scale of EW symmetry breaking, the SM NC Lagrangian may be written as

$$-\mathcal{L}^{SM}_{NC} = g_{L}J^{3\mu}_{L}W^{3}_{L\mu} + g_{Y}J^{\mu}_{Y}B_{Y\mu}, \tag{2.2.3}$$

where g_L and g_Y are the $\mathrm{SU}(2)_L$ and $\mathrm{U}(1)_Y$ gauge couplings, respectively. In the Sequential Standard Model (SSM) an additional neutral gauge boson is introduced with fermionic couplings generated identically to those of the SM Z boson,

$$g'Q'_{SSM} = g_{Z}Q_{Z} = \frac{g_{L}}{\cos\theta_{W}}\left(T^{3}_{L} - \sin^{2}\theta_{W}Q_{e}\right), \tag{2.2.4}$$

where the weak mixing angle θ_W is defined by $\tan\theta_W = g_Y/g_L$.[2] The fermionic couplings of this Z'_{SSM} are uniquely determined by well defined eigenvalues of the T^3_L and Q_e generators, the third component of weak isospin and the Electromagnetic (EM) charge,

respectively. This Z' differs only in being generically heavier than the Z boson and, consequently, by having a larger decay width (Eq. 2.4.8).

The GSMs allow for a general linear combination of these generators,

$$Q'_{\rm GSM} = \cos\theta' T_L^3 + \sin\theta' Q_e. \tag{2.2.5}$$

The Z' coupling is fixed by the condition that $g_Z Q_Z \equiv g' Q'_{\rm GSM}$ for a particular value of θ', implying that the SSM case is recovered when

$$g' = \frac{g_L}{\cos\theta_W}\sqrt{1+\sin^4\theta_W} \approx 0.76, \qquad \theta' = -0.072\pi. \tag{2.2.6}$$

New models are generated by keeping g' fixed and varying θ' over its range, $-\pi/2 \leq \theta' \leq \pi/2$. Clearly, at its extremes we recover pure T_L^3 (left-chiral coupling) and Q_e (heavy photon) models.

In order to demonstrate the derivation of the axial-vector couplings, let's recover the SSM model via its parameterisation angle, $\theta' = -0.072\pi$,

$$\begin{aligned} g'^u_L &= \frac{1}{2}\cos\theta' + \sin\theta'\frac{2}{3} = 0.338, & g'^u_R &= \frac{2}{3}\sin\theta' = -0.150, \\ g'^d_L &= -\frac{1}{2}\cos\theta' - \frac{1}{3}\sin\theta' = -0.413, & g'^d_R &= -\frac{1}{3}\sin\theta' = 0.0748. \end{aligned} \tag{2.2.7}$$

Therefore, recalling that $g'^f_{V,A} = g'^f_L \pm g'^f_R$, the axial-vector couplings are $g'^u_V = 0.19$, $g'^u_A = 0.5$, $g'^d_V = -0.34$, and $g'^d_A = -0.5$. The axial-vector couplings for the remaining models of this class may be found in Tab. 2.2.3.

2.2.2 Generalised Left-Right symmetric models

The LR symmetric model introduces a new isospin group $\mathrm{SU}(2)_R$ perfectly analogous to the $\mathrm{SU}(2)_L$ weak isospin group of the SM, but which acts on right-handed fields. The $\mathrm{SU}(2)_R$ symmetry may then be broken to $\mathrm{U}(1)_R$, linked to the generator T_R^3 associated to the third (diagonal) component of right isospin with eigenvalues $+\frac{1}{2}$ for (u_R, ν_R) and $-\frac{1}{2}$ for (d_R, ν_R),

$$\mathrm{SU}(2)_L \times \mathrm{SU}(2)_R \times \mathrm{U}(1)_{B-L} \to \mathrm{SU}(2)_L \times \mathrm{U}(1)_R \times \mathrm{U}(1)_{B-L}. \tag{2.2.8}$$

Here $\mathrm{U}(1)_{B-L}$ relates to the generator $T_{BL} = \frac{1}{2}(B-L)$ and conserves the difference between the Baryon (B) and Lepton (L) numbers.

[2] $\cos\theta_W = m_W/m_Z$ defines the weak mixing angle experimentally.

Furthermore, the gauge symmetry,

$$\mathrm{SU}(3)_C \times \mathrm{SU}(2)_L \times \mathrm{U}(1)_R \times \mathrm{U}(1)_{B-L}, \tag{2.2.9}$$

arises naturally in the course of breaking an SO(10) GUT, either via $\mathrm{SU}(2)_R$ or directly from a larger intermediate gauge symmetry (Fig. 2.2.1), leading to a NC Lagrangian,

$$-\mathcal{L}_{NC}^{LR} = g_L J_L^{3\mu} W_{L\mu}^3 + g_R J_R^{3\mu} W_{R\mu}^3 + g_{BL} J_{BL}^{\mu} B_{BL\mu}. \tag{2.2.10}$$

All of these versions are anomaly-free after including the three right-handed neutrinos ν_R [23].

To reproduce the standard model, the hypercharge preserving symmetry must be recovered,

$$\mathrm{U}(1)_R \times \mathrm{U}(1)_{B-L} \to \mathrm{U}(1)_Y, \tag{2.2.11}$$

at a scale $m_{Z'} >> m_Z$, making the hypercharge generator $T_Y = T_R^3 + T_{BL}$, with the mass eigenstates of the fields described by orthogonal relations,

$$B_Y^{\mu} = \cos\phi W_R^{3\mu} + \sin\phi B_{BL}^{\mu}, \tag{2.2.12}$$

$$Z_{LR}^{\prime\mu} = -\sin\phi W_R^{3\mu} + \cos\phi B_{BL}^{\mu}. \tag{2.2.13}$$

Here $\tan\phi = g_R/g_{BL}$ and B_Y^{μ} is the massless boson of the $\mathrm{U}(1)_Y$ symmetry, such that its gauge coupling constant is defined through the relation $1/g_Y^2 = 1/g_R^2 + 1/g_{BL}^2$.

Therefore, equating the coupling g'_{LR} with the GUT normalised g_Y of the SM, $Z_{LR}^{\prime\mu}$ couples to a current associated with the charge,

$$Q'_{\mathrm{LR}} = \sqrt{\frac{5}{3}}\left(\tan\phi T_R^3 - \cot\phi T_{BL}\right), \tag{2.2.14}$$

$$\tan\phi = \sqrt{\frac{g_R^2}{g_L^2}\cot^2\theta_W - 1}, \tag{2.2.15}$$

$$g_Y = \sqrt{\frac{3}{5}} g_L \tan\theta_W \approx 0.46. \tag{2.2.16}$$

Furthermore, we may consider Generalised LR (GLR) symmetric models, in which the Z' corresponds to a general linear combination of $\mathrm{U}(1)_R$ and $\mathrm{U}(1)_{B-L}$,

$$Q'_{\mathrm{GLR}} = \cos\theta' T_R^3 + \sin\theta' T_{BL}, \tag{2.2.17}$$

The gauge coupling g' is fixed by $g'_Y Q'_{\mathrm{LR}} \equiv g' Q'_{\mathrm{GLR}}$ for a specific θ', so that the original LR model may be recovered by setting $g' = 0.595$ and $\theta' = -0.128\pi$, providing the following

couplings to quarks,

$$g_L'^u = \frac{1}{3}\sin\theta' = -0.13, \qquad g_R'^u = \frac{1}{2}\cos\theta' + \frac{1}{3}\sin\theta' = 0.33,$$
$$g_L'^d = \frac{1}{3}\sin\theta' = -0.13, \qquad g_R'^d = -\frac{1}{2}\cos\theta' + \frac{1}{3}\sin\theta' = -0.59. \tag{2.2.18}$$

This leads to axial-vector couplings $g_V'^u = 0.33$, $g_A'^u = -0.46$, $g_V'^d = -0.59$, and $g_A'^d = 0.46$. Three further special cases may be identified. Obviously, taking $\theta' = 0, \pi/2$ produces purely T_R^3, T_{BL} generated resonances, respectively, while $\theta' = \pi/4$ leads to a Z' which couples directly to hypercharge (Tab. 2.2.3).

2.2.3 E_6 inspired models

One may propose that the gauge symmetry group at the GUT scale is E_6. As illustrated in Fig. 2.2.1, this proceeds via a series of symmetry breaking mechanisms until the SM gauge symmetry is recovered. For this study, the important mechanisms are those that lead to an extra residual $\mathrm{U}(1)$, namely,

$$\mathrm{E}_6 \to \mathrm{SO}(10) \times \mathrm{U}(1)_\psi, \tag{2.2.19}$$
$$\mathrm{SO}(10) \to \mathrm{SU}(5) \times \mathrm{U}(1)_\chi, \tag{2.2.20}$$
$$\mathrm{SU}(5) \to \mathrm{SU}(3)_C \times \mathrm{SU}(2)_L \times \mathrm{U}(1)_Y. \tag{2.2.21}$$

All of these may occur around the GUT scale, yet it is possible for the $\mathrm{U}(1)_\psi$ and $\mathrm{U}(1)_\chi$ to survive down to the TeV scale. The g' gauge coupling is assumed to be equal to the GUT normalised hypercharge coupling of the SM,

$$g_1(M_Z) = 5/3(e/c_W) \approx 0.462. \tag{2.2.22}$$

All fermions are considered to live in the 16-dimension irreducible spinor representation of $\mathrm{SO}(10)$; thus, by GUT normalisation, all carry a T_ψ charge of $1/\sqrt{24}$. $\mathrm{SO}(10)$ may then be broken as $16 \to \bar{5} + 10 + 1$. Normalisation further implies that the T_χ charges of the $\mathrm{SU}(5)$ representations $\bar{5}$, 10, and 1 are $3/\sqrt{40}$, $-1/\sqrt{40}$, and $-5/\sqrt{40}$, respectively. Furthermore, it may be shown that q, u^c and e^c emerge from the breaking the 10 irrep, while ℓ and d^c emerge from $\bar{5}$ (see Tab. 1.2.1). Right-handed neutrinos ν^c also make an appearance in the trivial representation (Tab. 2.2.2).

Six special cases of E_6 inspired Z' models are considered here, with couplings to quarks $g'Q_{E_6}$. These may be reproduced using an angularly parameterised linear combination of these generators,

$$Q_{E_6} = \cos\theta' T_\chi + \sin\theta' T_\psi. \tag{2.2.23}$$

Two of these cases simply maximise the contribution from either the T_ψ or T_χ generator. The η model occurs in the Calabi-Yau compactifications of the heterotic string if E_6

SU(5) representation	Fields	T_χ charge
$\bar{5}$	q, u^c, e^c	$3/\sqrt{40}$
10	ℓ, d^c	$-1/\sqrt{40}$
1	ν^c	$-5/\sqrt{40}$

Table 2.2.2: The Standard Model (plus right-handed neutrinos) matter fields, their SU(5) representations and T_χ charges.

breaks directly to a rank-5 group [32], In the secluded sector model (S) the U(1) is broken in a sector coupled minimally to ordinary fields [33]. while the inert (I) model has an orthogonal charge to that in the η model via an alternative E_6 breaking pattern [34]. The N model formulates a U(1) symmetry in which ν^c have zero charge, allowing very heavy Majorana masses suitable to take part in a seesaw mechanism to yield small ν masses [35].

Let's take the N model ($\theta' = 0.42\pi$) as an example, remembering that f_R carry the opposite charges of f^c,

$$g'^u_L = \cos\theta' \frac{3}{\sqrt{40}} + \sin\theta' \frac{1}{\sqrt{24}} = 0.316, \quad g'^u_R = -\cos\theta' \frac{3}{\sqrt{40}} - \sin\theta' \frac{1}{\sqrt{24}} = -0.316,$$
$$g'^d_L = \cos\theta' \frac{3}{\sqrt{40}} + \sin\theta' \frac{1}{\sqrt{24}} = 0.316, \quad g'^d_R = \cos\theta' \frac{1}{\sqrt{40}} - \sin\theta' \frac{1}{\sqrt{24}} = -0.158. \quad (2.2.24)$$

Therefore, the axial-vector couplings are $g'^u_V = 0$, $g'^u_A = -0.316$, $g'^d_V = -0.158$, and $g'^d_A = 0.474$. The axial-vector couplings for the remaining models of this class may be found in Tab. 2.2.3.

2.2.4 Summary

For each of the model classes described in sections 2.2.1, 2.2.2 and 2.2.3 g' is fixed and the angular parameter dictating the relative strengths of the component generators is varied until interesting limits for each class are recovered. For the generalised models, in addition to the central values, the interesting limits simply maximise the contribution from either generator. The interesting limits for E_6 inspired models are described in section 2.2.3. The resulting parameters are summarised in Tab. 2.2.3.

2.3 Technicolor and Composite Higgs models

In section 1.5, I outline the hierarchy problem of the SM; namely, the vast difference in scale between the EW scale (v) and the Planck scale, and the consequent fine tuning necessary to retain the observed Higgs mass. While introducing a GUT theory reduces the size of the 'desert' above v, any new scales are generally high.

Class	g'	Model	θ'	g'^u_V	g'^u_A	g'^d_V	g'^d_A	$\Gamma_{Z'}/m_{Z'}$ (%)
GSM	0.760	L	0	0.5	0.5	-0.5	-0.5	4.7
		Q	0.5π	1.333	0	-0.666	0	12.5
		SSM	-0.072π	0.193	0.5	-0.347	-0.5	3.2
GLR	0.595	R	0	0.5	-0.5	-0.5	0.5	2.5
		BL	0.5π	0.333	0	-0.333	0	1.5
		LR	-0.128π	0.329	-0.46	-0.591	0.46	2.1
		Y	0.25π	0.589	-0.353	-0.118	0.354	2.4
E_6	0.462	χ	0	0	-0.316	-0.632	0.316	1.2
		ψ	0.5π	0	0.408	0	0.408	0.5
		η	-0.29π	0	-0.516	-0.387	0.129	0.6
		S	0.129π	0	-0.129	-0.581	0.452	1.2
		I	0.21π	0	0	0.5	-0.5	1.1
		N	0.42π	0	-0.316	-0.158	0.474	0.6

Table 2.2.3: Benchmark model Z' parameters and the resultant axial-vector couplings to quarks, in addition to the decay-width to resonant-mass ratio as a percentage [21].

Another approach is to consider the dynamic generation of v taking inspiration from the features of QCD. In QCD, a scale (Λ_{QCD}), where the strength of the strong coupling becomes large, is dynamically generated with independence of the cut-off scale due to the Yang-Mills self-interactions. Furthermore, another scale emerges in the mechanism of chiral symmetry breaking. In the massless limit QCD possesses a global $\mathrm{SU}(N)_L \times \mathrm{SU}(N)_R$ symmetry in which the left (L) and right (R) chiral components of the N flavours of quark may be independently rotated. However, this asymmetry is then dynamically broken by a chiral condensate in the quantised theory due to a non-zero, non-perturbative QCD vacuum for $q^\dagger_L q_R$ operators. This then possesses an $\mathrm{SU}(N)_V$ vector symmetry ensuring L and R components must be rotated identically. The $N^2 - 1$ generators corresponding to axial transformations of $\mathrm{SU}(N)_A$, in which L and R components are rotated oppositely, then give rise to massless Nambu-Goldstone bosons (NGB), which are pseudoscalar multiplets that may be identified with mesons.

In the SM, the quarks are not massless, but acquire a mass through the EWSB mechanism (section 1.4.1). Thus, the chiral symmetry is broken explicitly. However, for the three lightest quark flavours, $q = u, d, s$, an inexact symmetry exists strong enough to produce pseudo-NGB (pNGB) after SSB leading to the pions (π), kaons (K), and η mesons (η), which have considerably lower masses than the scalar and vector mesons.

So, we see motivation to introduce a new strongly coupled theory, Technicolor, where v will be generated naturally via new matter interactions, and its own scale Λ' will emerge due to Yang-Mills dynamics, analogously with Λ_{QCD} [36, 37]. A host of new NGB will then arise following the automatic chiral symmetry breaking due to the non-zero technicolor vacuum. These composite NGB states may then be 'eaten' by the EW gauge bosons to acquire longitudinal degrees of freedom and masses around the v scale. Additional bound

states, analogous to π's, K's and η's, may also be predicted. Thus, we see that there is no longer any need for a scalar Higgs boson, and the hierarchy problem is no longer a direct cause for concern. Unfortunately, strongly interacting theories require non-perturbative calculations to accurately simulate their dynamics. Minimal Technicolor models with SU(3) symmetries often have their dynamics predicted with direct analogy to QCD. Unfortunately, the light scalar boson observed at the LHC is not predicted by these minimal models. However, the diverse possibilities of a new strongly interacting theory and the natural scale generation it offers is tantalising.

A branch of technicolor is also manifest in composite Higgs models. In these models a light scalar Higgs boson is embedded as a pNGB due to the dynamic symmetry breaking of a new strong sector [38, 39]. These theories introduce a range of gauge group extensions and new global symmetries. Typically, they require multiple new scalar multiplets that explicitly break a partially gauged global symmetry, resulting in a range of new Gauge bosons and pNGBs. The underlying dynamics can radiatively recreate the desired quartic potential of the SM Higgs and new top partners must be introduced to protect from top-induced radiation corrections. A commonly introduced global symmetry is SO(5)/SO(4) which, when dynamically broken, minimally embeds the four degrees of freedom required by a complex doublet scalar Higgs boson, while retaining the accidental SO(4) of the Higgs doublet in the residual symmetry. An example of such a model is the minimal 4D composite Higgs model (4DCHM) [40], which possesses partial compositeness. This features new gauge fields and fermionic partners to third generation quarks associated with bound vector states. The top and bottom quarks thereby gain larger masses and a fermionic mass hierarchy is introduced. This also means that the third generation of quarks feature a stronger coupling to the multiple new Z' gauge fields, motivating top pair production as a discovery channel over dilepton searches [41, 42]. While the analyses presented in this thesis do not investigate this model, it motivates the development of the techniques and framework to investigate top phenomenology with the eventual aim of conducting such an analysis.

2.4 Z' boson decay width

In order to compute cross sections for processes involving a Z' it is necessary to know the decay width. We must consider a number of decay modes for the new particle. The most apparent mode is

$$Z' \to f\bar{f}, \tag{2.4.1}$$

which is present for all considered models. Furthermore, many models allow a mixing between the Z and Z' eigenstates. This results in mixed mass eigenstates, and permits

additional decay modes for the Z' boson,

$$Z' \to W^+W^-, \tag{2.4.2}$$

$$Z' \to hZ. \tag{2.4.3}$$

If kinematically allowed, additional decay modes, equivalent to the above, may be present for BSM scalars and charged/neutral vector bosons. Furthermore, models with multiple Z', and additional mixing, can lead to further decay modes.

2.4.1 Fermionic partial decay width

In order to calculate the cross section for BSM top quark pair production, the decay width of $Z' \to f\bar{f}$ for a specific f pair must be known. As the top pair will be included, the mass of the fermions should be considered. In addition, the total width considers unpolarised initial and final state particles. Therefore, it is convenient to use the trace method to make the calculation and work from the axial-vector cast of the Lagrangian term in Eq. 2.1.3,

$$i\mathcal{M} = -\frac{1}{2} ig' \epsilon_\mu \bar{u} \gamma^\mu (g_V - g_A \gamma_5) v. \tag{2.4.4}$$

Squaring the amplitude and rearranging gives,

$$|\mathcal{M}|^2 = -\frac{1}{4} \epsilon^*_\mu \epsilon_\nu v \bar{v} \gamma^\mu (g_V - g_A \gamma_5) u \bar{u} \gamma^\nu (g_V - g_A \gamma_5). \tag{2.4.5}$$

Keeping track of suppressed spinor indices, this has the form of a trace. Averaging over initial polarisation, summing over final helicities, rearranging and applying the completeness relations gives,

$$\frac{1}{3} \sum_{spin} |\mathcal{M}|^2 = -\frac{1}{12} \left(-g_{\mu\nu} + \frac{k_\mu k_\nu}{m_{Z'}} \right) \mathrm{tr} \left[(\not{p}_2 - m) \gamma^\mu (g_V - g_A \gamma_5) (\not{p}_1 - m) \gamma^\nu (g_V - g_A \gamma_5) \right]. \tag{2.4.6}$$

This must be expanded to 32 terms, and solved individually, which can be automated using Mathematica, with FeynmanParameter [43, 44]. Substituting this solution in to the golden rule for 2-body decays [12],

$$\mathrm{d}\Gamma = \frac{|\mathbf{p}_1|}{32\pi^2 m^2_{Z'}} |\mathcal{M}|^2 \, \mathrm{d}\phi_1 \, \mathrm{d}\cos\theta_1, \tag{2.4.7}$$

gives,

$$\Gamma(Z' \to f\bar{f}) = \frac{g^2_{Z'} m_{Z'}}{48\pi} \beta \left[\frac{3 - \beta^2}{2} c_V^2 + \beta^2 c_A^2 \right], \tag{2.4.8}$$

where

$$\beta = \sqrt{1 - 4\frac{m_f^2}{m_{Z'}}}. \tag{2.4.9}$$

In the massless limit this reduces to [21]

$$\Gamma(Z' \to f\bar{f}) = \frac{g_{Z'}^2 m_{Z'}}{48\pi}\left[g_V^2 + g_A^2\right]. \tag{2.4.10}$$

This may also be expressed using left-right couplings,

$$\Gamma(Z' \to f\bar{f}) = \frac{m_{Z'}}{24\pi}\beta\left[\left(1 - \frac{m_f^2}{m_{Z'}^2}\right)(g_L^2 + g_R^2) + 6\frac{m_f^2}{m_{Z'}^2}g_L g_R\right]. \tag{2.4.11}$$

which would be arrived at naturally, if using the helicity amplitude method [45].

When calculating the width for quarks, we must include the number of colours N_c, and also include the QCD K-factor, $1+\frac{1.045}{\pi}\alpha_s$. A subroutine that automatically performs this calculation for any given Z' is included in the generation tool described in section 4.1.

CHAPTER 3

Top quark production and observables

3.1 The top quark

Prior to the discovery of the Higgs boson at the LHC in 2012, the top quark was the most recently discovered elementary particle, and it remains easily the most massive. The unexpectedly large 173 GeV mass of the top quark also places it the closest to the Electroweak symmetry breaking scale of 246 GeV and means that it is strongly coupled to the SM Higgs via a Yukawa mechanism. This makes it the main contributor to the quadratic divergences of the SM Higgs mass. The top quark is, therefore, highly relevant to new BSM scenarios that seek to explore these mechanisms.

At the LHC top quark pairs are dominantly produced via QCD processes, with subleading s-channel contributions from EW processes (Fig. 3.2.1). Experimentally we only consider the electron and muon final states as taus are unstable and appear as jets which complicates the event reconstruction. With the 13 TeV upgrade, the number of $t\bar{t}$ events increases by approximately a factor of five compared with 8 TeV running, ensuring that top physics is even more significant for the exploration of new physics models.

At LO the decay width of the top quark is given in the SM by

$$\Gamma_t = \left[|V_{td}|^2 + |V_{ts}|^2 + |V_{tb}|^2\right] \frac{g^2}{64\pi} \frac{m_t^3}{m_W^2} \left(1 - \frac{m_W^2}{m_t^2}\right)^2 \left(1 + 2\frac{m_W^2}{m_t^2}\right), \tag{3.1.1}$$

where $V_{t\{d,s,b\}}$ are elements of the CKM quark-mixing matrix, with respective values of

$(8.1\pm0.5)\times10^{-3}$, $(39.4\pm2.3)\times10^{-3}$, and 1.019 ± 0.025, according to latest experiments [46]. It follows that the branching ratio for top quark decay via $t \to bW^+$ is 99.8%. As the top decays almost exclusively via $t \to bW^+$, the final state objects are entirely determined by the decay of the W^+ boson. The $W^+(W^-)$ boson may decay either via $W^+(W^-) \to l^+\nu(l^-\bar{\nu})$ or $W^\pm \to q\bar{q}'$. This leads to three classifications of a $t\bar{t}$ event: if both t and $\bar{t}$ decay via the latter process, this is known as the fully hadronic channel; if both decay via the former process, the channel is dileptonic; else, it is semileptonic, or, based on its collider signature, lepton-plus-jets.

At LO the partial decay width of the W boson to leptons can be calculated as

$$\Gamma(W \to e\nu_e) = \Gamma(W \to \mu\nu_\mu) = \Gamma(W \to \tau\nu_\tau) = \frac{g_W^2 m_W}{48\pi}. \tag{3.1.2}$$

For decays to quark pairs, accounting for the colour factor and unitarity of the CKM matrix, determines that

$$\Gamma(W \to qq') = 6\Gamma(W \to e\nu_e). \tag{3.1.3}$$

Hence,

$$\Gamma_W = 9\Gamma(W \to e\nu_e). \tag{3.1.4}$$

Taking into account the combinatorics for two top decays, branching ratios for each $t\bar{t}$ production channel at LO are

$$\begin{aligned} R_{ee} = R_{\mu\mu} = R_{\tau\tau} &= 1/81, \\ R_{e\mu} = R_{e\tau} = R_{\mu\tau} &= 2/81, \\ R_{ej} = R_{\mu j} = R_{\tau j} &= 12/81, \\ R_{jj} &= 36/81. \end{aligned} \tag{3.1.5}$$

So, about 44.4% of top production is fully hadronic/all jets, 44.4% is semileptonic and 11.1% is dileptonic. However, τ final states are rarely considered experimentally due to their appearance as jets and we often look at e or μ channels in isolation. Therefore, the values in Eq. 3.1.5 provide useful branches ratios for lepton-plus-jets when $\ell = e, \mu$. We see that the semihadronic cross section is twelve times larger than the dileptonic for a particular channel. When accounting for higher order QCD corrections the hadronic branching fractions will be enhanced, and $\mathrm{BR}(t \to be\nu_e)$ decreases.

The large 1.3 GeV decay width of the top quark gives it an extremely short lifetime, meaning that it decays prior to its hadronisation. Consequently, information, such as spin, is transmitted to daughter particles and may be reconstructed from the angular distribution of the decay products. The electromagnetic charge of the top may also be tagged via the decay lepton. Additionally, its large mass induces non-trivial space/spin effects. These reasons allow us to make use of variables that cannot be reconstructed for other

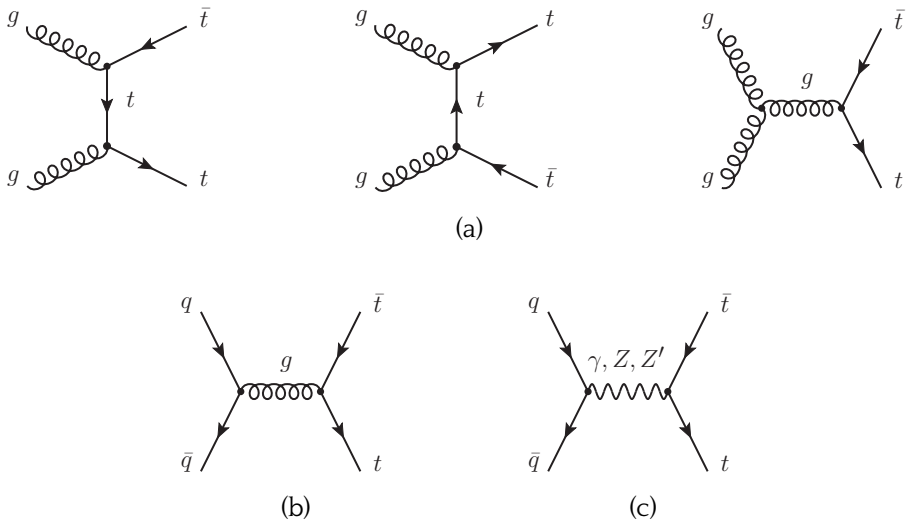

Figure 3.2.1: Leading Order Feynman Diagrams for top pair production in the SM and BSM: (a) gluon-gluon fusion; (b) gluon mediated quark-antiquark annihilation; (c) signal processes are mediated by an interfering photon, Z boson and Z' boson.

discovery channels, such as asymmetry observables.

3.2 Top pair production via a Z' boson

Top-antitop pairs are an alternative observation channel to Drell-Yan for Z' bosons (see chapter 2). Its reduced importance for the discovery of a Z' is due to the larger background, which includes irreducible QCD production of $t\bar{t}$ pairs, in addition to the EW irreducible background, for each top decay signature. Furthermore, there are reducible backgrounds, especially severe in the fully hadronic decay mode. The complex six-body final state results in fact in either multi-jet signatures, with a large QCD background, or events with one or multiple sources of missing transverse momentum (because of neutrinos escaping detection).[1] This reduces the potential for first discovery in $t\bar{t}$ compared to the DY channel. However, there are theoretical scenarios that favour strong couplings between a new Z' and top quarks. These can arise due to leptophobic Z', or extra bosons with an enhanced coupling to third generation fermions, as is common in, for example, Composite Higgs Models [41]. Thus, this channel lends itself to searches for models with enhanced third generation couplings (section 2.3).

In addition to their importance in extracting the couplings to top quarks, resonance searches in the $t\bar{t}$ channel can offer additional handles on the properties of a Z'. This is due to unique variables available for this channel, owing to the fact that (anti)top quarks decay prior to hadronisation, meaning spin information is effectively transmitted to their decay products. The couplings of initial and final state fermions to the Z' are differ-

[1] While missing transverse momentum is, in general, the correct technical terminology, throughout this thesis missing transverse mass may be used interchangeably, as is common in the experimental literature.

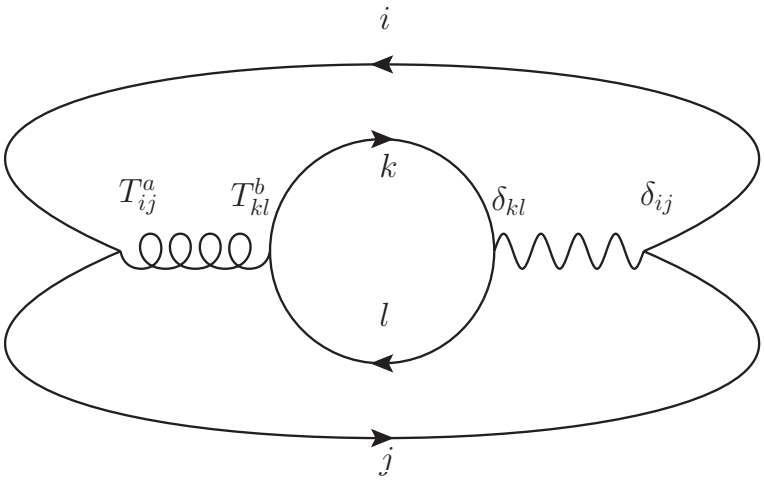

Figure 3.3.1: Feynman diagram showing the vanishing interference term in quark-antiquark annihilation between a gluon, as a colour octet, and a colour singlet (γ, Z or Z') mediated in the s-channel.

ent between charge/spin asymmetries and cross sections. This implies that charge/spin asymmetries provide additional information on the nature of the underlying Z'. However defining these asymmetries requires the reconstruction of the top-antitop quark pair. It is difficult to fully reconstruct the system in dilepton $t\bar{t}$ events which feature two sources of missing transverse momentum, while fully hadronic $t\bar{t}$ events come with very large backgrounds. Chapter 7 focuses on the lepton-plus-jets channel at the parton level, while chapter 8 presents an analysis on the dilepton channel at the detector level.

3.3 Differential cross section

While both gluons and the neutral electroweak bosons mediate top pair production via a $q\bar{q}$ initial state (Fig. 3.2.1), the interference term vanishes. This can be seen in Fig. 3.3.1 where the gluon-quark-antiquark vertex is associated with an SU(3) generator T^a_{ij}, where i, j traverse the colour space. As the electroweak mediators are colourless, the equivalent vertex carries a δ_{ij} factor. The resulting trace over the colour indices will vanish for the traceless generators.[2] I.e. the colour octet cannot undergo interference with a colour singlet object in the s-channel. Due to this, and the differing initial states of gluon-gluon fusion and quark-quark annihilation, the square matrix element may be linearly separated as,

$$|\mathcal{M}(pp \to t\bar{t})|^2 = |\mathcal{M}(\mathrm{QCD})|^2 + |\mathcal{M}(\gamma, Z, Z')|^2. \tag{3.3.1}$$

[2] Another way to explain this is that quarks annihilating to a colourless object must carry opposite charge of the same colour, while in QCD quarks will annihilate to a coloured gluon carrying a combination of two colour charges in a superposition of states governed by the Gell-Mann matrices. Thus, the colour lines are incompatible and the diagram is forbidden.

It follows that the Z' boson interferes only with the neutral EW bosons, with total square matrix element [47],

$$|\mathcal{M}(\gamma, Z, Z')|^2 = \frac{\hat{s}^2}{24}\frac{D^{ij}}{1+\delta^{ij}}\left\{C_q^{ij}\left[C_t^{ij}(1+\beta^2\cos^2\theta)+B_t^{ij}(1-\beta^2)\right]+2A_q^{ij}A_t^{ij}\beta\cos\theta\right\}, \tag{3.3.2}$$

with q denoting the initial quark species and t the final top quark. The square energy in the parton centre of momentum frame is denoted $\hat{s}$, a fraction of the overall collider square energy, s. Here, indices $i, j = 0, 1, 2$ represent the vector bosons and repeated indices are summed over. The angle θ lies between the top quark momentum and the incoming quark direction, in the $t\bar{t}$ centre of mass frame, and $\beta = \sqrt{1-4m_t^2/\hat{s}}$. For fermion species f,

$$A_f^{ij} \equiv g_V^{if}g_A^{jf} + g_A^{if}g_V^{jf}, \qquad B_f^{ij} \equiv g_V^{if}g_V^{jf} - g_A^{if}g_A^{jf}, \qquad C_f^{ij} \equiv g_V^{if}g_V^{jf} + g_A^{if}g_A^{jf}, \tag{3.3.3}$$

while the propagator structure is given by

$$D_{ij} \equiv \frac{(\hat{s}-m_i^2)(\hat{s}-m_j^2)+m_i m_j\Gamma_i\Gamma_j}{\left((\hat{s}-m_i^2)^2+m_i^2\Gamma_i^2\right)\left((\hat{s}-m_j^2)^2+m_j^2\Gamma_j^2\right)}. \tag{3.3.4}$$

Eq. 3.3.4 illustrates the potential for interference between the SM vector bosons and new resonances when $i \neq j$. If we take the Z' boson in isolation ($i = j = 2 ='$) and integrate over $\cos\theta$, the coupling structure for the cross section is

$$\hat{\sigma} \propto \left(g_V'^{q\,2}+g_A'^{q\,2}\right)\left((4-\beta^2)g_V'^{t\,2}+g_A'^{t\,2}\right), \tag{3.3.5}$$

where the coupling $g'^{q(t)}$ is between the Z' and the initial (top) quark species.

3.4 Asymmetry observables

Due to the properties of the top quark discussed in section 3.1, in addition to standard kinematic variables, we may make use of spatial/spin asymmetries to uniquely profile Z' couplings.

Asymmetries are defined most generally as

$$A = \frac{N_1 - N_2}{N_1 + N_2}, \tag{3.4.1}$$

where the number of events N are divided into two mutually exclusive categories, N_1 and N_2. As these are defined by dividing event numbers, they negate some systematic uncertainties. Two common classifications of asymmetries are based on charge and spin. Variables, such as this, are interesting because they demonstrate a unique dependence on the couplings to Z'; therefore, serving to distinguish between new models

and the SM, as well as between themselves. They may also represent a viable discovery mechanism for Z', with more significant distinction between signal and background than the usual event-counting, bump-hunt search methods. From the decay products of the tops, we may construct observables that correlate with these asymmetries.

3.4.1 Asymmetry uncertainty and significance

The general equation for calculating the uncertainty of a function f dependent on two independent variables x and y is

$$\delta f(x,y) = \sqrt{\left(\frac{\partial f}{\partial x}\delta x\right)^2 + \left(\frac{\partial f}{\partial y}\delta y\right)^2}. \tag{3.4.2}$$

For an asymmetry observable (Eq. 3.4.1),

$$\frac{\partial A}{\partial N_1} = \frac{1}{N} - \frac{N_1 - N_2}{N^2} = \frac{2N_2}{N^2}, \qquad \frac{\partial A}{\partial N_2} = -\frac{1}{N} - \frac{N_1 - N_2}{N^2} = -\frac{2N_1}{N^2}. \tag{3.4.3}$$

Assuming Gaussian errors, i.e. $\delta N = \sqrt{N}$, and substituting into Eq. 3.4.2,

$$\delta A = \frac{2}{N}\sqrt{\frac{N_1 N_2}{N}}. \tag{3.4.4}$$

The number of events N is related to the cross section by $N = L\epsilon\sigma$, where ϵ is the efficiency, L the integrated luminosity and σ the cross section. Hence, [48]

$$\delta A = \sqrt{\frac{1 - A^2}{L\epsilon\sigma}}. \tag{3.4.5}$$

A general definition of the significance S between predictions for an observable O with uncertainty δO from hypotheses 1 and 2 is

$$S = \frac{O_1 - O_2}{\sqrt{(\delta O_1)^2 + (\delta O_2)^2}}. \tag{3.4.6}$$

This can be calculated on a bin-by-bin basis to compare significances for asymmetry observables to more standard variables, like the invariant top quark pair mass [48]. While a more sophisticated evaluation of significance is employed in this thesis, this variable has value as an initial test, and has been employed in numerous previous studies.

3.5 Charge asymmetries

Charge conjugation (C) is an operation that transforms between a field describing a particle and one describing the corresponding antiparticle,

$$\psi = -i\gamma^2\gamma^0\bar{\psi}, \tag{3.5.1}$$

while parity (P) transforms between left and right-handed fields. The neutral-current weak interactions preserve the combined operations of charge conjugation and parity (CP), but not each when applied individually. Thus, when measuring the asymmetry of a process under parity, charge conjugation is simultaneously probed. The effect of a parity transformation may be effectively probed in the spatial (angular) distributions of decay products. Consequently, in top pair production a charge asymmetry equates to an asymmetry in the angular dependence of the two-body decay products.

If the quark direction could be known with certainty, i.e. there existed some way to build a collider of bare quarks and antiquarks, and its direction was identified with $+z$, the charge asymmetry could be defined by taking the difference of events where the (anti)top is found in the $+z$ or $-z$ hemisphere of the phase space,

$$A_C^{t(\bar{t})} = \frac{N(\cos\theta_{t(\bar{t})} > 0) - N(\cos\theta_{t(\bar{t})} < 0)}{N(\cos\theta_{t(\bar{t})} > 0) + N(\cos\theta_{t(\bar{t})} < 0)}, \tag{3.5.2}$$

where the angle $\theta_{t(\bar{t})}$ spans between the (anti)top quark momentum and the incoming quark direction, in the centre of mass frame of the top quark pair. $A_C^{t(\bar{t})}$ can equivalently be defined via the (anti)top rapidity $y_{t(\bar{t})}$. This asymmetry separates the cross section by integrating over opposite halves of the angular phase space,

$$\hat{\sigma}_F = \int_0^1 \frac{\mathrm{d}\hat{\sigma}}{\mathrm{d}\cos\theta}\,\mathrm{d}\cos\theta, \qquad \hat{\sigma}_B = \int_{-1}^0 \frac{\mathrm{d}\hat{\sigma}}{\mathrm{d}\cos\theta}\,\mathrm{d}\cos\theta. \tag{3.5.3}$$

Applying these integrations on Eq. 3.3.2 and taking the difference, as found in the A_C^t numerator, leaves only the final term. Neglecting SM mediators and their interference, the dependence due to the Z' term, in isolation, for this asymmetry is

$$A_{FB}^{\prime t} \propto g_V^{\prime q} g_A^{\prime q} g_V^{\prime t} g_A^{\prime t}. \tag{3.5.4}$$

Comparing this with Eq. 3.3.5 one observes that A_{FB}^t depends linearly on all axial-vector couplings, providing more information on their properties than magnitude alone. The SM encodes a positive charge asymmetry due to the contribution from Z boson mediated quark-antiquark annihilation. This means that the top quark preferentially propagates in the same direction as the incoming quark in the centre of momentum frame of the interacting quark-antiquark pair.

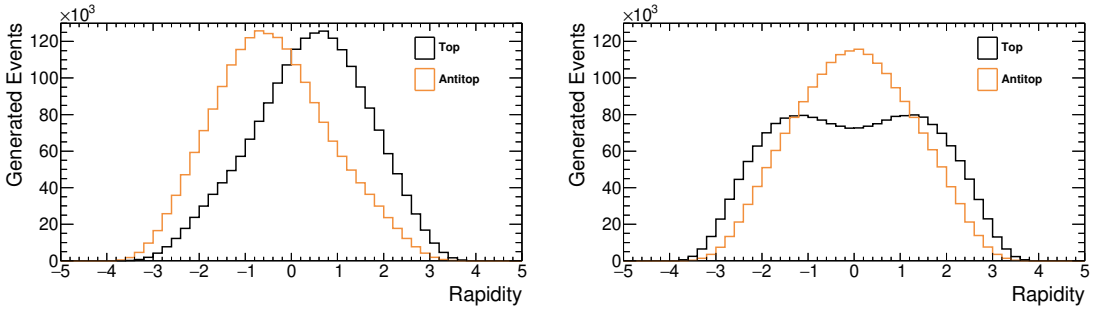

(a) $p\bar{p}$ collisions, e.g. Tevatron (b) pp collisions, e.g. LHC

Figure 3.5.1: Truth rapidity distributions for the top and antitop in top pair production mediated by a photon, Z boson and 2 TeV GLR-R Z' boson in $p\bar{p}$ and pp collision, such as found at the Tevatron and LHC experiments, respectively.

3.5.1 Forward-Backward asymmetry

The forward-backward asymmetry is constructed by splitting the detector region into two hemispheres, forward ($+z$) and backward ($-z$), and taking the difference between the number of events where the (anti)top quark is detected on either side,

$$A_{FB}^{t(\bar{t})} = \frac{N(\cos\theta_{t(\bar{t})} > 0) - N(\cos\theta_{t(\bar{t})} < 0)}{N(\cos\theta_{t(\bar{t})} > 0) + N(\cos\theta_{t(\bar{t})} < 0)}, \tag{3.5.5}$$

where the angle $\theta_{t(\bar{t})}$ spans between the (anti)top quark momentum and the $+z$-direction defined in the $q\bar{q}$ centre of momentum frame. A_{FB}^{t} can equivalently be defined via the (anti)top rapidity $y_{t(\bar{t})}$.

At proton-antiproton ($p\bar{p}$) colliders, such as the Tevatron, A_{FB}^{t} is very useful as the $+z$-direction of the detector, defined by the direction of the colliding p, is used to define $\cos\theta$. In this case the p direction is highly correlated with the incoming q direction, as the contribution due to an interaction between a sea q from the $\bar{p}$ and a sea $\bar{q}$ from the p is vanishing, i.e. the q has an overwhelming probability for positive momentum in the z-dimension of the lab frame. Therefore, the top quark preferentially emerges in the $+z$ half of the detector, i.e. with positive rapidity, for processes with positive charge asymmetry, as shown in Fig. 3.5.1a.

3.5.2 Central asymmetry

At the LHC, however, the incoming quark has an equal probability of coming from either proton, and each event will receive a contribution from both configurations. Hence the forward and backward region are not tied to the couplings (Eq. 3.5.4) any longer. This is important for EW processes - dependent on chiral couplings - where the incoming parton direction is important. This means that the $+z$ direction is uncorrelated with the top direction, independent of the underlying charge asymmetry for the process, and a

symmetric rapidity distribution is found, as shown in Fig. 3.5.1b. However, observe that for processes with non-zero charge asymmetry the top and antitop distributions are distinct. For events with overall positive charge asymmetry the antitop distribution becomes centralised, while the top distribution peaks on either side of zero. So, at the LHC, it is preferential to define a variable dependent on the difference between the absolute rapidities of the top and antitop in the collider frame, $\Delta|y_t| \equiv |y_t| - |y_{\bar{t}}|$,

$$A_C^t = \frac{N(\Delta|y_t| > 0) - N(\Delta|y_t| < 0)}{N(\Delta|y_t| > 0) + N(\Delta|y_t| < 0)}. \tag{3.5.6}$$

This variable is known within the ATLAS collaboration as A_C, denoting central – or simply, charge – asymmetry. In some literature it is called A_{RFB} for rapidity-difference forward-backward asymmetry.

3.5.3 Reconstructed Forward-Backward asymmetry

For the same underlying reasons motivating the definition of A_C^t (section 3.5.2), $\cos\theta_t$ is not useful to define an A_{FB} at the LHC; at proton-proton colliders incoming particles carry identical parton density functions (PDFs). Thus, the detector $+z$-direction may no longer be identified with the incoming quark direction. However, due to the shape of the PDFs, the q is likely to have a larger partonic momentum fraction than the $\bar{q}$. Therefore, the z^* axis may be chosen along the boost direction of the top pair resulting in a reference axis highly correlated with the incoming quark direction [48]. In practice, one may multiply the cosine of the angle measured with respect to the collider z axis by the sign of the rapidity of the top quark pair in the collider frame y_{tt},

$$\cos\theta_t^* = \frac{y_{tt}}{|y_{tt}|}\cos\theta_t, \tag{3.5.7}$$

and use it to define the reconstructed forward-backward asymmetry,

$$A_{FB^*}^t = \frac{N(\cos\theta_t^* > 0) - N(\cos\theta_t^* < 0)}{N(\cos\theta_t^* > 0) + N(\cos\theta_t^* < 0)}. \tag{3.5.8}$$

It is not immediately apparent, but the sign of this variable is always the same as $\Delta|y_t|$, as they are effectively picking out the same direction to define the coordinate system. This can be demonstrated by evaluating the sign of $\cos\theta_t^*$ for all possible values of $|y_t|$ and $|y_{\bar{t}}|$, remembering that $y_{t(\bar{t})}$ is measured in the lab frame, and rapidity transforms linearly, i.e. $y_t = y_{tt} + y_t^*$, etc. Thus, $A_{FB^*}^t$ is effectively equivalent to the central asymmetry, A_C, used by LHC collaborations. A cut on y_{tt} may be made in order to probe the region of high partonic momentum fraction and enhance the contributions from the $q\bar{q}$ initial state.

$\mathbf{f}$	l	d	ν	u	W	b
$\kappa_{\mathbf{f}}$	1	1	0.3	0.3	0.39	-0.39

Table 3.6.1: Spin analysing powers of $t\bar{t}$ decay products.

3.6 Spin asymmetries

An interesting feature of the top quark is its decay prior to hadronisation due to its short lifetime. Information on the spin configuration is, therefore, retained in the angular distributions of its decay products.

Treating the top quark in the narrow width approximation, the total partonic matrix element squared for top pair production, including decay channels, is

$$|\mathcal{M}|^2 \propto \mathrm{tr}[\bar{\rho} R \rho] = \bar{\rho}_{\lambda'_{\bar{t}}\lambda_{\bar{t}}} R_{\lambda_{\bar{t}}\lambda'_{\bar{t}},\lambda_t\lambda'_t} \rho_{\lambda_t\lambda'_t}, \tag{3.6.1}$$

where $\lambda_{(\bar{t})t}$ denotes the spin of the (anti)top and R represents the density matrix for on-shell top pair production from initial partons, averaged over initial spins [45]. Here, $(\bar{\rho})\rho$ is the density matrix corresponding to the decay of the polarised (anti)top,

$$\rho_{\lambda_t\lambda'_t} = \frac{\Gamma_f}{2}\Big(1 + \kappa_f \boldsymbol{\sigma}\cdot\mathbf{q}_f\Big)_{\lambda_t\lambda'_t}, \tag{3.6.2}$$

where $\boldsymbol{\sigma}$ are the Pauli matrices, and κ_f is the 'spin analysing power' of the particular decay product f with decay width Γ_f and 3-momentum $\mathbf{q}_f$. Information about the top spin is preserved in the distribution of $\cos\theta_f^t$, the angle between the top momentum (measured in the $t\bar{t}$ rest frame) and the momentum of the decay fermion f (in the t rest frame). This distribution has the form:

$$\frac{1}{\Gamma_f}\frac{\mathrm{d}\Gamma_f}{\mathrm{d}\cos\theta_f^t} = \frac{1}{2}(1 + \kappa_f P_t \cos\theta_f^t), \tag{3.6.3}$$

where P_t is the polarisation of the top ensemble. The spin analysing powers at tree level for different decay product species are shown in Tab. 3.6.1, and it is observed that the lepton has maximal spin analysing power.

3.6.1 Top polarisation asymmetry

The top polarisation asymmetry, or single spin asymmetry (A_L), measures the net polarisation of the (anti)top quark by subtracting events with positive and negative helicities,

$$A_L = \frac{N(+,+) + N(+,-) - N(-,-) - N(-,+)}{N(+,+) + N(+,-) + N(-,-) + N(-,+)}, \tag{3.6.4}$$

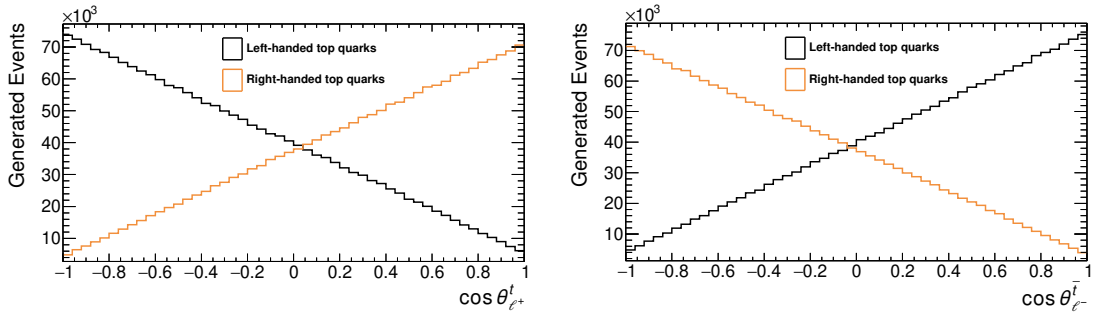

(a) $\cos\theta^{t}_{\ell^+}$ (b) $\cos\theta^{\bar{t}}_{\ell^-}$

Figure 3.6.2: Truth $\cos\theta^{t}_{\ell^+}$ and $\cos\theta^{\bar{t}}_{\ell^-}$ distributions for the antilepton originating in the decay of a top (via a W-boson) in top pair production mediated by a 2 TeV GLR-R Z' (right-chiral coupling only) and GSM-T3L Z' boson (left-chiral coupling only) in pp collisions, such as found at LHC experiments.

where $N(\lambda_t, \lambda_{\bar{t}})$ denotes the number of events observed with eigenvalues of the helicity operator $\lambda_t = \pm$ and $\lambda_{\bar{t}} = \pm$ for the top quark and antitop quark, respectively.

In order to determine the coupling structure for the numerator of A_L, it is necessary to first calculate the polarised matrix elements of Z' production and decay $\mathcal{M}(\lambda_t, \lambda_{\bar{t}})$. These calculations have been performed and verified against Ref. [45]. This is most straightforward using the left-right couplings. With these, and suppressing the propagator factor, the matrix element terms that survive in the numerator can be shown to have the form

$$\mathcal{M}_{A_L} = \frac{\hat{s}^2}{12}\left\{(q_L^2 + q_R^2)(t_L^2 - t_R^2)(1 + \cos^2\theta) + 2(q_L^2 - q_R^2)(t_L^2 + t_R^2)\cos\theta\right\}, \tag{3.6.5}$$

where θ is as defined in Eq. 3.3.2. Once again, examining the Z' in isolation shows the coupling structure,

$$A_L \propto \left(g_V^{q\,2} + g_A^{t\,2}\right) g_V^t g_A^t. \tag{3.6.6}$$

Interestingly, the incoming quark dependence is proportional to the square of the couplings (symmetric), while the dependence on the top couplings is linear (antisymmetric). This observable is, therefore, directly sensitive to the chirality of the Z' coupling to the top [49, 50].

The linear relationship in Eq. 3.6.3 enables A_L to be probed directly in lepton-plus-jets and dilepton events, using the angular distribution of the decay $\ell^+(\ell^-)$ in the $t(\bar{t})$ rest frame, $\cos\theta^{t}_{\ell^+}$ ($\cos\theta^{\bar{t}}_{\ell^-}$). For (left)right-polarised (anti)top quarks the distribution has a positive (negative) gradient, as shown in Fig. 3.6.2.

The product $\kappa_f P_t$ is equivalent to the A_L observable as defined for stable polarised top

quarks (Eq. 3.6.4). Complimentary polarisation asymmetries can be defined as,

$$A_{P_+} = \frac{N(\cos\theta^t_{\ell+} > 0) - N(\cos\theta^t_{\ell+} < 0)}{N(\cos\theta^t_{\ell+} > 0) + N(\cos\theta^t_{\ell+} < 0)}, \qquad A_{P_-} = \frac{N(\cos\theta^{\bar{t}}_{\ell-} > 0) - N(\cos\theta^{\bar{t}}_{\ell-} < 0)}{N(\cos\theta^{\bar{t}}_{\ell-} > 0) + N(\cos\theta^{\bar{t}}_{\ell-} < 0)}. \tag{3.6.7}$$

Assuming CP invariance, these two measurements can be combined to give the total polarisation $P = 2AP = A_{P+} + A_{P-})$. Alternatively, the variable $P^{CPV} = 2A^{CPV} = A_{P+} - A_{P-}$ measures possible polarisation introduced by a maximally CP-violating process.

3.6.2 Top spin correlation

The top spin correlation asymmetry, or double spin asymmetry (A_{LL}), measures the net spin correlation of the (anti)top quark by subtracting events with aligned and anti-aligned helicities,

$$A_{LL} = \frac{N(+,+) + N(-,-) - N(+,-) - N(-,+)}{N(+,+) + N(-,-) + N(+,-) + N(-,+)}. \tag{3.6.8}$$

It can be shown that the resulting coupling structure for this observable is:

$$A_{LL} \propto \left(g'^{q\,2}_V + g'^{q\,2}_A\right)\left((2+\beta^2)g'^{t\,2}_V + 3g'^{t\,2}_A\right). \tag{3.6.9}$$

Through comparison with Eq. 3.3.5, one may observe that this coupling structure is not significantly different from that of the cross section. This makes the spin correlation a potentially less interesting observable than the single spin asymmetry.

As CP is conserved at leading order, we may obtain the polarised antitop density matrix by making the replacement $\kappa_f \to -\kappa_f$. From Eq. 3.6.3, the differential cross section for $t\bar{t}$ production with a dilepton final state has dependency

$$\frac{1}{\sigma}\frac{\mathrm{d}^2\sigma}{\mathrm{d}\cos\theta^t_{\ell+}\,\mathrm{d}\cos\theta^{\bar{t}}_{\ell-}} \propto \frac{1}{4}\left(1 + \kappa_{\ell+}P_t\cos\theta^t_{\ell+} + \kappa_{\ell-}P_{\bar{t}}\cos\theta^{\bar{t}}_{\ell-} + \kappa_{\ell+}\kappa_{\ell-}C_{t\bar{t}}\cos\theta^t_{\ell+}\cos\theta^{\bar{t}}_{\ell-}\right), \tag{3.6.10}$$

where $C_{t\bar{t}}$ specifies the coefficient of top spin correlation, with $\kappa_{\ell+}\kappa_{\ell-}C_{t\bar{t}} = A_{LL}$. The angles are calculated in the helicity basis, between the $t(\bar{t})$ spin axis, which is taken to be the t momentum direction in the parton centre of mass frame, and the $\ell^+(\ell^-)$ momentum direction in the $t(\bar{t})$ rest frame.

Thus, A_{LL} may be probed using the $\cos\theta^t_{\ell+}\cos\theta^{\bar{t}}_{\ell-}$ distribution. In models with negligible top polarisation, such as the SM, using equation 3.6.10, the spin correlation can be extracted from the mean of the $\cos\theta^t_{\ell+}\cos\theta^{\bar{t}}_{\ell-}$ distribution via

$$A_{LL} = -9\left\langle \cos\theta^t_{\ell+}\cos\theta^{\bar{t}}_{\ell-}\right\rangle. \tag{3.6.11}$$

This formula is quoted regularly in all ATLAS spin correlation papers. However, the assumption of zero net top polarisation ceases to be valid in many BSM scenarios. Therefore, a suitable variable for probing spin correlation may require further investigation.

It is also possible to construct an asymmetry in the style of A_{FB} using the product $\cos\theta^{t}_{\ell^+}\cos\theta^{\bar{t}}_{\ell^-}$ as the defining variable,

$$A_{c_1c_2} = \frac{N(\cos\theta^{t}_{\ell^+}\cos\theta^{\bar{t}}_{\ell^-} > 0) - N(\cos\theta^{t}_{\ell^+}\cos\theta^{\bar{t}}_{\ell^-} < 0)}{N(\cos\theta^{t}_{\ell^+}\cos\theta^{\bar{t}}_{\ell^-} > 0) + N(\cos\theta^{t}_{\ell^+}\cos\theta^{\bar{t}}_{\ell^-} < 0)}. \tag{3.6.12}$$

The cosine of the opening angle φ between the two lepton momenta measured in the rest frames of their respective parent (anti)top quark is also sensitive to spin correlations,

$$A_{\cos\varphi} = \frac{N(\cos\varphi > 0) - N(\cos\varphi < 0)}{N(\cos\varphi > 0) + N(\cos\varphi < 0)}. \tag{3.6.13}$$

Measurement of these observables require top reconstruction, as all angles are determined in the (anti)top rest frames.

3.7 Summary of coupling dependence for observables

In summary, the observables demonstrate dependence on the couplings ($g_{V,A}$) of the neutral vector bosons to initial state fermions (i) and final top quarks (t),

$$\sigma \propto \left((g^i_V)^2 + (g^i_A)^2\right)\left(3(g^t_A)^2 + (g^t_V)^2(2+\beta^2)\right), \tag{3.7.1}$$

$$A_{FB} \propto g^i_V g^i_A g^t_V g^t_A, \tag{3.7.2}$$

$$A_{LL} \propto \left((g^i_V)^2 + (g^i_A)^2\right)\left(3(g^t_A)^2 + (g^t_V)^2(2+\beta^2)\right), \tag{3.7.3}$$

$$A_L \propto \left((g^i_V)^2 + (g^i_A)^2\right) g^t_A g^t_V \beta, \tag{3.7.4}$$

where $\beta = \sqrt{1-4m_t^2/\hat{s}}$. These provide multiple distinguishing handles for profiling Z' bosons embedded by different BSM theories.

CHAPTER 4

Event generation and analysis tools

4.1 Overview

The analyses in this thesis make use of a custom Monte Carlo (MC) event generation program for simulation of the hard scattering processes leading to top pair production and decay. The amplitude calculations for these processes are made at Leading Order (LO) and based on helicity amplitudes (section 4.4) assembled with HELAS subroutines [51]. The foundational SM square matrix elements are created by MadGraph [52] and modified by hand for BSM. The VEGAS AMPlified (VAMP) package [53], based on the earlier VEGAS package [54], is used for the multi-dimensional numerical phase-space integration and the generation of unweighted events. A number of different Parton Distribution Function (PDF) sets are available for use with the tool. The most recent of these are the CT14 LO tables [55]; however, CTEQ6 [56] and MRS99 [57] sets are provided, particularly for verification with previous results (section 4.7). Generally, the CT14LL (LO) tables are used for PDFs throughout this thesis, with a factorisation/renormalisation scale of $Q = \mu = 2m_t$ [58]. The b and t quarks are assigned masses of 4.18 GeV and 172.5 GeV, respectively, while the lighter quarks are treated in the massless limit.

The program can write the minimal event information (event weight, PDG particle IDs, and 4-vectors) directly to a ROOT n-tuple, in binary format, using RootTuple, which minimises storage space and eases a parton-level root analysis. Alternatively, if one wishes to further process the events with a parton shower / hadronisation tool, an output text file in the standard Les Houches Event Format (LHEF) can be produced [59].

The results of this tool have been validated against Refs. [48] and [60] using the same parameter choices and – upon resolving a bug in the former paper resulting in a factor of four increase in the calculation of the Z' decay width – results agree perfectly.

In this thesis the full chain of event generation begins with the custom parton-level generator. Calculations may be limited to $2 \to 2$ stable top/lepton pair production, though this is utilised in this thesis for validation/comparison purposes only. All results presented in thesis include off-shell W-boson and top decay using $2 \to 6$ matrix elements, unless stated otherwise. For the lepton-plus-jets focused analysis, presented in chapter 7, the event analysis and top reconstructions begins here with the six-body final state at the parton-level. In chapter 8 the dilepton final state is further evolved using Pythia8 [61, 62, 63] in order to simulate parton-shower and hadronisation to a complex multiple particle system; the final state then undergoes detector simulation and object reconstruction using Delphes [64, 65, 66].

4.2 Higher-order corrections

The Next-to-Leading Order (NLO) QCD corrections to the SM $t\bar{t}$ cross-section have been developed extensively, proceeding from stable, on-shell tops [67, 68, 69, 70] to those that account for their decay using a spin-correlated narrow-width approximation [71, 72, 73] to fully off-shell calculations [74, 75, 76, 77]. The NLO EW corrections have also been studied comprehensively for stable tops [78, 50, 49, 79, 80]. More recently NNLO QCD corrections have been fully calculated [81, 82, 83], as well Next-to-next-to-leading log threshold resummation of soft radiation [84, 85, 86].

In this analysis, all events are generated at Leading Order (LO) without higher-order corrections to SM or BSM processes. This is justified by several points.

Firstly, the NLO QCD corrections to a new neutral heavy resonance are calculated in Refs. [87, 88] It shows that the total cross section for $Z' \to t\bar{t}$ can be enhanced by a K-factor of 1.2 – 1.4, depending on the mass of the resonance. However, the shape of the NLO distributions are not significantly different from those at LO, with a negligible effect on the spin correlation of the top quark pair.[1]

Secondly, the focus of this analysis is primarily asymmetry observables, and their potential for distinguishing model classes. At LO A_{FB} and A_L are flat as a function of m_{tt}.[2] NNLO predictions and experiment show a linearly increasing A_{FB} with m_{tt} between 350 GeV and 750 GeV [89, 82]. However, this trend may not be extrapolated to higher energies, and the NNLO behaviour of SM processes at TeV energies is unknown. LHC

[1] N.B. While not a model considered here, a Randall-Sundrum KK Graviton can have a total NLO K-factor as high as 2.0, with distributions significantly different from those at LO.

[2] In the SM there is a non-zero LO contribution to A_L from the Z boson.

measurements with $\sqrt{s} = 8$ TeV data show a negligible charge asymmetry over the full energy range [90, 91, 92, 93]. Likewise NLO predictions of top polarisation indicate negligible top polarisation [50], which persists experimentally [94]. Therefore, the assumption is made that NLO and NNLO contributions cancel in the asymmetries, and higher-loop effects may be safely ignored for the purposes of this study.

4.3 Parton-level event generation

This section outlines the mathematical formulation necessary to simulate proton-proton collisions at the LHC.

Working in the high energy limit, we may assume the protons to be massless. Therefore, in the pp centre-of-momentum frame, which corresponds also to the collider frame as the protons collide with the same energies, the proton momenta take the explicit forms:

$$P_1 = (E_{col}, 0, 0, E_{col}); \qquad P_2 = (E_{col}, 0, 0, -E_{col}) : \qquad s = 4E_{col}^2. \tag{4.3.1}$$

To proceed, we must apply the parton model. This makes the simple assumption that, for a hadron with momentum P, a constituent parton i will have some longitudinal fraction $0 < \xi < 1$ of P, in the hadron momentum direction.[3]

$$p_i = \xi_i P_i \tag{4.3.2}$$

This assumption is valid to leading order in QCD. The partons may be any quark or anti-quark: u, d, s, c, b; or a gluon g ($F_t(x) \approx 0$). The contribution to the interaction amplitude due to a parton of species f with a longitudinal fraction of ξ is given by $F_f(\xi)\,\mathrm{d}\xi$, where $F(\xi)$ is the parton distribution function (PDF). The measurement of the momentum transfer q uniquely determines the value of ξ: $\xi = x$. The PDFs also depend upon the scale of the interaction Q, which we take to be $Q = 2m_t$. If we work in the parton centre of mass frame, remembering that all initial particles have zero mass, we can identify that the total energy in this frame is $\sqrt{\hat{s}} \equiv E$. In the following formulation variables will be measured in the parton centre-of-momentum frame, henceforth called the parton frame, unless stated otherwise.

It has been shown in Ref. [95] that for all orders in perturbation theory the cross section takes the form of the hard scattering process convolved with structure functions for the incoming hadrons. The structure functions encompass all the collinear singularities and spectator parton interactions. It follows that the partonic cross-section for a particular

[3] Note that here 'parton-level' may refer to this treatment of the initial state particles, while in the rest of this report we are referring to the final state particles.

interaction at the LHC is:

$$\sigma(pp \to \{j\}) = \sum_i \int \mathrm{d}x_1 \int \mathrm{d}x_2 \, F_i(x_1) F_{\bar{i}}(x_2) \hat{\sigma}(i(x_1 P_1)\bar{i}(x_2 P_2) \to \{j\}). \tag{4.3.3}$$

Here $j = 3..N$ labels the final particles. We also sum over initial partons which includes all species of quarks/antiquarks u, d, s, c, b, as well as gluons g.

The most general formula for the cross-section of a $2 \to n$ particle collision is given by [12]

$$\mathrm{d}\hat{\sigma} = \frac{1}{2E_1 2E_2 |v_1 - v_2|} \left| \mathcal{M}\left(X_1(p_1)X_2(p_2) \to \{X_j(p_j)\}\right) \right|^2 \mathrm{d}\Pi_n. \tag{4.3.4}$$

And the phase space integral over the final states has the form

$$\mathrm{d}\Pi_n = \left[\prod_j \frac{\mathrm{d}^3 p_j}{(2\pi)^3} \frac{1}{2E_j} \right] (2\pi)^4 \delta^{(4)} \left(\sum p_j - p_1 - p_2 \right). \tag{4.3.5}$$

We are interested in top pair production; if t and $\bar{t}$ can be directly detected, we are interested in a $2 \to 2$ interaction. In this limit the differential cross-section becomes

$$\text{``} \frac{\mathrm{d}^2 \hat{\sigma}}{\mathrm{d}\cos\theta \, \mathrm{d}\phi} = \frac{1}{2\hat{s}} \frac{1}{(2\pi)^2} \frac{|\mathbf{p}_3|}{4E} |\mathcal{M}|^2. \tag{4.3.6}$$

The calculation of $\mathbf{p}_3$ follows from solving a standard two-body decay problem. So, the full parton-level $2 \to 2$ cross-section is

$$\frac{\mathrm{d}\sigma}{\mathrm{d}\cos\theta \, \mathrm{d}\phi} = \sum_f \int \mathrm{d}x_1 \int \mathrm{d}x_2 \; f_f(x_1) f_{\bar{f}}(x_2) \frac{1}{2\hat{s}} \frac{1}{(2\pi)^2} \frac{|\mathbf{p}_3|}{4E} |\mathcal{M}|^2. \tag{4.3.7}$$

In reality, of course, the tops decay very rapidly and cannot be detected directly. Due to the large Yukawa coupling, by far the most common decay channel is $t \to bW^+ \to bf\bar{f}'$, where f is a fermion. We are interested, therefore, in a $2 \to 6$ process. This makes the phase space integration much more complex. The calculation is performed using sequential 2-body decays. This also increases the complexity of the matrix element calculation.

4.4 Matrix Element Calculation using Helicity Amplitudes

At the LHC we have no control over the initial polarisation of the partons and the ATLAS detector, likewise, can not determine, directly, the spins of detected particles. Therefore, we average over the initial particle states and sum over the final ones. So, we are

interested in

$$\frac{1}{2}\sum_{\lambda_1}\frac{1}{2}\sum_{\lambda_2}\sum_{\lambda_3}...\sum_{\lambda_N}|\mathcal{M}(\lambda_1\lambda_2\to\{\lambda_j\})|^2=\frac{1}{4}\sum_{spins}|\mathcal{M}|^2\equiv\left\langle|\mathcal{M}|^2\right\rangle. \tag{4.4.1}$$

For simple $ab \to cd$ interactions, we could write down the amplitude using the Feynman rules and calculate the summation by taking a trace over the gamma matrices and using the spin and polarisation completeness relations. However, for tree-level diagrams with many vertices such as in figure 7.4.1, this calculation becomes much more complex, slowing computer performance. One might consider separating the $2 \to 2$ cross-sections and subsequent decays and combining the results. However, the high instability the top means that it may be highly off-shell (section 4.6). Hence,

$$\mathcal{M}(q\bar{q}\to t\bar{t}\to bW^+\bar{b}W^-)\neq\mathcal{M}(q\bar{q}\to t\bar{t})\mathcal{M}(t\to bW^+)\mathcal{M}(\bar{t}\to\bar{b}W^-). \tag{4.4.2}$$

Therefore, we must calculate the full irreducible 6-vertex diagram, resulting in proliferation of the terms $(\mathcal{M}_i\mathcal{M}_j)$. To resolve this we may use an alternative method, known as the Helicity Amplitude technique. The matrix elements may be given explicit form as a complex number: we can calculate the amplitudes for each helicity combination, then add the individual results and take the square. For example, we can calculate a $2 \to 2$ process using

$$\left\langle|\mathcal{M}|^2\right\rangle=\frac{1}{4}\left[|(\mathcal{M}(++;++)|^2+|\mathcal{M}(-+;++)|^2+...+|\mathcal{M}(--;--)|^2\right]. \tag{4.4.3}$$

In the massless limit, chiral spinors have a definite helicity and we may choose a basis such that we can construct spinor products $s(p_1,p_2)=\bar{u}(p_1,\lambda_1)u(p_2,\lambda_2)$ as explicit complex numbers. The formalism behind selecting a suitable basis to construct these spinor products; the identities used in spinor calculations; and how the technique may be extended to include massive particles, is detailed in [96] and [97]. To understand the form these calculations take, we will outline the calculation for $q\bar{q}\to t\bar{t}$, in the massless limit, via the photon.

Via usual application of the Feynman rules, we can instantly write down the following amplitudes (in the Feynman gauge):

$$i\mathcal{M}=\frac{e^2}{s}\bar{u}(p_2,\lambda_2)\gamma_\mu u(p_1,\lambda_1)\bar{u}(p_3,\lambda_3)\gamma^\mu u(p_4,\lambda_4) \tag{4.4.4}$$

Where s is the square photon energy. If we make the spinor indices explicit, and use $\pm$ notation for spin up and spin down wavefunctions, we can write this as

$$i\mathcal{M}(\lambda_1\lambda_2;\lambda_3\lambda_4)=\frac{1}{s}\left[\bar{u}^{\lambda_1}(p_2)\gamma_\mu u^{\lambda_2}(p_1)\right]\gamma^\mu_{\alpha\beta}\,\bar{u}^{\lambda_3}_\alpha(p_3)u^{\lambda_4}_\beta(p_4) \tag{4.4.5}$$

To proceed further we must select the initial and final helicities and apply the identities from [98, 96, 99].

$$i\mathcal{M}(++;++) = \frac{1}{s}\left[\bar{u}^{+}(p_2)\gamma_\mu u^{+}(p_1)\right]\gamma_{\alpha\beta}\bar{u}^{+}_{\alpha}(p_3)u^{+}_{\beta}(p_4) \tag{4.4.6}$$

$$= \frac{1}{s}\left[2u^{+}(p_1)\bar{u}^{+}(p_2) + 2u^{-}(p_2)\bar{u}^{-}(p_1)\right]_{\alpha\beta}\bar{u}^{+}_{\alpha}(p_3)u^{+}_{\beta}(p_4) \tag{4.4.7}$$

$$= \frac{1}{s}\left[2\bar{u}^{+}(p_3)u^{+}(p_1)\bar{u}^{+}(p_2)u^{+}(p_4) + 2\bar{u}^{+}(p_3)u^{-}(p_2)\bar{u}^{-}(p_1)u^{+}(p_4)\right] \tag{4.4.8}$$

$$= \frac{1}{s}2s(p_3,p_2)s(p_4,p_1) \tag{4.4.9}$$

So, we see that calculations can be performed sequentially. This allows us to efficiently reuse generated wavefunctions, as well as vector currents common to multiple diagrams: which is well suited to electronic computation. For the numerical calculations, we perform the explicit summations using HELAS subroutines [51].

SM diagrams and matrix element calculations are generated automatically using MadGraph [52], with generalisations when necessary. BSM processes are added by including new HELAS subroutines with the required Z' properties.

4.5 Monte Carlo Integration

We wish to generate events that simulate nature, which is determined by the probabilistic quantum mechanics described in section 1.1. To do this, we can use Monte Carlo integration to naturally sample the phase space. This works by approximating the integration like so:

$$\int_{x_1}^{x_2} f(x)\,\mathrm{d}x = (x_2 - x_1)\,\langle f(x)\rangle \tag{4.5.1}$$

$$\langle f(x)\rangle = \frac{1}{N}\sum_{i=1}^{N} f(x_i). \tag{4.5.2}$$

The VEGAS algorithm [54] improves upon this basic method using importance sampling. This makes the integration more accurate with less overall phase space points. VEGAS AMPlified (VAMP) improves on this algorithm and provides functions for parallel event generation [53].

To increase the efficiency of the integration the integrand is flattened. To do this we make a shift of integration variables

$$\mathrm{d}x_1\;\mathrm{d}x_2 \to \mathrm{d}x^1\;\mathrm{d}x^2; \quad x^2 = \frac{E - m_3 - m_4}{E_{max} - m_3 - m_4}; \quad x^1 = \frac{x_1 - \tau}{1 - \tau}, \tag{4.5.3}$$

such that Eq. 4.3.7 becomes:

$$\frac{\mathrm{d}\sigma}{\mathrm{d}\cos\theta\,\mathrm{d}\phi} = \sum_f \int \mathrm{d}x^1 \int \mathrm{d}x^2 F_f(x_1) F_{\bar{f}}(x_2) \frac{1}{2\hat{s}} \frac{1}{(2\pi)^2} \frac{|\mathbf{p}^3|}{4E} (1-\tau) \frac{2E}{s} (E_{\max} - m_3 - m_4) |\mathcal{M}|^2 \tag{4.5.4}$$

This is the final $2 \to 2$ integrand for use with the VEGAS algorithm. In the case of $2 \to 6$ phase space integration, the propagators of the massive unstable intermediate t and W introduce resonant peaks in the integrand which have the form of a Breit-Wigner distribution, introducing peaks in the integrand. One can again perform a Jacobian transformation so that the integral is flatter in the new integration variable. For integrals of the form,

$$I = \int_{M^2_{\min}}^{M^2_{\max}} \mathrm{d}m^2 \frac{1}{(m^2 - M^2)^2 + M^2\Gamma^2} \tag{4.5.5}$$

the transformation considered is $m^2 \to \rho$, where

$$m^2 = M\Gamma \tan\rho + M^2, \tag{4.5.6}$$

with corresponding Jacobian is given by:

$$J = \left| \frac{\partial m^2}{\partial \rho} \right| = M\Gamma \sec^2 \rho. \tag{4.5.7}$$

Thus, the integral becomes

$$I = \frac{1}{M\Gamma} \int_{\rho_{\min}}^{\rho_{\max}} \mathrm{d}\rho. \tag{4.5.8}$$

This transformation is used for each unstable particle in the $2 \to 6$ space, i.e. each $t(\bar{t})$ and $W^+(W^-)$ to reduce the variance.

4.5.1 Symmetrising the integral

When the forward-backward asymmetry is small, the numerator comprises the subtraction of two very large numbers of generated events to give approximately zero. Therefore, small errors in the integration result in a very inaccurate calculation of A^*_{FB}. It is, therefore, preferable to symmetrise the integral of the phase-space in the dimension of the variable used in defining the asymmetry. Therefore, for each phase space point generated by VEGAS, we also include the negative phase space point along this dimension. The drawback of this, is that the code takes twice as long to run for each symmetrisation.

Figure 4.5.1 shows the A^*_{FB} with and without symmetrisation in $\cos\theta$ and well as x_1 and x_2, the parton momentum fractions of the partons from proton 1 and 2, which are interchanged for each VEGAS point. We see that the interchange of x_1 and x_2 offers the greatest improvement in A^*_{FB} when $A_{FB} \approx 0$, with little improvement when including

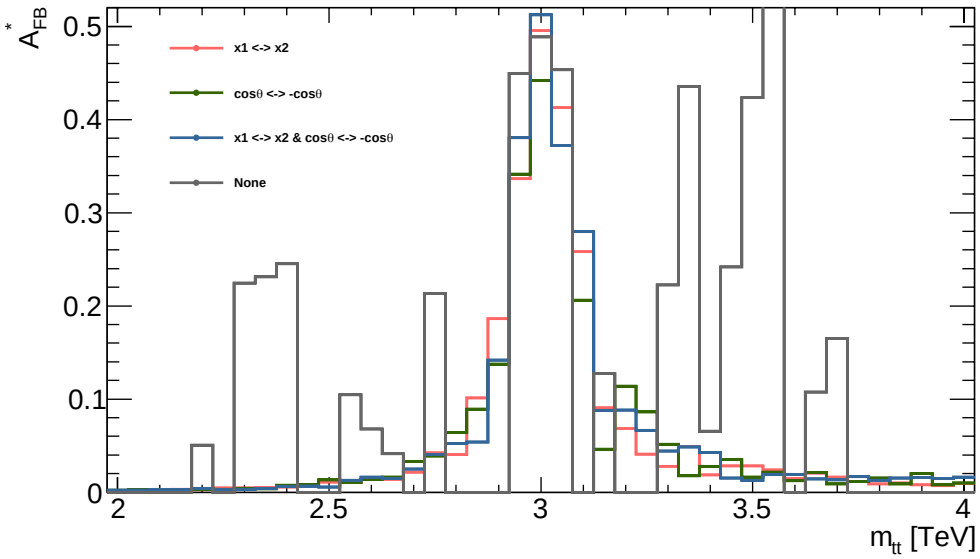

Figure 4.5.1: Plot comparing the of A_{FB} with (1) exchange of x_1 and x_2, (2) exchange of $\cos\theta$ and $-\cos\theta$, (3) both of the above, and (4) none of the above.

the symmetrisation over $\cos\theta$, therefore, we include only the former technique in our simulations.

4.6 The Breit-Wigner and Narrow Width Approximations

There are two common approximations made when calculating the cross section for unstable particles. The first is the Breit-Wigner (BW) approximation, where we effectively make the substitution $M \to M - \frac{i\Gamma t}{2}$ in the propagator, and assume that Γ is sufficiently small to neglect the Γ^2 term.[4]

$$\frac{-ig_{\mu\nu}}{q^2 - M^2} \to \frac{-ig_{\mu\nu}}{q^2 - (M^2 - i\Gamma/2)^2} \approx \frac{-ig_{\mu\nu}}{q^2 - M^2 + iM\Gamma} \tag{4.6.1}$$

The form of the propagator comes from the re-summation of 1-PI loop corrections on the bare propagator. As usual the real part of the pole of the propagator defines the renormalised mass and the imaginary part defines the width. When we have multiple fields coupling to the same particle, the propagator may be written as a matrix with off-diagonal contributions, generating mixings in the masses and widths. In general, diagonalising for the mass eigenstates will leave off diagonal terms in the width [100]. In the SM, for $pp \to t\bar{t}$ the Z-boson is the only unstable intermediate particle and so the BW approximation is valid. The BW propagator is still a good approximation in BSM scenarios, if different unstable particles have independent BW profiles, however, when

[4]The full propagator for the Z is in fact $\frac{-i\left(g_{\mu\nu} - \frac{q_\mu q_\nu}{M^2}\right)}{q^2 - M^2}$, but when neglecting fermion masses we may neglect the $\frac{q_\mu q_\nu}{M^2}$ part.

resonances are close together we must take account of these effects [22]. This becomes important when multiple Z' models are considered.

The Narrow Width Approximation (NWA) is widely used in the calculation of cross sections involving the production of short-lived particles. Formally, when making the NWA, we factorise the phase space and integrate out the BW resulting from the squared denominator of the resonant particle's propagator (see [101]). Effectively, this assumption replaces the BW propagator with a Dirac delta function, ensuring the massive particle is produced at its pole as an asymptotic, real particle. Hence, its subsequent decay may be treated as an independent process, enforcing the equality in Eq. 4.4.2,

$$\mathcal{M}(q\bar{q} \to t\bar{t} \to bW^+\bar{b}W^-) \Rightarrow \mathcal{M}(q\bar{q} \to t\bar{t})\mathcal{M}(t \to bW^+)\mathcal{M}(\bar{t} \to \bar{b}W^-). \tag{4.6.2}$$

This introduces an estimated uncertainty of $\mathcal{O}(\Gamma/M)$. Its use is valid when the following five conditions are met [102].

1. The total decay width of a particle is much smaller than its mass: $\Gamma \ll M$.
2. The decay products have a much smaller mass than the parent: $m \ll M$.
3. The scattering energy is much larger than the parent mass: $\sqrt{\hat{s}} \gg M$.
4. There is no significant interference with other resonant or non-resonant processes.
5. The resonant propagator is, effectively, separable from the matrix element.

The NWA is widely valid and widely used for calculating SM processes, but may cease to be so for many BSM scenarios. This has been shown in the case of the MSSM in Ref. [102]. In particular, this is true for theories with quasi-degenerate resonances, where even the BW assumption loses validity [100]. Such is the case for extra-dimensional theories such as the AADD [22].

In our event generation tool all intermediate particles are produced off-shell.[5] However, we may optionally enforce the NWA for the tops by making $\Gamma_t << m_t$. This allows us to test the validity of the NWA approximation for particular BSM models.

4.7 CT14 Parton Distribution Functions

The tool makes use of the latest leading order CT14 Parton Distribution Functions (PDFs) from the CT collaboration [55]. Fig. 4.7.1 shows the m_{tt} distribution on a logarithmic scale for the previously dominantly used CTEQ6L1 PDF set [57] and the equivalent updated set from CT14. Overall the cross section increases over the full mass range with CT14 PDFs,

[5] This introduces an issue with gauge invariance, as we do not include the full set of diagrams giving the same final state. This is normally a subleading effect.

but with a marked decrease above approximately 10(12) TeV for quark-quark annihilation (gluon-gluon fusion). On this scale one can see that the distributions are lower at very high m_{tt} for all species. Fig. 4.7.2 shows the m_{tt} distributions for processes mediated by γ, Z and Z' on linear scale where it is apparent that the differential cross section increases on resonance for the $u\bar{u}$ initial state, and decreases for the $d\bar{d}$ initial state. The impact of the updated PDFs on $A^t_{FB^*}$ is also shown in Fig. 4.7.3. Overall $A^t_{FB^*}$ decreases over the full mass range with CT14 PDFs. This is most apparent in the low to mid mass region. In the high mass region the asymmetry shows less variation for the updated the PDF sets.

4.8 Validation of results

4.8.1 Validating polarised Top level asymmetries

Firstly, we must validate our results against the previous findings in Ref. [103]. This group evaluated the same range of benchmark model Z's with masses of 2 TeV. These predictions were made assuming a collider energy (E) of 14 TeV with 100 fb^{-1} of integrated luminosity (L) and an overall reconstruction efficiency (ϵ_{reco}) of 0.1. The comparison for reconstructed forward-backward asymmetry $(A_{RFB}/A_{FB}*)$ is shown in figure 4.8.1. These plots indicate that our results for the magnitude and uncertainty of $A_{FB}*$ is correct. However, there is a factor of four discrepancy in the Z' widths. This may come from an error converting from V-A to L-R couplings in [103] due to the form of the neutral current Lagrangian.

4.8.2 Validating Z' production in Drell-Yan processes

In section 4.8.1 we found that the predicted decay widths of the Z's are four times larger in [103]. To validate our results we compare our results with those of [60]. This group evaluated the same range of benchmark model Z's with masses of 3 TeV using the Drell-Yan final state. These predictions were made assuming a collider energy (E) of 13 TeV with 100 fb^{-1} of integrated luminosity (L). The comparisons for the differential cross section, reconstructed forward-backward asymmetry $(A_{FB}*)$ and the corresponding significances (calculated using Eq. 3.4.6) are shown figure 4.8.2. Plots agree very well, despite being calculated using completely different (Mathematica-based) framework.

4.9 Parton Shower

Every process that contains electrically and/or colour charged particles in the initial and final state will radiate photons and/or gluons. These take of the form of sequential branching decays $a \to bc$ forming a tree-like structure. These are at sufficiently high energies that perturbative QCD is valid, and formally these showers represent higher-

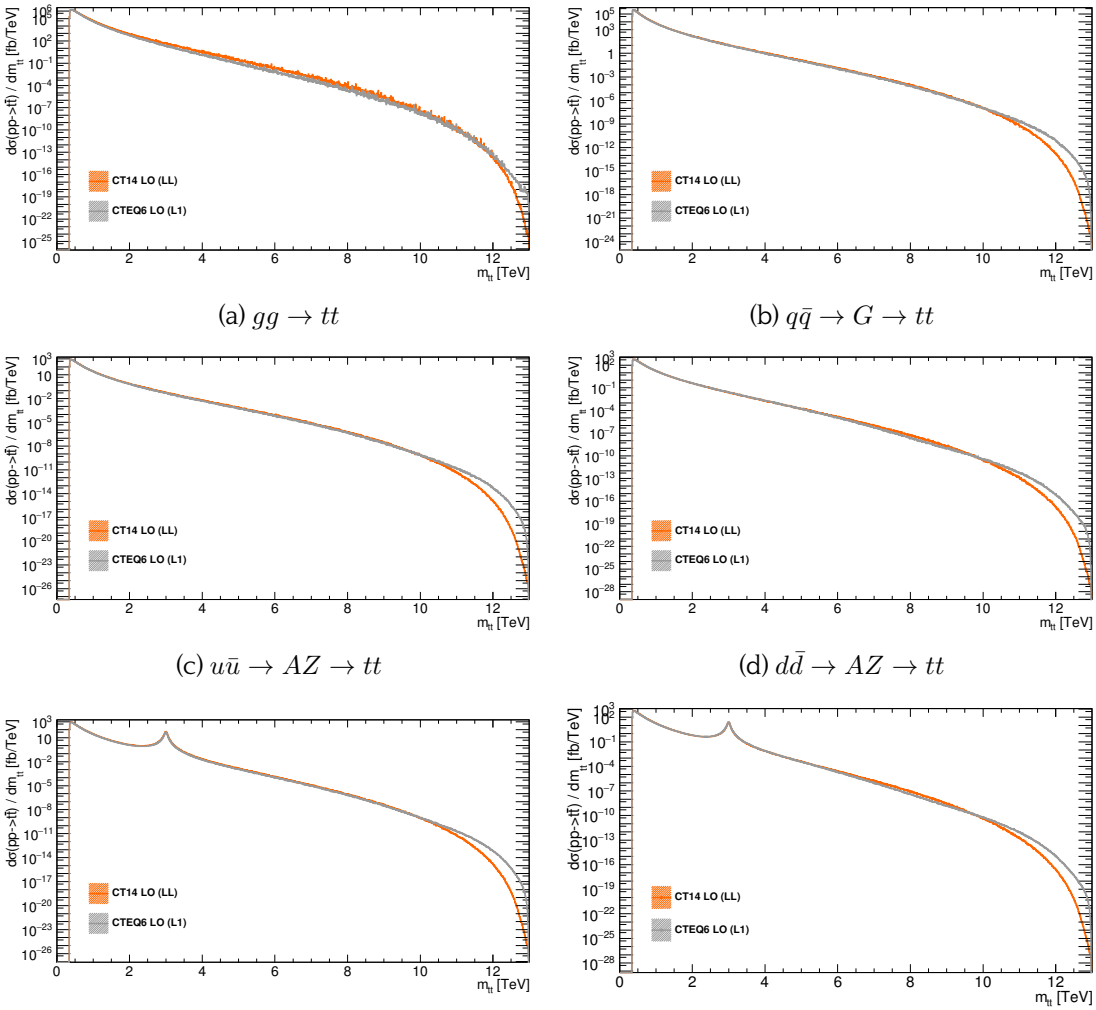

(a) $gg \to tt$

(b) $q\bar{q} \to G \to tt$

(c) $u\bar{u} \to AZ \to tt$

(d) $d\bar{d} \to AZ \to tt$

(e) $u\bar{u} \to \gamma Z Z'_{\mathrm{GLR-R}} \to tt$

(f) $d\bar{d} \to \gamma Z Z'_{\mathrm{GLR-R}} \to tt$

Figure 4.7.1: Plot of the differential cross section distribution with respect to the stable top pair invariant mass comparing Leading Order CTEQ6 (grey) and new CT14 (orange) Parton Distribution Functions (PDFs) in log scale for 13 TeV collisions. Processes are shown for gluon-gluon fusion, gluon and EW mediated quark-quark annihilation, and quark-quark annihilation including an interfering 3 TeV GLR-R Z' boson. Error bands show uncertainty in the integration.

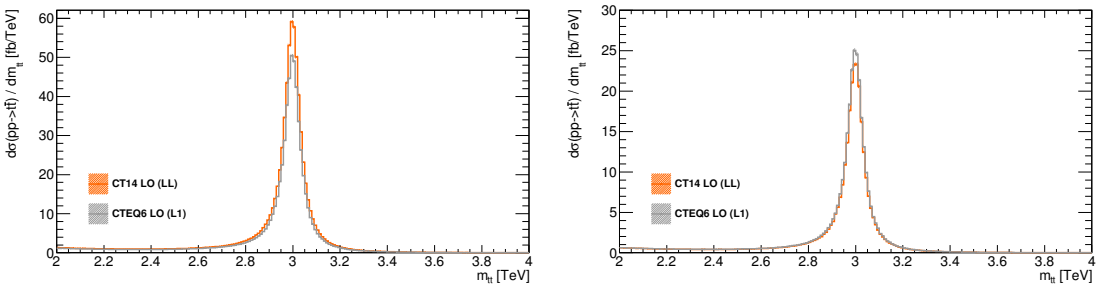

(a) $u\bar{u} \to \gamma Z Z'_{GLR-R} \to tt$ (b) $d\bar{d} \to \gamma Z Z'_{GLR-R} \to tt$

Figure 4.7.2: Plot of the differential cross section distribution with respect to the stable top pair invariant mass comparing Leading Order CTEQ6 (grey) and new CT14 (orange) Parton Distribution Functions (PDFs) in linear scale for 13 TeV collisions. Processes are shown for quark-quark annihilation including an interfering 3 TeV GLR-R Z' boson. Error bands show uncertainty in the integration.

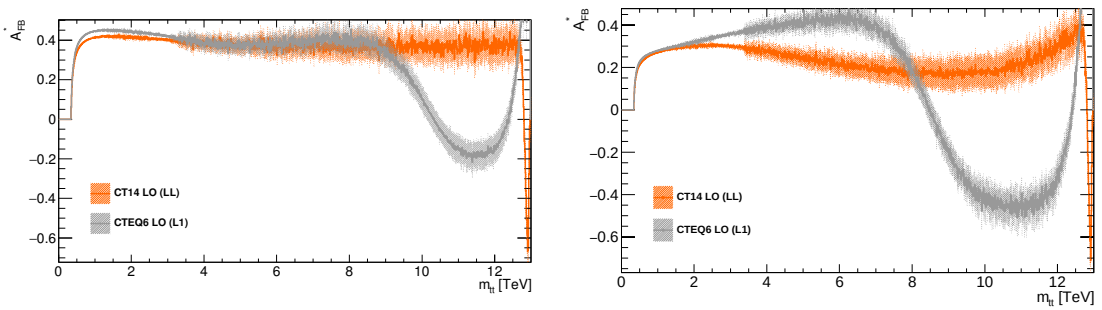

(a) $u\bar{u} \to \gamma Z Z'_{GLR-R} \to tt$ (b) $d\bar{d} \to \gamma Z Z'_{GLR-R} \to tt$

Figure 4.7.3: $A^t_{FB^*}$ plots comparing LO CT14 (orange) and CTEQ6 (grey) PDFs [55, 57] for 13 TeV collisions. Processes are shown for quark-quark annihilation including an interfering 3 TeV GLR-R Z' boson for u, d quarks. Error bands show uncertainty in the integration.

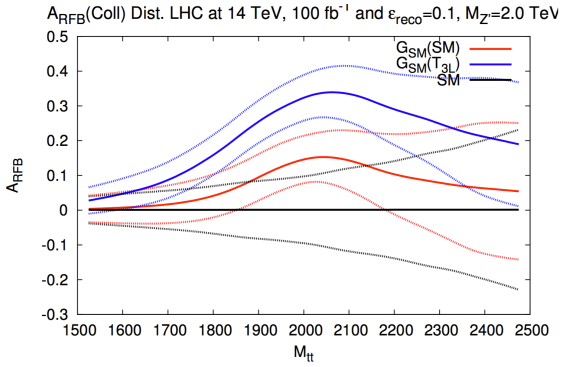

(a) GSM (Basso et al)

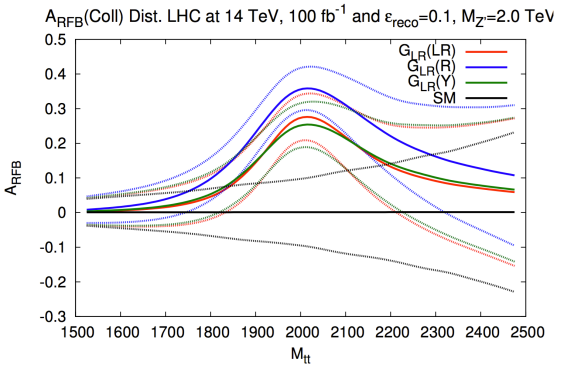

(b) GLR (Basso et al)

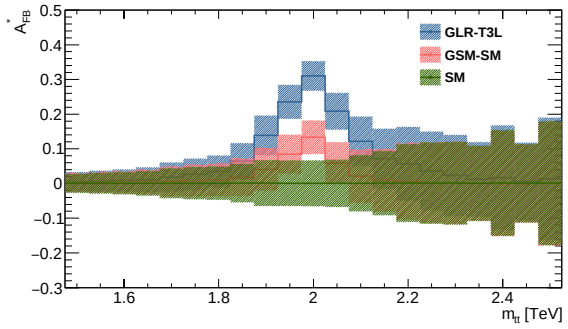

(c) GSM

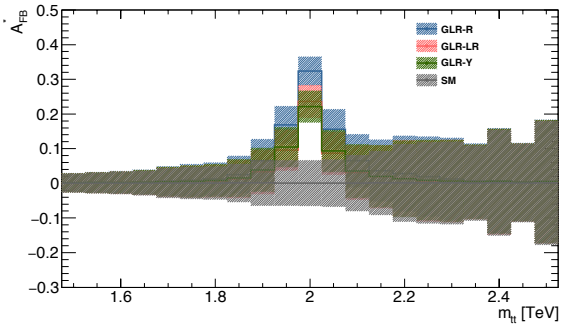

(d) GLR

Figure 4.8.1: $A_{FB}*$ for a 2 TeV Z' at $E = 14$ TeV with $L = 100$ fb^{-1} and $\epsilon_{reco} = 0.1$. We compare our results with those from Basso et al [103].

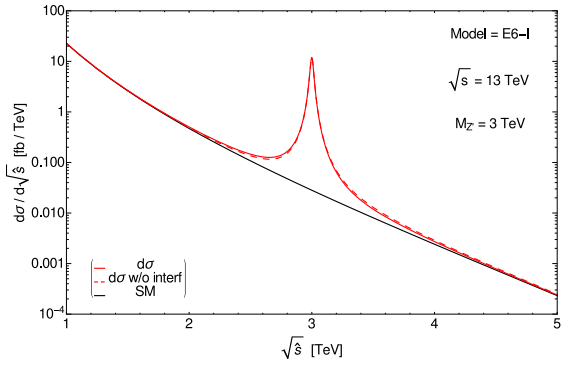

(a) σ (Accomando et al)

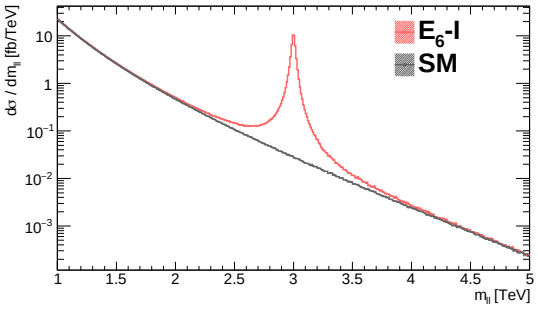

(b) σ

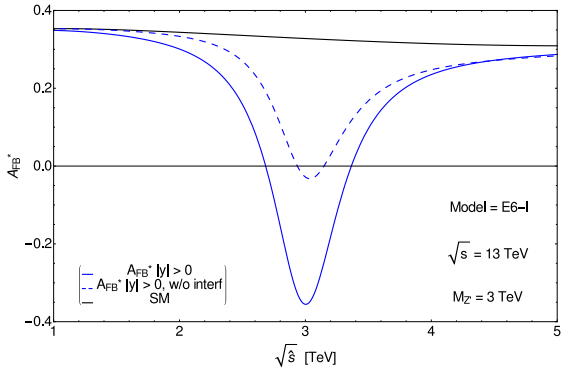

(c) $A_{FB}*$ (Accomando et al)

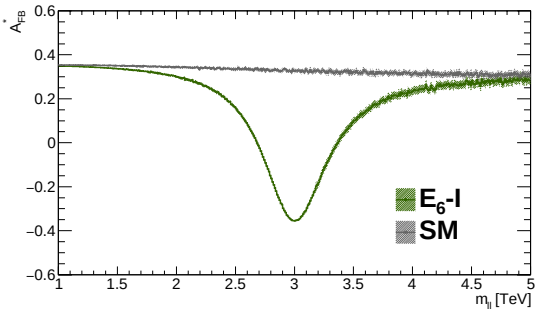

(d) $A_{FB}*$

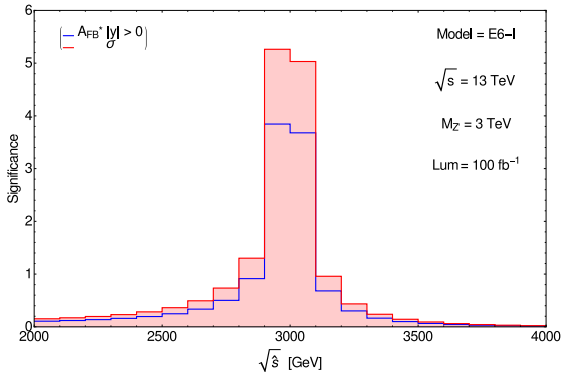

(e) Significance (Accomando et al)

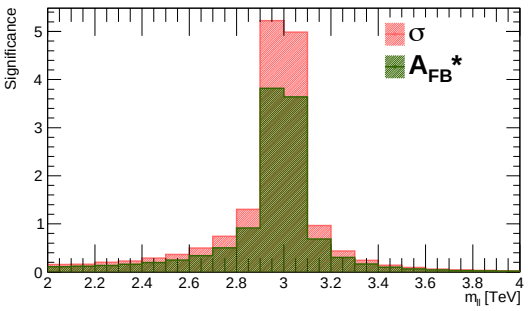

(f) Significance

Figure 4.8.2: Cross section (σ) and reconstructed forward-backward asymmetry $A_{FB}*$ and the corresponding significances for a 3 TeV $E_6 - I$ Z' at $E = 13$ TeV comparing my results with those of Ref. [60].

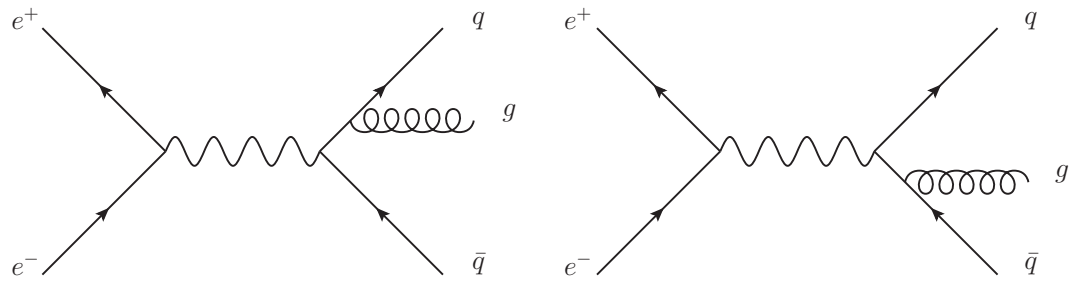

Figure 4.9.1: The two leading order Feynman Diagrams for $e^+e^- \to q\bar{q}g$.

order corrections to the underlying process. However, the high number of non-abelian vertices leads to a very difficult and time-consuming exact calculation. Approximations may be made that drastically simplify the calculation by retaining only the dominant contributions with the parton shower approach.

Consider producing a gluon alongside a quark-antiquark pair in the final state of electron-positron annihilation (Fig. 4.9.1). The scattering amplitude for $e^+e^- \to q\bar{q}g$ contains two singularities dictating the dominant contributions. These occur when gluon momentum becomes soft, i.e. goes uniformly to zero, and as the quark momentum and gluon momentum become collinear. In these limits the amplitude may be factorised into a finite part, excluding the radiated gluon, and a divergent part that depends on the energy and angle of the radiation.

Each branching is characterised by an evolution variable: the virtual mass squared or virtuality, Q^2, and the fraction of a's energy carried by b, z.[6] The splitting function is contingent on z and the azimuthal angle of b relative to a, $P_{a\to bc}(z,\phi)\ \mathrm{d}z\,\mathrm{d}\phi$. The differential cross section for a process σ_{n+1}, in terms of the cross section before splitting σ_n, is given, as a function of $t = \log(Q^2/\Lambda_{QCD})$, by

$$\mathrm{d}\sigma_{n+1} \approx \mathrm{d}\sigma_n\ \mathrm{d}t\ \frac{\alpha_{abc}}{2\pi}\,\mathrm{d}z\,\mathrm{d}\phi\,P_{a\to bc}(z,\phi). \tag{4.9.1}$$

The coupling α_{abc} may be α_s or α_{em} for strong or electromagnetic interactions, respectively, evaluated at the appropriate scale. After averaging over ϕ, the LO splitting functions – dictating the probability of a branching to occur – are dictated by the QCD evolution equations for parton densities. These evolution equations may also be referred to as the DGLAP Equations [104, 105, 106]. The form of the splitting amplitudes for each interaction, e.g. $q \to qg$ or $g \to gg$, may be found in Ref. [61].

A parton shower for each charged/coloured parton is simulated using repeated sequential application of Eq. 4.9.1. The values of z, t, and ϕ for each splitting are generated using a Monte Carlo method. Magnitudes of Q^2 that produce dominant contributions follow an

[6] Other evolution variables may be chosen such as the transverse momentum scale of the branching.

ordering scheme with partons strongly off-shell close to the hard process. The size of Q^2 gradually increases towards the hard scattering in initial-state showering, approaching a maximum energy t_{max} matched to the hard scale. For final state showers the parton begins with a time-like Q^2 and gradually decreases in energy away from the hard interaction with the evolution cut off at a minimum scale $Q^2_{min} \approx 1$ GeV.[7] At this point showering is terminated and further evolution according to the hadronisation scheme, described in section 4.10.

As well as the real collinear radiation corrections, the parton shower scheme accounts for virtual loop corrections at the appropriate order of perturbation theory. These corrections are covered in the probability of splitting to not occur during evolution from a scale t_1 to t_2 given by the Sudakov form factor:

$$S_a(t_1, t_2) = \exp\left\{ -\int_{t_1}^{t_2} \mathrm{d}t \frac{\alpha_{abc}}{2\pi} \int_{t_{min}/t}^{1-t_{min}/t} \mathrm{d}z \int_0^{2\pi} \mathrm{d}\phi \, P_{a\to bc}(z, \phi) \right\}. \tag{4.9.2}$$

The limits on z specify the range for which a splitting is resolvable (by some detector), i.e. not too soft.

The procedure for parton shower via Monte Carlo generation, therefore, begins by solving the equation $S_a(t_0, t_1) = R_1$, where t_0 is the initial scale, t_1 the next scale, and R_1 is a uniformly generated random number between 0 and 1. Variables z and ϕ are generated via Monte Carlo according to the distribution $P_{a\to bc}(z\phi)$. If $t_i < t_{min}$ then the splitting radiation was unresolvable and the showering procedure for that parton is halted. Else, the procedure continues for partons b and c, e.g. using $S_b(t_1, t_2) = R_2$. This then continues for all daughter partons until $t_i < t_{min}$ for all attempted splittings.

4.10 Hadronisation

The parton shower is an effective approach at high energies where perturbative QCD is valid. At lower energies, as α_s runs larger, perturbation theory breaks down. Presently, there are no suitable techniques for calculating non-perturbative QCD dynamics. Therefore, we must resort to phenomenological models based on the observed behaviour of QCD in the low energy limit, informed by non-perturbative techniques such as lattice computation. The two most widely used approaches are the string fragmentation model and the cluster model, used by Pythia [63] and Herwig [107], respectively. Each of these have been shown to well match distributions made with experimental data. In the analysis described in Chapter 8, the Pythia software package is used, which also handles the parton shower described in section 4.9 so I will briefly outline the string model here.

[7] When simulating the hard process, the final state is generated assuming on-shell partons. However, Eq. 4.9.1 cannot be applied for on-shell partons, necessitating a redistribution of momentum.

The principle motivation for the string model is the lattice observation that, at large distances ($d >> 1$ fm), the potential energy of colour charged objects increases linearly with separation. This mimics the behaviour of a force of tension independent of the degree of displacement, modelling the self-attracting gluon field as a string ≈ 1 fm thick.

Consider a $q\bar{q}$ pair produced via the decay of a photon. The q and $\bar{q}$ are connected by a gluonic string and flying rapidly apart. As the string stretches its potential energy increases while the kinetic energy of the quarks decreases. When the potential energy gets to the order of hadronic mass, it becomes energetically favourable for the string to split into two segments. This is achieved by creating a new $q\bar{q}$ pair at the severed ends of the string, i.e. a new q is born at the end of the $\bar{q}$ segment, and a new $\bar{q}$ at the end of the q segment. The new segments then begin to stretch and the process repeats itself until all the available energy has been transformed into pairs of quarks, forming mesons. For more complex parton systems hadronisation is much more complicated and depends on the particular colour structure, which is treated in the limit of a large number of colours.

The final step in particle-level event generation is the sequential decay of the large fraction of unstable hadrons produced during hadronisation. Experimental observation indicates a large proportion of final-state particles originate in exited-state hadron decays. Thus, an extensive list of particle states and their decay modes must be accounted for, with complete colour multiplets for each spin and parity. In many cases, particularly for the heavy flavours, c and b, experimental information on all decay modes is unavailable, so, to reach unity on the sum of all branching ratios, unlisted decays must be modelled.

CHAPTER 5

The LHC and the ATLAS detector

5.1 The Large Hadron Collider

The Large Hadron Collider (LHC) at CERN is presently the highest energy particle accelerator ever constructed. Principally a proton-proton (pp) collider, the design centre-of-mass energy for these collisions is $\sqrt{s} = 14$ TeV, with a nominal instantaneous luminosity of 10^{34} cm^{-2}s^{-1} [109]. Proton beams for the LHC are accelerated in pulses, distributing the particles into bunches comprising approximately 10^{11} protons. Each beam consists of 2808 bunches, which are nominally separated by a 25 ns spacing.

During running in 2010 and 2011 the pp energy was $\sqrt{s} = 7$ TeV, increasing to $\sqrt{s} = 8$ TeV by 2012. In the 2015, following the first long shut-down in 2013 and 2014, the LHC began operating with stable collisions at $\sqrt{s} = 13$ TeV and this energy has continued to be employed throughout 2016 and 2017. Previously, up to 2012, the LHC was operated using a 50 ns bunch spacing achieving a peak instantaneous luminosity of 7.7×10^{33} cm^{-2}s^{-1} and an integrated luminosity of 21 fb^{-1}. The attainment of design-specification bunch spacing allowed the LHC to exceed its nominal instantaneous luminosity in 2016, delivering 4.2 fb^{-1}, 38 fb^{-1} and 50.2 fb^{-1} in 2015, 2016 and 2017, respectively.

The high energy and luminosity provided by the LHC enables the observation of rare high-energy particle interactions, enabling the probing of previously inaccessible regions of phase space, and allowing the verification (or not) of previously untested theories.

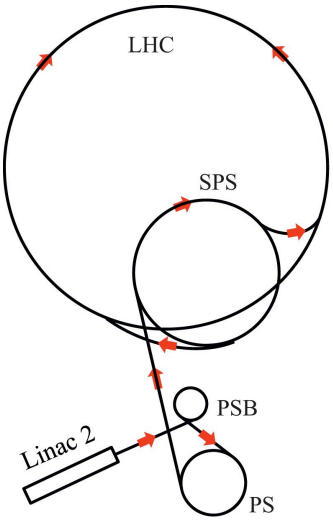

Figure 5.1.1: Schematic of the LHC proton injector chain. [108]

The accelerator chain begins when protons are fed into the linear accelerator (Linac 2) reaching energies of 50 MeV (Fig. 5.1.1). They are subsequently boosted by the Proton-Synchrotron Booster (PSB) to 1.4 GeV and injected into the Proton Synchrotron (PS), which accelerates them up to 26 GeV. Upon reaching this energy, the protons are inserted into the Super Proton Synchrotron (SPS) which increases their energy to 450 GeV.

The particles are then injected into the LHC, which is installed within a tunnel of 27 km circumference 50–175 m beneath the French-Swiss border. Around the ring, there are eight straight sections, interspersed with sections designed to bend the beams using magnetic fields. A single straight section contains the microwave cavities responsible for accelerating the protons to their final collision energy. Two sections use magnetic fields to focus the beams ensuring they maintain a small cross-sectional area. When the luminosity of the beams has dropped below useful limits they are directed into another straight section, the beam-dump, designed to safely absorb the high energy radiation.

The remaining four straight sections are designed to cross the beams to create interaction points. When running with stable beams, bunch crossings occur with a frequency of 40 MHz, each triggering multiple pp collisions. Installed on these sections are the detectors that measure the generated energies and momenta in order to reconstruct the resultant interactions. The largest detectors (and accompanying collaborations) are A Large Ion Collider Experiment (ALICE), LHCb, Compact Muon Solenoid (CMS), and, the subject of this thesis, A Toroidal LHC ApparatuS (ATLAS). The latter two detectors are similar in design and perform as general-purpose experiments, enabling the study of as many processes as possible. ATLAS and CMS often serve to verify each other's results and minimise the possibility of false discoveries.

5.2 ATLAS coordinate system

The coordinate system and nomenclature used to describe the ATLAS detector is outlined briefly here, since it will be referred to repeatedly. The ATLAS detector is located at Point One on the LHC ring, with the nominal interaction point defined as the origin of the ATLAS coordinate system. In cartesian space, the z-axis is defined by the beam axis, with the x-y plane perpendicular to beam direction. The positive x-direction points towards the centre of the LHC ring, with the y-direction pointing directly upwards. Due to the symmetry of ATLAS, it is also common to use cylindrical co-ordinates: $\{r, \phi, z\}$. The transverse radial distance from the beam pipe r is given by $r = \sqrt{x^2 + y^2}$, while the azimuthal angle ϕ is measured relative to the positive x-axis. Finally, the polar angle θ is measure from the positive z-axis [110].

For describing tracks of the high energy particles it useful to define the rapidity, y, in terms of the longitudinal momentum (along the beamline), p_L,

$$y = \frac{1}{2} \log \frac{E + p_L}{E - p_L} \tag{5.2.1}$$

This is because differences in the y coordinate between two events are invariant under longitudinal Lorentz boosts (in the z-direction). This is desirable, as hard-scattering processes at the LHC occur due to interactions between partons carrying an indeterminable fraction of the hadron's total momentum and thus carry unknown longitudinal momentum p_z. Therefore, it is also convenient to define the transverse momentum of an object,

$$p_T = \left(p_x^2 + p_y^2\right)^{\frac{1}{2}} \tag{5.2.2}$$

In the ultra-relativistic (massless) limit the rapidity can be closely approximated by the pseudorapidity,

$$\eta = \frac{1}{2} \log \frac{|\mathbf{p}| + p_z}{|\mathbf{p}| - p_z} = -\log \left(\tan \left(\frac{\theta}{2} \right) \right). \tag{5.2.3}$$

This limit is often suitable due to the very high energy of LHC collisions. Note that the pseudorapidity depends only on the angle between the beam line and not on the energy of the particle. This parameter is convenient for describing the coverage of the detector. The forward sections of ATLAS refer to regions of the detector that are at high pseudorapidity (Fig. 5.2.1).

Therefore, the kinematics of an object can largely be captured by its position in $\{p_{\mathrm{T}}, \eta, \phi\}$ coordinates and it is useful to measure the separation between two objects in η-ϕ space by defining

$$\Delta R = \left((\Delta\eta)^2 + (\Delta\phi)^2 \right)^{\frac{1}{2}}, \tag{5.2.4}$$

which is also invariant under longitudinal Lorentz boots.

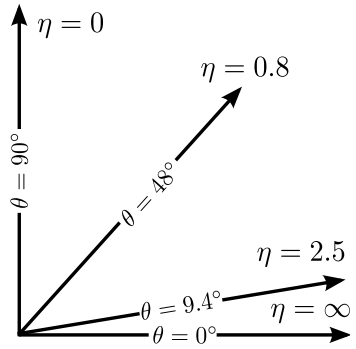

Figure 5.2.1: Pseudorapidity diagram. As the polar angle (θ) goes to zero, pseudorapidity (η) asymptotically approaches infinity.

5.3 Detector Anatomy

ATLAS, along with CMS, is one of two general purpose detectors on the LHC designed to track and identify the particles created in proton-proton collisions. The resulting high particle energies and multiplicities, interaction rates and need for precision measurements necessitate that ATLAS sets very high standards in particle detection [110].

One important standard is hermeticity, which addresses the capacity of a particle detector to observe all possible decay products of an interaction. A hermetic detector incorporates maximum coverage around the interaction and accounts for all particle multiplicities with various types of sub-detectors. In order to accurately recreate high energy physics events it is important to maximise the hermeticity of the detector as it allows for measurements of missing momentum. This is necessary for identifying particles such as neutrinos that interact very weakly with matter, where a direct detection is practically impossible.

The ATLAS detector comprises a symmetric cylinder 44 m long, 25 m in diameter and weighing 7×10^6 kg, composing multiple subsystems. These components can be approximately separated into four categories: the inner detector, calorimeter systems, muon spectrometer and magnet systems. The first three compose the main detector systems of ATLAS. Moving radially outward from the interaction point, the first system is the Inner Detector (ID) which measures the momentum of charged particles as they interact with it while curving in the magnetic field. Next the calorimeter systems determine the energy of most charged and neutral particles via their direct absorption. In the outer region comes the muon system, which measures the momentum of the principle detectable particles penetrating the calorimeters.

Each particle has a unique combination of signals in each detector subsystem, allowing different particles to be identified. The distinct information from these interactions together allow the accurate tracking multiple particles, and an accurate reconstruction

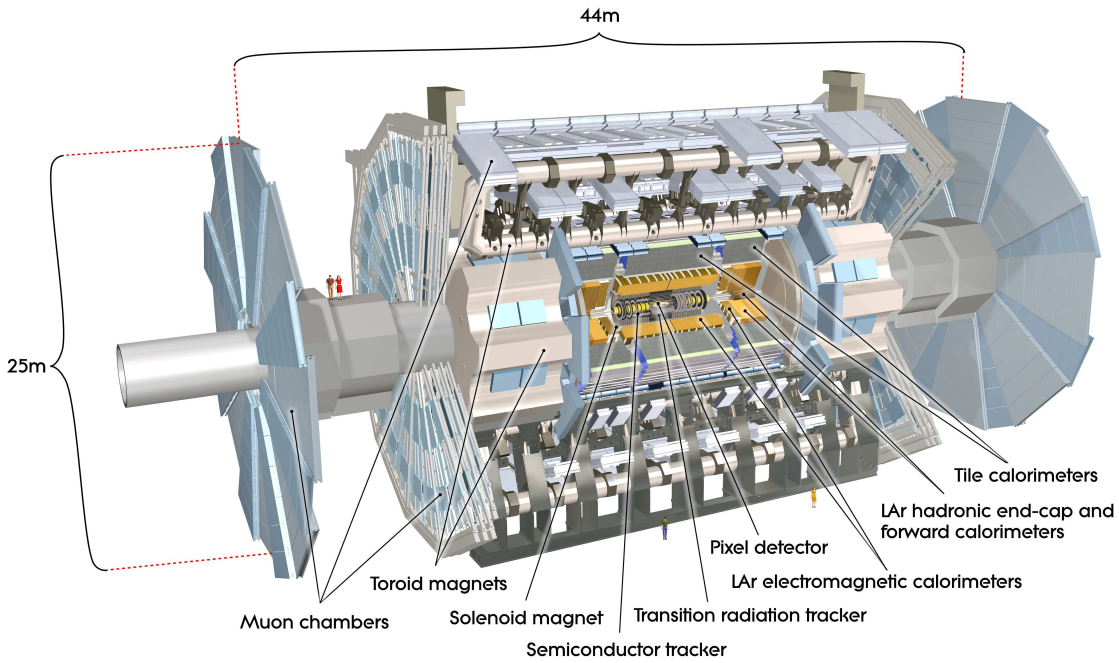

Figure 5.3.1: A schematic of the full ATLAS apparatus, labelling principle detector components. A sense of scale may be inferred from those people drawn on the shielding and floor. [111]

of each event. Fig. 5.3.1 shows a cutaway diagram, labelling the principle components of the detector. Each subsystem composes a central barrel region which is responsible for particle tracking in the central (low η) region and two end-caps covering the forward regions. The total pseudorapidity coverage of the ATLAS detector is $|\eta| = 4.9$ [110].

5.4 Magnet Systems

ATLAS requires two independent magnet systems. The first is a central solenoid surrounding the inner detector, providing a field strength of 2.0 T. Situated in front of the calorimeter systems, it is designed to be as thin as possible, so as to minimise the energy loss of a particle prior to reaching the surrounding subsystems.

The second magnetic system is toroidal and encloses the muon-spectrometer. It consists of eight large coils in the barrel region and eight smaller coils in each of the end-caps, providing field strengths of 1.0 T and 0.5 T, respectively.

The super-conducting magnets are cooled to temperatures of 4 K using a system of liquid helium cryogenics. Both magnet systems serve the same purpose: they bend the paths of charged particles traversing the encompassed subsystems so as to resolve their momenta.

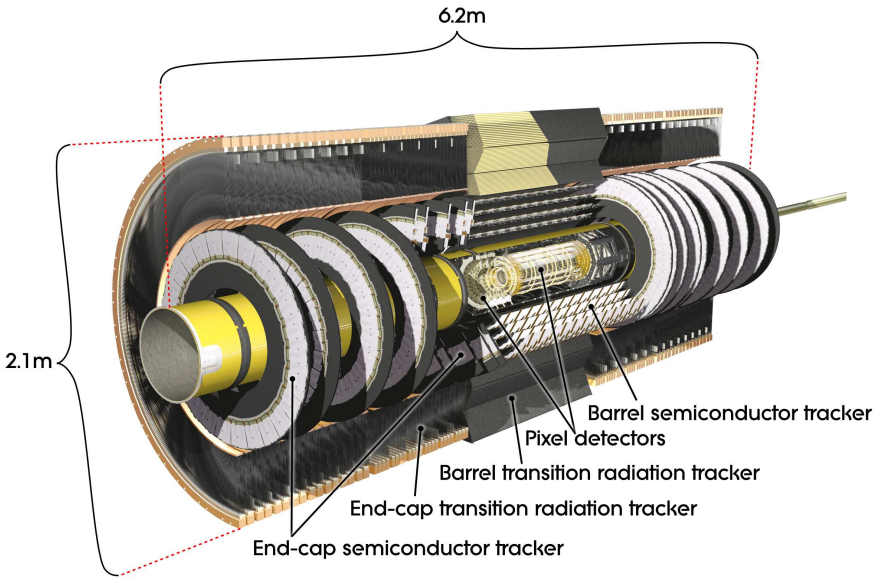

Figure 5.5.1: A cutaway schematic of the ATLAS Inner Detector, labelling principle subsystems. [111]

5.5 Inner Detector

The Inner Detector (ID) is the frontline detector system, situated closest to the origin and is presented schematically in Fig. 5.5.1. It has an η coverage of ± 2.5 for particles of $p_{\mathrm{T}} > 0.5$ GeV. The principle purpose of the ID is the precise measurement of position and momentum for charged particles. This information is critical in determining the primary vertex positions and impact parameters of interactions.

For every bunch crossing a large number of particles with high multiplicity emerge within $|\eta| < 2.5$, creating an extremely high track density in the detector [110]. To achieve the required momentum and vertex resolutions for isolating frontier physics processes, a fine detector granularity is required. The ID system provides this function using three subsystems; moving radially outward from the interaction point these are: the Pixel detector, the Semiconductor Tracker (SCT) and the Transition Radiation Tracker (TRT).

The Pixel detector is a semiconductor detector [110, 112]. Sensors are embedded with 2D arrays of small, rectangular p-type silicon, or 'pixels'. There are 80 million of these pixels in total between 0.05 and 0.1 m from the beam pipe. With a pitch of $50\,\mu\mathrm{m} \times 400\,\mu\mathrm{m}$ they provide a resolution of $14\,\mu\mathrm{m}$ in $r\phi$ and $87\,\mu\mathrm{m}$ in z. Their high granularity makes them ideal for distinguishing tracks at high particle flux density. This data allows accurate 3D vertex reconstruction for charged tracks and the determination of the transverse impact parameter to $<15\,\mu\mathrm{m}$. During the long shut-down, an additional subsystem was added to the pixel tracker called the Insertable B-Layer (IBL). At 3.3 cm, this sits even closer to the interaction point for enhanced vertex and impact parameter resolution, b-jet tagging,

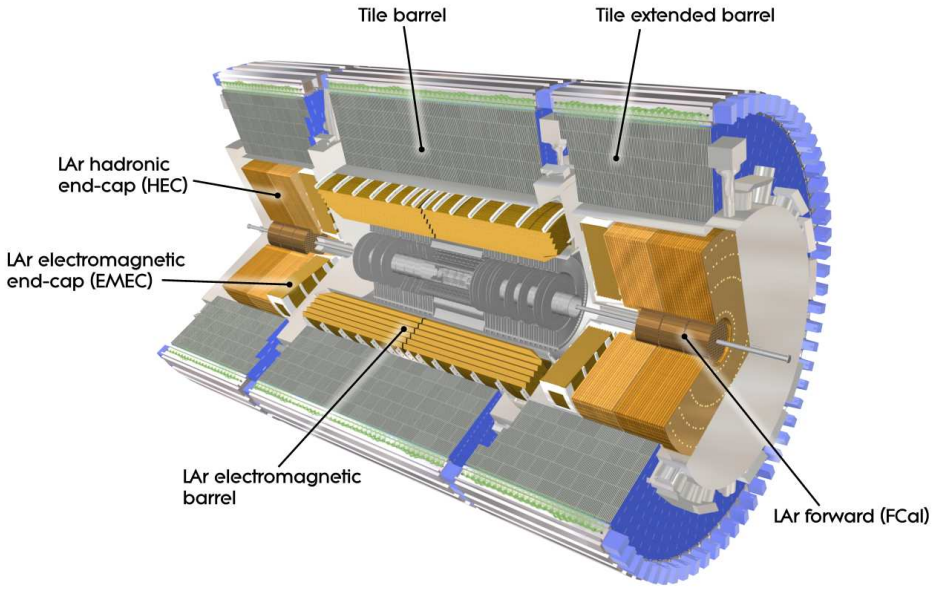

Figure 5.6.1: A cutaway schematic of the ATLAS Calorimeter, labelling principle subsystems. [111]

and fake track reduction at high instantaneous luminosity [113].

The SCT operates similarly to the Pixel detector, yet features silicon strips. It sits approximately 0.3 m from the beam pipe with 4088 silicon strip modules. With a pitch of approximately $80\,\mu\mathrm{m}$ the system provides an $r\phi$ resolution per measurement of $16\,\mu\mathrm{m}$. The sensor on one side of a module is also rotated by a small stereo angle of $40\,\mathrm{mrad}$ from the sensor on the opposing side. This provides a positional resolution of $580\,\mu\mathrm{m}$ along z or r in the barrel or end-caps, respectively.

Surrounding the SCT, the TRT provides a large number of additional lower-resolution tracking measurements, as well as some particle identification. Rather than silicon detectors it consists of $300,000$ straws: gas filled tubes 4 mm in diameter embedded in dense radiator material. During run-1, the gas used was xenon, which was replaced with argon for run-2. Ultra-relativistic particles emit transition radiation when crossing the interface of two media with different dielectric constants [114] The frequency of this radiation is dependent on the Lorentz factor $\gamma = \frac{E}{mc^2}$. This factor is different for particles of the same momentum, but different mass, allowing the TRT to distinguish between electrons and other particles, such as pions.

Altogether the ID provides a p_{T} and η dependant momentum resolution for tracks between 1.4 and 11%.

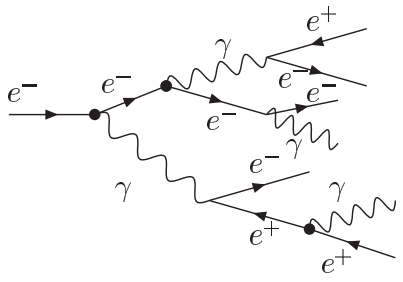

Figure 5.6.2: Schematic of an electromagnetic particle shower.

5.6 Calorimeter system

The calorimetry system aims to stop and directly measure the energy deposits of neutral and charged particles, such as electrons, photons and jets. This consists of alternating layers of dense absorbing and scintillating material, followed by photo-detectors. The intensity of the light is used to determine the energy of the particles.

The calorimetry system composes an electromagnetic calorimeter surrounded by a hadronic calorimeter (Fig. 5.6.1). Low mass electromagnetically interacting particles such as electrons and photons are absorbed by the first calorimeter, while hadronic matter penetrates further. Only neutrinos and high energy muons may escape through the calorimeter system. Particle showering is an important process for this procedure.

Particle showering effects are due to high energy particles interacting with the dense material of the detector systems and producing cascades of secondary particles. Particle showers can be split into two categories: Electromagnetic and Hadronic. The second category of showers are dominated by successive inelastic hadronic interactions. At high energy, these are characterised by excited nuclei undergoing nuclear decay, resulting in multi-particle production. Products are made up predominantly of nucleons and pions.

Electromagnetic showers are caused by particles that interact primarily via electromagnetism. Charged particles undergo deceleration when deflected by the electric field of an another charged particle. Bremsstrahlung refers to the photon that is emitted by the decelerating particle, in order to conserve energy, as well as to the process itself. For high-energy electrons travelling through a dense medium and interacting with atomic nuclei, this is the dominant form of energy loss. Emitted photons of sufficient energy then undergo electron-positron pair production through interaction with a nucleus.[1] These decay products then undergo further bremsstrahlung. The cascading nature of these processes constitute the primary source of EM showers (Fig. 5.6.2).

[1]Participation of the nucleus is required in order to satisfy the energy and momentum conservation laws [115].

This cascade continues until the photon energy falls below the threshold for pair production. Following this lower energy electromagnetic interactions dominate, such as Compton scattering and the photoelectric effect [116].

While these processes occur through the apparatus, scattering processes are encouraged in the calorimeter system, where they are used to determine the energy of the traversing particles. Unfortunately, the products of these showers are emitted in many directions; therefore, particularly at large $|z|$ and r, showers can propagate back into the inner detector.

The electromagnetic calorimeter (ECAL) has an η coverage of $|\eta| < 3.2$ with a crack between at barrel and end-cap regions at $|\eta|$ 1.5. Liquid Argon (LAr) is used as the active material with lead for absorbing layers. The ECAL alone provides an energy resolution of 1.3-2.3% for 50 GeV electrons, and $1.0 - 1.5\%$ for 100 GeV photons.

The hadronic calorimeter (HCAL) is a tile calorimeter targeted at hadronic particles such as pions. The barrel section with coverage of $|\eta| < 1.7$ comprises alternating layers of steel and scintillating tiles, while the end-cap regions use tungsten and LAr between $1.5 < |\eta| < 3.2$. A Forward Calorimeter (FCAL) extends this further to $|\eta| < 4.9$ using one EM layer with copper for absorption and two tungsten hadronic layers. The HCAL allows a 1 TeV jet resolution of 2%.

5.7 Muon spectrometer

Muons μ are the sole detectable particles able to traverse both the inner detector and calorimeters. The Muon Spectrometer (MS), along with the accompanying toroidal magnets, dominate the outward appearance of the ATLAS detector (Fig. 5.7.1). The system consists of thousands of drift chambers, similar in design to the straws of the TRT, but with larger diameters. Single wired Monitored Drift Tubes (MDT) provide precision tracking within $|\eta < 2$, while multi-wired Cathode Strip Chambers (CSC) cover the forward region $2.0 < |\eta| < 2.7$. By altering the paths of muons using the magnet system (section 5.4) and tracking the resultant motion their momentum is determined with high precision. However, the drift time for these chambers is too long for rapid triggering with 40 MHz collisions, necessitating two complimentary faster systems. Covering $|\eta| < 1.05$ and $1.05 < |\eta| < 2.7$ these are Resistance Plate Chambers (RPCs) and Thin Gap Chambers (TGCs), respectively. The first uses parallel electrode plates instead of central wires, while later are super-fast CSCs. These ensure that muons can be be triggered on, and associated to the correct bunch crossing.

The MS provides a momentum resolution of 4–10% depending on the η and p_{T} of the candidate muon.

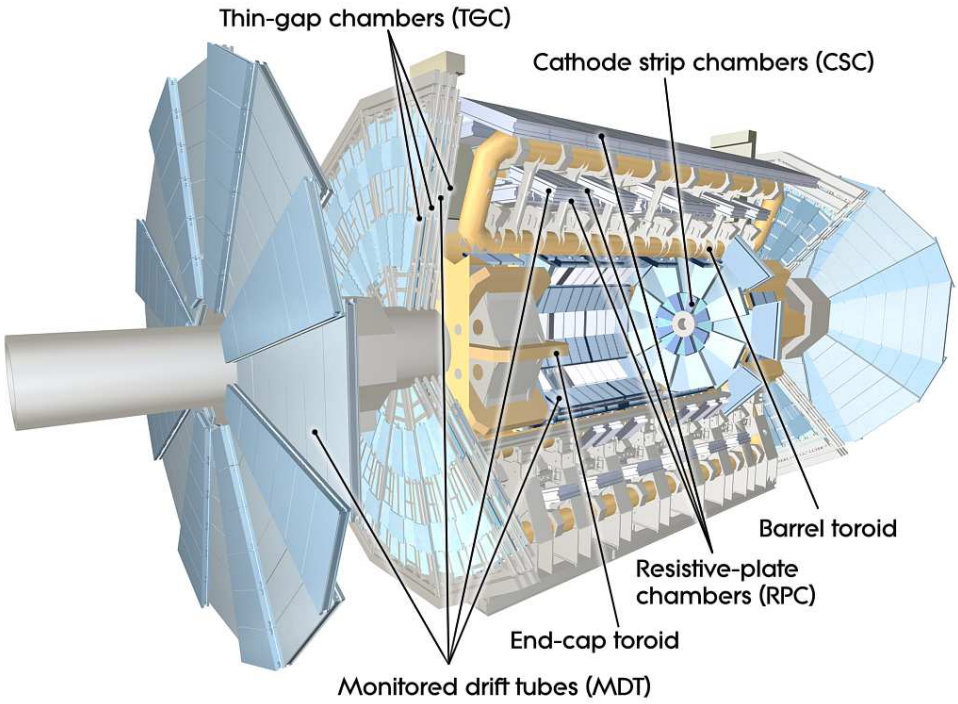

Figure 5.7.1: A cutaway schematic of the ATLAS Muon system, labelling principle subsystems. [111]

CHAPTER 6

Single electron trigger efficiency studies

6.1 Introduction

The primary topic of this thesis is the phenomenology of top pair production, with specific focus on semileptonic and dileptonic decays (lepton-plus-jets and dilepton final states), featuring both electrons and muons. The accurate reconstruction and identification of electrons and positrons, henceforth, collectively referred to as electrons, is, therefore, critical to resolve these events. While the phenomenological studies use solely simulated data, any future searches will require a firm understanding of electron trigger efficiencies in order to decide which collisions will be kept for later analyses, and to resolve any new physics.

Electrons propagating within the ATLAS detector (chapter 5) leave energy deposits in the electromagnetic (EM) calorimeter, preceded by tracks in the inner detector (ID). The calorimeter signals are used in the first level trigger system (L1), and are combined with tracks to reconstruct electron candidates used for the high level trigger (HLT) decision algorithms, which discriminates against background objects, such as hadrons and non-prompt electrons. This later step makes the final decision on which candidate objects will be recorded as electrons for later analysis. As well as studying the overall efficiency for each trigger chain, we may examine individual requirements within the chain and the percentage of candidates that fail each step, i.e. the sources of inefficiency for each

trigger.[1]

This chapter describes the studies I made of the single electron trigger efficiencies, particularly the individual sources of inefficiency, as part of the E/gamma Signature Trigger Group, within the ATLAS collaboration. This study constituted the bulk of work necessary for my qualification as an ATLAS author. Firstly, I will give a brief overview of the ATLAS trigger system, followed by an outline of the reconstruction, identification, isolation, and trigger algorithms used to select electrons. I will then describe the methodology used to measure the trigger (in)efficiencies. Subsequently, I will present the inefficiencies measured during Run-1, describe the changes made to the trigger system, specifically as they relate to the single electron trigger, for Run-2, followed by an account of the specific inefficiency measurements made using 2016 and 2017 data, and the results thereof.

6.2 The ATLAS trigger system

With Run-2 the nominal proton bunch-spacing is 25 ns, half of that used in Run-1. Thus, the LHC is now colliding proton bunches at a rate of 40 MHz, resulting in record-high luminosities. However, this frequency is far too high to allow the data for every collision to be recorded to disk, as ATLAS is limited in recording speed to approximately 1 kHz. Even if the data could be written sufficiently quickly, this would result in far too many events and the available permanent storage would be rapidly saturated. Additionally, many of these events are of little interest, corresponding only to glancing collisions and soft interactions occurring at large distances between incoming hadrons.

Hence, we must discard the data from most collisions before recording it, in a systematic way that minimises the loss of interesting data. To select only the most interesting events for storage, a 'trigger' system is used [110]. Only when the trigger is 'pulled' is data 'fired' to permanent storage, which must only occur when objects satisfy basic minimum requirements. The ATLAS trigger system for Run-2 is a two step process (Fig. 6.2.1) [117].

The first part - Level-1 (L1) - is a hardware trigger based only on information from calorimeters and muon detectors [119]. This is because only these systems have read-out rapid enough to be processed by the L1-trigger. Muon detectors are not relevant for electron reconstruction, so will not be described here. The L1Calo hardware trigger is the speedy front-line in data filtration. It makes use of signals from ≈ 7000 trigger towers consisting of $\Delta\eta \times \Delta\phi = 0.1 \times 0.1$ blocks in the calorimeter system. It identifies regions-of-interest (RoIs) by scanning for 2×2 trigger tower clusters in the EM calorimeter where one or

[1] The word trigger is used liberally within the collaboration, and can refer to the system as a whole, various sub-systems, as well as specific trigger chains, and even individual selection criteria.

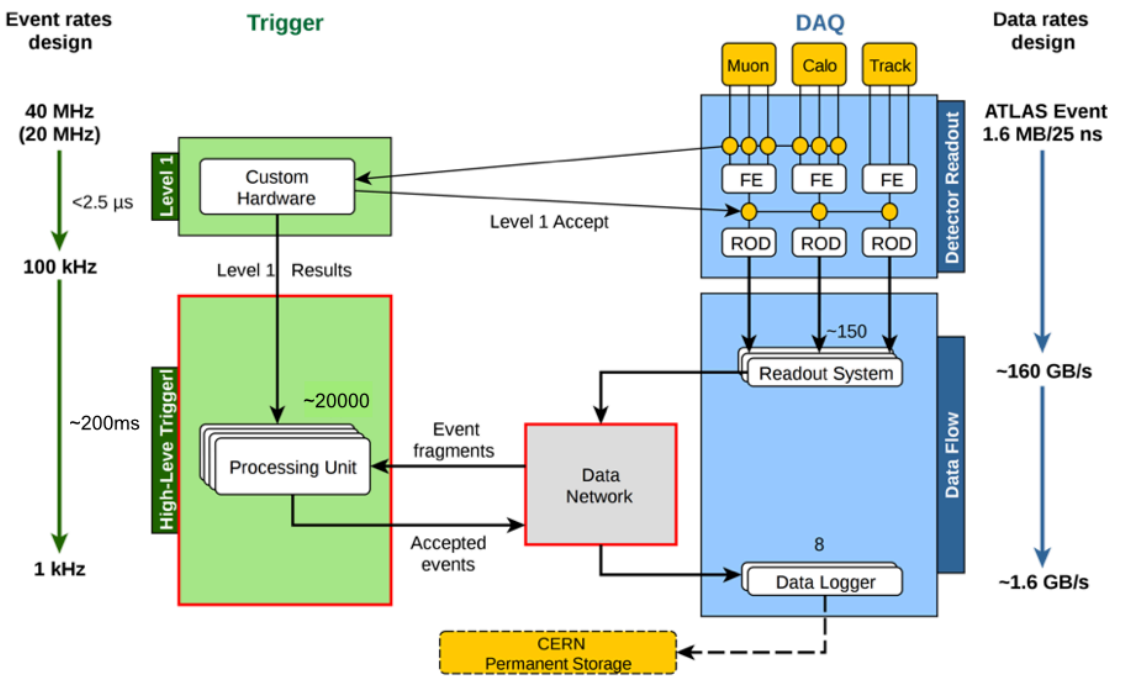

Figure 6.2.1: Schematic diagram of the ATLAS Run-2 trigger system and data acquisition [118].

more of the four pairs of nearest neighbour towers have an $E_{\mathrm{T}} > E_{\mathrm{T}}^{\mathrm{theshold}}$. Additional veto requirements can be made on the surrounding trigger towers to ensure these RoI are isolated. For EM isolation this takes into account the adjacent 12 trigger towers, while hadronic isolation requirements can be made on the central 2×2 core behind the RoI, and on the neighbouring 12-tower hadronic ring. For jet reconstruction, RoIs are defined using 4×4 or 8×8 blocks of trigger towers around a central 2×2 core. Thresholds are set on the sum of E_{T} from both the EM and hadronic calorimeter energy deposits. The cores defined by the local maxima define the jet RoI coordinates. Additional features of the L1 algorithm, as they specifically relate to electron reconstruction are described in section 6.6.1.

The second stage is a software trigger. This processes events using finer-granularity calorimeter information, and tracking information from the inner detector (and precision hits in the muon spectrometer). In Run-2 the Level-2 (L2) trigger and Event Filter (EF) from Run-1 are merged into the High-Level Trigger (HLT) using a single data preparation system. However, the HLT still occurs in sequential stages, and the old jargon is still used. The L2 is a fast HLT selection that uses a first-pass reconstruction to reject the bulk of events. This is followed by the EF, which further filters the events before more sophisticated ID algorithms using slower precision reconstruction are applied. The HLT algorithms can be applied only within the RoIs identified at L1 or executed using the full

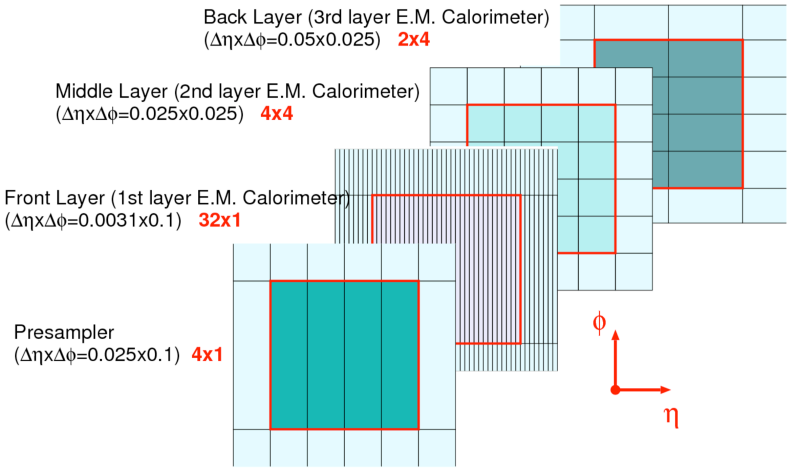

Figure 6.3.1: ATLAS calorimeter granularity for different layers in an LAr calorimeter barrel module. Current Trigger Tower definition: $\Delta\eta \times \Delta\phi = 0.1 \times 0.1$ [120].

detector. However, electron and photon triggers are always L1 ROI seeded. The composition of the HLT algorithms is obviously highly dependant on the target objects, and is described more comprehensively for electrons in section 6.6.2.

6.3 Electron reconstruction

Electrons may be reconstructed within the central region of the ATLAS detector. This process is sequential, starting with calorimeter energy deposit clustering and proceeding to track reconstruction, followed by track-cluster matching (Fig. 6.4.1).

Firstly, the EM calorimeter is scanned over using a sliding window in $\eta \times \phi$ space. The size of this window is 3×5 (Fig. 6.3.1), in units corresponding to the EM calorimeter middle layer resolution of 0.025×0.025. This searches for longitudinal towers with a total cluster transfer energy greater than 2.5 GeV. The towers constitute kernels around which a subsequent algorithm, using an extended window of position-dependent dimension, assembles clusters and strips out duplicate candidates. Overall this cluster search ranges from 95% efficient at $E_{\mathrm{T}} = 7$ GeV to more than 99% for $E_{\mathrm{T}} \geq 15$ GeV.

The next step comprises track reconstruction, which proceeds in two steps: pattern recognition and track fitting. Track seeds are constructed from three hits in different layers of the silicon detectors and required to have $E_{\mathrm{T}} > 1$ GeV. Pattern recognition first tries to extend this to a full track, of at least seven hits, under the hypothesis that the track originated from a pion. Such hypothesis allows for energy loss at each intersection with the detector to account for interactions with the material, and up to 30% due to bremsstrahlung. If this is unsuccessful, or is not associated with one of the provided RoIs in the EM calorimeter, the process is repeated under an electron hypothesis that allows for increased energy loss during propagation through the detector material. The

successful hypothesis is then passed to the ATLAS Global χ^2 Track Fitter [121] to fit the respective track to the candidate. If a candidate was recognised as a pion, but fails the subsequent fit, it is then re-fit under the electron hypothesis.

To reduce candidates attributable to secondary particles, tracks associated with the electron hypothesis are further required to be compatible with the primary interaction vertex of the hard collision, by passing the following requirements:

$$d_0/\sigma_{d_0} < 5, \qquad \Delta z_0 \sin\theta < 0.5\,\mathrm{mm}, \tag{6.3.1}$$

where d_0 labels the impact parameter: the distance of closest approach between the track and the measured beam-line, and σ_{d_0} its uncertainty. The z_0 measures the distance between the beam-spot position, along the beam-line (which defines the local z-axis) to where it intersects d_0, while Δz_0 stretches between the track and the primary vertex with the highest E_{T} sum of associated tracks. The θ measures the polar angle of the track.

Electron candidate tracks are then extrapolated to the middle layer of the EM calorimeter and loosely matched in $\eta - \phi$ space to the cluster barycentre. The number of precision hits in the silicon detector affects the strictness of the matching process, which also allows for bremsstrahlung energy loss. Tracks that have four or more precision hits and are loosely associated to cluster seeds are refit, further accounting for non-linear bremsstrahlung losses by the optimised Gaussian Sum Filter [122], and subjected to stricter matching conditions. Electron candidates must be associated to a track; unassociated electron candidate clusters are considered to be photons. If multiple tracks are associated to the same cluster seed, the primary track is chosen using an algorithm utilising the total number of pixel hits, with preference for the first layer, as well as the cluster-track separation under different momentum hypotheses.

The cluster seed is then used to construct a full cluster using 3×7 longitudinal towers of EM calorimeter cells in the barrel, and 5×5 in the endcap. Multivariate techniques based on simulated data use the original energy of the reconstructed electron to calibrate the energy of these reformed clusters [123]. The electron four-momenta are calculated using the energy of the calibrated energy clusters, while the η and ϕ measurements are given by the primary tracks associated to the cluster seed.

6.4 Electron identification

Electron identification (ID) algorithms distinguish signal-like reconstructed objects from background-like ones. These background objects can be due to, for example, hadronic jets or "non-prompt" background electrons arising from photon conversions and heavy flavour hadron decays. Twenty independent variables are used to help determine be-

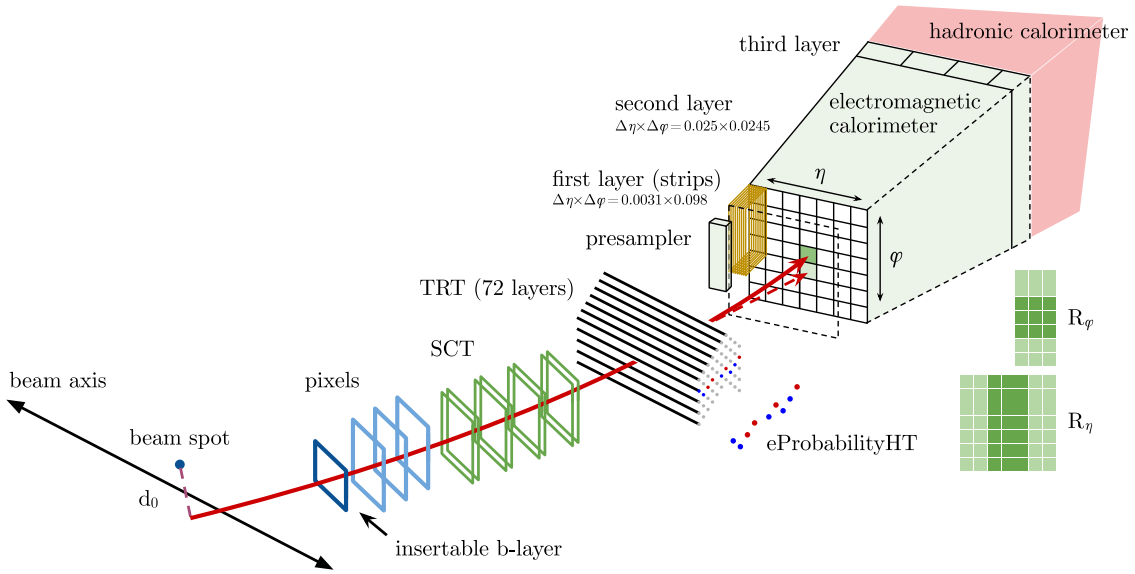

Figure 6.4.1: Schematic diagram of electron reconstruction and identification [117].

tween these hypotheses, which are summarised in Tab. 6.4.2. These quantities relate to both track and cluster measurements, including shower shape variables, track properties, TRT information, and those that evaluate the impact of bremsstrahlung.

The standard ID algorithm is a likelihood-based (LH) method. This is a multivariate analysis (MVA) technique which constructs a single discriminating variable from multiple properties of the reconstructed objects. Requirements on the discriminant evaluate all characteristics of each candidate simultaneously. Almost all electron discriminating variables shown in Tab 6.4.2 are used in the MVA, with the exception of E/p, w_{stot}, and $\Delta\phi_2$, as well as the number of precision hits in a track, which are subject only to simple, sequential (cut-based) selection requirements. This enables improved background rejection when compared to an entirely cut-based scheme.

Signal (s) and background (b) Probability Density Functions (PDFs) are constructed for the included fourteen discriminating variables (d_i) using Monte Carlo simulated data samples. These come from $Z \rightarrow ee$ and dijet events at high E_{T}, with $J/\psi \rightarrow ee$ and minimum bias[2]covering events at low E_{T}. These PDFs are taken in combination to inform overall signal and background probabilities for an object:

$$\mathcal{L}_s(\vec{d}) = \prod_i P_i^s(d_i) \quad \text{and} \quad \mathcal{L}_b(\vec{d}) = \prod_i P_i^b(d_i). \tag{6.4.1}$$

[2] Minimum bias labels the soft partonic processes that dominate interactions at hadronic colliders. These occur at large distances between incoming hadrons, in conglomerate, with minimal momentum transfer. The final state is characterised by many low momentum ($p_{\text{T}} \approx 0.5$ GeV) particles, covering a large volume of phase space, largely collinear with the beam line. The ATLAS trigger is designed to record these events with as little detector bias as possible.

Type	Description	Name
Hadronic leakage	Ratio of E_{T} in the first layer of the hadronic calorimeter to E_{T} of the EM cluster (used over the range $\lvert\eta\rvert < 0.8$ or $\lvert\eta\rvert > 1.37$)	R_{had1}
	Ratio of E_{T} in the hadronic calorimeter to ET of the EM cluster (used over the range $0.8 < \lvert\eta\rvert < 1.37$)	R_{had}
Back layer of EM calorimeter	Ratio of the energy in the back layer to the total energy in the EM accordion calorimeter. This variable is only used below 100 GeV because it is known to be inefficient at high energies.	f_3
Middle layer of EM calorimeter	Lateral shower width, $\sqrt{(\Sigma E_i \eta_i^2)/(\Sigma E_i) - ((\Sigma E_i \eta_i)/(\Sigma E_i))^2}$, where E_i is the energy and η_i is the pseudorapidity of cell i and the sum is calculated within a window of 3×5 cells	$w_{\eta 2}$
	Ratio of the energy in 3×3 cells over the energy in 3×7 cells centred at the electron cluster position	R_ϕ
	Ratio of the energy in 3×7 cells over the energy in 7×7 cells centred at the electron cluster position	R_η
Strip layer of EM calorimeter	Shower width, $\sqrt{(\Sigma E_i (i - i_{max})^2)/(\Sigma E_i)}$, where i runs over all strips in a window of $\Delta\eta \times \Delta\phi \approx 0.0625 \times 0.2$, corresponding typically to 20 strips in η, and i_{max} is the index of the highest-energy strip	w_{stot}
	Ratio of the energy difference between the largest and second largest energy deposits in the cluster over the sum of these energies	E_{ratio}
	Ratio of the energy in the strip layer to the total energy in the EM accordion calorimeter	f_1
Track conditions	Number of hits in the innermost pixel layer; discriminates against photon conversions	n_{Blayer}
	Number of hits in the pixel detector	n_{Pixel}
	Number of total hits in the pixel and SCT detectors	n_{Si}
	Transverse impact parameter with respect to the beam-line	d_0
	Significance of transverse impact parameter defined as the ratio of d_0 and its uncertainty	d_0/σ_{d_0}
	Momentum lost by the track between the perigee and the last measurement point divided by the original momentum	$\Delta p/p$
TRT	Likelihood probability based on transition radiation in the TRT	eProbabilityHT
Track-cluster matching	$\Delta\eta$ between the cluster position in the strip layer and the extrapolated track	$\Delta\eta_1$
	$\Delta\phi$ between the cluster position in the middle layer and the track extrapolated from the perigee	$\Delta\phi_2$
	Defined as $\Delta\phi_2$, but the track momentum is rescaled to the cluster energy before extrapolating the track from the perigee to the middle layer of the calorimeter	$\Delta\phi_{\mathrm{res}}$
	Ratio of the cluster energy to the track momentum	E/p

Table 6.4.2: Definitions of Run-2 electron discriminating variables in 2016 [117].

Fixed operating point	$E_{\mathrm{T}}^{\mathrm{cone0.2}}$	$p_{\mathrm{T}}^{\mathrm{varcone0.2}}$
Loose	0.20	0.15
Tight (Track-only)	-	0.06
Tight	0.06	0.06

Table 6.5.1: Fixed isolation operating points. The definitions of $E_{\mathrm{T}}^{\mathrm{cone0.2}}$ and $p_{\mathrm{T}}^{\mathrm{varcone0.2}}$, used to define the calorimeter and tracking isolation, respectively, may be found in the text.

From this an overall discriminant ($d_{\mathcal{L}}$) variable may be calculated:

$$d_{\mathcal{L}} = \frac{\mathcal{L}_s}{\mathcal{L}_s + \mathcal{L}_b}. \tag{6.4.2}$$

The strictness of the electron ID varies between three operating points: Loose, Medium and Tight. While all operating points use the same collection of discriminating variables ($\vec{d}$), each requires a tighter selection on the discriminant, in the order listed. Thusly, Tight requires the greatest level of background rejection and is defined such that samples selected under its paradigm form a subset of those selected by medium, which shares the equivalent relationship with the Loose ID. Hence, any electron candidate accepted under the Tight ID will be selected also by Medium and Loose.

The Tight operating point is not used for electron candidates with $E_{\mathrm{T}} > 125$ GeV. This is because electrons with sufficiently high momentum will propagate through the first layers of the EM calorimeter without depositing large fractions of their energy. Thus, the discriminate will diagnose a larger deposit of energy in the outer layers, and even the hadronic calorimeter, which will be penalised at the Tight operating point. The Medium ID is more forgiving of later energy deposition and hadronic leakage, so is substituted at high E_{T}. To supplement the background rejection of the Tight ID, it is instead supplemented with sequential rectangular requirements on w_{stot} and E/p. Additionally, the operating points are optimised across multiple bins in E_{T} and $|\eta|$. This is important, as the properties of tracks and shower shapes vary significantly with E_{T}, and the differing volumes of detector material intercepted by electrons at different $|\eta|$ affects the resulting shower shapes. Furthermore, the pileup, i.e. the number of interactions per bunch crossing (μ), can influence the distributions of the shower shapes. Thus, the selection applied to the discriminant is loosened with an increasing number of reconstructed primary vertices, which is indicative of μ. As a result, while the efficiency at high μ is preserved, the background rejection is lowered.

6.5 Electron isolation

Electrons can be required to be isolated from other activity in the calorimeter or inner detector to further distinguish prompt electrons, due to heavy-resonance decays, from objects such as converted photons or mis-identified light hadrons. To do this, the sum of energy (or momentum) surrounding each candidate is quantified using isolation variables.

To ensure isolation in the EM calorimeter, topological T clusters [124] are constructed with a cone of $\Delta R = 0.2$ around the candidate cluster. An isolation parameter $E_{\mathrm{T}}^{\mathrm{cone}}$ is computed as the sum of E_{T} for all these clusters, minus the E_{T} of a cluster built within $\Delta\eta \times \Delta\phi = 0.125 \times 0.175$ of the candidate barycentre. To account for leakage of the cluster outside this rectangle, a correction is applied as a function of the candidate E_{T} and η.

To evaluate track isolation, all tracks within a variable-sized cone around the principal candidate track are summed. The size of this cone is determined by $\Delta R = \min(0.2, 10\ \mathrm{GeV}/E_{\mathrm{T}})$. Included tracks have $E_{\mathrm{T}} > 1$ GeV, and pass track quality requirements:

$$n_{\mathrm{Si}} \geq 7, \quad n_{\mathrm{Si}}^{\mathrm{hole}} \leq 2, \quad n_{\mathrm{Pixel}}^{\mathrm{hole}} \leq 1, \quad n_{\mathrm{mod}}^{\mathrm{sh}} \leq 1, \tag{6.5.1}$$

where "hole" in superscript labels the number of missing hits in the respective tracking layer, while $n_{\mathrm{mod}}^{\mathrm{sh}}$ represents the number of hits in the silicon detector assigned to multiple tracks. Additionally, each track must be associated with the reconstructed primary vertex of the hard collision $|\Delta z_0 \sin\theta| < 3$ mm. Tracks associated with the electron are excluded; as well as the primary electron track, this includes additional tracks identified as converted photons from bremsstrahlung. These requirements define the track isolation variable $p_{\mathrm{T}}^{\mathrm{varcone0.2}}$. Previously, a fixed cone isolation was used for electrons of $\Delta R = 0.2$, defining a variable $p_{\mathrm{T}}^{\mathrm{cone0.2}}$.

The requirements placed on these variables, which may be used singularly, or together, depend on the nature of the analysis. As well as a number of fixed isolation points of varying strictness (see table 6.5.1), they may be varied, optionally as a function of E_{T}, to achieve a desired target isolation efficiency.

6.6 Electron trigger

The ATLAS online data processing system provides information for reconstruction and identification of candidate electrons using both the L1 trigger and HLT.

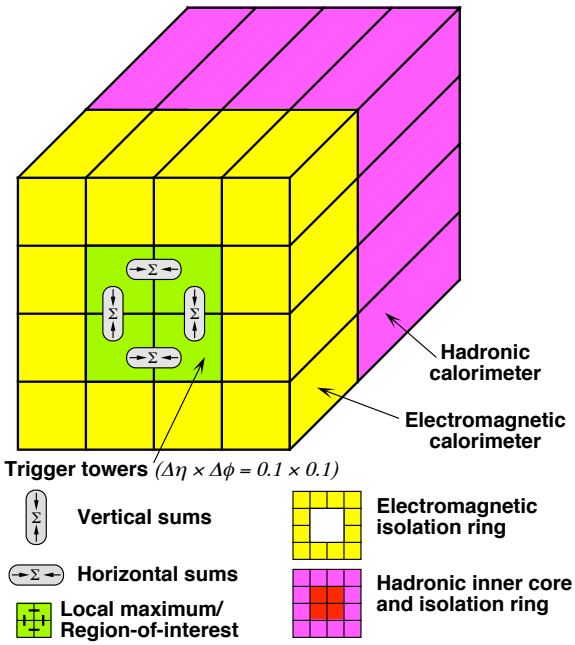

Figure 6.6.1: ATLAS calorimeter elements used for e/γ and τ/hadron reconstruction [125].

6.6.1 Level-1

Electron triggers use signals recorded in 4×4 blocks of trigger towers in the EM and hadronic calorimeters, equivalent to $\Delta\eta \times \Delta\phi = 0.4 \times 0.4$ (Fig. 6.6.1). The triggers calculate the energy within a core region of 2×2 towers, as well as the encircling outer towers. The ratio of the energy in the outer region to energy in the core may be used to inform an isolation requirement at L1. In addition, a limit on the maximum energy recorded in the hadronic calorimeter relative to the EM cluster energy in the core region (R_{had}) enables a hardware cut on the hadronic leakage. Electron candidates with energy exceeding 50 GeV need not satisfy the leakage requirement. The trigger E_{T} thresholds can be adjusted as a function of η for different trigger towers (corresponding to granularity of 0.1 in η) to account for the varying detector response in a given region. The energy is calibrated to the EM energy scale, thus the energy deposited by particles in an electromagnetic shower are correctly reconstructed, but the energy deposited by hadrons is underestimated. Regions that pass these requirements are designated Regions-of-Interest (RoIs) which can seed all later steps. Electron and photon (e/γ) triggers are always seeded by L1 RoIs; there are no full-scan e/γ triggers.

6.6.2 High-level trigger

At the HLT, candidate electrons undergo reconstruction and identification in successive steps, with the aim of rejecting unsuitable candidates as soon as possible. Previously the HLT consisted of two distinct steps: Level-2 (L2) and the Event Filter (EF). And, while the

data preparation for the previous L2 and EF stages has been merged in Run-2, rate reduction in the HLT still happens in several stages, meaning the L2 and EF jargon remains (Fig. 6.6.2). Once the rate has been reduced sufficiently, more sophisticated algorithms that use both tracking and calorimeter information may be applied. While these mimic the highly precise offline algorithms as closely as possible, they are limited by the permitted latency range. L2 now labels the earliest steps in the HLT trigger, which consist of fast cut-based calorimeter requirements, followed by simple track-cluster matching cuts.

Fast algorithms build clusters using the calorimeter cells from the $\Delta\eta \times \Delta\phi = 0.4 \times 0.4$ RoIs selected at the hardware level. The cell with the largest deposited transverse energy in the second layer of the EM calorimeter, within the ROI is also found. Successful Level-2 Calorimeter (L2Calo) electron candidates must pass requirements on the shower shape variables R_η, E_{ratio} and the transverse energy of the cluster, as well as on the energy deposit in the hadronic calorimeter R_{had}. Assuming L2Calo is satisfied, tracks are reconstructed using a faster, simplified tracking algorithm. To pass L2 these fast tracks require a minimum p_{T} of 1 GeV, and must be associated to a cluster within $\Delta\eta < 0.2$.

The second step of the HLT relies on precise offline-like algorithms, based on candidates selected at L2. Firstly, more sophisticated EM calorimeter clusters are built up using the method described in section 6.3. The HLT clusters are calibrated using a Multivariate Analysis (MVA) based technique, and these calibrated objects persist through to form reconstructed objects. The first selection algorithm is a calorimeter-only likelihood selection (EFCalo), which makes a decision based on more sophisticated clusters constructed after L2. These additional requirements on the shower shapes are applied to further reduce the rate before precision tracking is necessary. After passing this step, precision tracks are reconstructed and extrapolated to the second layer of the EM calorimeter. Electrons are then constructed by matching clusters to these tracks within $|\Delta\eta| < 0.05$ and $|\Delta\phi| < 0.05$.

At the HLT, the standard electron ID algorithms are also based on likelihood profiles, and are otherwise tuned, as closely as possible, to mimic the offline selection process described in section 6.4. However, naturally, the discriminant is optimised using the online reconstructed shower shapes and track variables. The online ID is performed using the same discriminating variables as the offline algorithm, summarised in table 6.4.2, with the exception of $\Delta p/p$. This variable is an indictor of the momentum lost in a track associated with bremsstrahlung, which is not considered online.

As is done offline, three levels of identification operating points are defined, in order of increasing strictness: Loose, Medium, and Tight. The discriminant requirements are not optimised according to E_{T} and $|\eta|$, as is done offline. However, in order to account for pileup effects they are relaxed with increasing μ.

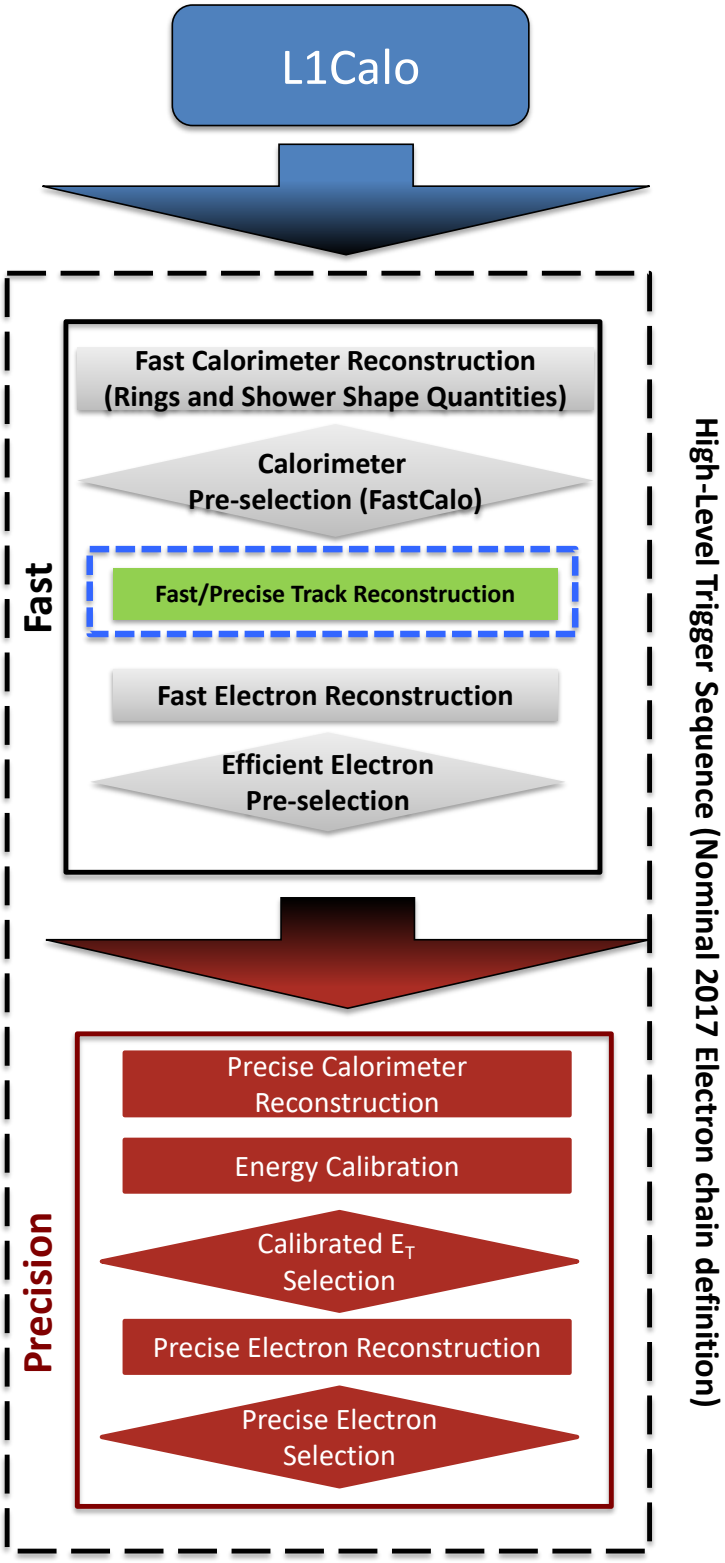

Figure 6.6.2: Electron trigger flow diagram showing sequences of reconstruction (in rectangles) and hypothesis algorithms (in triangles) an electron candidate must pass through for reconstruction from L1Calo to the final identification. The calibrated E_{T} selection are added in Run-2, and apply an MVA-based calibration to HLT calorimeter clusters. Courtesy of the ATLAS Trigger group.

2015	2016	2017
e24_lhmedium_L1EM20VH	e26_lhtight_nod0_ivarloose	e26_lhtight_nod0_ivarloose
e60_lhmedium	e60_lhmedium_nod0	e60_lhmedium_nod0
	e60_medium	
e120_lhloose	e140_lhloose_nod0	e140_lhloose_nod0
	e300_etcut	e300_etcut

Table 6.6.3: Recommended HLT single electron triggers in 2015, 2016, and 2017.

6.6.3 Trigger chains and naming conventions

The trigger proceeds in a series of sequential steps; a chain of trigger decisions. Individual trigger chains are named to illustrate some of these decisions. Take as an example `e24_lhlight_nod0_iloose_L1EM20VHI`. Here the initial `e` indicates that the target HLT object is an electron; (`g` would denote a photon γ). It can be preceded by a number that indicates object multiplicity for non-single triggers. The HLT E_{T} threshold in denoted by the subsequent digits (`24`).

The next string of characters labels the object identification that has been applied: `lhtight`, the tight operating point of the likelihood identification. Cut-based identification, which has not been widely used since 2016, is noted by an absence of the `lh` prefix. This label can be followed by additional modifications on the ID, for example `nod0` indicates that the d_0 parameter was not used to construct the likelihood discriminant.[3]

The level of isolation required is indicated by, for example, `iloose`. This indicates that the $p_{\mathrm{T}}^{\mathrm{cone0.2}}$ isolation variable was used, with the Loose operating point (section 6.5). The use of the $p_{\mathrm{T}}^{\mathrm{varcone0.2}}$ variable would be denoted by `ivarloose`.

The final label specifies that a non-default L1 trigger seeded this trigger chain: `L1EM20VHI`. This label itself carries information on the `L1_EM20VHI` trigger. Firstly, that its nominal E_{T} threshold in the EM calorimeter is 20 GeV. The next three characters indicate: that an E_{T} dependent trigger threshold has been applied (within $+2$ and -3 of the nominal), that hadronic core isolation has been applied, and that EM ring isolation has been applied, respectively.

6.7 Electron trigger efficiencies, inefficiencies, and scale factors

If an electron is produced in a collision, we are required to know the probability that ATLAS will detect it. We can estimate this by determining the total electron efficiency

[3]This is an example of a "misalignment robust" tune. In 2015 the `nod0` tune was found to increase the electron efficiency of the trigger, without overly affecting background rejection, and is used for most recommended trigger chains from 2016 onwards. I also studied the effect of misalignment robust tunes on efficiency as part of my qualification task.

for the ATLAS detector ϵ_{total}. This can, nominally, be divided into four components:

$$\epsilon_{total} = \epsilon_{reco} \times \epsilon_{ID} \times \epsilon_{trig} \times \epsilon_{add}. \tag{6.7.1}$$

These efficiencies are applied sequentially: the reconstruction efficiency ϵ_{reco} is measured with respect to clusters reconstructed in the electromagnetic calorimeter; the identification efficiency ϵ_{ID} is taken with respect to reconstructed electrons; trigger efficiencies are calculated for reconstructed electrons passing a specific identification criteria; the efficiency of any additional selection criteria ϵ_{add}, such as isolation cuts, i.e.

$$\epsilon_{ID} = \frac{N(reco \times ID)}{N(reco)}, \tag{6.7.2}$$

$$\epsilon_{trig} = \frac{N(reco \times ID \times trig)}{N(reco \times ID)}. \tag{6.7.3}$$

Where $N(reco \times ID)$ are the number of electrons passing reconstruction and identification, for example.

The efficiency ϵ_{trig} for a specific trigger chain is defined with respect to the equivalent offline ID and isolation operating point. It is defined as the fraction of events selected by the trigger in a sample of events with electrons reconstructed and identified by the offline algorithms.

So, a particular trigger efficiency may be interpreted as the probability for an offline-identified particle, from a sample S, to pass the trigger selection A, denoted $\epsilon_A(S)$, i.e.

$$\epsilon_A(S) = P(A|S) \approx \frac{k}{n}, \tag{6.7.4}$$

where n is the number of offline particles in S, and k is the number of offline particles in S that pass the trigger selection A. This can be determined as a function of E_{T} and η of the candidate electron, or the number of primary vertices.

The accuracy of the detector simulation in modelling the electron measurement efficiency is critical for searches for new physics. In order to reliably compare results from Monte Carlo (MC) simulation and data, for physics results, the MC samples must be corrected to reproduce the efficiencies measured in data. This is done using the scale factor $\mathcal{S}$, a multiplicative factor, defined as the ratio of the efficiency in data to that from MC

$$\mathcal{S} = \frac{\epsilon_{data}}{\epsilon_{MC}}. \tag{6.7.5}$$

The data measurements are compared to the simulation as a function of the candidate E_{T} and η to calculate accurate corrections.

In data, we have to be careful defining S, as all events in the data must, necessarily, have

already triggered one or more triggers, therefore, biasing the efficiency measurement. The approach used to gather such a sample is described in the following section.

In addition to the overall efficiency of the trigger, we can measure the inefficiency of each step in the trigger chain by matching the online and offline candidates and examining at which step the online candidate was rejected. The measurement methodology for such an analysis likewise begins with the sample selection described below.

6.8 $Z \to ee$ Tag and Probe

To select a clean and unbiased sample S of electrons, the tag and probe method is used. In general, this technique makes use of the characteristic resonance peak signatures in the invariant mass spectrum of certain decay processes; i.e. the large contribution to the cross section in the kinematic region around the unstable particle's pole mass. For electron efficiency measurements, the most commonly used decay processes to electrons are $Z \to ee$ and $J/\psi \to ee$. Due, to their respective invariant masses, the later process covers a low E_{T} range, between 7 and 20 GeV. $Z \to ee$ events are useful for probes with transverse energy larger than 15 GeV and are used in all these measurements.

By selecting events in which a di-electron invariant mass around the Z mass can be calculated (Fig. 6.8.1(a)), and for which one candidate electron (the "tag") has passed strict selection criteria, the second electron ("the probe") may be subjected to much looser requirements, while retaining a relatively pure sample. This probe may then be used to measure multiple efficiencies in electron reconstruction and identification. Every valid combination of pairs in the event is considered, so single events can provide multiple probes.

6.8.1 Event selection

Each event is required to have at least two offline reconstructed electron candidates of opposite charges. The event-wise selection uses a single electron trigger with LH tight identification requirements, a HLT E_{T} threshold of 26 GeV and loose isolation requirements (`e26_lhtight_nod0_ivarloose`). Events are required to be taken under the stable beam condition with all relevant sub-detectors fully operational.

One of these electrons must satisfy the strict tag requirements (Fig. 6.8.1(b)). Namely, it must satisfy the LH tight offline identification, with $E_{\mathrm{T}} > 27$ GeV, and lie outside the transition region of the barrel and end-cap calorimeters, $1.37 < |\eta| < 1.52$. Additionally, the tag electron must satisfy a matching condition with a HLT candidate, requiring a separation of $\Delta R < 0.07$.[4]

[4] During Run-1, the tag matching requirement was $\Delta R < 0.15$.

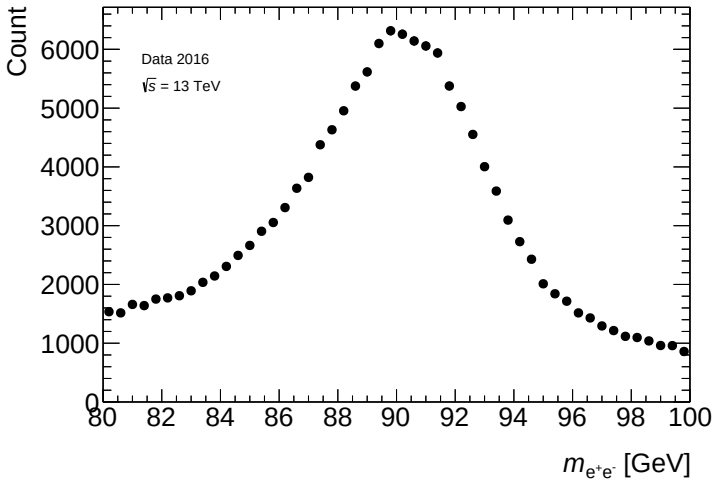

(a) The invariant mass, $m_{e^+e^-}$, of the oppositely charged offline reconstructed tag and probe electrons. No background subtraction is applied.

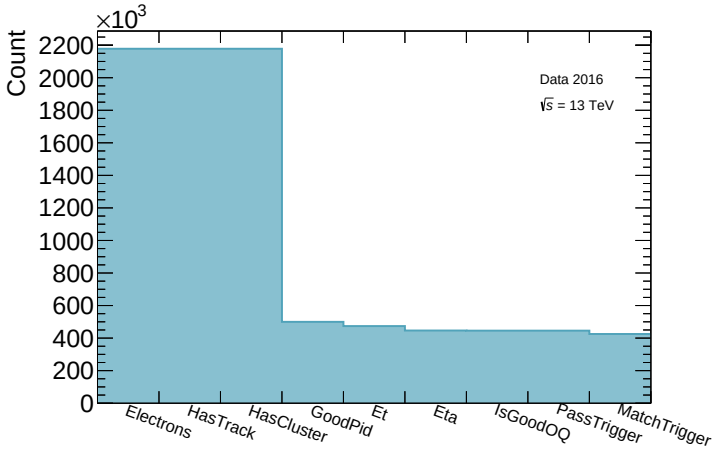

(b) Counts of the offline tag electron candidates for each step of the tag selection.

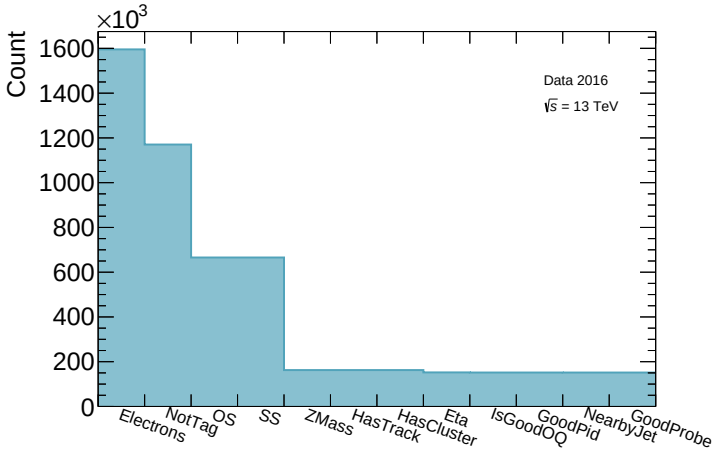

(c) Counts of the offline probe electron candidates for each step of the probe selection.

Figure 6.8.1: The invariant mass, $m_{e^+e^-}$, of the oppositely charged offline reconstructed tag and probe electrons after passing their respective selections is shown in (c). The counts following each selection criterion are shown in (b) and (c) for the tag and probe candidates, respectively. These are made using data collected by ATLAS in 2016 at $\sqrt{s} =$ 13 TeV. More details on the data sets can be found in section 6.11.1.

.

A second electron is then required lying within $|\eta| < 2.47$, excluding the transition region, that satisfies the Loose offline identification and has $E_{\mathrm{T}} > 4$ GeV. This second electron may be considered a probe electron if it carries opposite sign to the tag electron, and the invariant mass of the combined pair lies within the range $80 < m_{e^+e^-} < 100$ GeV. The probe is discarded if there is a jet with $p_{\mathrm{T}} > 20$ GeV within $\Delta R < 0.4$ (Fig. 6.8.1(c)).

6.8.2 Tools

Primarily, there are two software frameworks used to measure electron efficiencies with the ATLAS detector using the tag-and-probe method.

`TagAndProbeFrame` is a common central framework used for calculating electron scale factors. It is capable of background subtraction, and dominantly used to determine offline reconstruction and identification efficiencies. I worked on adding interfaces to trigger chains to allow the measurement of trigger efficiencies within this framework as a minor task within the e/γ signature trigger group.

`TrigEgammaAnalysisTools` is a package belonging to the Athena framework, which also features methods to measure the trigger efficiencies and inefficiencies. This environment is used to monitor the performance of the triggers during data taking, and was used for all measurements presented in this chapter. Modifications made by myself, specifically relating to the measurement of inefficiencies, were incorporated into the central framework.

6.9 Run-1 results for the sources of L2 and EF trigger inefficiency

The sources of inefficiency for the HLT, with respect to the offline reconstruction, were previously measured during Run-1 using approximately 4×10^5 $Z \to ee$ events, in data collected during 2012 [126, 127]. The inefficiencies were measured with a tag-and-probe method using $Z \to ee$ decays, by analysing probe electrons that pass the offline identification, but fail the online identification.

Public results were released for the `e24vhi_medium1` trigger. This is seeded by a level-1 trigger `L1_EM18VH` that allows at most 1 GeV energy deposited in the hadronic calorimeter behind the electron candidate's electromagnetic cluster. It requires an electron candidate with $E_{\mathrm{T}} > 24$ GeV satisfying a cut-based medium identification, as well as an isolation requirement of $p_{\mathrm{T}}^{\mathrm{iso}}/E_{\mathrm{T}} < 0.1$, where $p_{\mathrm{T}}^{\mathrm{iso}}$ is calculated by summing over the p_{T} of all tracks within a cone of $R = 0.2$ around the candidate track (excluding the candidate track itself).

The offline reconstructed electron was required to have a transverse energy of $E_{\mathrm{T}} > 25$ GeV, in order to avoid the turn-on curve, as well as passing the medium offline iden-

tification.

The results at the level-2 (L2) trigger are shown in Fig. 6.9.1 and at Event Filter (EF) in Fig. 6.9.2. Since a single candidate can fail more than one identification requirement, it may contribute to multiple bins: i.e. these plots do not feature exclusive categories. The inefficiencies due to candidates for which no corresponding track was found are distinguished by colour in the EF histogram, due to differences in the respective trigger identification algorithms.

The dominant sources of HLT electron trigger inefficiency can be seen to relate to track identification. By some margin, the leading contribution at L2 to the overall inefficiency are missing tracks associated to the EM cluster. Additionally, a number of candidates fail when the extrapolated track lies too far away in η from the cluster for a match. At the EF, clusters unassociated with a track cause approximately a third of failed candidates, though candidates with tracks still fail multiple track requirements.

6.10 Methodology of HLT inefficiency measurements in Run-2

While the methodology of these measurements remains largely the same in Run-2, a number of upgrades to the trigger system and changes in requirements for reconstruction have resulted in several improvements.

During Run-1 the online identification algorithms were entirely cut-based; i.e. each candidate was required to pass sequentially applied rectangular cuts on each of the discriminating variables. However, applying a multivariate likelihood-based ID algorithm offline and a cut-based selection online can lead to greater inefficiency. Hence, the dominant online ID algorithms used during Run-2 employs an adapted version of the offline ID. While cut-based algorithms are not used for Run-2 analyses, they do constitute an important sanity check of the LH-based trigger chains, and they largely use the same set of discriminating variables outlined in Tab. 6.4.2.

As in the LH approach, a number of different operating points are chosen that require different levels of background rejection. However, unlike the LH method, for which all operating points utilise the same set of discriminating variables, looser IDs use a subset of the variables used for the stricter operating points. The Loose cut-based identification depends on measurements of energy deposits in the front layers of the EM calorimeter, as well as hadronic leakage to reject background candidates. The Medium cut-based algorithm tightens these requirements, and supplements them with signals from the back layer in the EM calorimeter, as well as information pertaining to the TRT and the transverse impact parameter. As well as further tightening these requirements, the Tight cut-based ID includes criteria relating to track-cluster matching to further distinguish signal objects from background.

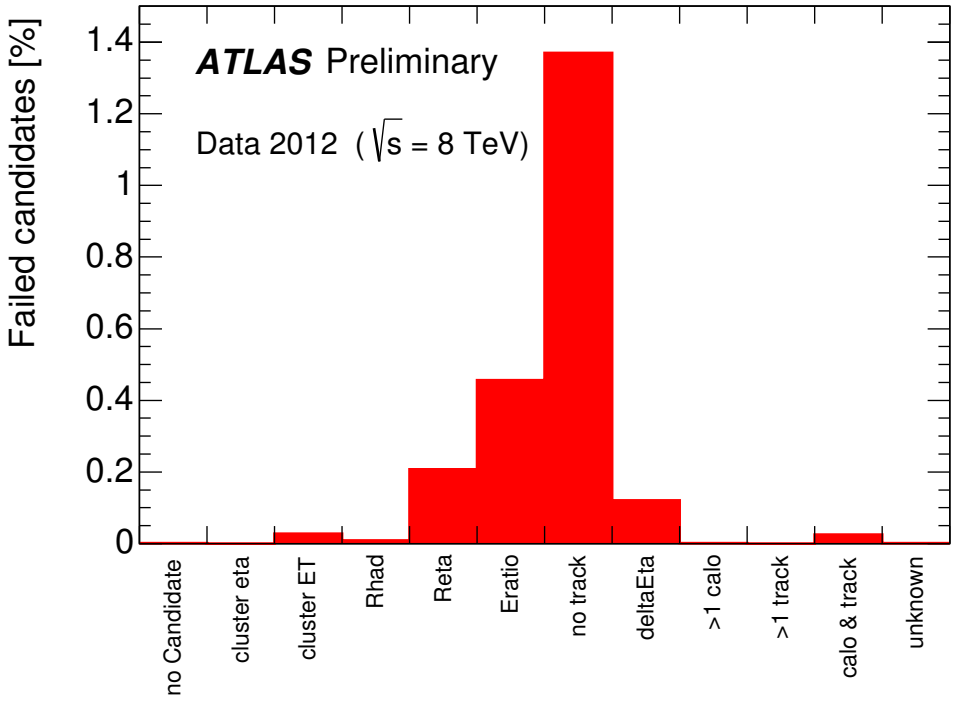

Figure 6.9.1: Inefficiencies for the `e24vhi_medium1` trigger at the level-2 trigger stage with respect to the offline reconstruction.

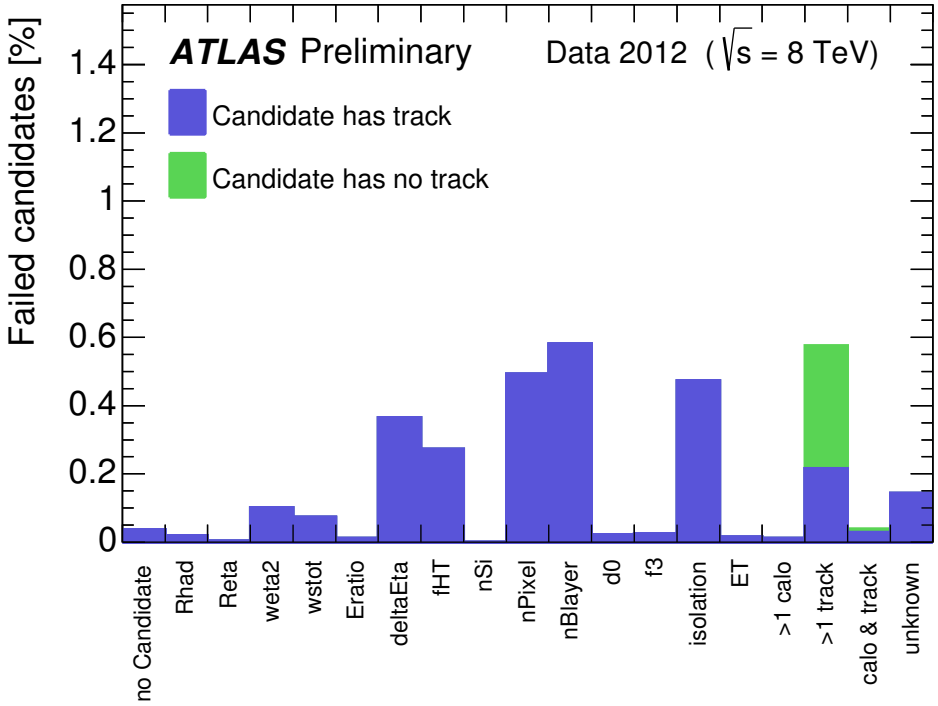

Figure 6.9.2: Inefficiencies for the `e24vhi_medium1` trigger for the Event Filter stage with respect to the offline reconstruction.

Throughout 2015, the cut-based algorithms continued to be optimised based on new data, and their sources of inefficiency were also studied. Due to differences in the available information for cut-based and LH-based trigger chains, the analysis tools have been written to recognise the trigger class and analyse inefficiencies such that cut-based and LH trigger performance may be compared directly.

As well as the shift to LH-based online algorithms, several changes to the discriminating variables have been introduced for the Run-2 electron ID. Firstly, the addition of the IBL provides an additional handle on discriminating prompt electrons (from $Z \to ee$ etc) and non-prompt electrons arising from photon conversions; previously, the second layer of the pixel layer served a similar purpose.

At Run-1, two variables relating to the TRT were used: the total number of hits (n_{TRT}), and the ratio of the number of high-threshold hits to the total number of hits F_{HT} to distinguish the signature transition radiation of electrons from hadrons. In Run-2, a single LH-based discriminant $ePrabilityHT$ is used which encompasses multiple characteristics of the TRT signals. This development was motivated, in part, by several changes to the TRT between Run-1 and Run-2. Primarily, the TRT gas has been changed from xenon to argon, the latter of which has a lower transition radiation absorption probability. The $ePrabilityHT$ uses the probability of each hit in the TRT to exceed the high-threshold limit, which changes as a function of the hit-position, the straw layer and gas, track-to-wire distance, and the Lorentz factor of the candidate track.

By analysing the trigger decision history for each probe I may establish the inefficiency due to individual cuts in the trigger chain, compared to loose, medium and tight offline configurations. Requirements are grouped into track, cluster, track-cluster matching and isolation based categories.

To determine the inefficiencies in the single electron trigger chains, I first collected an unbiased sample of electrons. This is achieved using the tag and probe method, as described in section 6.8. For each event, I consider all offline identified electrons and apply the event-wise selection. Each event that passes can contribute one or more tag-probe pairs, where the same offline object can satisfy both the tag and probe conditions.

Next I iterate over the trigger menu, selecting the trigger chains of interest and taking particular note of the threshold transverse energy $E_{\mathrm{T}}^{\mathrm{threshold}}$. For each trigger chain I loop over all offline probe electrons and match each probe to any trigger element with ΔR_{max} recursively down to L1. For HLT elements $\Delta R_{\mathrm{max}} = 0.07$, while for L1 $\Delta R_{\mathrm{max}} = 0.15$.[5] If no matching elements are found, the probe electron is still retained for subsequent analysis.

[5] During run-1, the matching requirement was $\Delta R < 0.15$ at L1 and the HLT.

Pos.	Name	Requirement
00	`Kinematic`	$\eta < 2.47$
01	`NSilicon`	$n_{\mathrm{Si}} \geq n_{\mathrm{Si}}^{\mathrm{min}}$
02	`NPixel`	$n_{\mathrm{Pixel}} \geq n_{\mathrm{Pixel}}^{\mathrm{min}}$
03	`NBlayer`	$n_{\mathrm{Blayer}} \geq n_{\mathrm{Blayer}}^{\mathrm{min}}$
04	`Conversion`	Not a converted photon
05	`LH`	LH discriminant passes
06	`TrackA0`	$d_0^{\mathrm{track}} \leq d_0^{\mathrm{max}}$
07	`TrackMatchEta`	$\Delta\eta_1 \leq \Delta\eta_1^{\mathrm{min}}$
08	`TrackMatchPhiRes`	$\Delta\phi_{\mathrm{res}} \leq \Delta\phi_{\mathrm{res}}^{\mathrm{min}}$
09	`WstotAtHighET`	$w_{\mathrm{stot}} \leq w_{\mathrm{stot}}^{\mathrm{min}}$
10	`EoverPAtHighET`	$E/p \leq (E/p)^{\mathrm{min}}$

Table 6.10.1: Bit allocation in the mask for recording selection decisions for likelihood-based trigger candidates.

Now we loop over the matched offline and online objects, first checking that the offline probe electron avoids the turn-on curve by comfortably exceeding the trigger threshold in transverse energy, $E_{\mathrm{T}}^{\mathrm{probe}} > E_{\mathrm{T}}^{\mathrm{threshold}} + 1$ GeV. We then step back through the trigger chain to identify the step that failed, meaning offline probes are matched to every step in the trigger chain, recursively. Assuming a matching element was found which passed the L1 Calorimeter step, but failed any subsequent step, we retrieve all matching trigger objects, including electrons, photons, clusters and tracks.

If a candidate fails after L1, but before the final ID algorithm (EFElectron), we record the inefficiency at the respective stage, i.e. Level-2 Calorimeter (L2Calo), Level-2 (L2), Event-Filter Calorimeter (EFCalo). If a candidate passes each of these stages, but fails at the highest level, we can further analyse the results using the trigger bit mask. These masks store the results for each selection criterion, and have a different structure if the trigger chain uses a cut-based or LH-based ID algorithm. The 32-bit `IsEM` mask for cut-based triggers stores the history of the 31 decisions made in the final step of selecting online electrons. The LH-based triggers also store final selection decisions in a bit mask, and there are a maximum of 11 requirements for this step, including that on the LH discriminant itself, which are allocated as shown in Tab. 6.10.1. In the Run-1 analysis, each of the online requirements was re-applied against the offline candidate in order to diagnose the failing conditions. However, for the Run-2 analysis the decision is retrieved from the respective decision bit mask. Additionally, in Run-2 electrons are always required to be associated with a track, which was not enforced in Run-1.

6.11 Run-2 results for the sources of HLT inefficiency

6.11.1 2016 data

The data sets used for the 2016 single electron trigger inefficiency analysis were collected in 2016, with a centre-of-mass energy of 13 TeV, and a bunch spacing of 25 ns. Specifically, data collected during 12 individual LHC runs were used.[6]

These data sets have already been passed through a minimal skimming selection process in readiness for $Z \rightarrow ee$ tag and probe analyses (using the EGAM1 derivation). Firstly, at least one of the following four requirements must be met: two oppositely-signed (OS) electrons, one satisfying tight offline LH ID requirements and $p_{\mathrm{T}} > 24.5$ GeV, and one passing the medium ID with $p_{\mathrm{T}} > 19.5$ GeV; two OS electrons each satisfying the medium ID with $p_{\mathrm{T}} > 19.5$ GeV; two central electrons, one passing medium ID with $p_{\mathrm{T}} > 24.5$ GeV, and another with $p_{\mathrm{T}} > 6.5$ GeV; one medium ID'd electron $p_{\mathrm{T}} > 24.5$ GeV, and one photon with $E_{\mathrm{T}} > 14.5$ GeV. Secondly, the invariant mass of at least one pair of electrons must exceed 50 GeV.

Events are selected using a Good Run List (GRL) which details periods of stable LHC collisions and full operation of all relevant ATLAS sub-detector systems. Furthermore, the status of the toroidal system is ignored for the purposes of this analysis.[7]

The offline likelihood identification algorithms used to measure the 2016 inefficiencies are constructed without accounting for the transverse impact parameter (d_0), for all operating points. Following the GRL and $Z \rightarrow ee$ selections, approximately $150,000$ tag-and-probe pairs remain.

The inefficiency results for two recommended single electron triggers in 2016 are shown in Fig. 6.11.1. Triggers `e26_lhtight_nod0_ivarloose` (a) and `e60_lhmedium_nod0` (b) are both seeded by a level-1 trigger that requires an isolated electromagnetic cluster with $E_{\mathrm{T}} > 22$ GeV (`L1_EM22VHI`). The `e26_lhtight_nod0_ivarloose`(`e60_lhmedium_nod0`) trigger requires an electron candidate with $E_{\mathrm{T}} > 26(60)$ GeV satisfying the likelihood-based tight identification, excluding the transverse impact parameter PDF. The offline reconstructed electron is required to have a transverse energy of $E_{\mathrm{T}}^{\mathrm{offline}} > 27(61)$ GeV and pass the likelihood-based tight(medium) identification without applying transverse impact parameter requirements interpolated smoothly over E_{T}. The `e26_lhtight_nod0_ivarloose` also requires a variable-size cone isolation, $p_{\mathrm{T}}^{\mathrm{varcone0.2}}/E_{\mathrm{T}} < 0.1$.

Results are presented in terms of the percentage of candidates that pass the offline se-

[6] Run numbers used in 2016 analysis: 298595, 298609, 298633, 298687, 298690, 298771, 298773, 299055, 299144, 299147, 299243, and 299340.

[7] 2016 GRL: `data16_13TeV.periodAllYear_DetStatus-v88-pro20-21_DQDefects-00-02-04_PHYS_StandardGRL_All_Good_25ns_ignore_TOROID_STATUS.xml`.

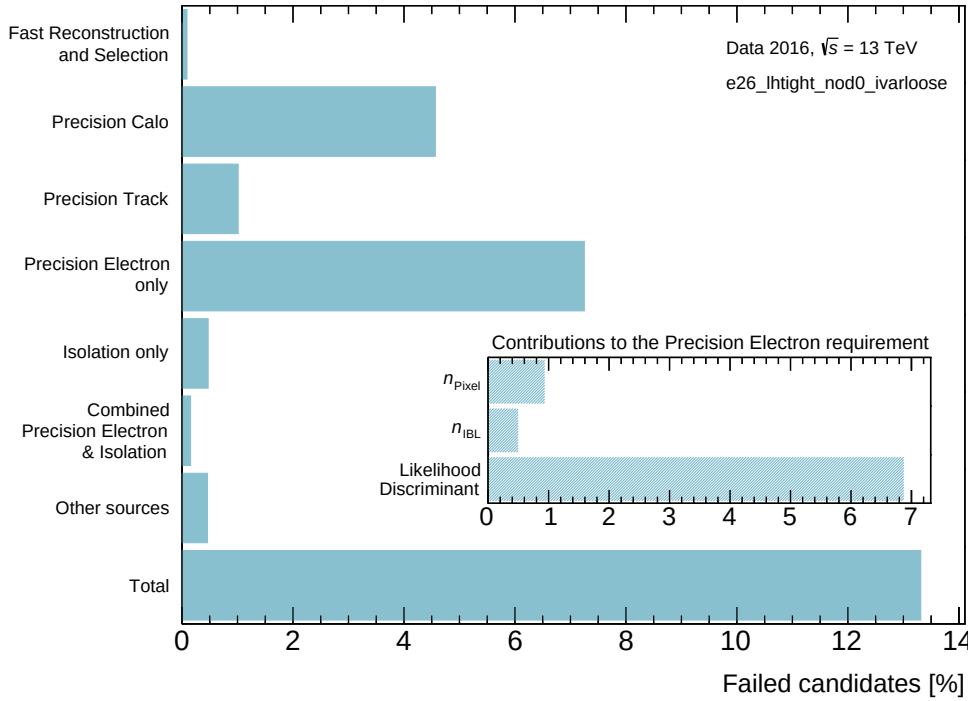

(a) The `e26_lhtight_nod0_ivarloose` trigger. This plot was made using approximately $80,000$ offline probe electrons.

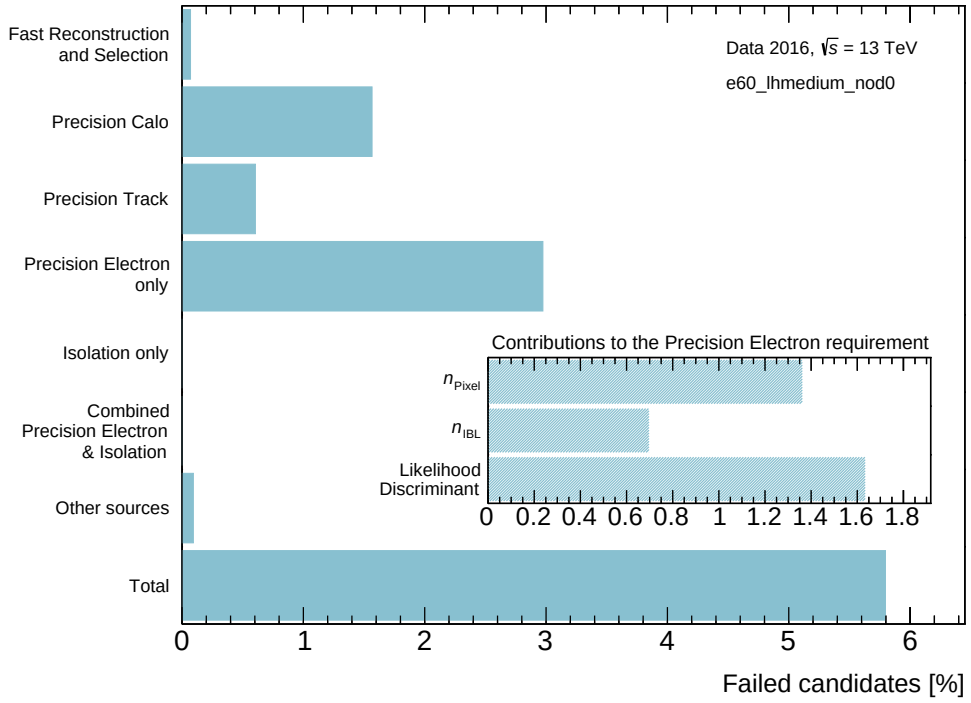

(b) The `e60_lhmedium_nod0` trigger. This plot was made using approximately 5000 offline probe electrons.

Figure 6.11.1: Sources of inefficiency for tag and probe compatible, recommended for 2016, Likelihood-based, single electron triggers at the HLT measured with respect to the offline reconstruction using data collected in 2016.

lection, but fail the indicated step in the online trigger sequence. These trigger chains are presented as their HLT E_{T} thresholds are compatible with the available energy range of $Z \to ee$ tag and probe. These both use a Likelihood-based (LH) online identification algorithm, without utilising the Probability Density Functions (PDFs) of the transverse impact parameter (d_0), and are seeded in η, ϕ, and energy by L1 EM RoIs with an E_{T} dependant nominal threshold of $E_{\mathrm{T}} > 22$ GeV, and that are fully isolated in the EM calorimeter ring, and hadronic core region (`L1_EM22VHI`). The first (Fig. 6.11.1(a)) features a HLT threshold of $E_{\mathrm{T}} > 26$ GeV, satisfying the tight operating point, and requires a variable-size cone isolation, $p_{\mathrm{T}}^{\mathrm{varcone0.2}}/E_{\mathrm{T}} < 0.1$. The second (Fig. 6.11.1(b)) requires a candidate with $E_{\mathrm{T}} > 60$ GeV, satisfying the medium operating point, with no isolation requirements. In each case the offline probe must have an energy at least 1 GeV higher than the HLT threshold, and have satisfied the respective offline LH operating point, Tight and Medium, respectively. Only inefficiency categories that are ever non-zero for any presented trigger are included in the figures. For example w_{stot} and E/p cuts are only used for online electron candidates exceeding $E_{\mathrm{T}} = 125$ GeV, not suitable for tag-and-probe analyses, and present requirements on n_{Si} do not cause any inefficiency.

The plots show that for both recommended trigger chains the calorimeter-only likelihood step (EFCalo) and high-level identification algorithm (ID) are the dominant source of inefficiency. Of the requirements for ID, the cut on the likelihood discriminant itself is the dominant source, particularly for `e26_lhtight_nod0_ivarloose`. This contribution is rivalled by the requirement on the number of precision hits in the pixel layers for `e60_lhmedium_nod0`.

Fig. 6.11.1(a) shows that the isolation inefficiency for this trigger is approximately 0.5%. The inefficiency using a variable cone isolation is marginally lower than when using a fixed cone isolation, as shown in Fig. 6.11.2(b), though this is not significant when measured over the full energy range. Improvements in efficiency should be expected at higher energies. Fig. 6.11.2(a) presents the same trigger chain, without isolation requirements. As expected the total inefficiency is reduced only due these missing requirements (though, of course, the background rejection for a less-pure sample would be significantly reduced).

Additionally, both plots in Fig. 6.11.1 feature an unknown source of inefficiency causing approximately 0.5% and 0.1% of candidates to fail the online reconstruction. This source of inefficiency is absent when analysing triggers in which the LH ID algorithm utilises d_0 PDFs. This is demonstrated in Figs. 6.11.3(a) and 6.11.3(b).

The total inefficiencies for the `e26_lhtight_nod0_ivarloose` and `e60_lhmedium_nod0` triggers in 2016 data are approximately 13% and 6%, respectively, over the full energy range of $E_{\mathrm{T}}^{\mathrm{threshold}} + 1$ GeV $\leq E_{\mathrm{T}}^{\mathrm{offline}} < 125$ GeV. Comparing the inefficiencies of the primary 2016 trigger (`e26_lhtight_nod0_ivarloose`) with those for the primary Run-1

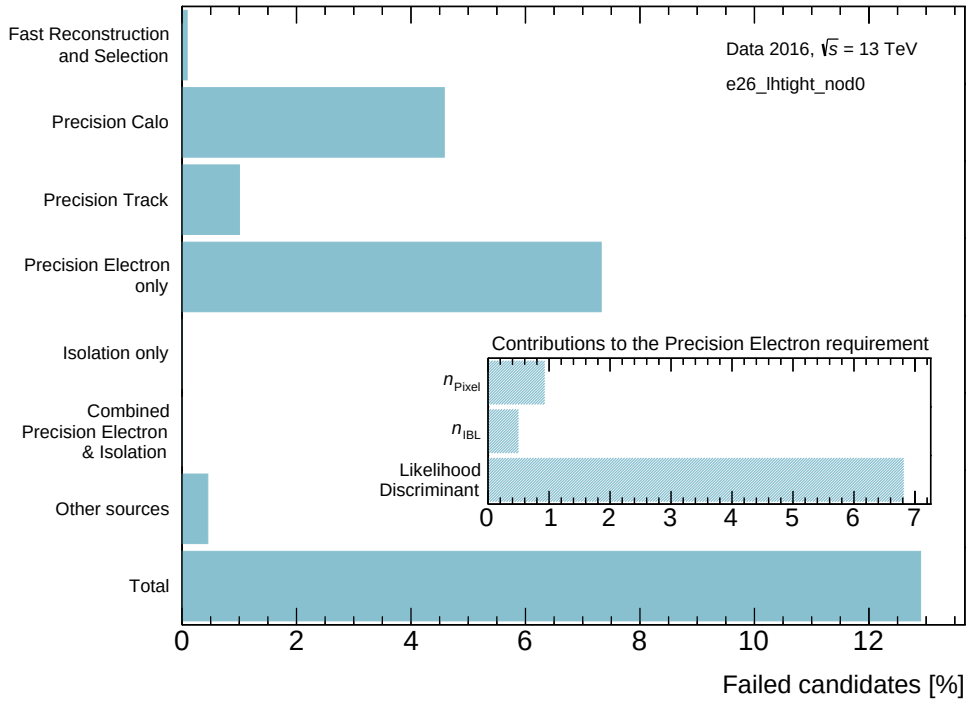

(a) No track-based isolation.

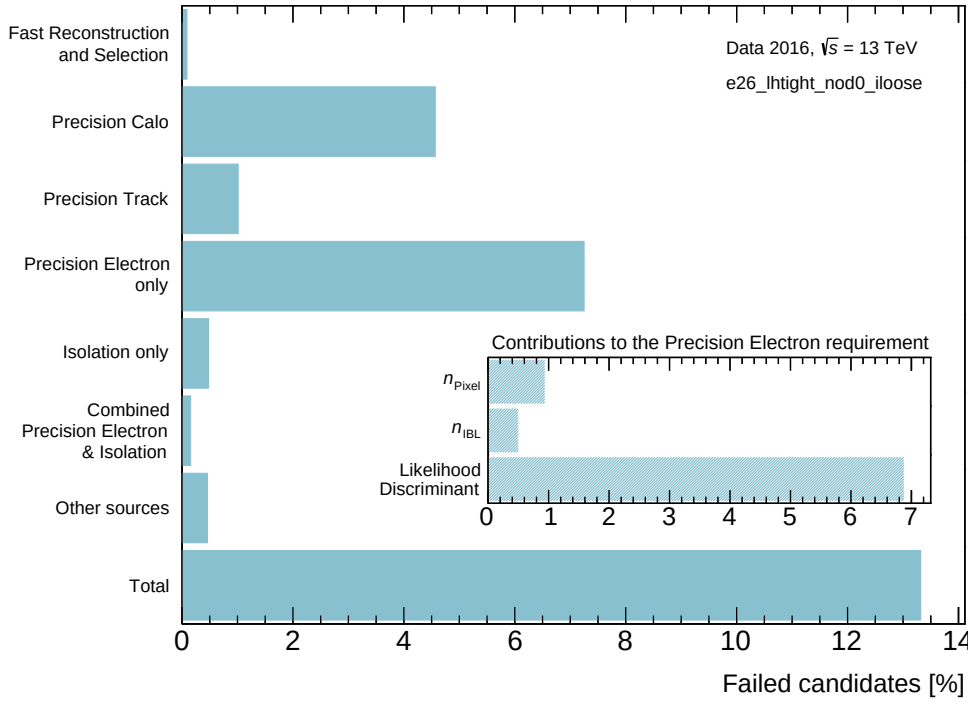

(b) Fixed-cone track-based isolation.

Figure 6.11.2: Sources of inefficiency for isolation variants of the primary recommended single electron trigger in 2016. The `e26_lhtight_nod0` (a), and `e26_lhtight_nod0_iloose` (b) triggers require no track-based isolation, and fixed-size cone isolation, $p_{\mathrm{T}}^{\mathrm{cone0.2}}/E_{\mathrm{T}} < 0.1$, respectively.

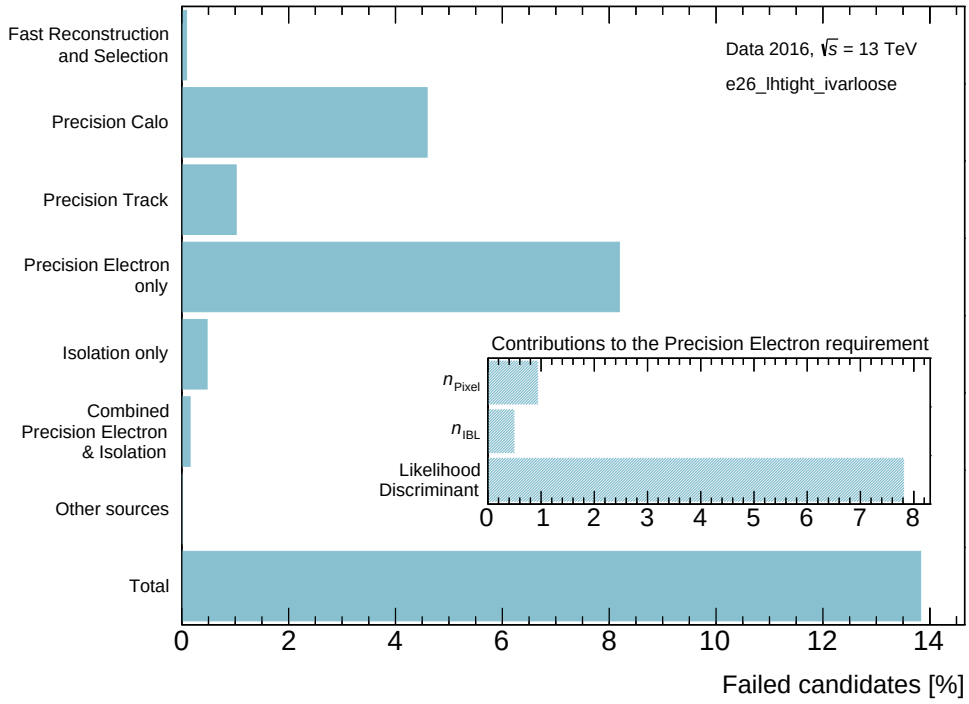

(a) Fixed-cone track-based isolation

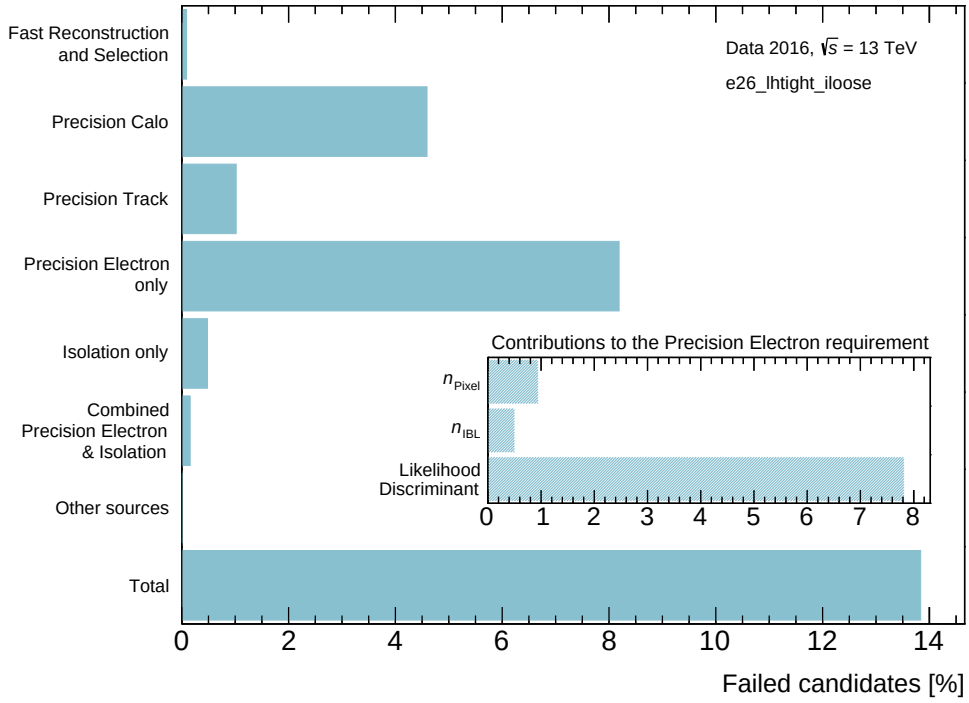

(b) Variable-cone track-based isolation

Figure 6.11.3: Sources of inefficiency for the primary recommended single electron trigger in 2016 using a Likelihood-based ID algorithm that includes the PDF of the transverse impact parameter (d_0). In both cases, the inefficiency in the Unknown category is unfilled for these LH trigger tunes that are inclusive of the d_0 PDFs.

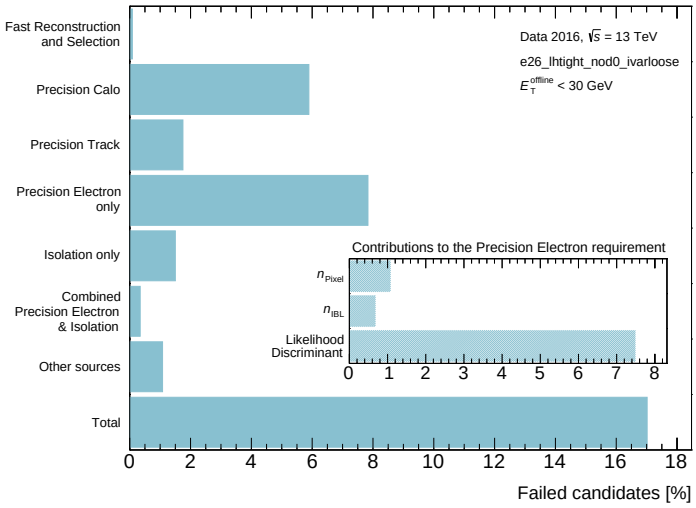

(a) $E_{\mathrm{T}}^{\mathrm{offline}} < 30$ GeV

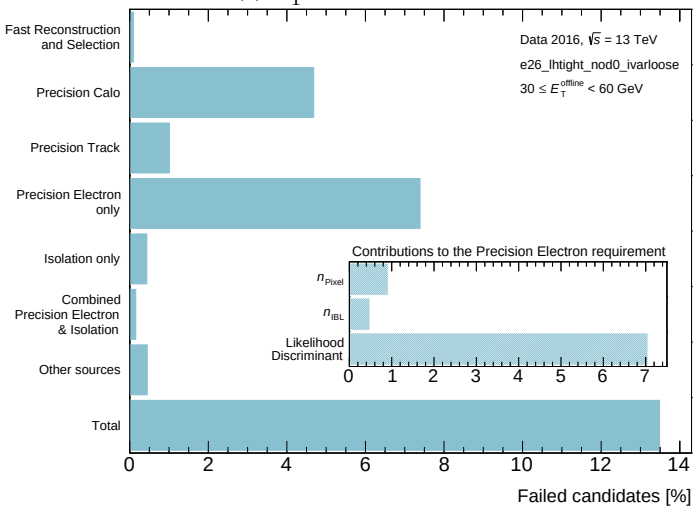

(b) $30 \leq E_{\mathrm{T}}^{\mathrm{offline}} < 60$ GeV

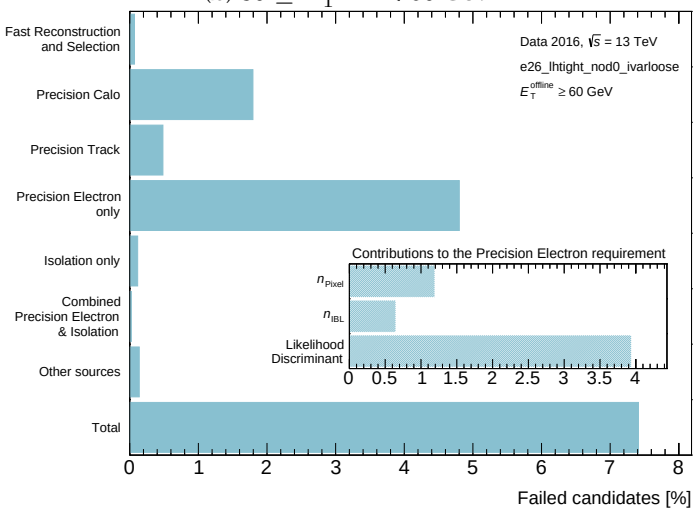

(c) $E_{\mathrm{T}}^{\mathrm{offline}} \geq 60$ GeV

Figure 6.11.4: Sources of inefficiency for the `e26_lhtight_nod0_ivarloose` High-Level Trigger with respect to the offline reconstruction in data collected in 2016 in three different bins of the offline probe electron transverse energy, $E_{\mathrm{T}}^{\mathrm{offline}}$.

trigger `e24vhi_medium1` presented in Figs. 6.9.1 and 6.9.2, the Run-2 inefficiencies in 2016 are significantly higher. The HLT efficiency dependence on $E_{\mathrm{T}}^{\mathrm{offline}}$ and η^{offline} is shown in Fig. 6.11.9 in overlay with the 2017 data. The inefficiency dependence with respect to the offline probe energy can be seen in Fig. 6.11.4, in which the measurements are binned in three different $E_{\mathrm{T}}^{\mathrm{offline}}$ ranges.

6.11.2 2017 data

The data sets collected in 2017 and used for the single electron trigger inefficiency also feature a centre-of-mass energy of 13 TeV, and a bunch spacing of 25 ns. A single run, number 338220, was analysed. The provided events were passed through the same skimming selection described in section 6.11.1. Events are again selected using a GRL which details periods of stable LHC collisions and full operation of all relevant ATLAS sub-detector systems. Following the GRL selection, and the $Z \to ee$ selection described in section 6.8, approximately $540,000$ tag-and-probe pairs remain.[8]

The inefficiency results for the two recommended single electron triggers in 2017 are shown in Figs. 6.11.5 and 6.11.6.[9] The methodology of the analysis and presentation of the results is largely the same as for the 2016 data. The offline likelihood identification algorithms used to measure the 2017 inefficiencies are re-tuned and constructed using the full range of discriminating variables, including the transverse impact parameter (d_0), for all operating points.

Between 2016 and 2017, several changes were made to the HLT electron selection sequence. Namely, the calorimeter-only likelihood requirement step, before precision tracks are extracted, has been dropped. Additionally, the PDFs of background and signal for each of the discriminating variables have been re-optimised using new online data, and the online algorithms tuned closer in performance to their offline counterparts.

The effect of these optimisations are clearly present for the primary single electron trigger shown in Fig. 6.11.5. The total inefficiency is reduced from $\approx 13\%$ to $\approx 8.5\%$.

One may examine the impact of looser operating points within the trigger chains in Fig. 6.11.7. In particular, note in Fig. 6.11.7(b) that when using the Loose operating point, the inefficiencies at L2, EFCalo, and the final ID are approximately equal, and the greatest contribution to inefficiency at the highest level is due to the cut on the number of precision pixel hits.

The inefficiency due to isolation requirements is shown in Fig. 6.11.5 to be approximately 1.5%. Fig. 6.11.8(a) confirms the impact of this requirement on the total inefficiency.

[8] 2017 GRL: `data17_13TeV.periodAllYear_DetStatus-v90-pro21-03_Unknown_PHYS_StandardGRL_All_Good_25ns_ignore_TOROID_STATUS.xml`

[9] These plots were made public. The long captions are retained for consistency with the public plots.

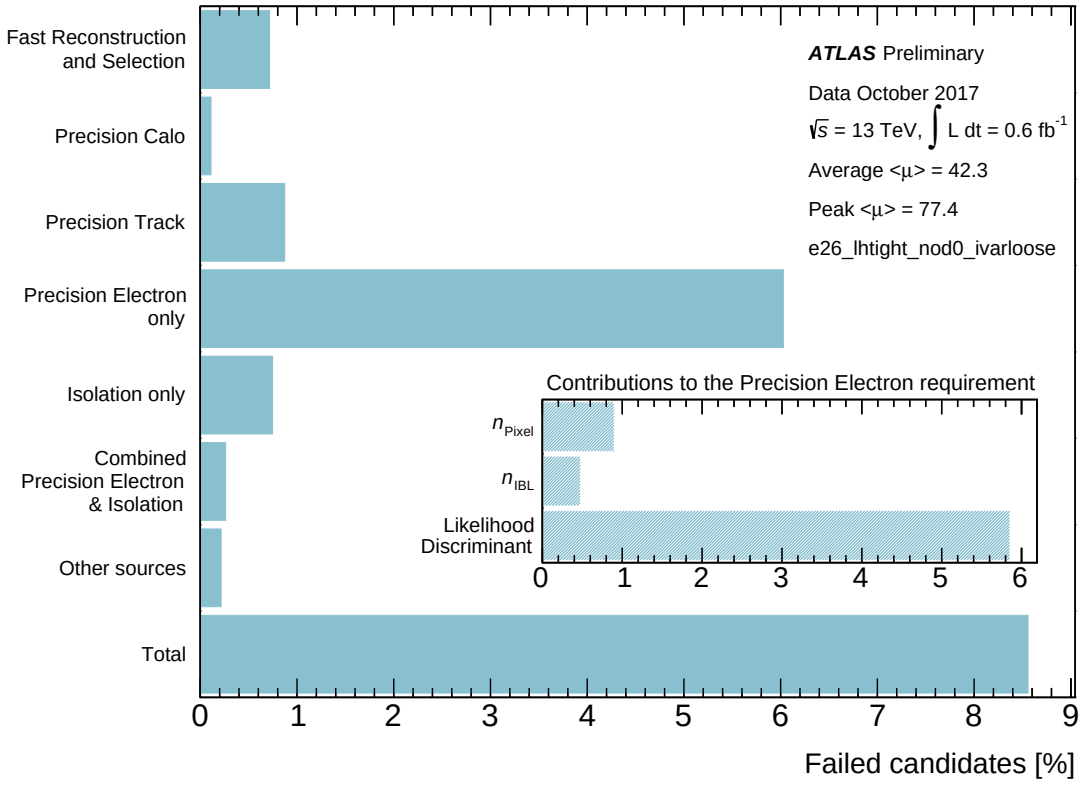

Figure 6.11.5: Sources of inefficiency for the `e26_lhtight_nod0_ivarloose` trigger at each selection step in the High Level Trigger (HLT) with respect to the offline reconstruction and the corresponding Level-1 (L1) requirements in a data run taken in October 2017. Electron reconstruction at the HLT is performed in the Region of Interest provided by the L1 and proceeds via a series of sequential steps. First, a Fast Reconstruction and Selection is performed; this constitutes a fast calorimeter reconstruction and neural-network-based selection using shower shape information, followed by a fast track reconstruction and electron pre-selection in which, in addition to track quality requirements, the calorimeter-tracking position matching quantities are used. In the Precision Calo step, HLT clusters are reconstructed and then calibrated using a multivariate technique, mirroring the offline identification. Subsequently, Precision Tracks are reconstructed and extrapolated to the second layer of the EM calorimeter. Electron candidates are then constructed by matching clusters to these tracks. The Precision Electron identification primarily utilises a Likelihood Discriminant based on calorimeter cluster shower shape, tracking and track-cluster matching variables, in addition to a required minimum number of hits in the (first layer of the) Pixel detector, n_{Pixel} (n_{IBL}). The inset plot provides supplementary information on these contributions to the Precision Electron requirement, which are mutually non-exclusive. Additionally, isolation requirements on the Precision Electron candidate may be applied; if the candidate fails the Precision Electron selection but passes isolation, Precision Electron only is filled; if the candidate passes Precision Electron buts fails isolation, Isolation only is filled; if both fail, Combined Precision Electron & Isolation is filled. The L1 requirement for this trigger, `EM22VHI`, requires an isolated electromagnetic cluster with $E_{\mathrm{T}} > 22$ GeV. The offline reconstructed electron is required to have a transverse energy of $E_{\mathrm{T}} > 27$ GeV and pass the likelihood-based tight identification (ID). The `e26_lhtight_nod0_ivarloose` trigger requires an electron candidate with $E_{\mathrm{T}} > 26$ GeV satisfying the likelihood-based tight ID, without applying transverse impact parameter requirements, but applying variable-size cone isolation, $p_{\mathrm{T}}^{\mathrm{varcone0.2}}/E_{\mathrm{T}} < 0.1$. The inefficiencies are determined by the percentage of candidates that pass the offline ID, but fail the online ID at the indicated step, measured with a tag-and-probe method using $Z \to ee$ decays providing $\sim 2.5 \times 10^5$ suitable probe electrons. The sizes of the contributions of the individual selection steps to the overall inefficiency depend on the p_{T} of the electron, and therefore, in this plot, depend on the p_{T} spectrum of the probe-electron of the $Z \to ee$ test sample.

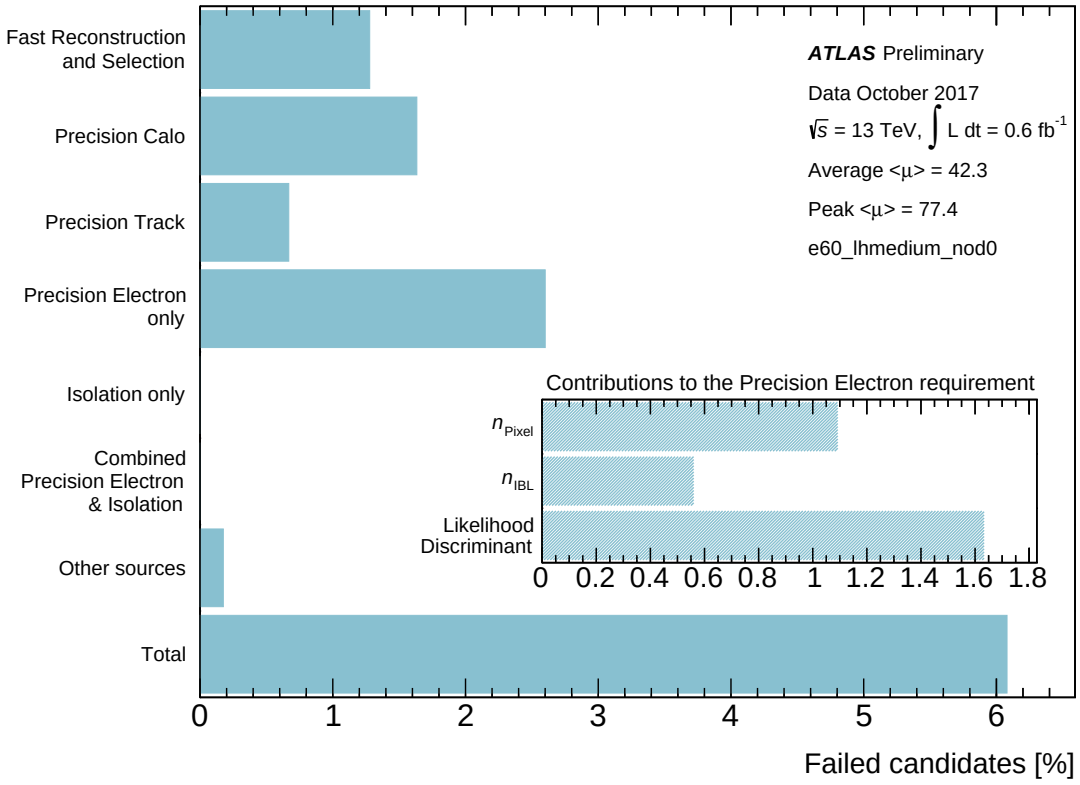

Figure 6.11.6: Sources of inefficiency for the `e60_lhmedium_nod0` trigger at each selection step in the High Level Trigger (HLT) with respect to the offline reconstruction and the corresponding Level-1 (L1) requirements in a data run taken in October 2017. Electron reconstruction at the HLT is performed in the Region of Interest provided by the L1 and proceeds via a series of sequential steps. First, a Fast Reconstruction and Selection is performed; this constitutes a fast calorimeter reconstruction and neural-network-based selection using shower shape information, followed by a fast track reconstruction and electron pre-selection in which, in addition to track quality requirements, the calorimeter-tracking position matching quantities are used. In the Precision Calo step, HLT clusters are reconstructed and then calibrated using a multivariate technique, mirroring the offline identification. Subsequently, Precision Tracks are reconstructed and extrapolated to the second layer of the EM calorimeter. Electron candidates are then constructed by matching clusters to these tracks. The Precision Electron identification primarily utilises a Likelihood Discriminant based on calorimeter cluster shower shape, tracking and track-cluster matching variables, in addition to a required minimum number of hits in the (first layer of the) Pixel detector, n_{Pixel} (n_{IBL}). The inset plot provides supplementary information on these contributions to the Precision Electron requirement, which are mutually non-exclusive. Additionally, isolation requirements on the Precision Electron candidate may be applied; if the candidate fails the Precision Electron selection but passes isolation, Precision Electron only is filled; if the candidate passes Precision Electron buts fails isolation, Isolation only is filled; if both fail, Combined Precision Electron & Isolation is filled. The L1 requirement for this trigger, `EM22VHI`, requires an isolated electromagnetic cluster with $E_{\mathrm{T}} > 22$ GeV. The offline reconstructed electron is required to have a transverse energy of $E_{\mathrm{T}} > 61$ GeV and pass the likelihood-based tight identification (ID). The `e60_lhmedium_nod0` trigger requires an electron candidate with $E_{\mathrm{T}} > 60$ GeV satisfying the likelihood-based tight ID, without applying transverse impact parameter requirements or isolation (the associated categories are retained here for consistency with other plots). The inefficiencies are determined by the percentage of candidates that pass the offline ID, but fail the online ID at the indicated step, measured with a tag-and-probe method using $Z \to ee$ decays providing $\sim 1.5 \times 10^4$ suitable probe electrons. The sizes of the contributions of the individual selection steps to the overall inefficiency depend on the p_{T} of the electron, and therefore, in this plot, depend on the p_{T} spectrum of the probe-electron of the $Z \to ee$ test sample.

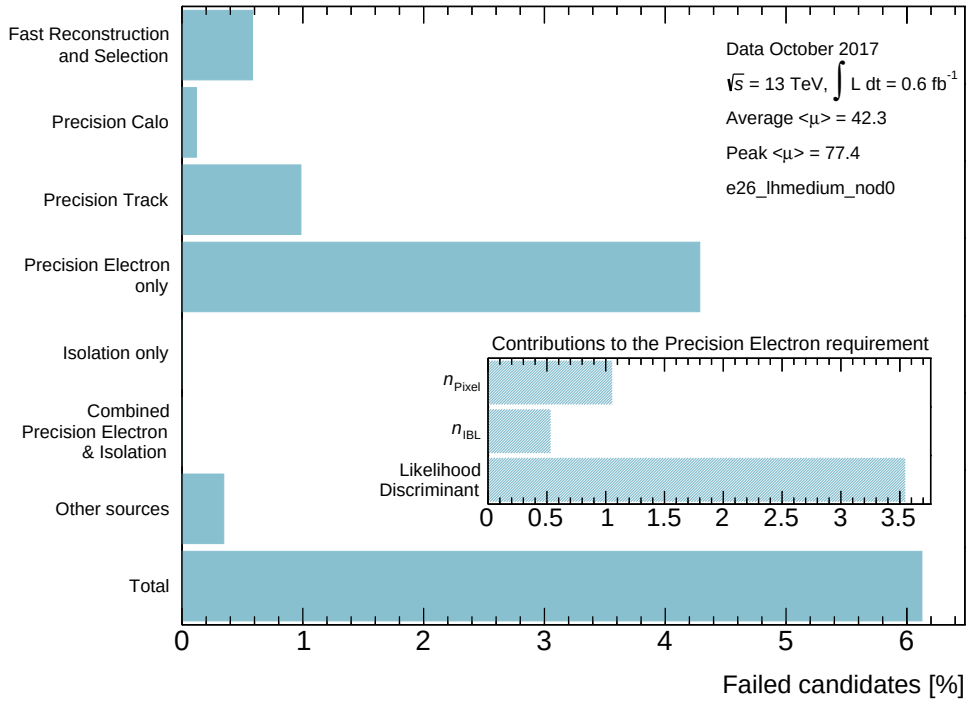

(a) The `e26_lhmedium_nod0` trigger.

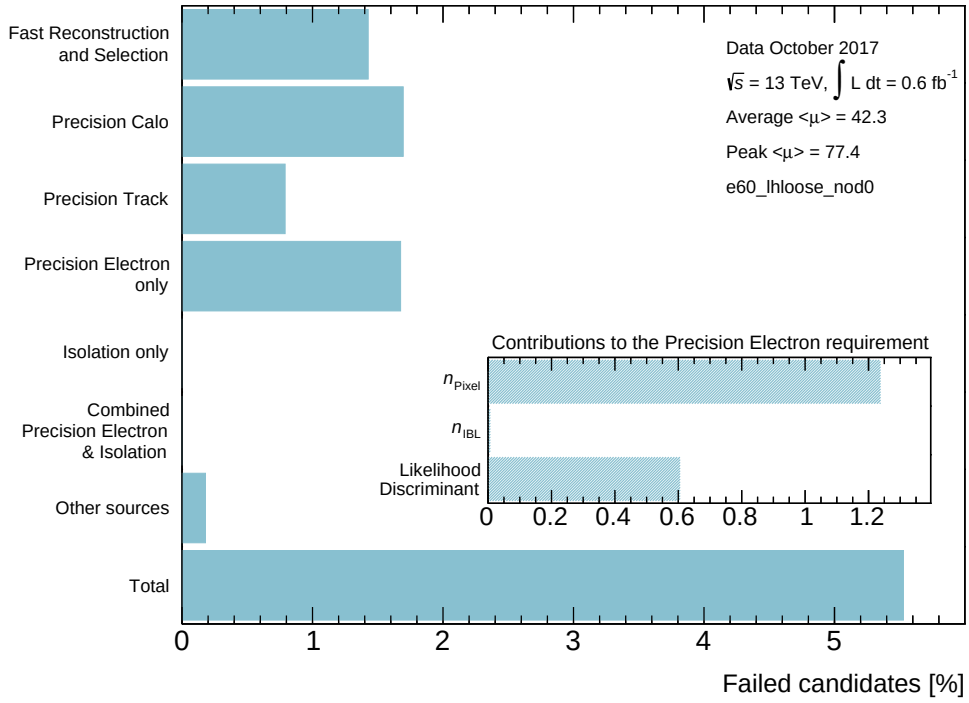

(b) The `e60_lhloose_nod0` trigger.

Figure 6.11.7: Sources of inefficiency for tag and probe compatible Likelihood-based, HLT single electron triggers, with looser operating points than their recommended counterparts, measured with respect to the offline reconstruction using data collected in 2017.

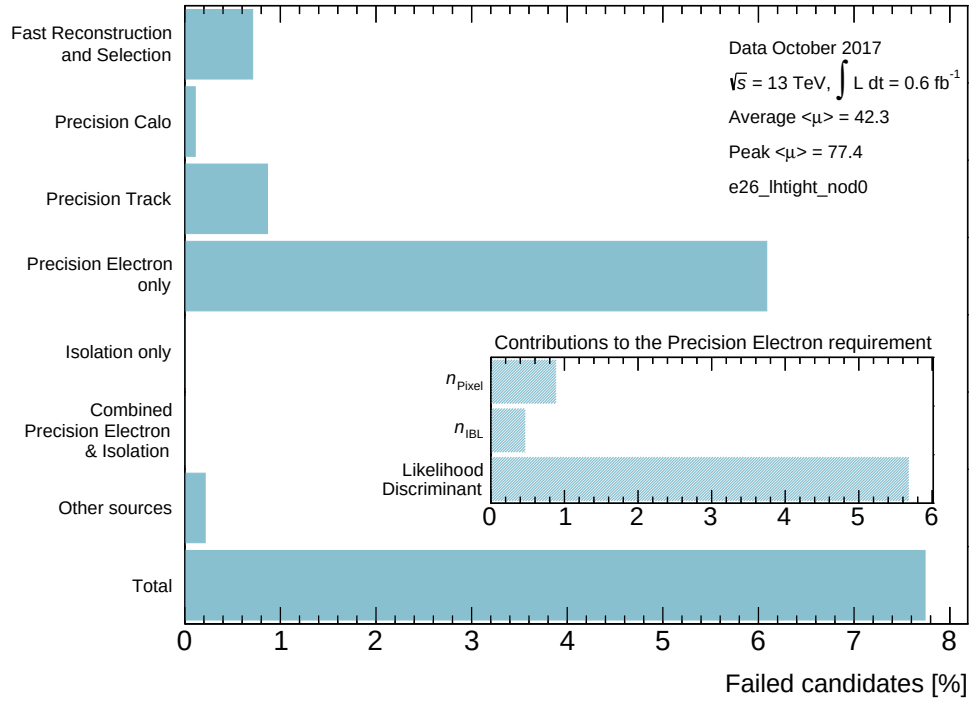

(a) The `e26_lhtight_nod0` trigger.

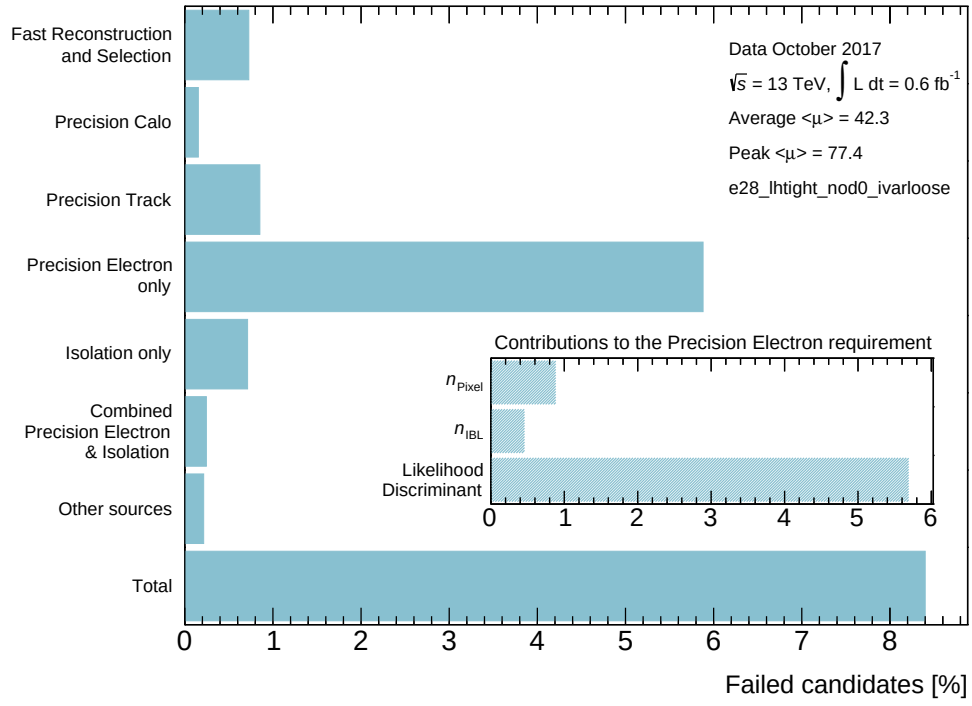

(b) The `e28_lhtight_nod0_ivarloose` trigger.

Figure 6.11.8: Sources of inefficiency for HLT single electron triggers measured with respect to the offline reconstruction using data collected in 2017. The first (a) is a non-isolating variant of the primary recommended trigger. The second (b) differs by having a HLT threshold higher by 2 GeV.

With a HLT threshold of 28 GeV, the results are largely unchanged, as demonstrated in Fig. 6.11.8(b).

The HLT efficiency dependence on $E_{\mathrm{T}}^{\mathrm{offline}}$ and η^{offline} is shown in Fig. 6.11.9 in overlay with the 2016 data. Overall the efficiency is higher in 2017, though at low $E_{\mathrm{T}}^{\mathrm{offline}}$ and high $|\eta^{\mathrm{offline}}|$ the efficiency is reduced with respect to 2016 data. The inefficiency dependence as a rough function of the offline probe $E_{\mathrm{T}}^{\mathrm{offline}}$ can be seen in data collected in 2017 in Fig. 6.11.10. Once again, the measurements are binned in three different $E_{\mathrm{T}}^{\mathrm{offline}}$ ranges: $E_{\mathrm{T}}^{\mathrm{offline}} < 30$ GeV, $30 \geq E_{\mathrm{T}}^{\mathrm{offline}} < 60$ GeV and $E_{\mathrm{T}}^{\mathrm{offline}} \geq 60$ GeV. Comparing this plot with Fig. 6.11.4 one can see that the inefficiencies have been reduced in all ranges, with significant improvements above 30 GeV.

6.12 Conclusions

The inefficiencies for the single electron triggers have been measured using LHC pp collision data collected by ATLAS at 13 TeV centre-of-mass energy in both 2016 and 2017. The efficiencies were measured with respect to offline reconstructed electrons selected using a $Z \to ee$ tag and probe method. Given the available energy range with this method, determined by the Z boson resonance, single electron triggers with a HLT threshold up to 60 GeV were analysed.

The primary sources of inefficiency in 2016 were found to come from the calorimeter-only likelihood requirement and the cut on the online-derived likelihood discriminant in the high-level identification algorithm. Informed by these results, the calorimeter-only likelihood selection at the EFCalo was dropped for data taking during 2017. Additionally, the ATLAS collaboration made use of new data-driven electron likelihood tunes that give higher efficiencies with respect to the offline algorithms. The impact of these changes may be observed in the results of data collected in 2017, with a significant decrease in the overall inefficiency for the primary single electron trigger coming particularly from increased efficiency of the online likelihood-based algorithm.

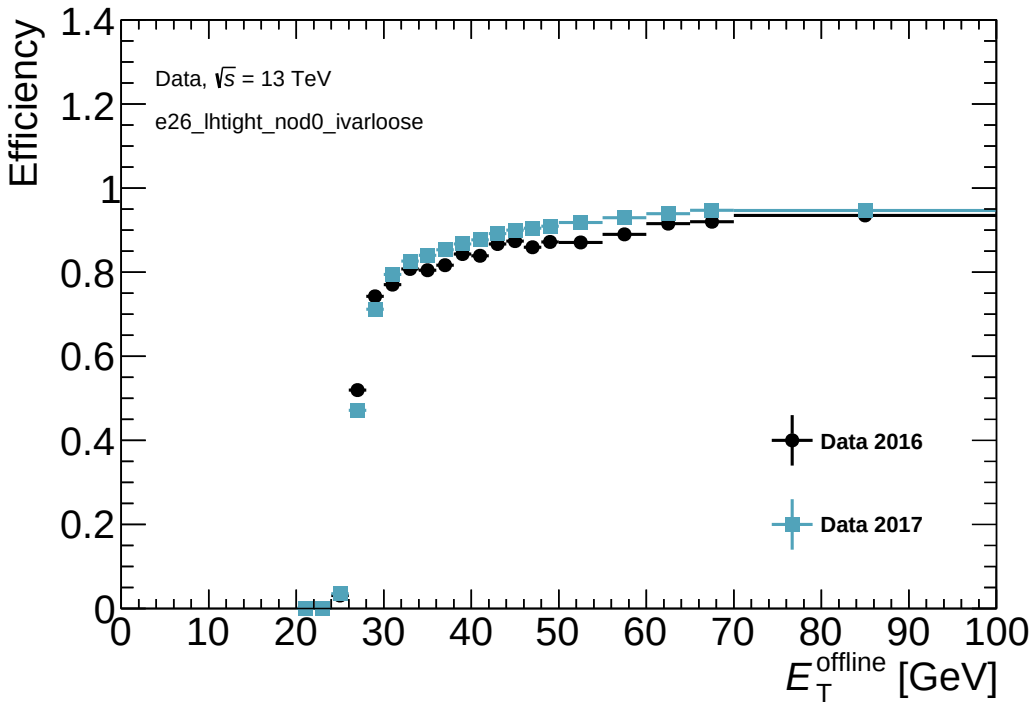

(a) $E_{\mathrm{T}}^{\mathrm{offline}}$

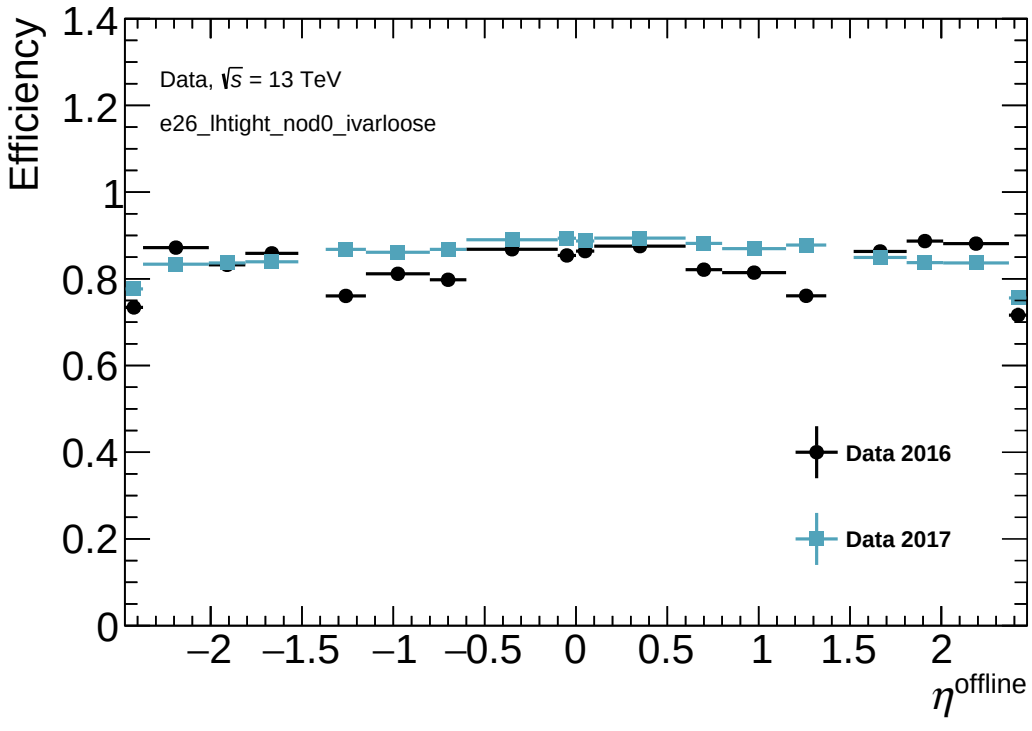

(b) η^{offline}

Figure 6.11.9: Efficiency for the `e26_lhtight_nod0_ivarloose` High-Level Trigger with respect to the offline reconstruction as a function of $E_{\mathrm{T}}^{\mathrm{offline}}$ and η^{offline} overlaying data collected in 2016 and 2017. No background subtraction is applied. The error bars show the statistical uncertainties.

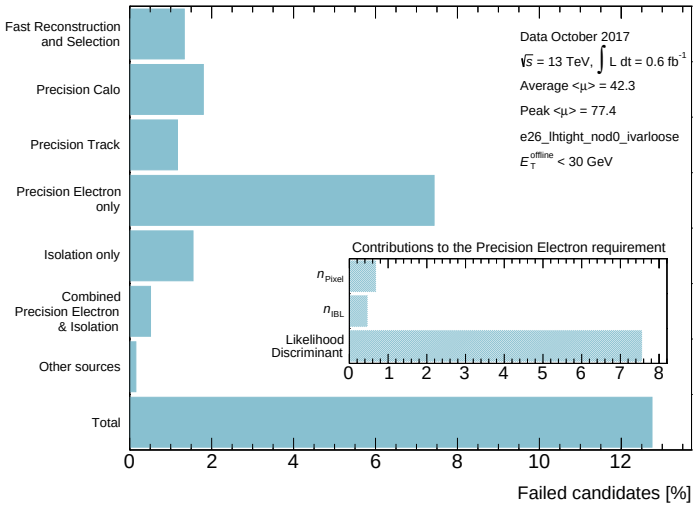

(a) $E_{\mathrm{T}}^{\mathrm{offline}} < 30$ GeV

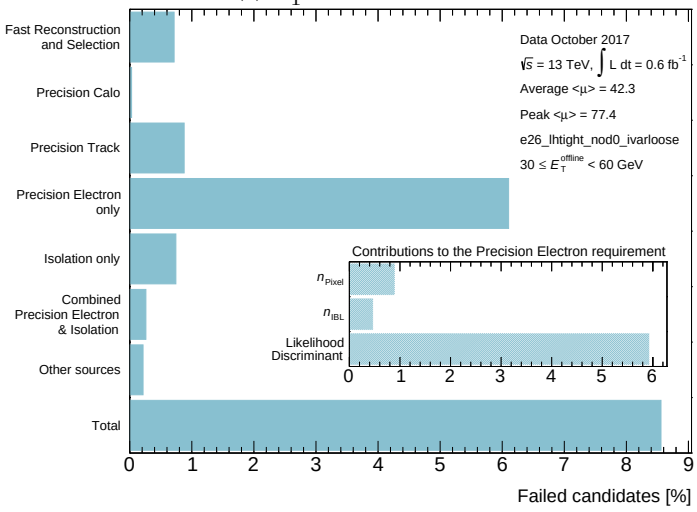

(b) $30 \leq E_{\mathrm{T}}^{\mathrm{offline}} < 60$ GeV

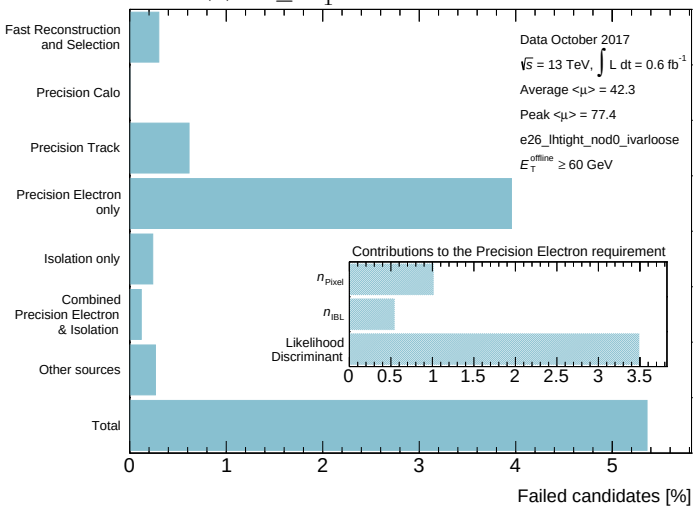

(c) $E_{\mathrm{T}}^{\mathrm{offline}} \geq 60$ GeV

Figure 6.11.10: Sources of inefficiency for the `e26_lhtight_nod0_ivarloose` High-Level Trigger with respect to the offline reconstruction in data collected in 2017 in three different bins of the offline probe electron transverse energy, $E_{\mathrm{T}}^{\mathrm{offline}}$.

CHAPTER 7

Distinguishing Z' bosons with the lepton-plus-jets final state

7.1 Introduction

In this chapter the sensitivity to the presence of a single Z' boson at the Large Hadron Collider (LHC) is studied for a number of generationally universal benchmark models, outlined in section 2.2. This same range of models is explored in Ref. [48]. That analysis is here extended to include the off-shell semileptonic decay of the top quarks and the consequently required reconstruction is emulated, with the corresponding decay-level observables described in section 7.3.

Numerous phenomenological papers have been produced that study the same or similar observables at the Large Hadron Collider (LHC) for a range of different BSM scenarios [128, 129, 130, 131], including those accounting for full showering/hadronisation and fast simulation of detector effects [132, 133, 134]. Other studies focus on different observables, particularly those suited to fully hadronic or dileptonic top decays [135, 136]. In addition to the specific selection of GUT derived models explored in our study, I uniquely study these observables in combination with the differential cross section, in a two dimensional analysis, and calculate the subsequent improvement in the statistical significance. I show how a combination of these observables enable us to distinguish between different classes of models.

This study concerns the lepton-plus-jets final state and imitates some experimental conditions arising for this channel. These include kinematic requirements and top quark

Model	L	Q	SSM	R	BL	LR	Y	χ	ψ	η	S	I	N
$m_{Z'}$ [TeV]	3.14	3.72	2.90	3.04	2.95	2.77	3.26	2.70	2.56	2.62	2.64	2.60	2.57

Table 7.2.1: Lower bounds on the mass of a new resonance ($m_{Z'}$) embedded by benchmark GUT models, based on $\sqrt{s} = 8$ TeV CMS results with an integrated luminosity of $L = 20.3$ fb^{-1} [14, 60].

pair reconstruction in the presence of missing transverse energy and combinatorial ambiguity in jet-top assignment, while remaining limited to the parton level (section 7.4). For each of the model classes described in section 2.2, g' is fixed and the angular parameter dictating the relative strengths of the component generators is varied until interesting limits for each class are recovered. The aim is to assess the prospect for an LHC analysis to profile a Z' boson mediating $t\bar{t}$ production, using both a standard bump-hunt via the cross section, as well as the charge asymmetry of the top quark system and the single top polarisation, with results and conclusions in section 8.8 and 7.7, respectively.

7.2 Models and present limits

The range of model classes considered in this analysis are described in section 2.2, with parameters summarised in Tab. 2.2.3. These models are all universal, with the same coupling strength to each generation of fermion. Therefore, as with an SSM Z', the strongest experimental limits come from the DY channel. Analysing 20.3 fb^{-1} of proton-proton data at $\sqrt{s} = 8$ TeV from the LHC, both the ATLAS experiment and CMS experiment exclude a Sequential SM (SSM) Z', at the 95% confidence level, for masses lower than 2.90 TeV, in the combined electron and muon channels [13, 14]. Based on these results, the limits for the GUT inspired models have been extracted in Ref. [60] (Tab. 7.2.1).

Using 3.2 fb^{-1} of $\sqrt{s} = 13$ TeV data, the ATLAS collaboration has published combined results in DY that place a lower limit on the mass of an SSM Z' at 3.36 TeV [15]. Presently unpublished results, from both collaborations, with approximately 13 fb^{-1} push this upper limit to 4 TeV [16, 17]. As indicated in Tab. 7.2.1, mass limits for the benchmark models are generally close to those of an SSM Z'; therefore, 4 TeV is selected as the benchmark mass for the new resonance.

7.3 Observables

Of the observables considered in chapter 3 only measurements of the top spin correlation are not suited to the lepton-plus-jets channel. Therefore, in addition to the differential cross section measured via the number of events distributed in the invariant mass of the top quark pair system (m_{tt}), two asymmetry observables are considered.

The charge asymmetry is defined using the cosine of the angle of the top quark mea-

sured with respect to the collider z-axis in the centre of mass frame of the top quark pair multiplied by the sign of the rapidity of the top quark pair in the collider frame (y_{tt}):

$$\cos\theta_t^* = \frac{y_{tt}}{|y_{tt}|}\cos\theta_t, \tag{7.3.1}$$

It is used to define the reconstructed forward-backward asymmetry:

$$A_{FB^*}^t = \frac{N(\cos\theta_t^* > 0) - N(\cos\theta_t^* < 0)}{N(\cos\theta_t^* > 0) + N(\cos\theta_t^* < 0)}. \tag{7.3.2}$$

The relationship outlined in Eq. 3.6.3 enables the top polarisation,

$$A_L = \frac{N(+,+) + N(+,-) - N(-,-) - N(-,+)}{N(+,+) + N(+,-) + N(-,-) + N(-,+)}, \tag{7.3.3}$$

to be probed using the angular distribution of the decay lepton in the top rest frame. Here $N(\lambda_t, \lambda_{\bar{t}})$ denotes the number of events observed with eigenvalues of the helicity operator $\lambda_t = \pm$ and $\lambda_{\bar{t}} = \pm$ for the top quark and antitop quark, respectively.

To compute A_L verses $m_{t\bar{t}}$, events are binned in two dimensional histograms of $m_{t\bar{t}} \times \cos\theta_\ell^t$. As A_L is best measured using the decay lepton, thus when the (anti)top decays, i.e. an $(\ell^-)\ell^+$ is detected in an event, events are binned in $\cos\theta_{\ell^+(\ell^-)}$. For the combined histogram of the positive and negative lepton channel ($m_{t\bar{t}} \times \cos\theta_\ell$), each mass slice is normalised by the integral of that slice - multiplied by two, due to the factor in Eq. 3.6.3 - and divided by the $\cos\theta_\ell$ bin width. For each mass slice a straight line is fitted to the $\cos\theta_\ell^t$ distribution and the fitted gradient is identified with the A_L per bin.

7.4 Top reconstruction in the lepton-plus-jets final state

As described in section 3.1, there are three classifications of $t\bar{t}$ event. This chapter presents an analysis focused solely on the lepton-plus-jets channel. In the EW sector, the Feynman diagram for this process at tree-level is shown in Fig. 7.4.1.

The generation tool employed for this analysis is a custom Monte Carlo (MC) simulation program described in chapter 4.1. In order to minimise dataset file size, the parton-level generation code is written to produce $2 \to 6$ top events in a generalised way, which can then be assigned a particular decay channel (dileptonic, lepton-plus-jets and fully hadronic) at the analysis stage. This can be done because, at parton-level, assuming only the bottom quark has a mass, the particle species of the decay products affect the cross section only up to an overall constant. This constant can then be applied at any point during the analysis stage.

This study is carried out at parton level, however, it incorporates multiple restraints en-

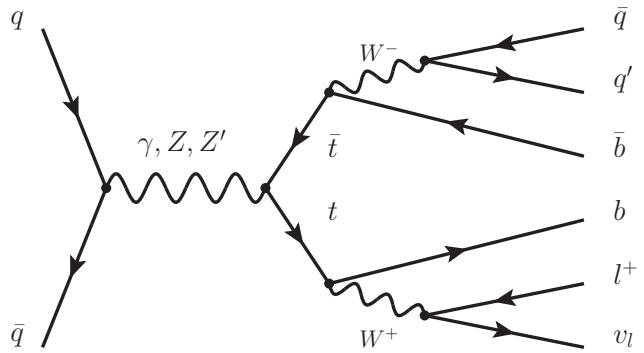

Figure 7.4.1: Feynman diagram for the signal process of LO lepton-plus-jets top pair production mediated by an interfering photon, Z boson and Z' boson.

countered in a genuine analysis performed on reconstructed data. The collider signature for our process is a single lepton produced with at least four jets, in addition to missing transverse energy, $E_{\mathrm{T}}^{\mathrm{miss}}$. The lepton may be either an electron or a muon, while taus are disregarded.[1]

Once the event has been classified as lepton-plus-jets, we select whether the top or antitop decays leptonically. To minimise data storage, this is done at the analysis rather than generation stage, as the kinematics at parton-level are unaffected. Such approach effectively doubles the number of events in the sample, i.e., each kinematic configuration is used twice.

The following considerations are meant to mimic realistic experimental conditions, in order to assess, in a preliminary way, whether these observables and techniques may be of value in an experimental analysis.

On the hadronically decaying leg of the decay, we must choose how many successful b-tags we will assume: zero, one or two. Experimentally, it is not possible to determine the charge of b-tagged jets. Therefore, there is ambiguity on which b-jet is associated with the parent top or anti-top, even with two b-tags. With two b-tags, there are ${}^2P_2 \times {}^2C_1 = 2$ possible arrangements, with one there are ${}^2P_1 \times {}^3P_1 \times {}^2C_2 = 6$ while with zero one has ${}^4P_2 \times {}^2C_2 = 12$.[2] Hence, we see that as b-tags are lost, the combinatorics increases rapidly. Of course, our analysis is further simplified as we do not account for background processes or initial/final state radiation, which contribute additional jets. All results presented in this chapter require a minimum of 2 b-tags.

[1] Tau leptons will decay leptonically approximately one third of the time, resulting in the same semilepton final state, but with an additional source of missing transverse energy with less energetic leptons. Unfortunately, this would disturb our proposed reconstruction, and this will distort the asymmetry distributions. This effect should be addressed in future work.

[2] We've used the notation ${}^nP_r$ (${}^nC_r$) to denote the permutation (combination) choosing r solutions from n possibilities.

On the leptonically decaying leg of the decay, we must reconstruct the (anti)top quark, accounting for the invisible neutrino. As there is only a single source of $E_{\mathrm{T}}^{\mathrm{miss}}$ in our final state, the transverse neutrino momentum may be identified with the $E_{\mathrm{T}}^{\mathrm{miss}}$ of the final state in the collider frame, i.e., the negative sum of all p_{T} for all the visible particles in final state (p_i):

$$p_{\mathrm{T}}^{\nu} = -\sum_i p_{\mathrm{T}}^i. \tag{7.4.1}$$

This then leaves a final unknown: the longitudinal component of the neutrino momentum p_z^{ν}. Assuming an on-shell $W^{\pm}$ and both e and μ to be massless,

$$m_W^2 = 2p_\nu p_e, \tag{7.4.2}$$

where

$$p_\nu = \left(\sqrt{{p^{\nu_{\mathrm{T}}}}^2 + {p^{\nu_z}}^2}, \mathbf{p}_{\mathrm{T}}^{\nu}, p_z^{\nu}\right), \tag{7.4.3}$$

$$p_e = \left(|p^e|, \mathbf{p}_{\mathrm{T}}^{e}, p_z^{e}\right). \tag{7.4.4}$$

Solving this equation leads to a quadratic equation,

$${p_{\mathrm{T}}^e}^2 {p_Z^{\nu}}^2 - 2kp_z^e p_z^{\nu} + {p_{\mathrm{T}}^{\nu}}^2 |p^e|^2 - k^2 = 0, \tag{7.4.5}$$

where

$$k = \frac{m_W^2}{2} + \mathbf{p}_{\mathrm{T}}^{e}\mathbf{p}_{\mathrm{T}}^{\nu}. \tag{7.4.6}$$

Therefore, the approximate neutrino momentum may be calculated with a two-fold ambiguity. The solutions to the quadratic equation can be either wholly real or complex and there are a number of options for how to treat these. When the solutions are complex, the event can be discarded, or only the real part taken – which is identical for each solution. For this study, the former option is selected.

In order to reconstruct the event, we account for bottom-top assignment and, in the case of two real solutions, p_z^{ν} solution selection simultaneously, using a chi-square-like test, by minimising the variable χ^2:

$$\chi^2 = \left(\frac{m_{bl\nu} - m_t}{\Gamma_t}\right)^2 + \left(\frac{m_{bqq} - m_t}{\Gamma_t}\right)^2, \tag{7.4.7}$$

where $m_{bl\nu}$ and m_{bqq} are the invariant mass of the leptonic and hadronic (anti)top quark, respectively, while m_t and Γ_t are the top quark mass and decay width, respectively.

The analysis code is written within the ROOT framework [137, 138], and processes the partonic ROOT n-tuples generated directly by the code described in section 4.1.

Simplified fiducial cuts are also applied for all final state particles comprising a 25 GeV

cut on p_T, and requiring $|\eta| < 2.5$. The results of this toy reconstruction, with and without fiducial cuts, for the three observables of interest (σ, $A^t_{FB^*}$, and A_L) are presented in Fig. 7.4.2. They show that, even accounting for the experimental constraints described above, each of the observables retains its characteristic shape. However, it should be reiterated that this scenario is an optimistic one, disregarding detector efficiencies, and neglecting additional jets from initial/final state radiation, which will significantly increase the complexity of the reconstruction. All subsequent plots show only variables that have undergone this toy reconstruction. Fig. 7.4.3 shows that the toy reconstruction skews somewhat the 2D distributions: biasing events towards zero in $\cos\theta^*$ and away from zero for $\cos\theta_\ell$.

As the Z' signal arises only from quark-antiquark fusion, where the phase space favours q having a higher parton momentum fraction than $\bar{q}$, it has been common to include a requirement on the rapidity of the top pair: $|y_{tt}| > 0.5$ [48, 134]. This enhances the new physics signal over the SM production by excluding events with a dominant contribution from gluon-gluon interactions (Figs. 7.4.4, 7.4.5 and 7.4.6). However, it also reduces the number of signal events, resulting in a drop in significance that somewhat counters the effect. For example, the significance for the $\mathrm{U}(1)_R$ model drops from 7.1σ to 3.6σ for a 1D analysis in $m_{t\bar{t}}$, and from 7.6σ to 4.0σ for a 2D analysis with $\cos\theta^*$, when including a 0.5 cut on $|y_{tt}|$. Consequently, for the resonant masses and luminosities considered in this study, we impose no requirement on y_{tt}.

7.5 Expected significance

In order to characterise the sensitivity of an LHC experiment to each of these Z' models, we calculate the significance that a benchmark data analysis would achieve, assuming these models describe Nature. Models that hypothesise a greater observational deviation from the SM generally predict a higher significance and, consequently, better motivate an LHC search. For our purposes, the null hypothesis (H_0) includes only the known $t\bar{t}$ processes of the SM. The alternative hypotheses (H) includes the SM processes with the addition of a single Z' for each BSM scenario. Therefore, we define the signal cross section (σ_s):

$$\sigma_s = \sigma_{(Z'+t\bar{t})} - \sigma_{t\bar{t}} = \sigma_{Z'} + \sigma_{int(Z',t\bar{t})}, \tag{7.5.1}$$

where we define $\sigma_{t\bar{t}}$ as the cross section for $t\bar{t}$ production in the SM only, and $\sigma_{Z'}$ as the $t\bar{t}$ cross section when mediated solely by a Z', with $\sigma_{int(Z',t\bar{t})}$ as the cross section corresponding exclusively to the interference term. The signal, therefore, comprises the isolated Z' contribution and the interference with the SM.

For each simulated event we may choose a number of kinematic variables ($\mathbf{x}$). Constructing a histogram, $\mathbf{n} = \{n_i\}$, in one or more of these variables, we may linearly separate the expectation value for each bin (i) in to signal (s_i) and background (b_i) contribu-

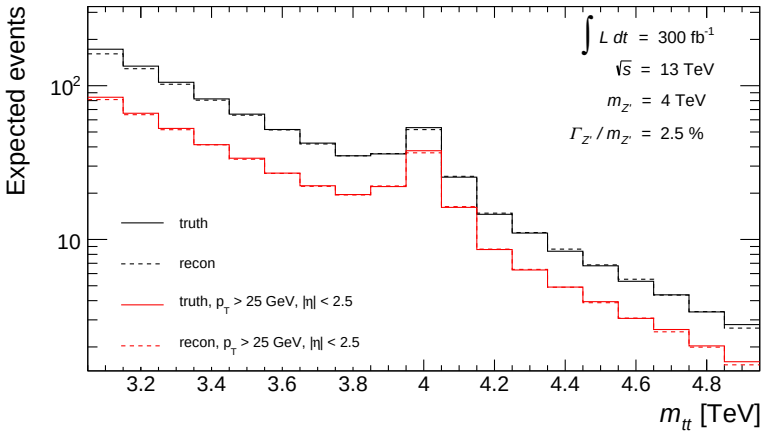

(a) Cross section

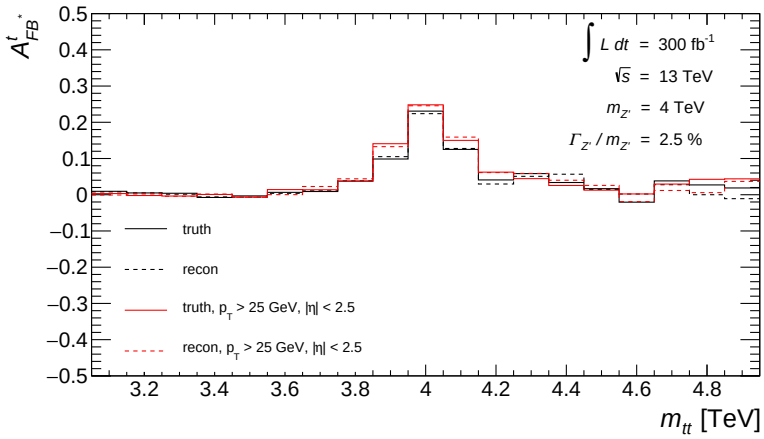

(b) $A^t_{FB^*}$

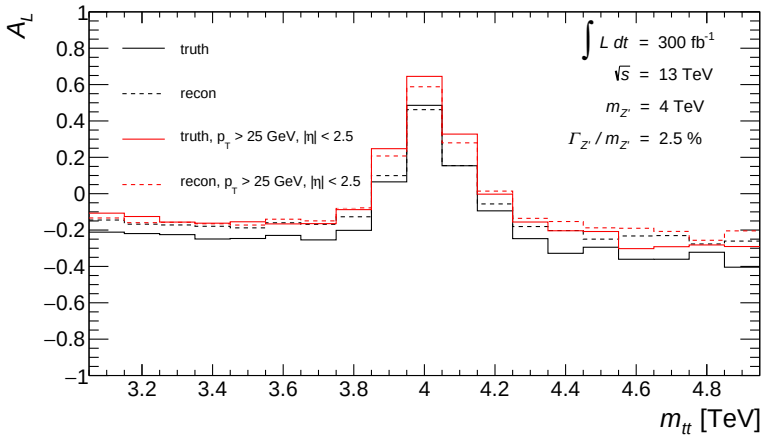

(c) A_L

Figure 7.4.2: Plots comparing the results of the toy reconstruction (section 7.4) with the truth for the cross-section, $A^t_{FB^*}$, and A_L, expected with an integrated luminosity of 300 fb^{-1}, at $\sqrt{s} = 13$ TeV, with and without fiducial cuts. The example model is GLR-R, with the pole mass of the Z' fixed at 4 TeV. The shaded bands indicate the projected statistical uncertainty, assuming Gaussian errors on the number of events (section 8.8).

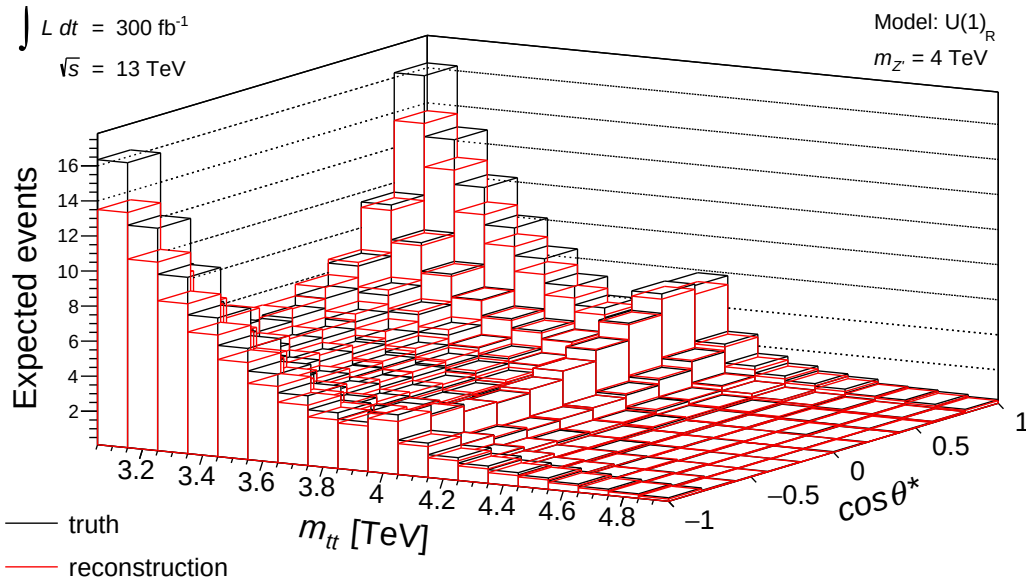

(a) $\cos\theta^*$

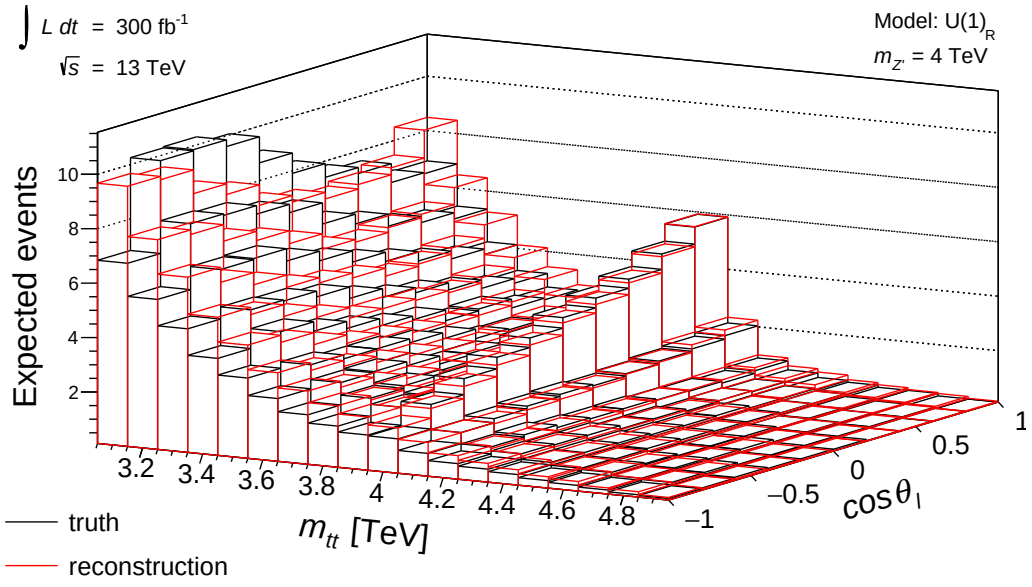

(b) $\cos\theta_\ell$

Figure 7.4.3: Plots comparing the results of the toy reconstruction (section 7.4) with the truth for the cross-section, $A^t_{FB^*}$, and A_L, expected with an integrated luminosity of 300 fb^{-1}, at $\sqrt{s} = 13$ TeV. The example model is GLR-R, with the pole mass of the Z' fixed at 4 TeV.

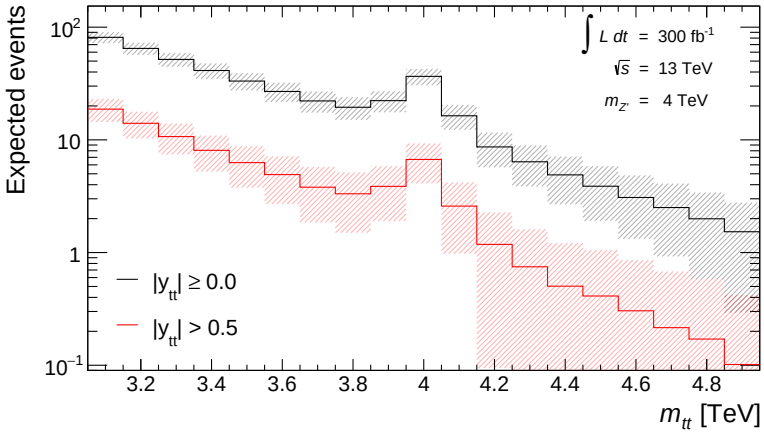

(a) Cross section

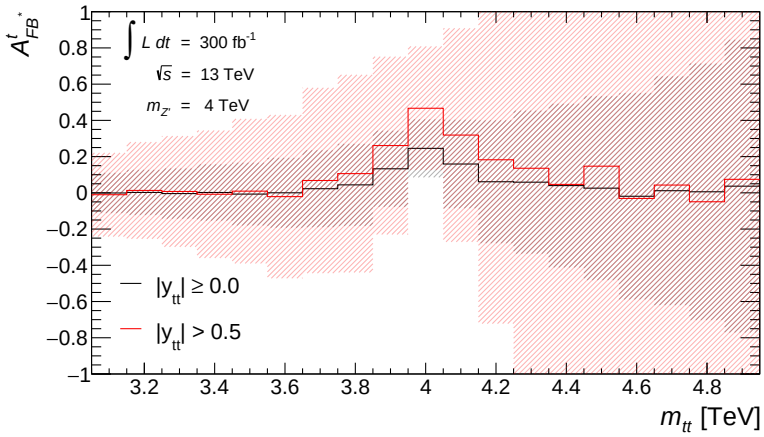

(b) $A^t_{FB^*}$

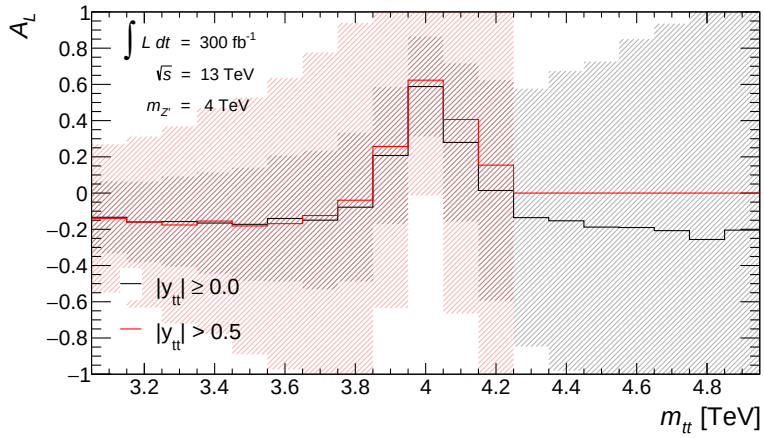

(c) A_L

Figure 7.4.4: The cross section, $A^t_{FB^*}$, and A_L expected with an integrated luminosity of 300 fb^{-1}, at $\sqrt{s} = 13$ TeV, shown with and without a $y_{tt} > 0.5$ cut. The shaded bands indicate the projected statistical uncertainty, assuming Gaussian errors on the number of events (section 8.8). The cut enhances the forward-backward asymmetry, particularly on peak. However, it also reduces the number of events significantly significance.

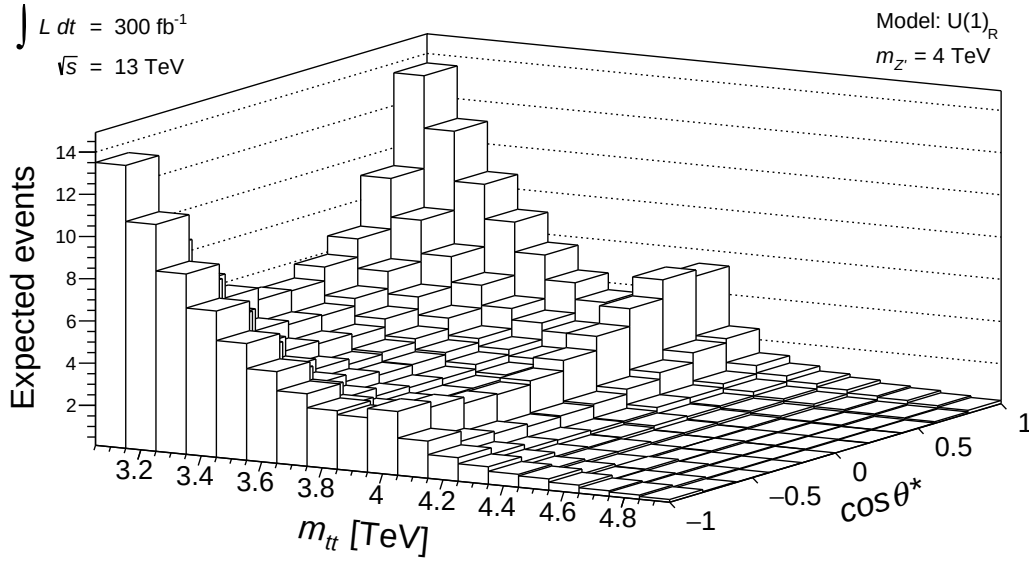

(a) $\cos\theta^*$ with no y_{tt} cut

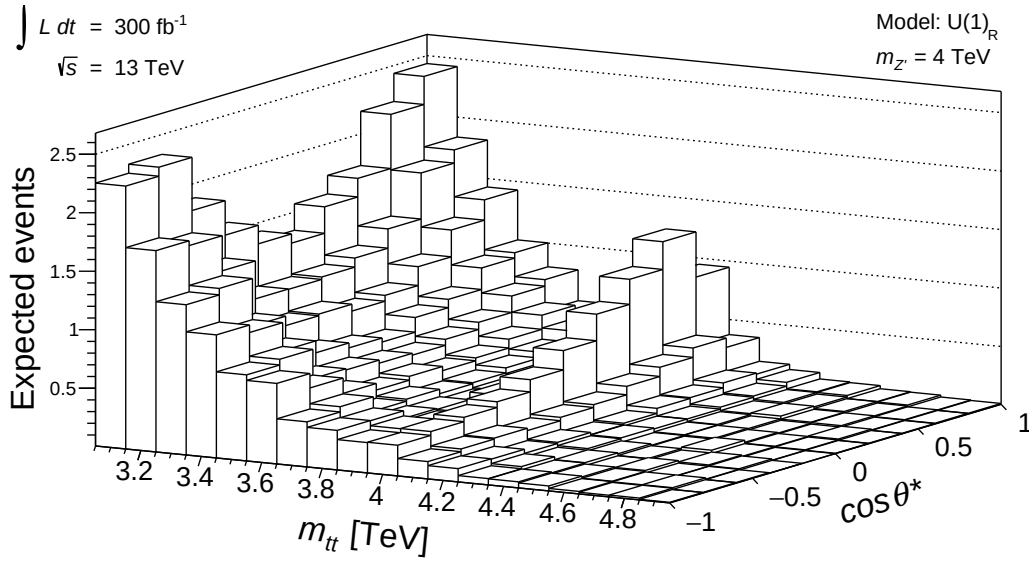

(b) $\cos\theta^*$ with $y_{tt} > 0.5$

Figure 7.4.5: Plots comparing the results for the 2D distributions with and without the y_{tt} cut, expected with an integrated luminosity of 300 fb^{-1}, at $\sqrt{s} = 13$ TeV.

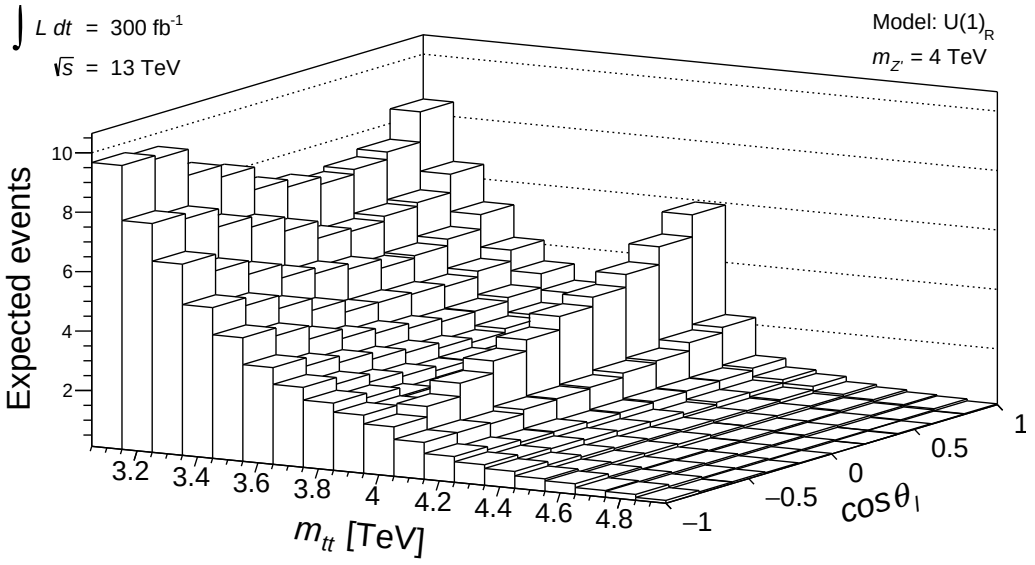

(a) $\cos\theta_\ell$ with no y_{tt} cut

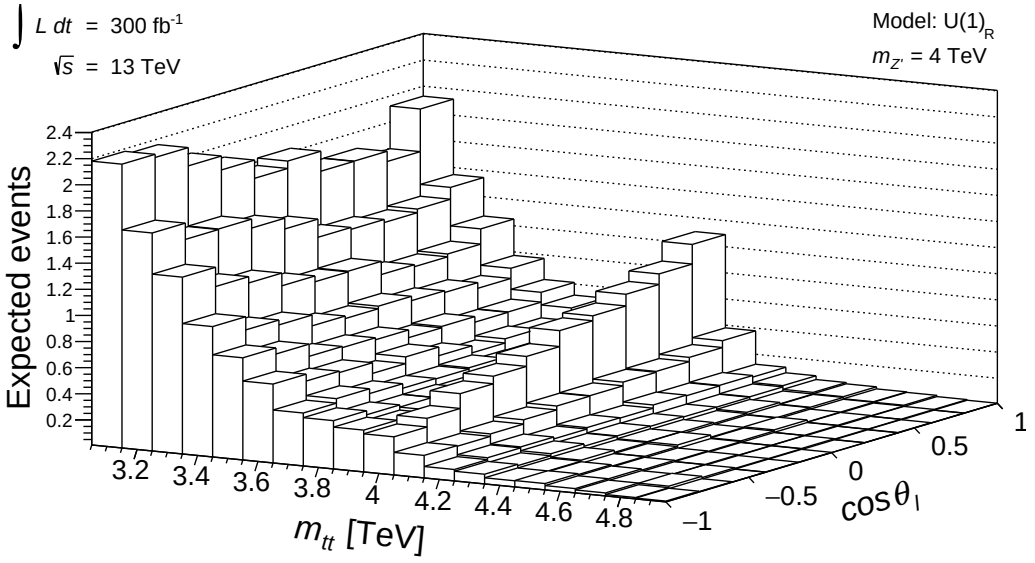

(b) $\cos\theta_\ell$ with $y_{tt} > 0.5$

Figure 7.4.6: Plots comparing the results for the 2D distributions with and without the y_{tt} cut, expected with an integrated luminosity of 300 fb^{-1}, at $\sqrt{s} = 13$ TeV.

tions,

$$\nu_i = \mu s_i + b_i, \tag{7.5.2}$$

where the μ parameter determines the strength of the signal process, with mean frequency

$$s_i(s_{tot}) = s_{tot}\alpha_i = s_{tot}\int_{x_i^{min}}^{x_i^{max}} f_s(\mathbf{x})\, d\mathbf{x}. \tag{7.5.3}$$

Here α_i represents the probability of finding an event with $\mathbf{x}$ in bin i, while s_{tot} is the total mean number of signal events. The probability density function (pdf) for $\mathbf{x}$ is denoted by f_s. An analogous relation exists also for b_i.

We wish to construct a suitable statistic for a test of $\mu = 0$, under the assumption of $\mu = 1$, i.e. where the simulated data for the BSM is playing the part of the experimental data, while the simulated SM data provides the hypothesis under investigation. Rejecting $\mu = 0$ signifies the discovery of a BSM signal, and the suitability of this model to motivate an LHC search. The standard experimental approach to tests of new physics uses frequentist inference: quantifying the level of agreement of the observed data with a given hypothesis by computing the p-value, using the likelihood ratio as a test statistic. The likelihood function is constructed as the product of a Poisson distribution for all bins:

$$L(\mathbf{x}|\mu) = \prod_i e^{\nu_i}\frac{\nu_i^{n_i}}{n_i!}, \tag{7.5.4}$$

from which we find the profile likelihood ratio

$$\lambda(\mu) = \frac{L(\mu)}{L(\hat{\mu})}. \tag{7.5.5}$$

Here $\hat{\mu}$ is the unconditional estimator of μ: the value of μ that maximises the likelihood. In order to test $\mu = 0$ it is convenient to define

$$q_0 = \begin{cases} -2\ln\lambda(0) & \mu \geq 0, \\ 0 & \hat{\mu} < 0. \end{cases} \tag{7.5.6}$$

In defining the statistic above, we have implicitly assumed that $\mu \geq 0$, i.e. the signal can only increase the mean frequency above what would be expected from H_0. Therefore, q_0 is only a valid test statistic as long as the interference is small. In this analysis, the large masses and narrow widths of the Z' ensure this condition is satisfied. Notice that higher values of q_0 imply increasing disagreement between the observed data (represented by the alternate hypothesis, H) and H_0. From q_0 we may directly quantify a measure of the agreement between H_0 and H, by recovering the p-value as

$$p_0 = \int_{q_{0,obs}}^{\infty} f(q_0|0)\, dq_0. \tag{7.5.7}$$

Therefore, in order to determine p_0, we require the sampling distribution $f(q_0|0)$. An approximation for the profile Likelihood ratio may be found in the large sample limit, as described in [139]. These Asymptotic formulae allow us to determine the significance for H, and the full sampling distribution, without involving computationally expensive Monte Carlo calculations.

As is common practice, we convert the p-value into the equivalent "σ value"; assuming the distribution of the test statistic under H_0 follows a normal distribution, we quote the number (Z) of standard deviations (σ) it would be found above the mean such that its upper-tail probability is equal to p_0,

$$Z = \Phi^{-1}(1 - p_0), \tag{7.5.8}$$

where Φ is the cumulative normal distribution. In the collider physics community, a significance of 5σ is generally considered necessary for rejecting H_0 and hailing a discovery of new physics.

The foremost kinematic variable used in a search for new physics is the invariant mass of the final state system $\sqrt{\hat{s}}$, which for a $t\bar{t}$ process defines the mass of the top pair ($m_{t\bar{t}}$). One-dimensional (1D) event distributions, binned in $m_{t\bar{t}}$, are the dominant discovery tool in any search for new resonances. Due to the cross section dependence on $\sqrt{\hat{s}}$ (Eq. 3.3.2), this "cut and count" methodology is known as "bump-hunting." We will produce this 1D distribution for all benchmark models, and extract the corresponding significance.

In addition to the usual bump-hunt, we have extended our study to include a number of asymmetry observables, as described in sections 3.5 and 3.6.1. The dominant purpose of these observables is to profile a newly discovered Z' by evaluating which models best describe their shape. However, we wish also to investigate the potential for these asymmetries to act as complementary discovery observables to the invariant mass distribution.

We approach this by binning events in two-dimensional (2D) histograms, where the second variable is related to the defining observable of the asymmetry, i.e. for $A^t_{FB^*}$, both $m_{t\bar{t}}$ and $\cos\theta^*$ are used, while for A_L, we bin in $m_{t\bar{t}}$ and $\cos\theta_\ell$. Note that Eqs. 7.5.2 and 7.5.3 are completely general, hence, the mean frequency in a given two 2D bin (i, j) is simply

$$\nu_{i,j}(\mu, \sigma_{t\bar{t}}, \sigma_{Z'}) = L_{int}[\epsilon_{i,j}\sigma_{t\bar{t}} + \mu\alpha_{i,j}(\sigma_{Z'} + \sigma_{int\{Z',t\bar{t}\}})], \tag{7.5.9}$$

with a corresponding likelihood function. Here L_{int} represents the integrated luminosity, ϵ and α represent the efficiencies for SM background and the signal, respectively, to fall in the bin i, j. This is dependent on both the asymmetry introduced by the model in question, and the efficiencies of the detector.

The bin width for $m_{t\bar{t}}$, in each case, is taken to be 50 GeV, compatible with the typical experimental resolution [93]. Reflecting the charge asymmetry, just two bins are created in $\cos\theta^*$: $-1 \leq \cos\theta^* < 0$ and $0 < \cos\theta^* \leq 1$. Twenty bins are used across the domain of $\cos\theta_\ell$.

Methods to perform the expected significance evaluation, as described above are available in RooStats [140], with the formalism and numerical implementation of these methods described in [139]. Tools to generate the statistical models for RooStats from the generated histograms were provided by HistFactory [141].

7.6 Results

We present here a selection of results profiling the benchmark Z' models, using the observables described in the previous section. These are the cross section (σ), in the form of the expected number of events, the reconstructed forward-backward asymmetry ($A^t_{FB^*}$), and the top polarisation asymmetry (A_L). Each of these variables are binned as a function of the top pair ($t\bar{t}$) invariant mass ($m_{t\bar{t}}$). Considering the current limits on the mass of the Z' (section 7.2) the Z' mass is fixed at 4 TeV. No experimental efficiencies, such as b-tagging efficiency, are accounted for. The centre of mass energy of the LHC is simulated at 13 TeV. All results assume the collection of a total integrated luminosity (L_{int}) of 300 fb^{-1}. The statistical error is quantified for this luminosity by binning the expected number of events ($L\sigma$) in $m_{t\bar{t}}$ for a bin width of 50 GeV, compatible with the typical experimental resolution [93], and assuming Gaussian errors, i.e. $\delta N = \sqrt{N} = \sqrt{\sigma L_{int}}$. The A_{FB} observable, as the division of two subtracted/summed quantities, under the assumption that the two are independent, has a statistical uncertainty

$$\Delta A = \frac{2}{N}\sqrt{\frac{N_1 N_2}{N}} = \sqrt{\frac{1-A^2}{\sigma L_{int}}}. \tag{7.6.1}$$

While it is expected that statistics is the dominant source of uncertainty, it is likely that there will be also be significant systematic uncertainties. These may be addressed when this study is extended to include the full parton-shower, hadronisation and detector reconstruction, in addition to the required efficiencies, and the assessment of the significance is already equipped to deal with these.

In the following, we will first present the distributions for the differential cross section, $A^t_{FB^*}$ and A_L, for the benchmark Z' models, and comment on their power to distinguish different classes of model from the SM and each other. Following this we will present the 1D significances for every model and the 2D significances where appropriate as well as remark on the scope of asymmetry observables to act as complementary discovery observables.

7.6.1 Distinguishing Z' bosons using asymmetries

Figs. 7.6.1 and 7.6.2 show plots for the differential cross section, $A^t_{FB^*}$ and A_L, for two models for the GSM class, and three from the GLR class, respectively. These models feature no vanishing axial and vector couplings to tops (Tab. 2.2.3), and, therefore, result in notable A_L and $A^t_{FB^*}$ (Eq. 3.5.4, 3.6.6). The remaining models, including all of the E_6 class, only produce an asymmetry via the interference term, which generally gives an undetectable enhancement with respect to the SM yield. Consequently, these distributions are not of value and, thus, not presented. However, the expected number of events, binned in $m_{t\bar{t}}$, for the remaining models is shown in Fig. 7.6.3.

The cross section, profiled in $m_{t\bar{t}}$, shows a very visible peak for all models in Figs. 7.6.1a and 7.6.2a. The GSM models feature a greater peak, and width, consistent with their stronger couplings, but the impact on the cross section is otherwise similar for both classes. Mirroring the cross section, the $A^t_{FB^*}$ distribution clearly distinguishes between the models and SM, most strongly for the GSM class, with the difference in width even more readily apparent (Figs. 7.6.1b and 7.6.2b). The best distinguishing power for the GLR models investigated comes from the A_L distribution, which features an oppositely signed peak comparing the GLR with the GSM classes (Figs. 7.6.1c and 7.6.2c).

The heavy photon scenario created by the GSM-Q model in Fig 7.6.3c shows a very strong response. In fact, a highly significant mass peak coupled with no response in $A^t_{FB^*}$ or A_L would be a strong signature for a model of this type. The model featuring a pure U_{B-L} symmetry, results in a negligible peak, so is of little phenomenological interest.

The E_6 class of models universally features a zero vector coupling to up type quarks and, therefore, have negligible asymmetry response. Additionally, the U_S, U_I and U_N realisations feature only a very small increase in the number of events on peak, while the U_χ, U_η and U_ϕ scenarios result in a narrow resonance. The absence of a corresponding peak in either asymmetry offers an additional handle on diagnosing a discovered Z'.

7.6.2 Asymmetries as complementary discovery observables

Using the statistical techniques outlined in section 7.5, we may assess the significance for each of these models if they are assumed to exist in Nature, against a test of the SM only. We apply these methods using the 1D histograms, binned as a function of $m_{t\bar{t}}$, as presented in Figs. 7.6.1a, 7.6.2a and 7.6.3. This gives an assessment of the distinguishing power of the standard bump-hunt versus the asymmetry observables for each of these models and their relative potential for observation in experiment.

In the previous subsection, we commented on the capacity for asymmetries to diagnose a previously discovered Z' candidate. Now we will assess their potential to contribute

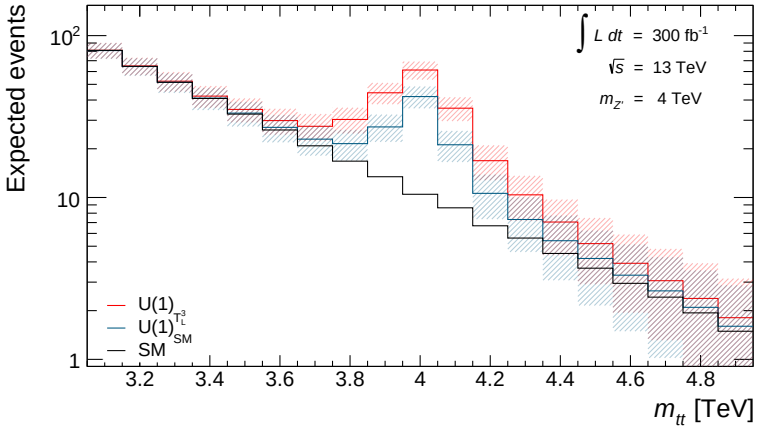

(a) Events expected - GSM models

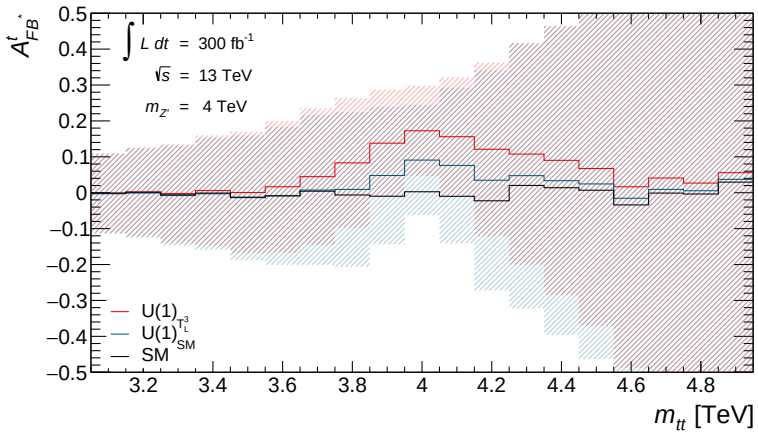

(b) $A^t_{FB^*}$ - GSM models

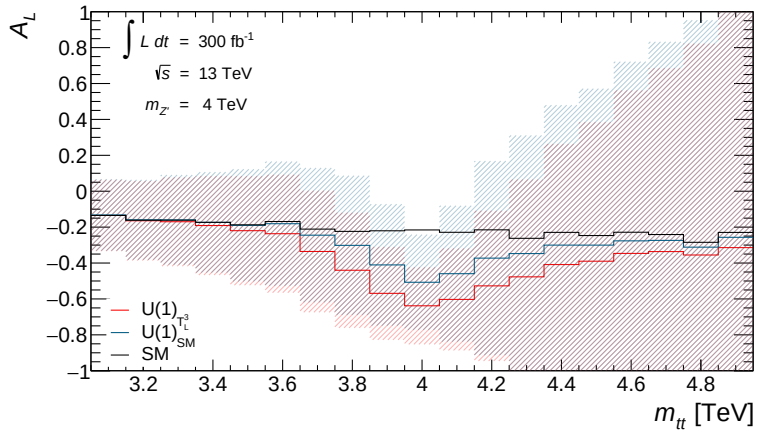

(c) A_L - GSM models

Figure 7.6.1: Expected distributions for each of our observables of interest, with an integrated luminosity of 300 fb^{-1}, at $\sqrt{s} = 13$ TeV. The pole mass of the Z' is fixed at 4 TeV for every model. The shaded bands indicate the projected statistical uncertainty, assuming Gaussian errors on the number of events (section 7.6). Shown from top to bottom are: the events expected (cross section) [a]; $A^t_{FB^*}$ [b]; and A_L [c].

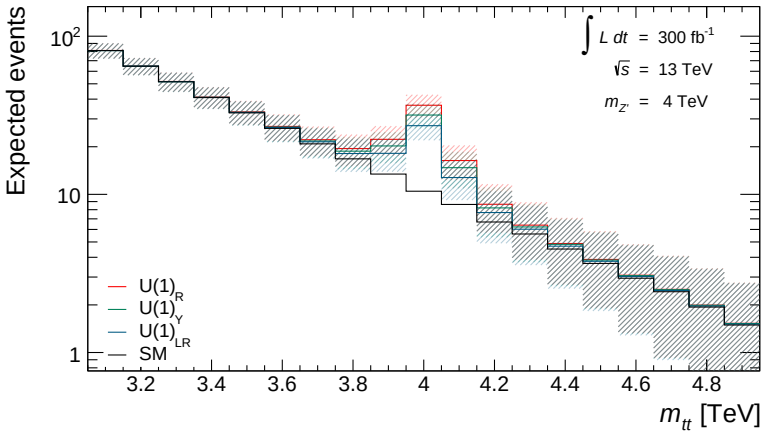

(a) Events expected - GLR models

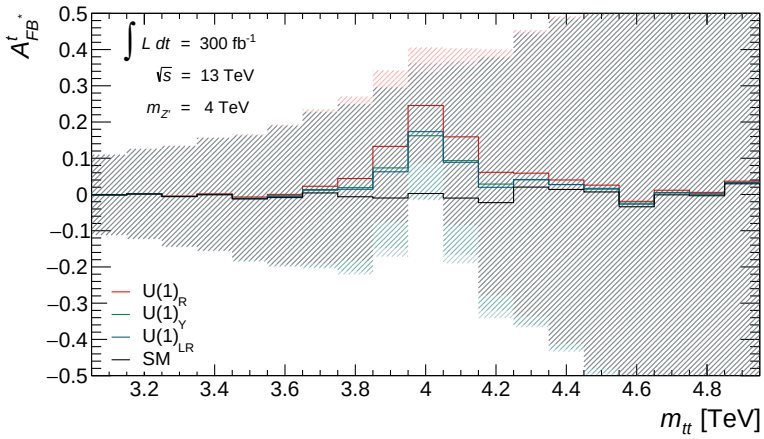

(b) $A^t_{FB^*}$ - GLR models

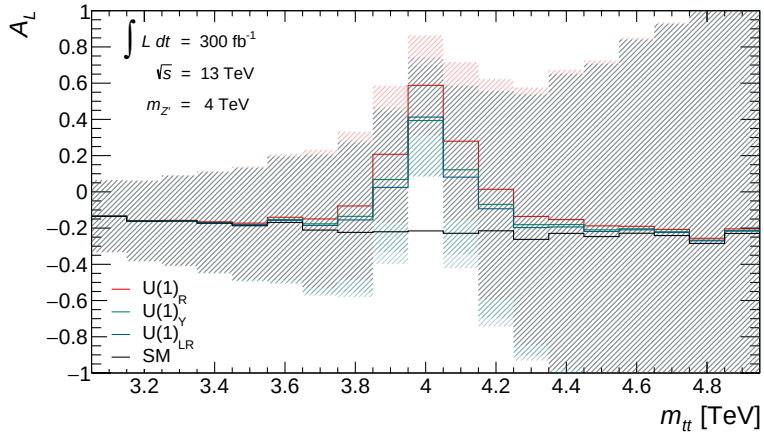

(c) A_L - GLR models

Figure 7.6.2: Expected distributions for each of our observables of interest, with an integrated luminosity of 300 fb^{-1}, at $\sqrt{s} = 13$ TeV. The pole mass of the Z' is fixed at 4 TeV for every model. The shaded bands indicate the projected statistical uncertainty, assuming Gaussian errors on the number of events (section 7.6). Shown from top to bottom are: the events expected (cross section) [a]; $A^t_{FB^*}$ [b]; and A_L [c].

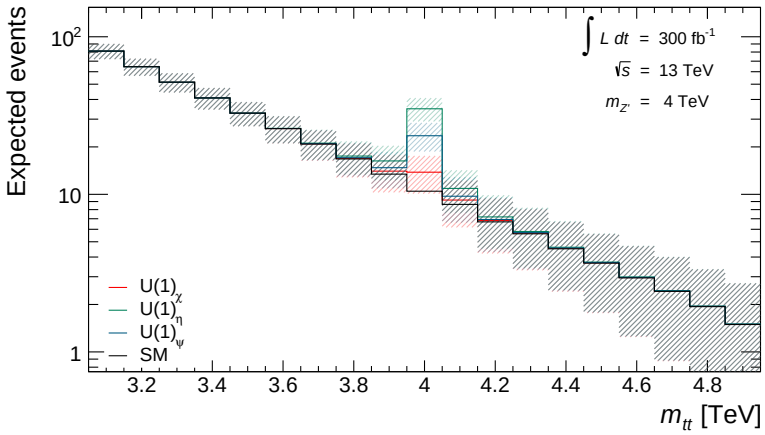

(a) Events expected - E_6 models (I)

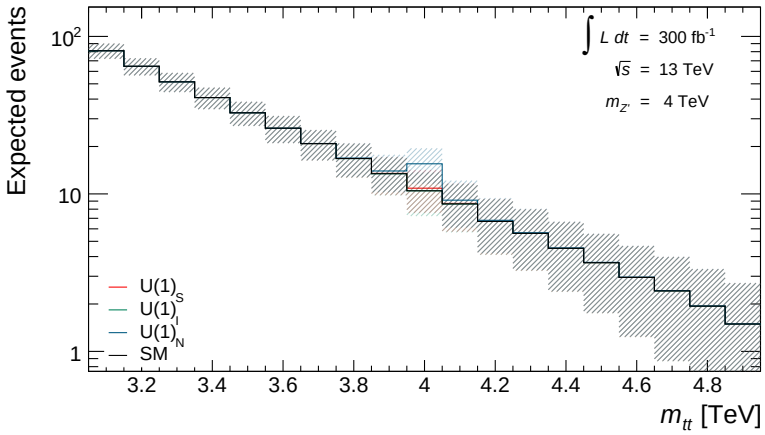

(b) Events expected - E_6 models (II)

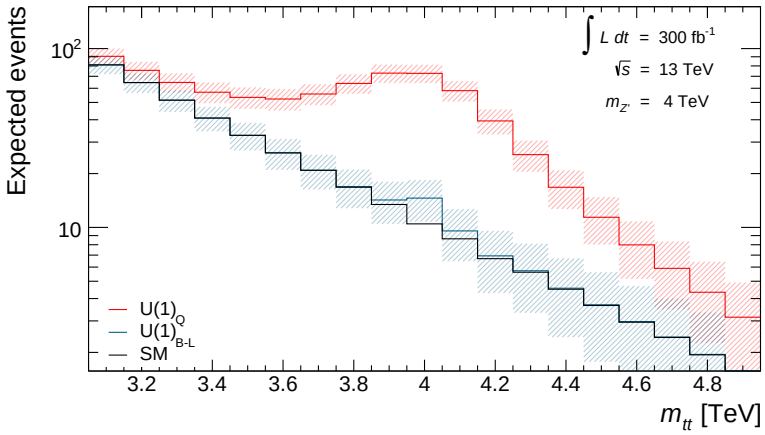

(c) Events expected - $U(1)_Q$ & $U(1)_{B-L}$ models

Figure 7.6.3: Expected $m_{t\bar{t}}$ distributions for models with negligible $A^t_{FB^*}$ and A_L, with an integrated luminosity of 300 fb^{-1}, at $\sqrt{s} = 13$ TeV. The pole mass of the Z' is fixed at 4 TeV for every model. The shaded bands indicate the projected statistical uncertainty, assuming Gaussian errors on the number of events (section 8.8).

to first detection of a Z' particle in the $t\bar{t}$ channel (hence of discovery in certain models). To do this we bin the generated events in both $m_{t\bar{t}}$ and the defining variable of the asymmetry. In the case of $A^t_{FB^*}$, the asymmetry is calculated directly, therefore, we divide the domain of $\cos\theta^*$ into just two equal regions. Instead, A_L is extracted from the gradient of the fit to $\cos\theta_\ell$ for each mass slice, with a bin width of 0.1, and we calculate the significance directly form this histogram.

The 2D histograms of $m_{tt} \times \cos\theta^*$ are presented in Figs. 7.6.4 and 7.6.5, for the GSM and GLR classes, respectively. It is observed that the SM plot shows a gradual slop towards zero with increasing mass, with no clear asymmetry in $\cos\theta^*$ for any mass slice. All BSM models feature a peak at 4 TeV where the number of events with $\cos\theta^* > 0$ is noticeably higher for all models, most prominently for the GSM-L model. Figs. 7.6.6, and 7.6.7 present histograms of $m_{tt} \times \cos\theta_\ell$. It is observed that the SM distribution is relatively consistent in $\cos\theta_\ell$ across all mass slices. The number of events with $\cos\theta_\ell < 0$ is significantly higher for GSM classes in the peak region, while events increase as $\cos\theta_\ell$ becomes more positive for the GLR class of models.

The final results of the likelihood-based test, using asymptotic formulae, as applied to each model and tested against the SM are presented in Tab. 7.6.8. The standard $m_{t\bar{t}}$ based bump-hunt shows that the GLR and GSM models generally report a higher significance that those of the E_6 class, as expected. Of this class, the $\mathrm{U}(1)_\eta$ model shows the best potential for observation. Further support for an E_6 derived Z' would be manifest in an accompanying negligible response in A_L and $A^t_{FB^*}$.

The models with non-trivial asymmetries consistently show an increased significance for the 2D histograms compared with using $m_{t\bar{t}}$ alone, illustrating their potential application in gathering evidence to herald the discovery of new physics. Additionally, we see that, in general, using $\cos\theta_\ell$ increases the significance more than when using $\cos\theta^*$. Combined with the potential for A_L to strongly distinguish between different classes of models, this observable represents the most interesting additional information when combined with the differential cross section.

7.7 Conclusions

In this chapter, the scope of the LHC in accessing semileptonic final states produced by $t\bar{t}$ pairs emerging from the decay of a heavy Z' state above and beyond the SM background induced by both QCD and EW processes was investigated. A variety of BSM scenarios embedding such a state were tested. The primary aim of this investigation was to extend earlier results produced limitedly to on-shell $t\bar{t}$ production which claimed that charge and spin asymmetry observables can be used to not only aid the diagnostic capabilities provided by the cross section in identifying the nature of a possible Z' signal but also to

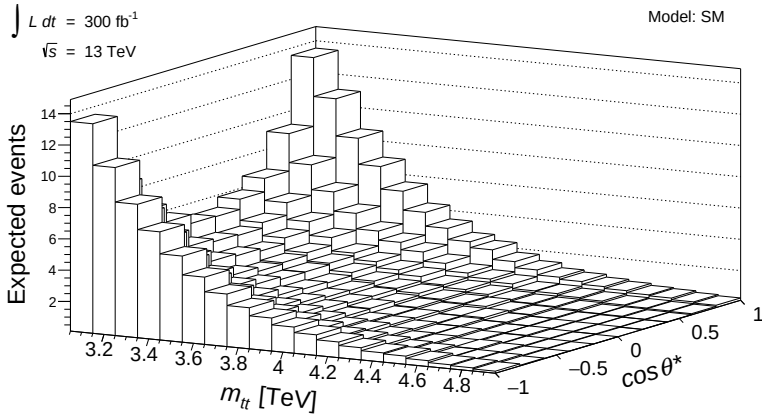

(a) SM

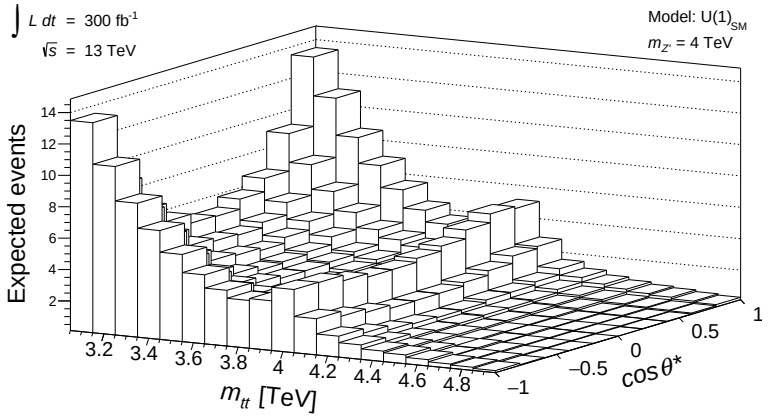

(b) SSM

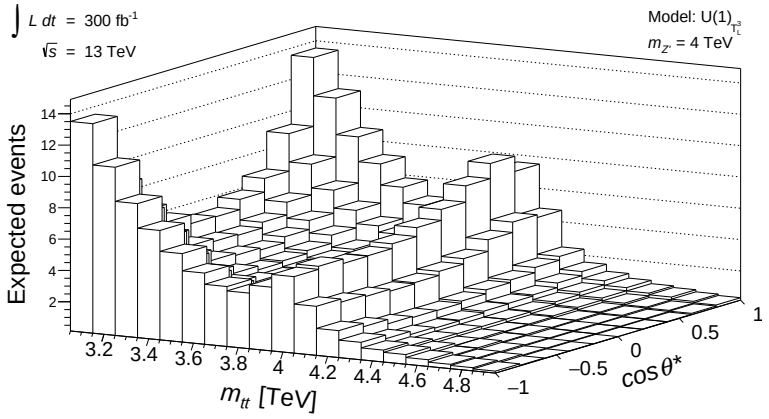

(c) GSM-L

Figure 7.6.4: Expected number of events binned in both $m_{t\bar{t}}$ and $\cos\theta^*$ after toy reconstruction. These plots are used to derive the 2D significances in these variables, and access the combined significance of using the $m_{t\bar{t}}$ distribution and $A^t_{FB^*}$.

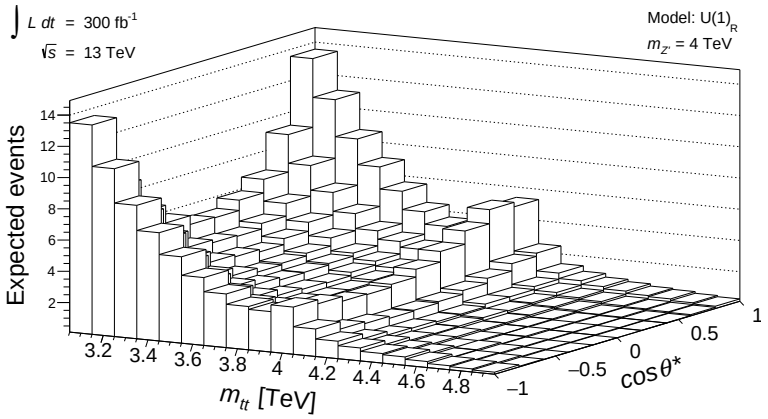

(a) GLR-R

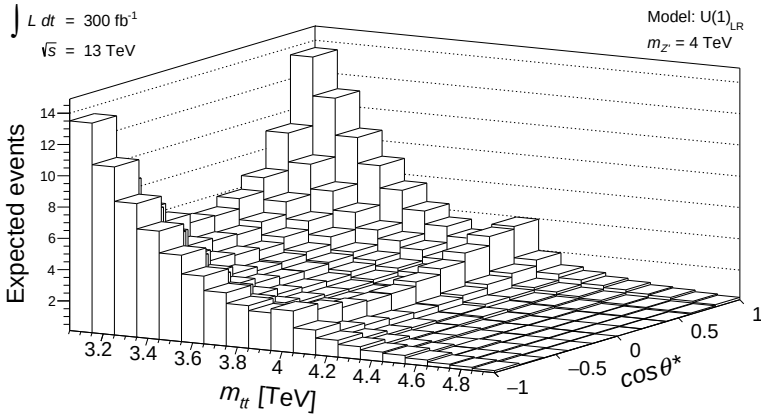

(b) GLR-LR

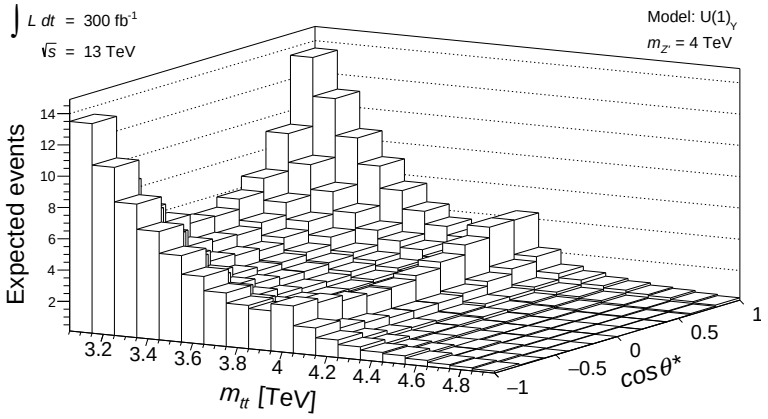

(c) GLR-Y

Figure 7.6.5: Expected number of events binned in both $m_{t\bar{t}}$ and $\cos\theta^*$ after toy reconstruction. These plots are used to derive the 2D significances in these variables, and access the combined significance of using the $m_{t\bar{t}}$ distribution and $A^t_{FB^*}$.

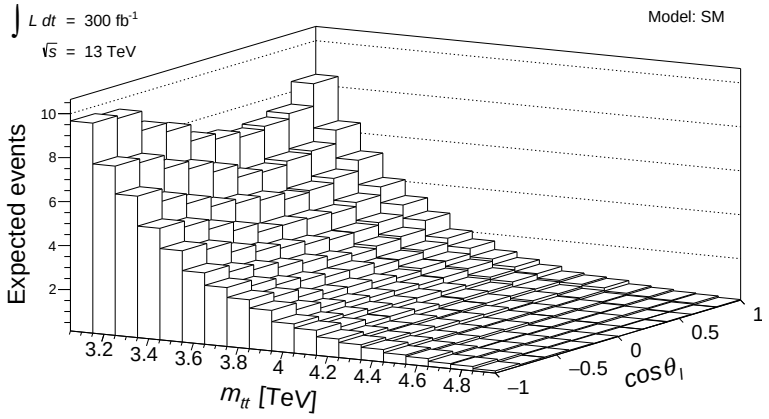

(a) SM

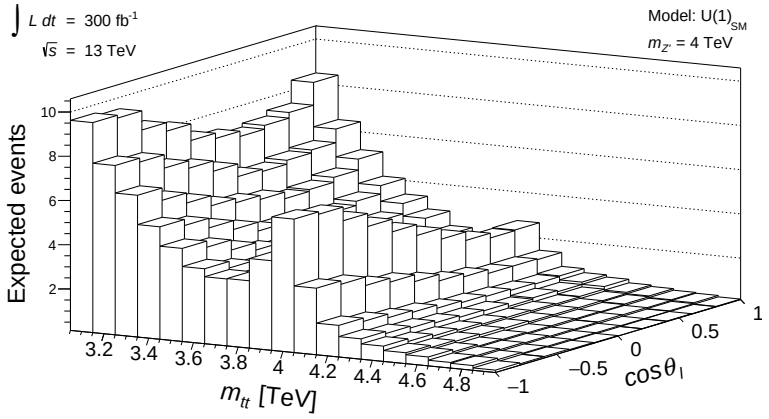

(b) GSM-SM

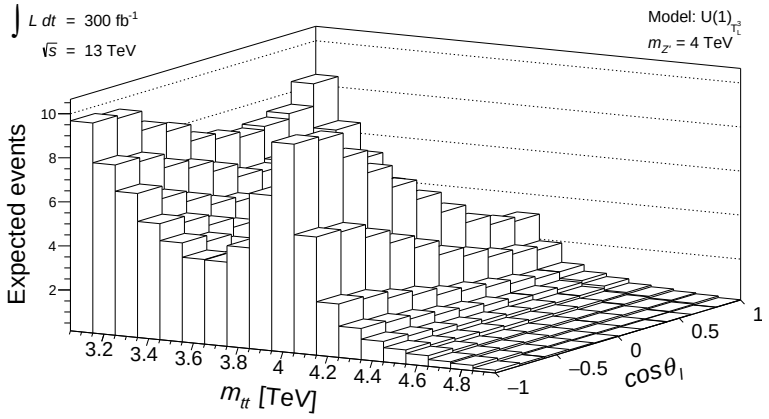

(c) GSM-L

Figure 7.6.6: Expected number of events binned in both $m_{t\bar{t}}$ and $\cos\theta_\ell$ after toy reconstruction. These plots are used to derive the 2D significances in these variables, and access the combined significance of using the $m_{t\bar{t}}$ distribution and A_L. Note the effect of the Z' around 4 TeV. The gradient of this slope is taken to extract A_L (after normalisation).

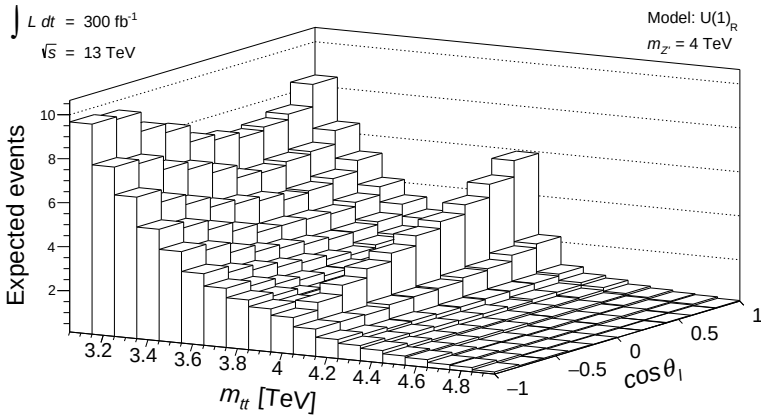

(a) GLR-R

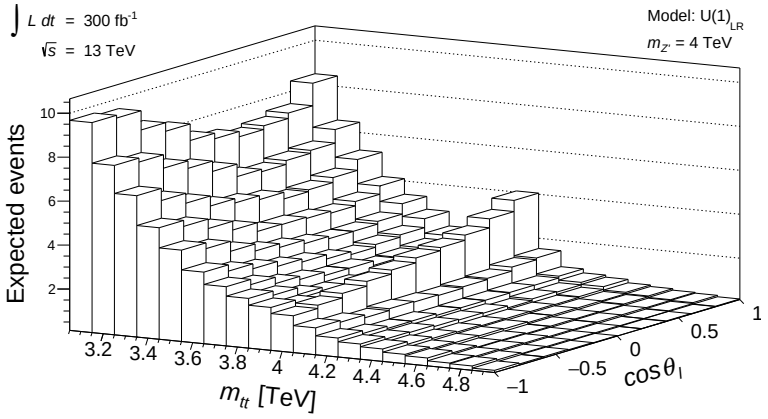

(b) GLR-LR

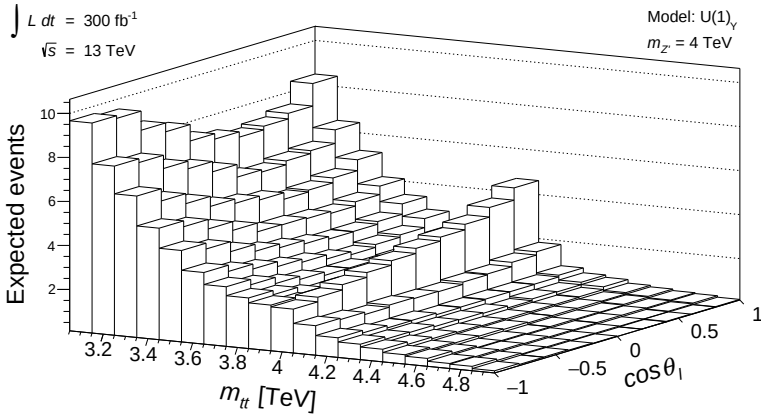

(c) GLR-Y

Figure 7.6.7: Expected number of events binned in both $m_{t\bar{t}}$ and $\cos\theta_\ell$ after toy reconstruction. These plots are used to derive the 2D significances in these variables, and access the combined significance of using the $m_{t\bar{t}}$ distribution and A_L. Note the effect of the Z' around 4 TeV. The gradient of this slope is taken to extract A_L (after normalisation).

Class	U(1)′	Significance (Z)		
		$m_{t\bar{t}}$	$m_{t\bar{t}}$ & $\cos\theta^*$	$m_{t\bar{t}}$ & $\cos\theta_\ell$
GLR	$\mathrm{U}(1)_R$	7.1	7.6	7.9
	$\mathrm{U}(1)_{B-L}$	1.3	1.3	1.3
	$\mathrm{U}(1)_{LR}$	4.7	5.0	5.2
	$\mathrm{U}(1)_Y$	6.0	6.2	6.4
GSM	$\mathrm{U}(1)_{T_L^3}$	15.3	15.9	15.6
	$\mathrm{U}(1)_{SSM}$	9.0	9.4	9.2
	$\mathrm{U}(1)_Q$	26.9	27.4	26.9
E_6	$\mathrm{U}(1)_\chi$	1.0	1.1	1.0
	$\mathrm{U}(1)_\psi$	3.5	3.6	3.5
	$\mathrm{U}(1)_\eta$	6.0	6.2	6.1
	$\mathrm{U}(1)_S$	0.1	0.1	0.1
	$\mathrm{U}(1)_I$	0.0	0.0	0.0
	$\mathrm{U}(1)_N$	1.5	1.6	1.5

Table 7.6.8: Expected significance, expressed as the Gaussian equivalent of the p-value. The E_6, $\mathrm{U}(1)_{B-L}$ and $\mathrm{U}(1)_Q$ models have negligible $A^t_{FB^*}$ and A_L, and thus no increase in significance when compared with the mass distribution alone.

increase the significance of the latter. This has been done by resorting to a $2 \to 6$ calculation accounting for all possible topologies for both signal and (irreducible) backgrounds including interference effects where appropriate. While the analysis was performed at the parton level, a reconstruction procedure of the (anti)top quark mass and momenta that closely mimics experimental conditions has been implemented. Finally, a statistical procedure enabling the combination of both differential and integrated significances from cross section and asymmetry signals has been devised.

Therefore, the stage is set for a fully-fledged analysis eventually also to include parton-shower, fragmentation/hadronisation, heavy flavour decay and (true) detector effects, which constitutes the subject of a forthcoming study; an extended analysis such as this is performed in chapter 8 for the dilepton final state. A core requirement, in pursuit of such an analysis, is the need to perform an appropriate boosted reconstruction for events in which top quark decay products are highly collimated. This approach must preserve high signal efficiency in the face of increasing top momentum and maintain control over associated systematic uncertainties which, given the special phase space region, can suffer from specific limitations (e.g. control regions for validation and determination of scale uncertainties can be depleted of events and modelling uncertainties in generator and hadronisation can also play a role). In the semileptonic final state, additional complications emerge due to overlapping jet constituents from hadronic top decay daughters, necessitating detailed analysis of the resulting "fat jets".

In short, for this chapter, we showed significant phenomenological advancement in proving that charge and spin asymmetry observables can have a strong impacts in ac-

cessing and profiling $Z' \to t\bar{t}$ signals during Run 2 of the LHC. This is all the more important in view of the fact that several BSM scenarios, chiefly those assigning a composite nature to the recently discovered Higgs boson, embed one or more Z' state which are strongly coupled to top (anti)quarks.

CHAPTER 8

Observing Z' bosons with the dilepton final state

8.1 Introduction

In the previous chapter the potential impact of Z' bosons on $t\bar{t}$ production was explored, with focus on the lepton-plus-jets final state. This was primarily limited in impact by being constrained to a parton-level analysis. This chapter focuses on applications of the dilepton channel for distinguishing different BSM theories. Therefore, I explore the potential for observation in the dilepton channel with multiple observables, including simulation of showering, hadronisation and detector reconstruction.

The details behind these simulations are given in section 8.2. A description of the subsequent object reconstruction is given in section 8.3, while the requirements for overlap removal and event selection are given in sections 8.4 and 8.5, respectively. In section 8.6 I examine the limitations regarding top reconstruction for this channel due to the multiple sources of missing transverse momentum, while the wealth of observables available in this channel are described in section 8.7. Results of the reconstruction for these observables are presented in section 8.8.1, and the final expected significance for observation of a 2 TeV Z' boson are provided in section 8.8.2. The conclusions of the analysis are presented in section 8.9.

q	Efficiency [%]
u, d, s	0.746
c	16.6
b	77.0

Table 8.2.1: Modified Delphes configuration for b-tagging efficiencies for each quark species (q). A b-tagging efficiency of 100% would result in every jet originating from a quark of that species being b-tagged. Based on Ref. [92].

8.2 Event Generation

Parton-level hard-scattering events are generated as described in chapter 4. The output of the hard-scattering process is written in the Les Houches Event Format [59]. These events are then processed using Delphes [64, 65, 66] which is directly interfaced with PYTHIA 8.2 [61, 62, 63]. Events are processed using PYTHIA to simulate showering and hadronisation via the string-fragmentation model for evolution of the partonic six-body final state to a complex multi-particle final state. Parton Distribution Functions (PDFs) are interfaced with using LHAPDF [142]. The CT14LL PDF set [55] is selected to match that used during parton-level event generation.

Delphes is a framework (written in C++) intended to perform fast response simulation for a general, customisable particle detector. The simulation structure includes calorimeters, and tracking and muon sub-systems embedded within magnetic fields. The simulated response accounts for the granularity, resolutions and efficiencies of all detector subsystems. For this analysis I use a custom modified version of the default ATLAS detector card (an overview of the ATLAS detector is provided in Chapter 5). Changes to the ATLAS detector card include altering the b-tagging efficiencies (Tab. 8.2.1), in addition to using $R = 0.4$ for jet construction (Eq. 8.3.1). The default electron, muon and photon isolation is disabled, as well as the scalar H_{T} calculation and the unique object selection as these are performed in the analysis, as described in section 8.4. The default lepton efficiencies of the Delphes ATLAS card, as functions of p_T and η, are retained. These are presented in Tab. 8.2.2.

8.3 Object reconstruction and selection

Lepton and jet requirements, including isolation are taken with reference to those in Refs. [143] and [144]. These are analyses performed by the ATLAS collaboration in top pair production with the dilepton final state and measure the charge asymmetry at 7 TeV, and differential cross section at 13 TeV, respectively.

Reconstructed electrons are required to have transverse momentum $p_{\mathrm{T}} > 27.0$ GeV and must have pseudorapidity $|\eta| < 2.47$ excluding the transition region between the

p_{T} [GeV]	η	Efficiency [%]
Electrons		
< 25.0		0
> 25.0	≤ 1.5	95
> 25.0	≤ 2.7	85
	> 2.7	0
Muons		
< 25.0		0
> 25.0	≤ 1.5	95
> 25.0	≤ 2.5	85
	> 2.5	0

Table 8.2.2: Electron and muon efficiencies with the default ATLAS Delphes card as a function of lepton transverse momentum (p_{T}) and pseudorapidity (η).

calorimeter barrel and endcaps $1.37 < |\eta| < 1.52$. In order to selected isolated electrons, candidates are discarded if the ratio of the sum of track p_{T} within a cone of $\Delta R < 0.3$ around the electron, divided by p_{T}^{e}, is greater than 0.12.

Muon candidates are reconstructed using a combination of information from the tracker and muon spectrometer simulations. They are required to have transverse momentum $p_{\mathrm{T}} > 27.0$ and $|\eta| < 2.5$. Muon isolation is dependent on p_{T}-dependent track-based criteria. They are discarded if the ratio of the sum of track p_{T} within a cone of $\Delta R < 10.0/p_{\mathrm{T}}^{\mu}$ around the muon, divided by p_{T}^{μ}, is greater than 0.05.

Jets are defined locally in the (η, ϕ) plane using electromagnetic and hadronic calorimetry. The transverse energies due to energy deposits are associated with cells in a grid. Due to high particle density in a jet, each cell may contain deposits due to multiple particles. There are then a set of calorimeter objects parameterised in $\{\eta, \phi, p_{\mathrm{T}}\}$. Distances between calorimeter objects are defined by

$$\Delta d_{ij} = \min\left(p_{\mathrm{T},i}^{2\alpha} - p_{\mathrm{T},j}^{2\alpha}\right) \cdot \frac{\Delta R_{ij}^2}{R^2} \tag{8.3.1}$$

where

$$\Delta R_{ij} = \left[(\eta_i - \eta_j)^2 + (\phi_i - \phi_j)^2\right]^{\frac{1}{2}} \tag{8.3.2}$$

and R is a chosen constant. The distance from the object to the beam is given by $d_{iB} = p_{T,i}^{2\alpha}$. Jets are constructed via an algorithm that combines these objects over the full grid, beginning with the pair that minimises d. The positions of the objects naturally shift as they are combined. Composite objects are no longer developed when the minimum distance is between itself and the beam. These final objects define the set of jets. There are a variety of cone jet algorithms corresponding to different values of R and α.

An important requirement of these algorithms is that they be "soft and collinear safe";

perturbative QCD features formally infinite probabilities for the radiation of soft gluons, and collinear splitting. Thus, the jet definition must be insensitive to these processes. It has been show in Ref. [145] that Eq. 8.3.1 satisfies these criteria for all values of α, and a value of $\alpha = -1$ is suggested. This anti-k_t algorithm [145] causes objects with high p_{T} to gather surrounding low p_{T} objects, resulting in smooth round jets in the (η, ϕ) plane. This analysis uses the Fast-Jet algorithm embedded within the Delphes program for jet clustering, using the anti-k_t configuration.

The value of R is selected to balance two factors: the loss of jet p_{T} due to radiation outside the cone, and the absorption of soft hadrons from the hard scattering. A value of $R = 0.4$ is used in this analysis, in keeping with the present ATLAS standard. In the final step of selection jets are required to have transverse momentum $p_{\mathrm{T}} > 25.0$ GeV and pseudorapidity $|\eta| < 2.5$.

As observed in real experiments, the average momentum of reconstructed objects often differs from the corresponding objects at the generator level. This is most apparent for jets, as generator-level components, including neutrinos, muons and looping particles, are lost during the clustering procedure. For events without pile-up simulation, the jet energy scale resolution is estimated using a smooth function,

$$\frac{\sigma(p_T)}{p_T} = \sqrt{\frac{\left(3 - \frac{|\eta|}{5}\right)^2 \mathrm{GeV}}{p_{\mathrm{T}} + 1\,\mathrm{GeV}}}. \tag{8.3.3}$$

This formula is used by default in the ATLAS Delphes card and is extracted from the analysis in Ref. [146].

As the operating luminosity of the LHC becomes increasingly high the collision multiplicity per bunch-crossing also increases. This pile-up has a direct impact on isolation and the reconstruction of jets and E_{T}. The level of pile-up is identified and quantified using vertex reconstruction. At sufficient distances from the hard scattering process these interactions may be re-constructed using a precise vertexing algorithm. Charged particle contamination can be identified using a combination of tracking vertexing information, while neutral particle pile-up must be estimated on average. Both neutral and charged pile-up correction are performed on jets and isolation variable. No attempt of missing E_{T} pile-up subtraction is attempted in Delphes, though advanced techniques are applied by experimental collaborations.

Delphes simulates pile-up using a sample of pre-generated minimum bias (low-Q^2) events. These interactions are then randomly placed along the beam axis in such a way that mimics the elongated shape of the beam-spot around the nominal interaction point. The number of pile-up interactions per bunch-crossing is randomly extracted from a poisson distribution around an average number of reconstructed primary ver-

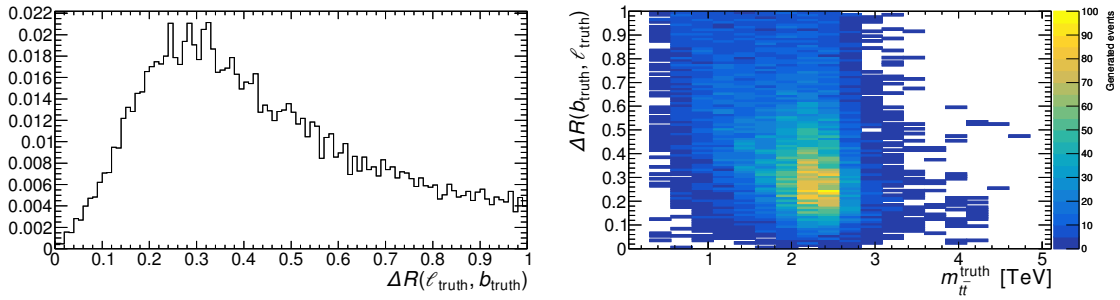

(a) True $\Delta R(\ell, b)$ (Normalised).

(b) True $m_{t\bar{t}}$ vs true $\Delta R(\ell, b)$

Figure 8.4.1: Plots of the normalised true $\Delta R(\ell, b)$ distribution and 2D distribution of $\Delta R(\ell, b)$ vs. the true invariant mass of the top pair for signal ($\gamma + Z + Z'$) events including a 2.5 TeV mass Z' boson. Observe that $\Delta R(\ell, b)$ has peak events lower than 0.4, such that the lepton falls inside the jet radius. This results in the loss of signal objects during overlap removal. To see this, reconstructed objects are truth-tagged and impact on this population is observed following selection requirements.

tices $< \mu >= 50$.

8.4 Overlap removal

Objects can satisfy both the jet and lepton selection criteria and, as such, a procedure called "overlap removal" is applied, in order to associate objects to a unique hypothesis. This procedure has an enormous impact on signal retention in this analysis, because, as shown in Fig. 8.4.1, true top-granddaughter leptons (top-leptons) often fall inside the jet radius of the true top-daughter b-quark (top-b's) for signal events. In Ref. [92] the following requirements are made, in the order listed.

To prevent double-counting of electron energy deposits as jets, the closest jet lying $\Delta R < 0.2$ from a reconstructed electron is discarded. If a jet has fewer than three tracks and is $\Delta R < 0.4/p_{\text{T}}^{\mu}$ from a muon, the jet is not considered. To reduce the impact of non-prompt leptons, if an electron is $\Delta R < 0.4$ from a jet, then that electron is removed. The muon is not considered if it is $\Delta R < 0.4$ from a jet which has at least three tracks.

To assess the impact of isolation and overlap removal requirements on the signal objects we *truth tag* the reconstructed objects: if a jet is within $\Delta R = 0.4$ of the true top-daughter b-quark; if an electron or muon is within $\Delta R = 0.01$ of the true top-lepton. The latter condition is motivated by Fig. 8.4.2 made by considering the closest true lepton from the top quark to each reconstructed lepton and calculating the ΔR.

The results of the default object overlap removal are shown in Figs. 8.4.3, 8.4.4, and 8.4.5. It's clear that the default isolation (w.r.t. Ref. [92]) removes many true top-electrons while retaining most true top-muons. The default dilepton overlap removal also discards

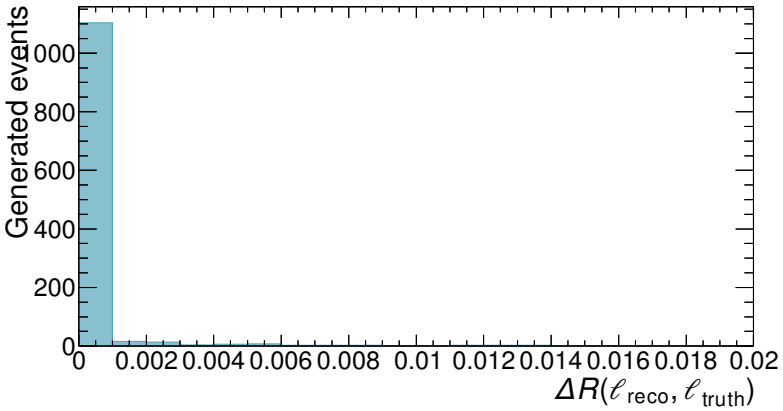

Figure 8.4.2: Plot displaying the distance in $\eta \times \phi$ space between reconstructed leptons and the nearest truth lepton: $\Delta R(\ell_{reco}, \ell_{truth})$. This is shown in order to justify the maximum distance for truth matching.

many true top-electrons while keeping most truth-tagged muons. Also, most truth tagged jets are removed in the electron-muon, and muon-muon channel.

To mitigate the dominant loss of the electron efficiency due to the isolation requirement it might be appropriate to introduce a p_T dependent formula, similar to that used for the isolation of muons. However, in my study I found that implementing this causes the overlap removal to become the dominant cause of efficiency loss. Based on these observations, the muon-based requirements in the overlap removal are not applied, as muons are largely separable from jets. The electron-based steps in the overlap removal, however, cannot be totally neglected, as electrons overlap strongly with jets. The ATLAS collaboration is developing advanced methods to separate electron-associated energy deposits from jets, prior to jet clustering that will likely improve the resolution of closely separated electrons and jets. However, the utilisation of these methods is beyond the scope of this phenomenological analysis. It might be possible to simulate these advanced techniques by identifying electrons overlapping with jets and directly subtracting their 4-momenta from the jet. Yet, as this is done after jet construction and scaling, this may introduce problems by changing the jet energy.

8.5 Event selection

The dilepton channel of top quark pair production labels those events in which both W^+ and W^- decay leptonically. The branching ratio for hadronic W boson decay is six times greater than that for leptonic decay, such that the dilepton channel accounts for only 11.1% of the $t\bar{t}$ cross section.

Tau leptons undergo further decay within the detector, beginning a showering process that leads to a jet. This makes identification difficult. Furthermore, the tau may decay

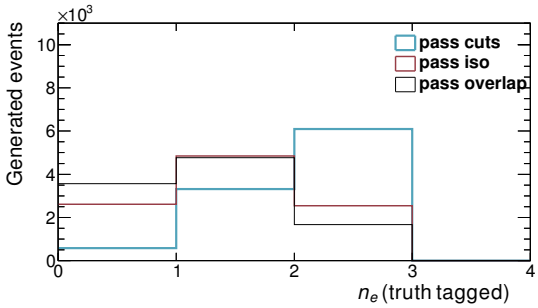

(a) Truth tagged Electrons

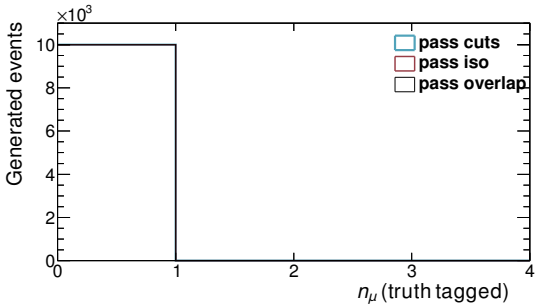

(b) Truth tagged Muons

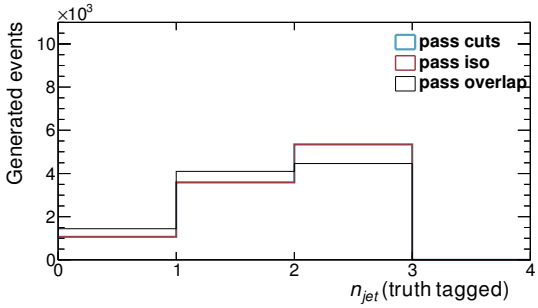

(c) Truth tagged Jets

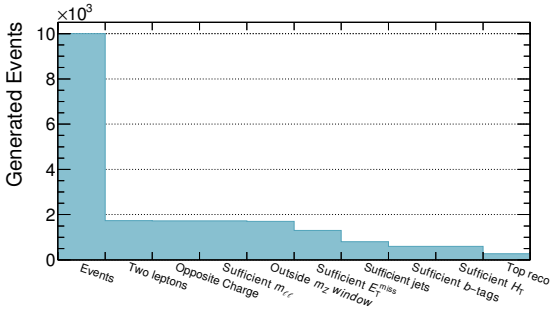

(d) Cutflow

Figure 8.4.3: Truth tagged objects - ee channel

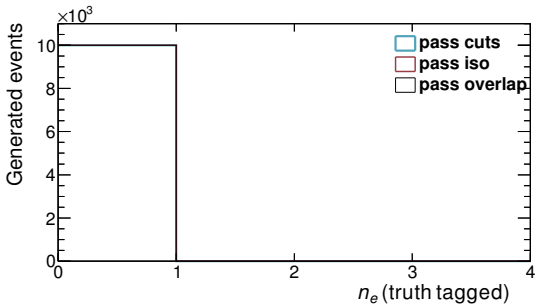

(a) Truth tagged Electrons

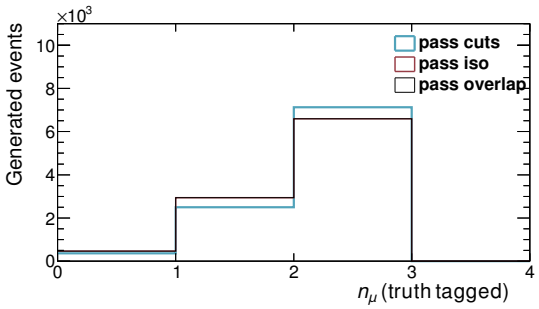

(b) Truth tagged Muons

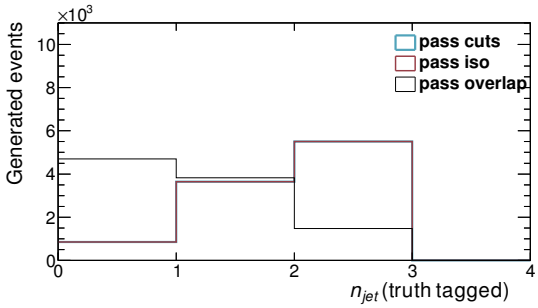

(c) Truth tagged Jets

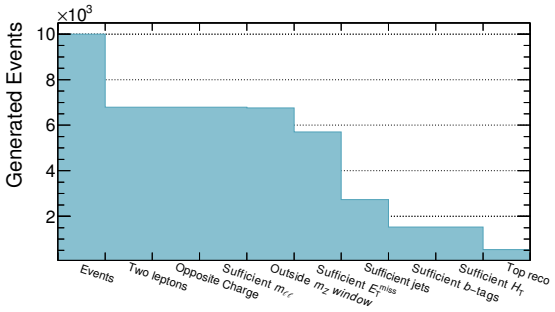

(d) Cutflow

Figure 8.4.4: Truth tagged objects - $\mu\mu$ channel

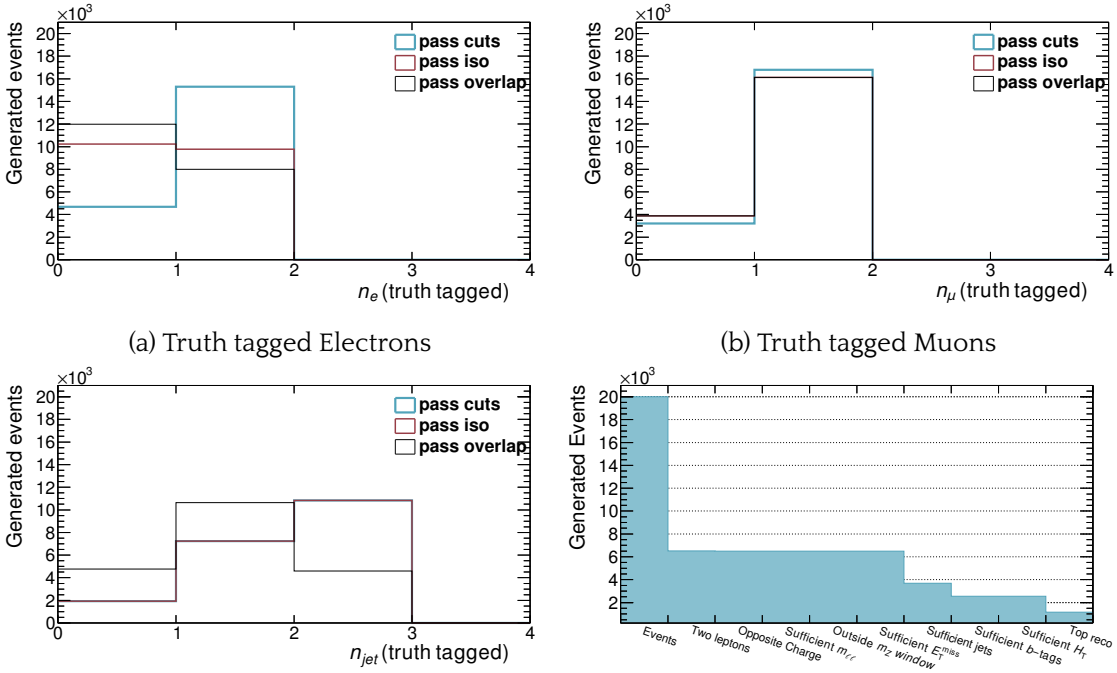

(a) Truth tagged Electrons

(b) Truth tagged Muons

(c) Truth tagged Jets

(d) Cutflow

Figure 8.4.5: Truth tagged objects - $e\mu$ channel

via $\nu_\tau + \mu + \nu_\mu$ or $\nu_\tau + e + \nu_e$, resulting in a final state identical to one arising from a W boson decaying directly to a muon or electron, but with the addition of a third neutrino. We presently limit our analysis to "true" dilepton decays featuring only electrons and/or muon final states. Consequently, the term dilepton henceforth solely refers to these processes.

In addition to the Z' background arising in SM $t\bar{t}$, there are several other sources of irreducible background. In order to enrich the data by biasing towards events that are characteristic of $t\bar{t}$ dilepton processes, we enforce several requirements on events, based on recent ATLAS analyses [92, 147]. Three different channels are considered in this analysis: events with two electrons in the final state (ee), events with two muons ($\mu\mu$), and those with one electron and one muon ($e\mu$). The first requirement is that an event contains exactly two leptons $\ell^+, \ell^- = e^+e^-, \mu^+\mu^-, e^\pm\mu^\mp$. The channel is then assigned depending on the lepton species, and these are required to carry opposite charge. In order to suppress the hadronic background (e.g. J/Ψ) one requires that the invariant mass of the two leptons is greater than 15 GeV. Additionally, for leptons of the same flavour, in order to suppress events attributable to jet-accompanied Drell-Yan production, events with lepton-pair invariant mass with 10 GeV of the Z-boson mass are rejected. Due to the two b-quarks in every final state, at least two jets are required in the event, and one may demand a minimum of none, one, or two b-tags. Differing minimum b-tag requirements are explored below. A requirement of at least 60 GeV of $E_{\mathrm{T}}^{\mathrm{miss}}$ accounts for the neutrinos, and further reduces the DY background. This requirement is not made of the

Requirements	$e^+e^-/\mu^+\mu^-$	$e^\pm\mu^\mp$
Leptons	2	2
Jets	≥ 2	≥ 2
$m_{\ell\ell}$	> 15 GeV	> 15 GeV
$\lvert m_{\ell\ell} - m_Z \rvert$	> 10 GeV	-
$E_{\mathrm{T}}^{\mathrm{miss}}$	> 60 GeV	-
b-tagged jets	$\geq 1, 2^*$	$\geq 1, 2^*$
H_{T}	-	> 130 GeV

Table 8.5.1: Summary of event selection requirements applied in each dilepton channel. * Minimum b-tagging requirements of both 1 and 2 are tested.

$e^\pm\mu^\mp$ channel, however, at least 130 GeV of H_{T} is made necessary in order to suppress $Z/\gamma^* \to \tau^+\tau^-+$ jets. These event selection requirements are summarised in Tab. 8.5.1.

As demonstrated in section 8.4 the electron channels suffer such a large loss of efficiency that the remaining sections of this chapter consider only the dimuon channel. Further work on this analysis will include all available channels.

8.6 Top reconstruction

The dileptonic $t\bar{t}$ channel features two neutrinos in the final state. These particles cannot be directly detected at colliders, preventing the calculation of the invariant mass m for all particles i in the system:

$$m = \sqrt{\left(\sum_i E_i\right)^2 - \left(\sum_i \vec{p}_i\right)^2}. \tag{8.6.1}$$

The presence of neutrinos in the final state may only be inferred from momentum conservation. At a hadron collider, the total longitudinal momentum of the colliding partons is also an unknown. Therefore, the total missing transverse momentum,

$$\vec{E}_{\mathrm{T}}^{\mathrm{miss}} = -\sum_i \vec{p}_{\mathrm{T}}^{\,i}, \tag{8.6.2}$$

is the only handle on undetected neutrinos. $E_{\mathrm{T}}^{\mathrm{miss}}$ may also be attributed to additional sources, including mis-measurement at the detector level due to the finite resolution available.

There are several approaches to finding a suitable replacement for m in the search for new resonances. One may consider alternative observables constructed solely from transverse and/or directly measurable observables (section 8.6.1). Alternatively, one may attempt to resolve the neutrino momenta and reconstruct the invariant mass. Assuming

that the masses of all final state particles may be taken *a priori*, and that they obey their mass-shell relations, there are a total of eighteen independent kinematic variables in the system. Twelve of these, the momenta of the charged leptons and two jets from b quarks, may be constrained through direct measurement, leading to an under-constrained system with kinematics described by the relations:

$$p_{W^+} = p_{\ell^+} + p_\nu, \tag{8.6.3}$$

$$p_{W^-} = p_{\ell^-} + p_{\bar{\nu}}, \tag{8.6.4}$$

$$p_t = p_b + p_{\ell^+} + p_\nu, \tag{8.6.5}$$

$$p_{\bar{t}} = p_{\bar{b}} + p_{\ell^-} + p_{\bar{\nu}}. \tag{8.6.6}$$

One can try to constrain the system further by enforcing further assumptions. The first pair of constraints come from assuming that the missing transverse momentum may be attributed solely to the two neutrinos:

$$E_x^{\text{miss}} = p_x^\nu + p_x^{\bar{\nu}}, \tag{8.6.7}$$

$$E_y^{\text{miss}} = p_y^\nu + p_y^{\bar{\nu}}. \tag{8.6.8}$$

Two further constraints follow under the assumption that the invariant mass of each lepton-neutrino pair is equal to the on-shell $W^\pm$ boson masses:

$$m_{W^+}^2 = (E_{\ell^+} + E_\nu)^2 - \left(p_x^{\ell^+} + p_x^\nu\right)^2 \tag{8.6.9}$$

$$- \left(p_y^{\ell^+} + p_y^\nu\right)^2 - \left(p_z^{\ell^+} + p_z^\nu\right)^2, \tag{8.6.10}$$

$$m_{W^-}^2 = (E_{\ell^-} + E_{\bar{\nu}})^2 - \left(p_x^{\ell^-} + p_x^{\bar{\nu}}\right)^2 \tag{8.6.11}$$

$$- \left(p_y^{\ell^-} + p_y^{\bar{\nu}}\right)^2 - \left(p_z^{\ell^-} + p_z^{\bar{\nu}}\right)^2. \tag{8.6.12}$$

Finally, the system may be fully constrained under assumption that the invariant mass of each jet-lepton-neutrino combination is equal to the on-shell (anti)top quark mass:

$$m_t^2 = (E_b + E_{\ell^+} + E_\nu)^2 - \left(p_x^b + p_x^{\ell^+} + p_x^\nu\right)^2 \tag{8.6.13}$$

$$- \left(p_y^b + p_y^{\ell^+} + p_y^\nu\right)^2 - \left(p_z^b + p_z^{\ell^+} + p_z^\nu\right)^2, \tag{8.6.14}$$

$$m_{\bar{t}}^2 = (E_{\bar{b}} + E_{\ell^-} + E_{\bar{\nu}})^2 - \left(p_x^{\bar{b}} + p_x^{\ell^-} + p_x^{\bar{\nu}}\right)^2 \tag{8.6.15}$$

$$- \left(p_y^{\bar{b}} + p_y^{\ell^-} + p_y^{\bar{\nu}}\right)^2 - \left(p_z^{\bar{b}} + p_z^{\ell^-} + p_z^{\bar{\nu}}\right)^2. \tag{8.6.16}$$

There are a number of methods in the literature that seek solutions based upon these constraints. In this paper two approaches are explored and compared: the first by finding an analytic solution through the construction of a quartic equation (section 8.6.2); the

other by assuming a pseudorapidity for the neutrinos and weighting each combination through comparison with $E_{\mathrm{T}}^{\mathrm{miss}}$ (section 8.6.3).

8.6.1 Transverse variables

The aim is to construct a viable alternative variable to the invariant mass which retains sensitivity to the mass of a Z' boson from transverse and directly detectable kinematic variables. The first variable to consider is H_{T}, the scalar sum of E_{T} for the two leptons and the jets selected as b-quark candidates.[1]

$$H_{\mathrm{T}} = E_{\mathrm{T}}^{b} + E_{\mathrm{T}}^{\bar{b}} + E_{\mathrm{T}}^{\ell^+} + E_{\mathrm{T}}^{\ell^-} \tag{8.6.17}$$

Increased sensitivity can be gained by combining this with the missing transverse momentum of the event:[2]

$$H_{\mathrm{T}} + E_{\mathrm{T}}^{\mathrm{miss}}. \tag{8.6.18}$$

In an attempt to find a more sensitive variable, one can begin by taking the invariant mass of all visible decay products.

$$m_{\mathrm{vis}}^2 = (E_b + E_{\bar{b}} + E_{\ell^+} + E_{\ell^-})^2 - (\vec{p}_b + \vec{p}_{\bar{b}} + \vec{p}_{\ell^+} + \vec{p}_{\ell^-})^2 \tag{8.6.19}$$

Then find the corresponding transverse energy of all visible decay products.

$$E_{\mathrm{T}}^{\mathrm{vis}\,2} = m_{\mathrm{vis}}^2 + \left(\vec{p}_T^{\,b} + \vec{p}_T^{\,\bar{b}} + \vec{p}_T^{\,\ell^+} + \vec{p}_T^{\,\ell^-}\right)^2 \tag{8.6.20}$$

Which can then be taken in combination with the scalar missing transverse momentum to form a new variable:

$$K_{\mathrm{T}} = E_{\mathrm{T}}^{\mathrm{vis}} + E_{\mathrm{T}}^{\mathrm{miss}}. \tag{8.6.21}$$

8.6.2 Analytic solution

This makes use of the analytic solution derived by L. Sonnenschein, the full calculation of which may be found in Ref. [148]. In summary, this proceeds via the following steps.

Firstly, the unknowns E_ν and $E_{\bar{\nu}}$ are eliminated by rearranging the invariant mass equation for the W bosons and top quarks (Eqs. 8.6.12, 8.6.16) and subtracting the two terms, for each parton branch individually. Using the linearly independent equations for the top and antitop quark parton branches separately, one may remove the dependence on p_z^ν. $p_x^{\bar{\nu}}$ and $p_y^{\bar{\nu}}$ may be eliminated using the two linear missing transverse momentum equations. One may then solve these two polynomials without loss of generality to p_x^ν by

[1] In some literature the definition of H_{T} includes all visible objects and/or $E_{\mathrm{T}}^{\mathrm{miss}}$. However, to avoid confusion with H_{T}, as defined for event-level selection requirements, I maintain a distinction.

[2] In some literature the definition of H_{T} includes $E_{\mathrm{T}}^{\mathrm{miss}}$ as well

computing the resultant with respect to the neutrino momentum p_y^ν to give a univariate polynomial quartic equation:

$$h_0 p_{\nu_x}^4 + h_1 p_{\nu_x}^3 + h_2 p_{\nu_x}^2 + h_3 p_{\nu_x} + h_4 = 0. \tag{8.6.22}$$

This quartic can be solved analytically, resulting in at most a four fold ambiguity. In our implementation these solutions are found using the Descartes-Euler method. For each solution one can compute $p_{\bar{\nu}_x}$ from the $E_{\mathrm{T}}^{\mathrm{miss}}$ equation. $p_{\nu(\bar{\nu})_y}$ and $p_{\nu(\bar{\nu})_z}$ may be calculated by rearranging equations derived in the initial elimination.

Thus, one can find four sets of solutions when the b quarks and leptons are perfectly matched. Experimentally, it is not feasible to tag the charge of these jets, thus the number of possible solutions must be multiplied by each combination of b quark jet candidates. In our analysis we allow two candidates through to the reconstruction stage (section 8.5), such that we always have an eightfold ambiguity in the solution.

The critical decision is how to best select the best solution, given this ambiguity. Choices include the minimum mass approach, the target mass approach and by characterising the decay products.

The first option method simply selects that solution which results in the smallest invariant mass for the full system. This decision works due to the decrease in differential cross section for top pair production with increasing top pair mass in the SM. Clearly, however, this also biases the solutions towards the SM $t\bar{t}$ processes, background in this search, with a negative effect on the signal processes. Due to the simplicity of this option, my own implementation for solving via the analytic method, uses this lowest invariant mass approach.

The target mass approach is similar to the former option, though it uses the solution closest to the *a priori* mass of the resonance that is selected. Obviously, this has the opposite problem: biasing against the background processes by preferentially selecting solutions nearest to the target mass, regardless of the true invariant mass. Additionally, this method suffers due to its dependance on a fixed target mass, as the analysis would need to be repeated, with each iteration corresponding to a different target mass.

The final approach is to characterise the decay of the top quark and use this information to obtain the best neutrino solution. Within the ATLAS collaboration it is known as the kinematic (KIN) method. This requires one to analyse the relative kinematics of the final state in order to profile particles resulting from top decay. As these processes are common to both signal and background, the algorithm remains unbiased. The system of assumptions and constraints enforced to find the analytic solution only contain a subset of kinematic information, thus adding the relative kinematic information of the final state particles provides an additional set of constraints to use as selection criteria for the

available solutions. Typically these criteria depend on the ΔR between the top its decay products, as well as between the decay products themselves, as well as their relative p_{T}s and energies. One first must produce distributions for each kinematic quantity, using a SM $t\bar{t}$ Monte Carlo sample, for each top quark momentum range, and then assign a probability value based on the normalised content of each bin. One then constructs a likelihood for each event based on the product of these probabilities:

$$\mathcal{L} = \prod_i P(\Delta R(\nu, i)) \cdot P(p_{\mathrm{T}}^{\nu}/p_{\mathrm{T}}^{i}) \cdot P(E^{\nu}/E^{i}), \tag{8.6.23}$$

where $i = b, \bar{b}, \ell^+, \ell^-$. The neutrino solution set that maximises this likelihood is then used to reconstruct the invariant mass of the top pair. This method appears best suited to resonance searches.

8.6.3 Neutrino Weighting method

Neutrino weighting (NW) reconstruction relies on ignoring $E_{\mathrm{T}}^{\mathrm{miss}}$ constraints and scanning over neutrino pseudorapidities (η). Along with a fixed m_W and m_t, assuming η_ν and $\eta_{\bar{\nu}}$ constrains each top(anti-top) system individually. Thus we have exchanged two constraints, E_x^{miss} and E_y^{miss}, for η_ν and $\eta_{\bar{\nu}}$. These may then be expressed via a quadratic equation for each decay leg and solved independently. The NW method was developed within the D0 Collaboration [149]. It has since been used for analyses by D0 [150, 151], CDF [152], and ATLAS [144]. I inherited the code from James Howarth who worked on the development of the code with ATLAS. This calculation is outlined below.

Firstly, by momentum conservation:

$$p_t = p_b + p_\ell + p_\nu, \tag{8.6.24}$$

$$p_W = p_\ell + p_\nu. \tag{8.6.25}$$

Squaring each side yields

$$m_t^2 = m_b^2 + m_\ell^2 + m_\nu^2 + 2p_b p_\ell + 2p_b p_\nu + 2p_\ell p_\nu, \tag{8.6.26}$$

$$m_W^2 = m_\ell^2 + m_\nu^2 + 2p_\ell p_\nu, \tag{8.6.27}$$

respectively. Each of these masses is assumed to be on-shell at the respective pole mass. The neutrino mass is assumed to be zero and dropped. While the lepton mass will likewise be assigned to zero later, as we are interested only in the electron, and muon final states, it will be retained in the calculations for generality. Combining Eqs. 8.6.26

and 8.6.27 allows us to eliminate $p_b p_\ell$ to give

$$p_b p_\nu = \frac{m_t^2 - m_b^2 + m_W^2}{2}, \tag{8.6.28}$$

$$p_\ell p_\nu = \frac{m_W^2 - m_\ell^2}{2}. \tag{8.6.29}$$

The expanded Lorentz products may be written explicitly component-wise. With the energy and longitudinal momentum component of the neutrino expressed in terms of its transverse momentum and pseudorapidity, the first may be written:

$$p_b p_\nu = E_b p_{\mathrm{T}}^\nu \sinh\eta_\nu - p_x^b p_x^\nu - p_y^b p_y^\nu - p_z^b p_{\mathrm{T}}^\nu \cosh\eta_\nu, \tag{8.6.30}$$

$$p_b p_\nu + p_x^b p_x^\nu + p_y^b p_y^\nu = p_{\mathrm{T}}^\nu \left(E_b \sinh\eta_\nu - p_z^b \cosh\eta_\nu \right) = p_{\mathrm{T}}^\nu k_b. \tag{8.6.31}$$

$$p_{\mathrm{T}}^\nu = \frac{p_x^b}{k_b} p_x^\nu + \frac{p_y^b}{k_b} p_y^\nu + \frac{p_b p_\nu}{k_b}, \tag{8.6.32}$$

$$= A_b p_x^\nu + B_b p_y^\nu + C_b. \tag{8.6.33}$$

An identical expression may be derived for the product involving p_ℓ:

$$p_{\mathrm{T}}^\nu = A_\ell p_x^\nu + B_\ell p_y^\nu + C_\ell. \tag{8.6.34}$$

Equating the two expressions in Eqs. 8.6.33 and 8.6.34 yields:

$$p_x^\nu = a p_y^\nu + c, \tag{8.6.35}$$

where,

$$a = \frac{B_\ell - B_b}{A_b - A_\ell}, \quad c = \frac{C_\ell - B_b}{A_b - A_\ell}. \tag{8.6.36}$$

Taking the square of Eq. 8.6.33 with substitution by Eq. 8.6.35 leads to the final quadratic equation:

$$\left[a^2 \left(A_b^2 - 1\right) + B_b^2 - 1\right] p_y^{\nu 2} + \left[2ac \left(A_b^2 - 1\right) + 2aA_bC_b + 2B_bC_b\right] p_y^\nu + c^2 \left[\left(A_b^2 - 1\right) + 2cA_bC_b + C_b^2\right] = 0. \tag{8.6.37}$$

Thus, there are at most two real solutions for each neutrino, each of which may be assigned a weighting. If no solution is found, this η is skipped, as well as the second (anti)neutrino. Once p_y^ν is determined, p_x follows immediately from Eq.8.6.35.

With this information one may determine their four-vectors, with two possible solutions for each. Furthermore, as the observable $E_{\mathrm{T}}^{\mathrm{miss}}$ was not used as a constraint, it may be used to assign a weight to each solution based on how closely the sum of the neutrino

p_{T}s reproduce it:

$$\omega = \exp\left(-\frac{E_x^{\mathrm{miss}} - p_x^{\nu} - p_x^{\bar{\nu}}}{2\sigma_x^2}\right)\exp\left(-\frac{E_y^{\mathrm{miss}} - p_y^{\nu} - p_y^{\bar{\nu}}}{2\sigma_y^2}\right), \tag{8.6.38}$$

where $\sigma_{x(y)}$ is the resolution of the $x(y)$ component of $E_{\mathrm{T}}^{\mathrm{miss}}$. This can be repeated for N iterations, scanning over the space of possible neutrino η combinations.

The weighted average of all possible solutions is then taken in order to reconstruct the system. An additional two-fold ambiguity is introduced by iterating over all possible lepton-jet combinations. For each event multiple attempts are made at performing a successful reconstruction. The scan over the (anti)neutrino pseudorapidities is performed using a Gaussian distribution centred on $(7\eta_{\ell^{+(-)}} - 1)/10$, with $\sigma = 1.4$.

8.7 Observables

The dilepton final state allows the definition of many observables as both tops decay to leptons which carry maximal spin analysing power (Tab. 3.6.1). Therefore, in contrast to the semilepton final state, it is possible to probe the spin correlation of the tops, in addition to the single top polarisation and charge asymmetry. In addition to the lower overall cross section (Eq. 3.1.5), this channel has a disadvantage with respect to the semilepton state due to the difficulty in reconstructing the top quarks in the presence of two sources of missing transverse momentum. Various techniques may be applied to overcome this limitation, though ultimately none of these can provide the top momentum resolution available in the semilepton channel (section 8.6). In the transverse strategy, no direct attempt at top reconstruction is made, and the analysis instead relies on observables constructed solely from directly detectable measurements, principally those transverse to the beam direction. When using reconstruction procedures the properties of the individual tops are reconstructed by restricting the system using several tactical assumptions. Therefore, in the latter strategy one may directly calculate all of the variables outlined in Chapter 3, notably the invariant mass, charge asymmetry, top polarisation and spin correlation asymmetry via the relevant angles and momenta of the reconstructed tops and decay products.

In the transverse strategy, it is necessary to compute alternative variables that provide a handle on top properties. In the case of the invariant mass, one may consider a number of variables constructed using the transverse momentum of visible particles, and the missing transverse momentum.

For the charge asymmetry one can evaluate an analogue of the rapidity difference de-

pendent forward-backward asymmetry in section 3.5.2 using the decay leptons,

$$A_C^{\ell\ell} = \frac{N(\Delta|\eta_{\ell\ell}| > 0) - N(\Delta|\eta_{\ell\ell}| < 0)}{N(\Delta|\eta_{\ell\ell}| > 0) + N(\Delta|\eta_{\ell\ell}| < 0)}. \tag{8.7.1}$$

where the difference between the absolute pseudorapidity of the positive and negative decay leptons is used, $\Delta|\eta_{\ell\ell}| = |\eta_{\ell^+}| - |\eta_{\ell^-}|$.

Similarly one can employ an analogue of the reconstructed forward-backward asymmetry in section 3.5.3 also using the decay leptons by defining

$$\cos\theta_\ell^* = \frac{\eta_{\ell\ell}}{|\eta_{\ell\ell}|}\cos\theta_\ell, \tag{8.7.2}$$

and constructing the asymmetry,

$$A_{FB^*}^{\ell} = \frac{N(\cos\theta_\ell^* > 0) - N(\cos\theta_\ell^* < 0)}{N(\cos\theta_\ell^* > 0) + N(\cos\theta_\ell^* < 0)}. \tag{8.7.3}$$

Measurement of the spin correlation also requires top reconstruction, as $\cos\theta_{\ell^+(\ell^-)}^{t(\bar{t})}$ is determined in the (anti)top rest frame. However, there are alternative variables that allow probing of the spin correlation without this reconstruction. For example, one may demonstrate the dependence of the cross section on the difference in lepton azimuthal angle,

$$\frac{1}{\sigma}\frac{\mathrm{d}\sigma}{\mathrm{d}\cos\Delta\phi_{\ell\ell}} = \frac{1}{2}(1 - D\cos\Delta\phi_{\ell\ell}). \tag{8.7.4}$$

And one may construct an asymmetry from this variable [153],

$$A_{\Delta\phi} = \frac{N(|\Delta\phi_{\ell\ell}| > \pi/2) - N(|\Delta\phi_{\ell\ell}| < \pi/2)}{N(|\Delta\phi_{\ell\ell}| > \pi/2) + N(|\Delta\phi_{\ell\ell}| < \pi/2)}. \tag{8.7.5}$$

8.8 Results

8.8.1 Performance of the top reconstruction

The impact of the event-level selection requirements as outlined in Tab. 8.5.1 is presented in a cutflow diagram in Fig. 8.8.1, along with the efficiency of the cutflow as a function of the true invariant top quark pair mass. Figs. 8.8.2 and 8.8.3 show the efficiency break down for the lepton-based and jet/transverse variable-based requirements respectively.

It's apparent that for the dimuon final state, the overall efficiency of the requirements increases with increasing $m_{t\bar{t}}$. The requirements on two leptons, two b-tagged quarks, and high missing $E_{\mathrm{T}}^{\mathrm{miss}}$ in the final state are the dominant causes for event rejection. The

efficiency of all these requirements increases with increasing $m_{t\bar{t}}$. The other requirements have a minimal impact.

Clearly the minimum of two b-tagged jets requirement removes the most events, but the efficiency increases with increasing invariant mass. The requirement of at least two jets has moderate impact which improves gradually with invariant mass. The requirement on H_{T} is not applied in this channel.

Two methods of reconstructing the top quarks in dilepton events are considered: analytically by minimising $m_{t\bar{t}}$ ($\min(m_{t\bar{t}})$) and via neutrino weighting (NW). These are described in sections 8.6.3 and 8.6.2, respectively. The overall performance of the methods are assessed using three estimators.

The reconstruction efficiency is defined as the percentage fraction of events entering the reconstruction algorithm for which a solution is found. An efficiency of 100% means that all the accepted events have at least one solution. The reconstruction efficiency results are presented in Tab. 8.8.6. These show that the NW efficiency for SM processes are approximately 75%, which drops to 68% for processes mediated by a photon, Z boson and 2 TeV GLR-R Z' boson. The reconstruction selecting analytic solutions according to minimisation of $m_{t\bar{t}}$ are much lower, at around 40%. This is an unfair assessment of the algorithm as no kinematic smearing is performed when using it. It is largely used as a sanity check against the more sophisticated NW method. The reconstruction efficiency of the NW method may be improved by further optimisation of the smearing process. The difference in reconstruction efficiency between the difference processes is likely attributable to the efficiency of the reconstruction with respect to the $m_{t\bar{t}}^{\mathrm{truth}}$. As shown in Fig. 8.8.4 the efficiency of NW reconstruction decreases with increasing $m_{t\bar{t}}^{\mathrm{truth}}$. Naturally, events due to processes mediated by Z' bosons peak at higher $m_{t\bar{t}}^{\mathrm{truth}}$, and events initiated by $q\bar{q}$ generally carry higher energy than gg.

The reconstruction quality is estimated by measuring the ΔR between the truth and reconstructed (anti)top. The distributions in ΔR for each separate process when using the NW reconstruction are shown in Fig. 8.8.5. If $\Delta R < 0.4$ it is considered a good quality reconstruction. The percentages of successfully reconstructed events that fulfil this condition for each reconstruction algorithm and each process and show in Tab. 8.8.6. The quality of the reconstruction is approximately 60% for both algorithms, with the analytic method peaking considerably higher at above 80% for the $\min(m_{t\bar{t}})$ method for events mediated with a Z' boson. The reason for the higher reconstruction quality for Z' bosons is again due to the higher energy of the typical Z' mediated event, where higher $\sqrt{s}$ events have higher reconstruction quality.

The relative reconstruction resolution is defined by taking the difference between the truth and reconstructed values of a given kinematic variable and dividing by the truth

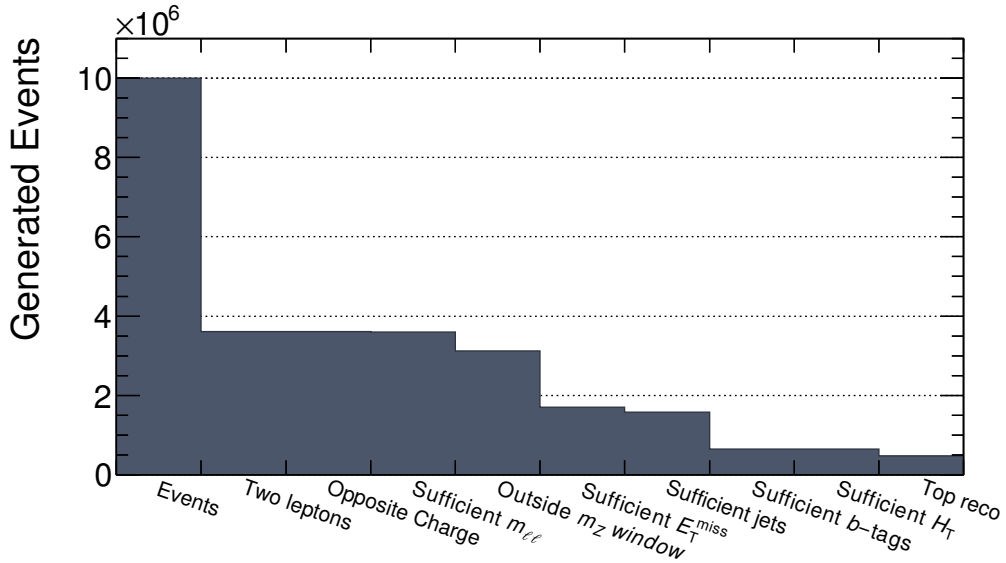

(a) Cutflow

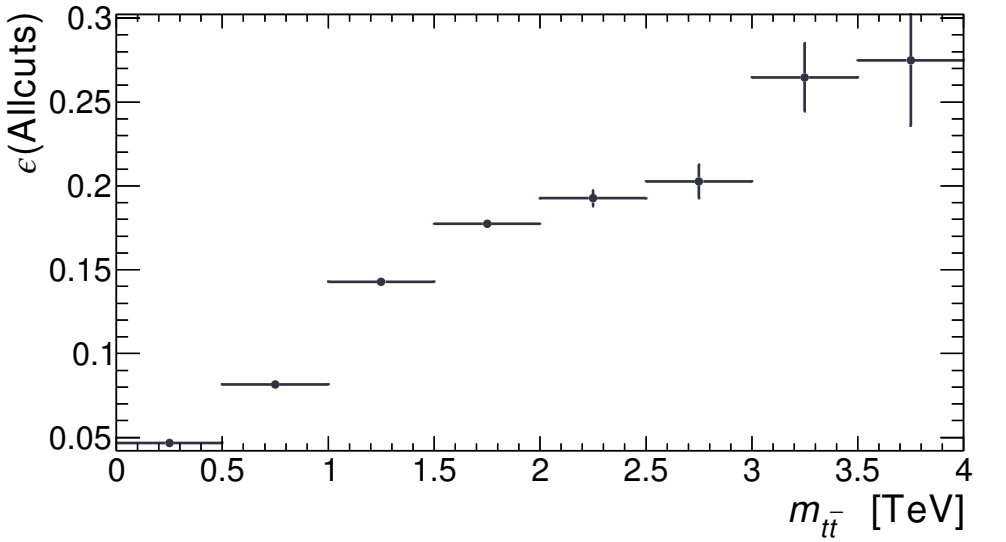

(b) All event-level selection requirements

Figure 8.8.1: Overall cutflow and efficiency of all event-level requirements distributed in bins of the true invariant mass of the top-antitop quark pair system for the dimuon channel.

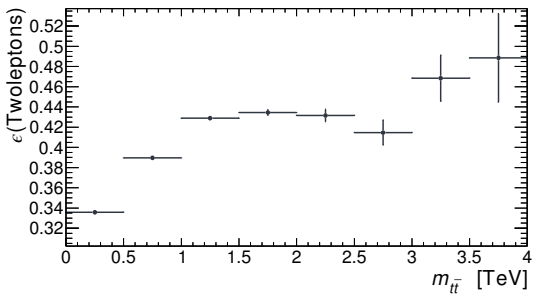

(a) Exactly two lepton requirement

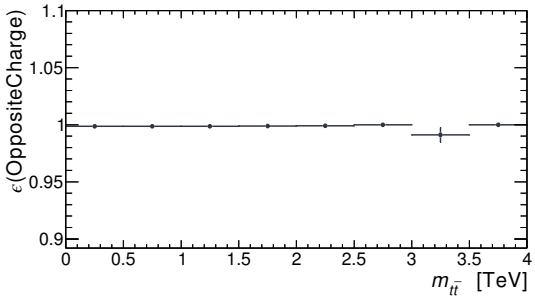

(b) Oppositely charged leptons requirement

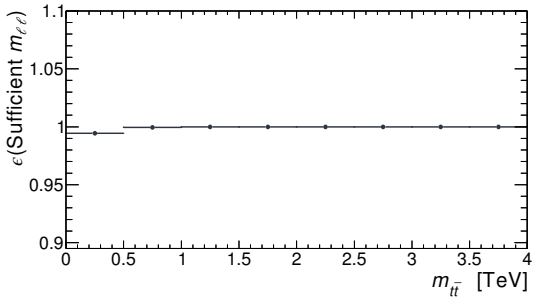

(c) $m_{ll} > 15$ GeV requirement

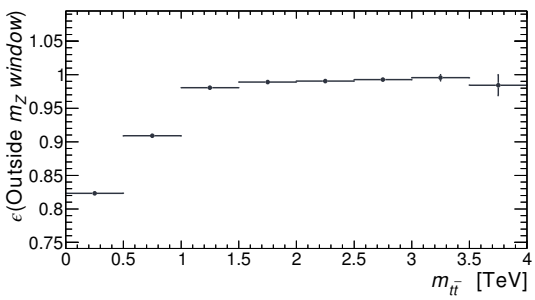

(d) $|m_{ll} - m_Z| > 10$ GeV requirement

Figure 8.8.2: Efficiency of the lepton-based requirements of the event selection distributed in bins of the true invariant mass of the top-antitop quark pair system for the dimuon channel.

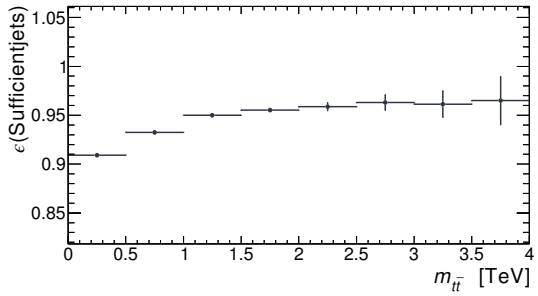

(a) At least two jets requirement

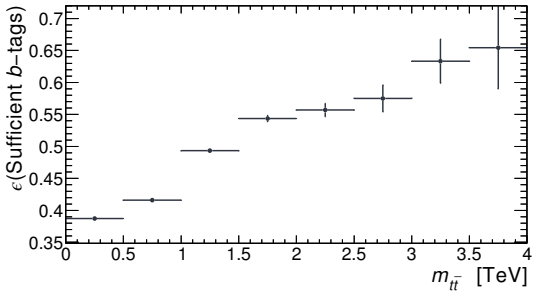

(b) At least two b-tagged jets requirement

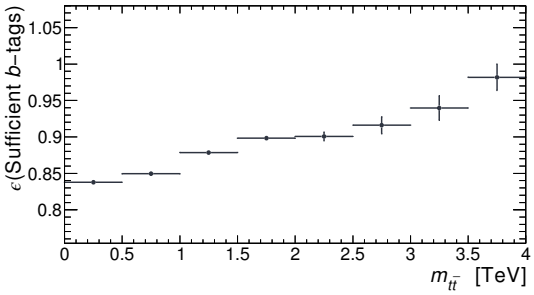

(c) At least one b-tagged jets requirement

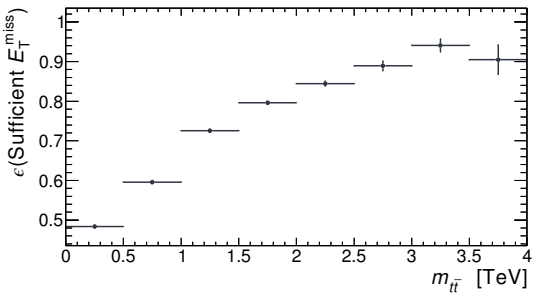

(d) $E_{\mathrm{T}}^{\mathrm{miss}} > 60$ GeV requirement

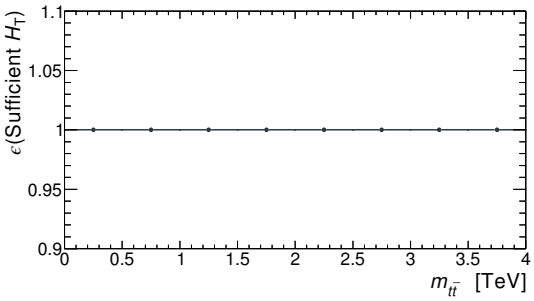

(e) $H_{\mathrm{T}} > 130$ GeV requirement

Figure 8.8.3: Efficiency of the jet and transverse energy requirements of the event selection distributed in bins of the true invariant mass of the top-antitop quark pair system for the dimuon channel.

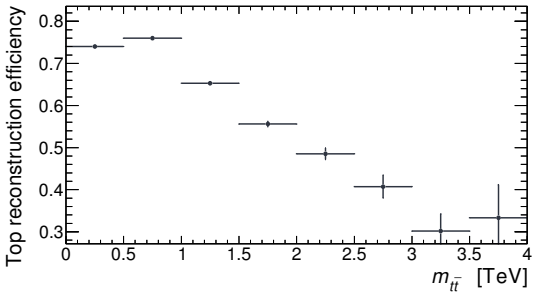

(a) Neutrino Weighting reconstruction

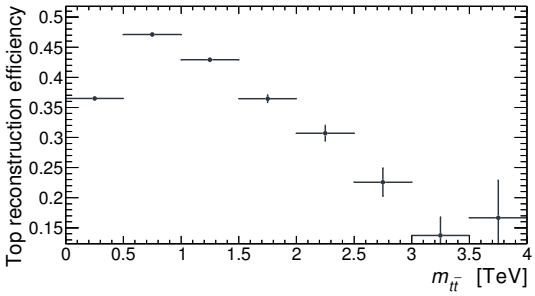

(b) Analytic $\min(m_{t\bar{t}})$ reconstruction

Figure 8.8.4: Efficiency of the two different reconstruction methods distributed in bins of the true invariant mass of the top-antitop quark pair system for the dimuon channel.

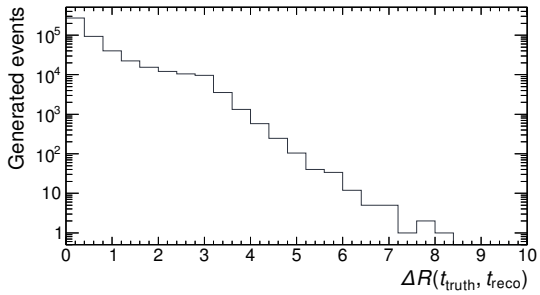

(a) gg initial state gluon mediated

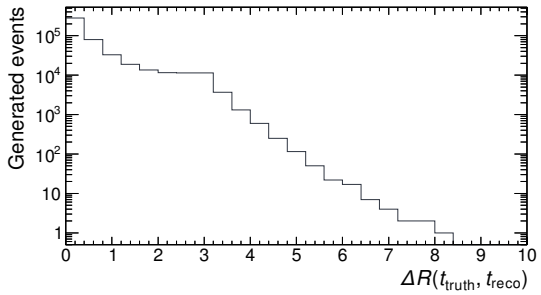

(b) qq initial state, gluon mediated

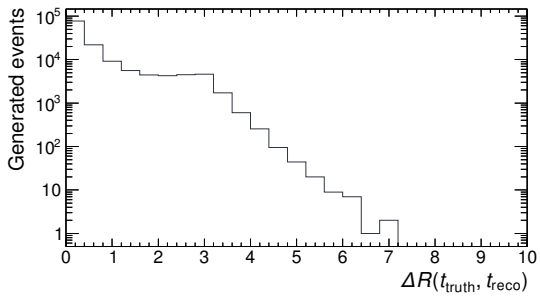

(c) qq initial state, γZ mediated

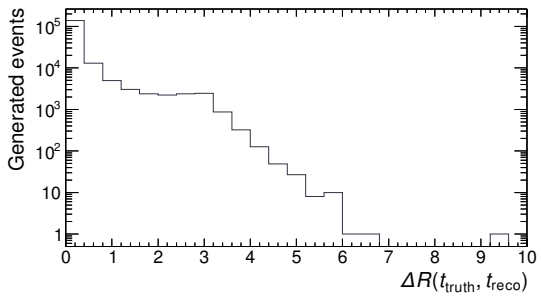

(d) qq initial state, $\gamma ZZ'$ mediated

Figure 8.8.5: Separation between the true and reconstructed top quarks $\Delta R(t_{truth}, t_{reco})$ for each dimuon $t\bar{t}$ production process using the NW reconstruction.

	gg	qq	γZ	$\gamma Z Z'$
Reconstruction efficiency [%]				
Neutrino Weighting	74	76	77	68
$\min(m_{t\bar{t}})$	42	43	47	41
Reconstruction quality [%]				
Neutrino Weighting	56	60	57	68
$\min(m_{t\bar{t}})$	63	63	63	84

Table 8.8.6: Top reconstruction efficiencies and reconstruction quality for two different reconstruction methods and four different process. The definitions of the efficiency and quality may be found in the text, along with a description and explanation of the results.

value. This is employed for the $p_{\mathrm{T}}^{t(\bar{t})}$, $\eta_{t(\bar{t})}$ and $\phi_{t(\bar{t})}$ of the reconstructed top and anti-top, and the $p_{\mathrm{T}}^{t\bar{t}}$, $\eta_{t\bar{t}}$ and $m_{t\bar{t}}$ of the top quark pair system. The resulting plots for these measurements are presented in Figs. 8.8.7 and 8.8.8. They show that NW reconstruction has bias towards high p_{T} for both individual top quarks and the top pair system though peaks at the true value. The same is true of the invariant mass of the top pair system. Note the double peak structure with a peak at 0 and 2 in the ϕ_t resolution. By checking the distribution of $\Delta\phi_t$ versus the angular distance of the two top quarks. Events around the peak at 2 are often those in which the two top quarks are collinear: where the two top quarks are recoiling against a high energy gluon. The reconstruction works in the assumption that the quarks are back to back. These misconstructed events are also responsible for the bias in the p_T resolutions, as the reconstructed tops, individually, and as a pair, are estimated with larger momentum in this scenario. For these events the top quarks are often reconstructed far away from their truth positions.

8.8.2 Significance of observables

Presently, just one BSM scenario is considered. This is a single 2 TeV Z' embedded by a Generalised Left-Right (GLR) symmetric model with couplings entirely generated by the breaking of a $\mathrm{U}(1)_R$ residual symmetry, with parameters given in Tab. 2.2.3. This is a narrow, universally coupling model, with leptophilic couplings. As such it is already excluded by limits set by LHC Drell-Yan analyses (section 2.1). However, it serves as a sufficient probe for exploring the potential of these observables considering reconstruction in the $t\bar{t}$ dilepton final state, for later use with more suitable top-philic models.

The Monte Carlo (MC) sample produced with a BSM model assumes the role of real experimental data with 300 fb^{-1} of 13 TeV data delivered by the LHC and analysed by the ATLAS detector using the Delphes set-up described in section 8.3. This is then tested for consistency with the SM hypothesis, where the SM MC sample serves the same purpose as in genuine analysis of ATLAS data, namely to compare with experimental data. The statistical framework for sensitivity analysis takes the form of a Likelihood Ratio Test,

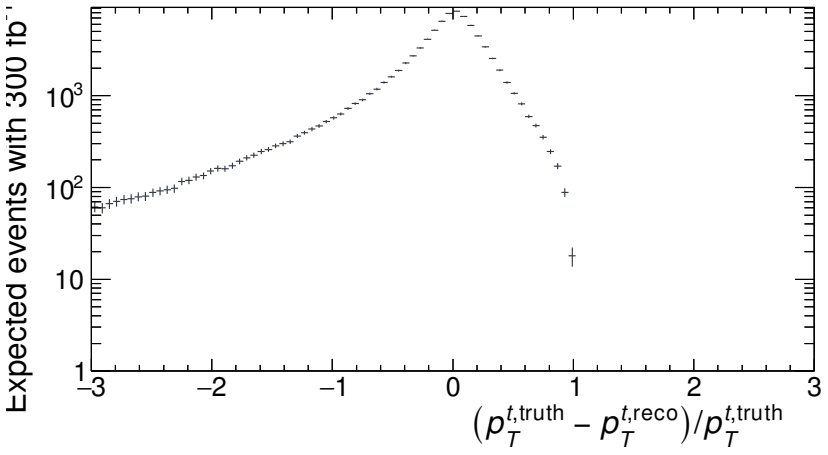

(a) p_{T}^{t} resolution

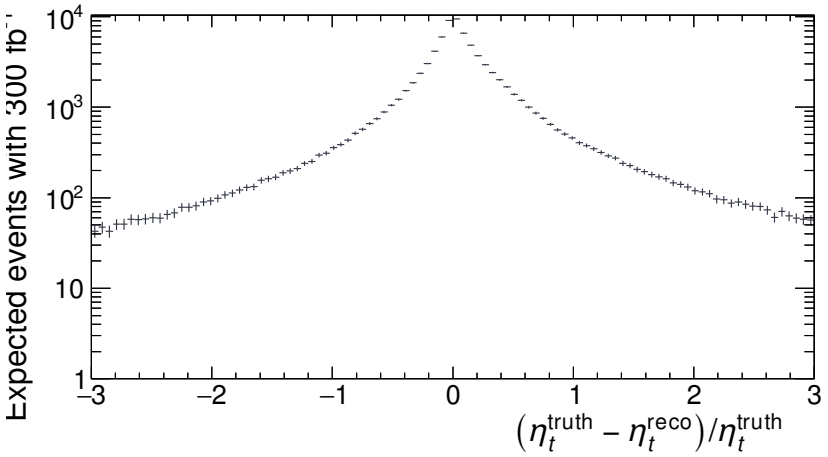

(b) η_t resolution

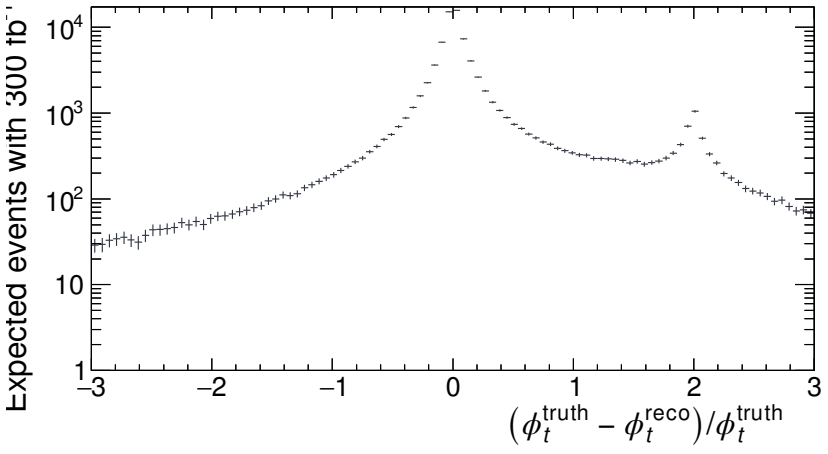

(c) ϕ_t resolution

Figure 8.8.7: Performance plots showing the resolution of the reconstructed top quark using the ratio of truth minus reconstruction over truth.

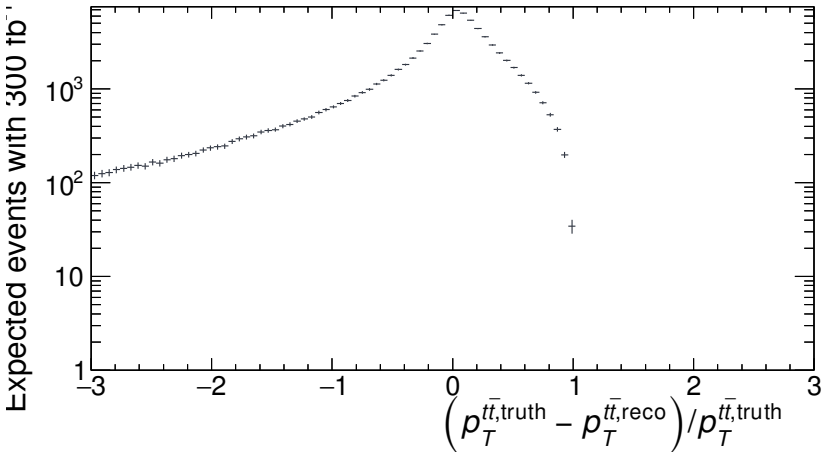

(a) $p_{\mathrm{T}}^{t\bar{t}}$ resolution

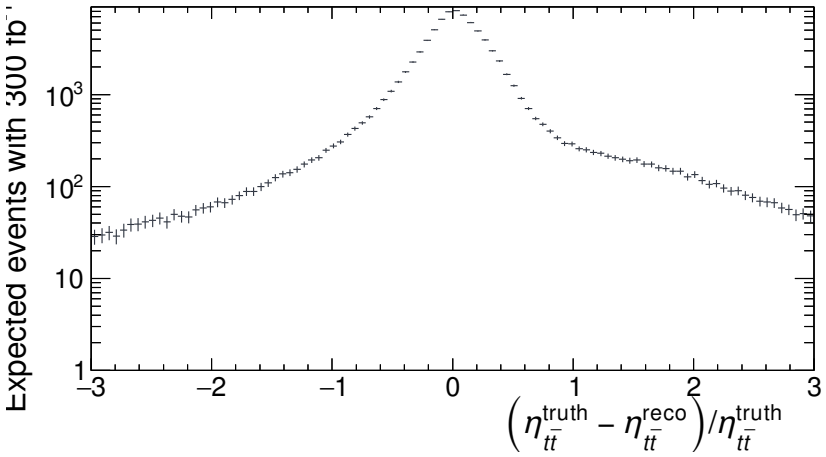

(b) $\eta_{t\bar{t}}$ resolution

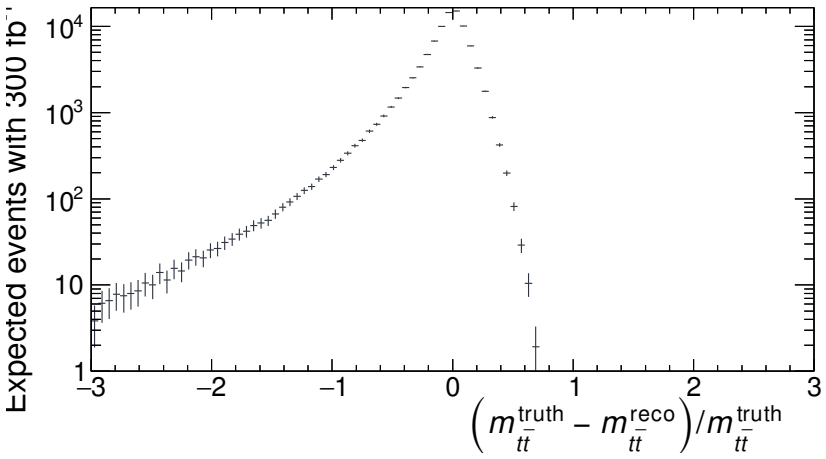

(c) $m_{t\bar{t}}$ resolution

Figure 8.8.8: Performance plots showing the resolution of the reconstructed top-antitop quark pair using the ratio of truth minus reconstruction over truth.

using asymptotic formulae as described in section 7.5. The bin widths of each of the observables is adjusted on a case-by-case basis in order to ensure a successful fit. For all results presented a minimum of two b-tagged jets are required. This strict require ensures that in an actual analysis, a relatively pure sample of $t\bar{t}$ events would be collected, minimising background contamination due to the reducible background.

Figs. 8.8.9 and 8.8.10 present the 1D distributions for $m_{t\bar{t}}$, $H_{\mathrm{T}} + E_{\mathrm{T}}^{\mathrm{miss}}$ and K_{T} at the truth and detector level, respectively. At the detector level, the $m_{t\bar{t}}$ observable was reconstructed using the NW method described in section 8.6.3, while the transverse variables are independent of the reconstruction scheme. The resulting significances for all observables, corresponding to these plots, are presented in Tab. 8.8.11.

At the truth-level, we see that $m_{t\bar{t}}$ has the highest significance, as expected, exceeding a 5σ deviation from the SM. This is followed by K_{T} with a significance of 4.6, closely followed by 4.5 for $H_{\mathrm{T}}+E_{\mathrm{T}}^{\mathrm{miss}}$. At the detector level, the situation is reversed, with $H_{\mathrm{T}}+E_{\mathrm{T}}^{\mathrm{miss}}$ just beating out K_{T} with significances of 3.6 and 3.5, respectively, while $m_{t\bar{t}}$ achieves only a 2.0σ significance. Thus, we see that the transverse observables out-perform the NW reconstruction scheme in a 1D analysis.

Also presented in Tab. 8.8.11 are the results of 2D significance analyses made by combining either $m_{t\bar{t}}$, $H_{\mathrm{T}} + E_{\mathrm{T}}^{\mathrm{miss}}$ or K_{T} with a kinematic observable sensitive to the chiral couplings of the embedded Z'. For the transverse observables only the charge asymmetry and spin correlation may be probed, using $\cos\theta_{\ell}^{*}$ (or $\Delta|\eta_{\ell\ell}|$) and $\Delta\phi_{\ell^{+}\ell^{-}}$, respectively. In both cases the resulting significance does not increase from the 1D case. When a finer binning is used the significance does not improve due to reduced event numbers per bin and the consequent increase in statistical uncertainty. It is possible that these observables still allow differentiation between two BSM signals with very different chiral coupling.

However, using the NW reconstruction procedure and available angular variables, a binning scheme can always be selected that increases the expected significance in a 2D analysis. Binning too finely will again reduce the significance with respect to the 1D analysis. In most cases only two bins in the angular variable were used, with limits matching those of the corresponding asymmetry observable. However, in the case of the polarisation asymmetry, measured using $\cos\theta_{\ell\pm}^{t}$, a bin width of 0.2 was found to be optimal. This observable was also shown to have the strongest distinguishing power increasing the significance from 2.0 to 2.6σ, though, based on the results of Chapter 7 this is due to the particular model. The charge asymmetry as measured using $\cos\theta_{t}^{*}$ increases the significance to 2.3σ, as does $\cos\theta_{\ell^{+}}^{t}\cos\theta_{\ell^{-}}^{t}$ as a measure of the spin correlation. Only a minor improvement is seen when combining $m_{t\bar{t}}$ with $\cos\varphi_{\ell\ell}$, another probe of spin correlation asymmetry.

It is to be noted, however, that the significances never approach those available using the transverse variables for any 2D analysis in the reconstruction scheme. Therefore, first observation is most likely using substitute variables for the invariant mass without performing reconstruction. However, the reconstruction scheme may prove very powerful for distinguishing Z' embedded by different BSM scenarios.

8.9 Conclusions

This chapter explored the potential for the ATLAS detector to observe the decay of a heavy Z' boson via the dilepton final state resulting from top pair production with full simulation of parton-shower, fragmentation/hadronisation, heavy flavour decay and detector effects. Presently, as proof of concept, only a single BSM model embedding one such a state has been tested, with an upcoming publication to address additional models.

The objective of this investigation is to extend the results of chapter 7 which was limited to a parton-level analysis of $t\bar{t}$ production via a Z' boson, targeting the lepton-plus-jets final state. As in the former chapter, a $2 \rightarrow 6$ calculation is used accounting for all possible leading order topologies for both signal and (irreducible) backgrounds including interference effects where appropriate. PYTHIA8 and Delphes are used for realistic simulation of particle-level effects and detector limitations. State-of-the-art techniques are used to reconstruct the top quarks and calculate observables sensitive to charge and spin asymmetries. As an alternative to reconstruction, several proxy observables are used in place of both the invariant top quark pair mass and the asymmetry-sensitive kinematic variables. A statistical procedure enabling the combination of both differential and integrated significances from cross section and asymmetry signals was employed to test the potential discovery significance of these observables.

It is found that transverse variables provide greater discovery potential than the reconstructed top quark pair system mass, but when coupled with angular information in an attempt to further differentiate the signal, the decreased statistical power of segregated events reduces the overall discovery significance. In contrast, while lower in one-dimensional significance, using a two-dimensional analysis with charge and polarisation sensitive angles in combination with invariant mass provided increased significance, in addition to their potential for differentiating different BSM theories.

Further work is required to analyse the full spectrum of BSM theories across all dilepton final states. However, the computational framework is now in place for such a study, which will form the basis of an upcoming publication based on this work. Results could further be refined by accounting for systematic theoretical and experimental uncertainties. There is also potential for a complementary analysis of the lepton-plus-jets final

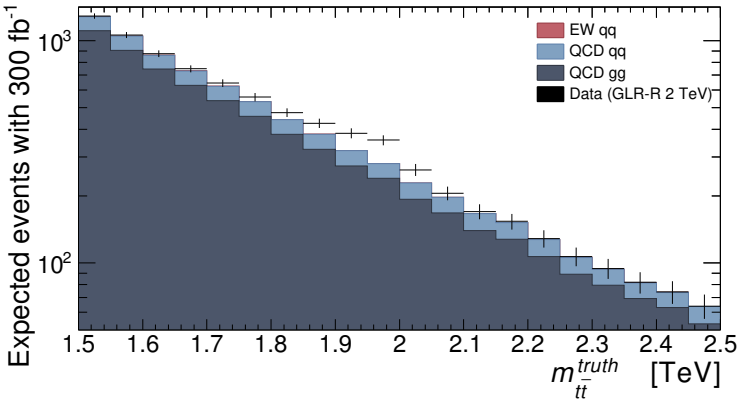

(a) $m_{t\bar{t}}$ (truth)

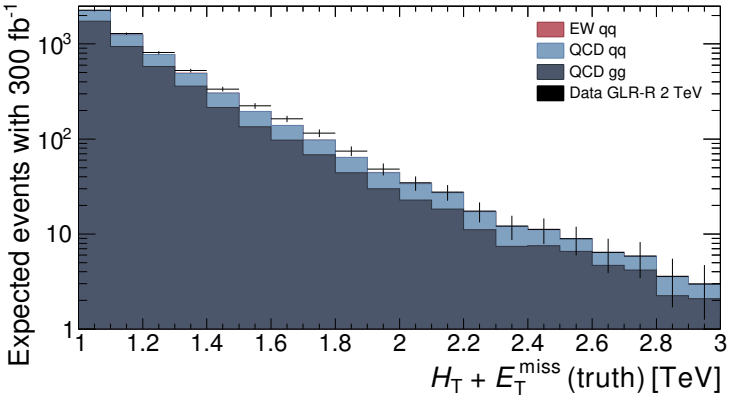

(b) $H_{\mathrm{T}} + E_{\mathrm{T}}^{\mathrm{miss}}$ (truth)

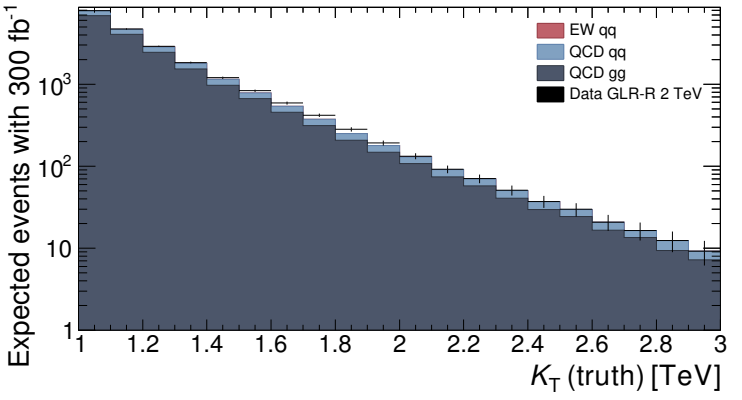

(c) K_{T} (truth)

Figure 8.8.9: Truth-level distributions of $m_{t\bar{t}}$, $H_{\mathrm{T}} + E_{\mathrm{T}}^{\mathrm{miss}}$ and K_{T} for the dimuon channel for events expected with 300 fb^{-1}.

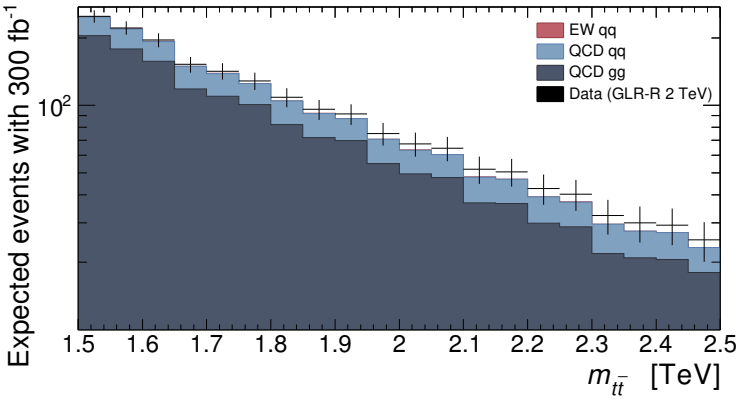

(a) $m_{t\bar{t}}$ (Detector reconstructed objects, NW top reconstruction)

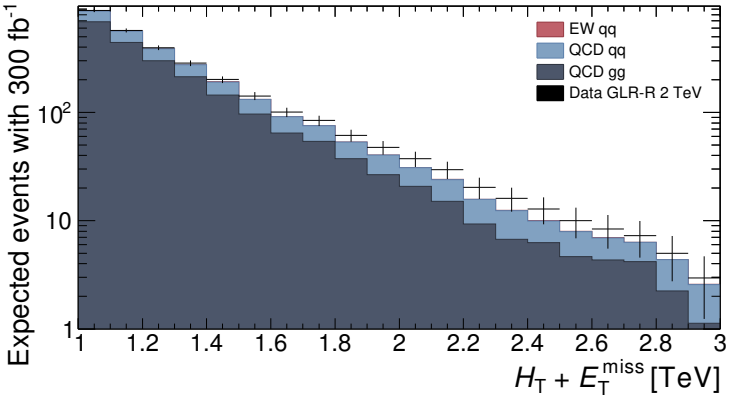

(b) $H_{\mathrm{T}} + E_{\mathrm{T}}^{\mathrm{miss}}$ (Detector Reconstructed objects)

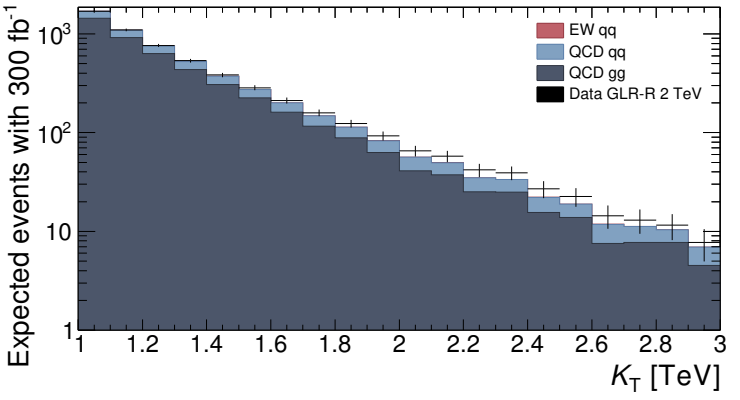

(c) K_{T} (Detector Reconstructed objects)

Figure 8.8.10: Detector-level distributions of $m_{t\bar{t}}$, $H_{\mathrm{T}} + E_{\mathrm{T}}^{\mathrm{miss}}$ and K_{T} for the dimuon channel for events expected with 300 fb^{-1}. Neutrino Weighting (NW) is used for top reconstruction in the case of $m_{t\bar{t}}$.

	Observable	Expected Significance (σ)
Truth-level	$m_{t\bar{t}}$	5.8
	$H_{\mathrm{T}} + E_{\mathrm{T}}^{\mathrm{miss}}$	4.5
	K_{T}	4.6
Detector level	$H_{\mathrm{T}} + E_{\mathrm{T}}^{\mathrm{miss}}$	3.6
	K_{T}	3.5
	$\Delta\phi_{\ell\ell}$	0.5
	$\Delta\lvert\eta_{\ell\ell}\rvert$	0.5
	$\cos\theta^*_{\ell}$	0.5
	$(H_{\mathrm{T}} + E_{\mathrm{T}}^{\mathrm{miss}}) \times \Delta\phi_{\ell\ell}$	3.6
	$K_{\mathrm{T}} \times \Delta\phi_{\ell\ell}$	3.5
	$(H_{\mathrm{T}} + E_{\mathrm{T}}^{\mathrm{miss}}) \times \cos\theta^*_{\ell}$	3.6
	$K_{\mathrm{T}} \times \cos\theta^*_{\ell}$	3.6
	$(H_{\mathrm{T}} + E_{\mathrm{T}}^{\mathrm{miss}}) \times \Delta\lvert\eta_{\ell\ell}\rvert$	3.6
	$K_{\mathrm{T}} \times \Delta\lvert\eta_{\ell\ell}\rvert$	3.6
Detector level and NW reconstruction	$m_{t\bar{t}}$	2.0
	$\Delta\lvert y_{tt}\rvert$	0.3
	$\cos\theta^*_{t}$	0.3
	$\cos\theta^{t}_{\ell^+}$	0.3
	$\cos\theta^{t}_{\ell^-}$	0.3
	$\cos\theta^{t}_{\ell^+}\cos\theta^{t}_{\ell^-}$	0.3
	$m_{t\bar{t}} \times \cos\theta^*_{t}$	2.3
	$m_{t\bar{t}} \times \cos\theta^{t}_{\ell^+}$	2.6
	$m_{t\bar{t}} \times \cos\theta^{t}_{\ell^-}$	2.6
	$m_{t\bar{t}} \times \cos\theta^{t}_{\ell^+}\cos\theta^{\bar{t}}_{\ell^-}$	2.3
	$m_{t\bar{t}} \times \cos\varphi_{\ell\ell}$	2.1

Table 8.8.11: Expected significance assuming the existence of 2 TeV GLR-R Z' in $t\bar{t}$ production with the dimuon final state tested against the SM hypothesis, expressed as the Gaussian equivalent of the p-value for 1D and 2D distributions. Definitions of each observables can be found in the text.

state, comparing the power of this channel with respect to dilepton when accounting for jet-embedded leptons and overlapping jet constituents from hadronic top decays.

In summary, for this chapter, I advanced previous studies to show that charge and spin asymmetry observables can continue to have an impact in accessing and profiling $Z' \to t\bar{t}$ dilepton signals at the LHC, even accounting for showering, hadronisation and detector resolution on the final state.

CHAPTER 9

Conclusions and outlook

A number of phenomenological studies have been presented examining the potential of top quark pair production at the LHC to provide a handle on the discovery and identification of new neutral resonances. Particular emphasis was placed on observables that probe the charge and spin asymmetries of a Z' boson. The top quark decays prior to hadronisation, preserving spin information in the angular distributions of decay products. This allows the definition of asymmetry observables able to probe the chiral coupling of the new particle. The top quark couplings, in particular, are useful due to the important role of the top quark in BSM modifications of the Electroweak Symmetry Breaking mechanism. This importance stems from the large contribution to the unstable radiative corrections of the scalar Higgs mass as a consequence of the large top quark mass.

The primary objective of these analyses was to extend previous studies conducted using stable tops at the parton-level. These demonstrated that charge and spin asymmetries in top pair production could provide a strong handle on the identification of different beyond the Standard Model theories, including models featuring multiple interfering new resonances. These studies were limited in impact by assuming perfect reconstruction of the top quarks for all decay channels, and, thus, not accounting for the effects of the decay, the parton shower, fragmentation/hadronisation of the decay products, or the detector resolution of the resultant complex multi-particle final states. In particular, the impacts of missing transverse momentum ($p_{\mathrm{T}}^{\mathrm{miss}}$) reconstruction, obligatory for resolving the single neutrino in lepton-plus-jets and the two neutrinos in the dilepton

final state, have a strong impact on accurate top reconstruction. It is particularly challenging to resolve $p_{\mathrm{T}}^{\mathrm{miss}}$ at hadron colliders, such as the LHC. Additionally, the statistical procedure used to assess the potential for discovery significance was limited to the procedure described in section 3.4.1. While a useful preliminary formula, a more sophisticated statistical analysis is required for convincing results. The conclusions of these studies were, therefore, limited, as, despite attempts to employ realistic efficiencies, the impact of these considerations on the asymmetry observables was unknown.

The first step towards a more realistic analysis was achieved by resorting to a $2 \to 6$ calculation accounting for all possible topologies for both signal and (irreducible) backgrounds, including interference effects, where appropriate. This meant that observables used to measure asymmetries were reconstructed using the distributions of the decays products, described in chapter 3. The tools employed for these simulations are described in chapter 4. These calculations allow for off-shell tops and $W^{\pm}$ bosons. It was found that while the assumption of the Narrow Width Approximation (NWA) had minimal impact on truth-level information, when employing the NWA at the generator-level subsequent top reconstruction is artificially improved.

The first study to utilise this $2 \to 6$ calculation is presented in chapter 7. This analysis focused on the lepton-plus-jets channel, as it is difficult to fully reconstruct the system in dilepton $t\bar{t}$ events which feature two sources of missing transverse energy, while fully hadronic $t\bar{t}$ events come with very large backgrounds. While the analysis was performed at the parton level, a reconstruction procedure of the (anti)top quark mass and momenta that closely mimics experimental conditions was implemented. A statistical procedure enabling the combination of significances from cross section and asymmetry signals was also employed. This analysis showed that the conclusions of the on-shell analysis hold true for a $2 \to 6$ analysis using decay-level observables. Namely, that these observables can serve to distinguish different BSM theories embedding Z' bosons with a broadly similar signature in differential cross section. Furthermore, it showed that these observables, in fact, offer potential for increased discovery significance than when using the differential cross section in isolation. At the same time, the fact that this channel cannot be competitive with the dilepton (Drell-Yan) channel motivates the former point: for its use as a complementary final state for differentiating different Z' bosons, rather than a straight discovery mode. However, this is typically only true for those benchmark models that feature no enhancements to third generation interactions or bear no suppression of leptonic couplings.

While this study was a promising next step towards a realistic analysis, it was still limited to the parton-level, and relied on individually resolving both leptonic and hadronic decay products. In reality, at such high centre-of-mass energies, the events would fall clearly in to the boosted regime. In this scenario, the jet constituents of hadronic decay products would heavily overlap, resulting in 'fat jets' that require specialised methods to

resolve. Additionally, leptonic decay products can be embedded within the jet radius.

This motivated the next analysis presented in chapter 8. For this study the parton-level generation tool described in chapter 4 was interfaced with the PYTHIA 8.2 and Delphes frameworks, in order to simulate parton-shower, hadronisation and detector resolution effects. The potential of the ATLAS detector, in particular, was explored, and an overview of the detector apparatus is given in chapter 5. Given the difficulty in resolving electrons for these analyses, the accurate reconstruction and identification of electrons and positrons is critical. Future searches using the ATLAS detector will require a firm understanding of electron trigger efficiencies in order to make improvements. On that account, a study of the sources of inefficiency for ATLAS single electron triggers is presented in chapter 6. These showed that there was significant improvement in efficiency between data taking in 2016 and 2017, due to modification of those parts of the trigger chain observed to be most detrimental in 2016.

The focus of the detector-level analysis was the dilepton final state and the analysis framework was modified to allow extraction of Delphes generated output. This final state features two neutrinos, necessitating more intricate reconstruction algorithms. Two approaches to top reconstruction were employed, with particular focus on Neutrino Weighting. While the fat-jet problem is not encountered in this final state, a critical concern is the resolution of top-granddaughter leptons embedded within the jet radius of top-daughter b quarks. To address this issue it was found to be necessary to relax requirements on the overlap removal procedures typically used in experimental analyses. While able to neglect requirements on the muons, electrons require specialised techniques to extract energy deposits before jet-clustering algorithms are employed. This lends the dimuon channel an advantage for the observation of Z' bosons. The results of the analysis indicate that transverse variables offer greater potential for observational significance than the reconstructed invariant mass. Additionally, combining these transverse variables with charge and spin sensitive angular information leads to no the overall improvement in significance due to the statistical impact of finer binning. However, the reconstructed top quark pair system mass, when coupled with angular information increases the overall discovery significance for observables sensitive to charge and top polarisation asymmetries. This suggests that the distinguishing power of this channel remains after detector simulation and top reconstruction, such that different BSM theories may be resolved. Given the difficulties for top reconstruction with the lepton-plus-jets final state in the strongly boosted region, this may allow the dilepton channel to be competitive for identifying high-mass resonances, particularly for broad resonances. Thus, it could constitute an invaluable window for studying, or even first discovery of, Z' bosons for models featuring strong third-generation couplings, or suppressed coupling to leptons.

All of the tools used in this analysis were heavily developed by myself. The parton-level

$2 \to 6$ generator was developed from a simple VEGAS Monte Carlo integration program, written in Fortran77, for calculating the cross section for QCD processes (written by my supervisor, Stefano Moretti) to a BSM unweighted event generator using VAMP [53], written in Fortran95 (compatible with Fortran08), using the most recent parton distribution functions, with output written either to an LHEF file or directly to a ROOT file. The C++/ROOT analysis code was written by myself from scratch, including the reconstruction in lepton-plus-jets, the quartic reconstruction in dilepton and the interface to the Neutrino Weighting method, which was modified to work in my analysis framework. The python code for the likelihood-based significance test using RooStats and HistFactory was adapted from example scripts by my collaborator, Francesco Spanò, and myself. The showering, hadronisation and detector simulation program using Pythia8 and Delphes was adapted by myself from example scripts.

Therefore, the tools are available, and the stage set, for a fully-fledged analysis in the dilepton channel for all available electron and muon-based final states, exploring a broad range of BSM scenarios, which constitutes the subject of a forthcoming publication. To test the potential of the dilepton channel to compete with lepton-plus-jets, it will also be necessary to conduct a study utilising the same tools and employing an appropriate boosted reconstruction that preserves high signal efficiency in the face of increasing momentum.

In general, the discovery of the long-awaited Higgs boson at the LHC in 2012 has opened a new chapter in particle physics. While an exciting discovery, and astounding success for the Standard Model of particle physics, additional measurements have not provided any conclusive hints at what might lie beyond. With many different directions to turn in next, it is more important than ever for theoretical and experimental particle physicists to collaborate on the search for new physics.

Bibliography

[1] J. C. Maxwell, *A Dynamical Theory of the Electromagnetic Field*, *Phil Trans Roy Soc Lond* **155** (1865) 459–512.

[2] A. A. Michelson and E. W. Morley, *On the Relative Motion of the Earth and the Luminiferous Ether*, *Am J Sci* **34** (1887) 333–345.

[3] H. A. Lorentz, *Simplified Theory of Electrical and Optical Phenomena in Moving Systems*, *KNAW Proc.* **1** (1899) 427–442.

[4] H. A. Lorentz, *Electromagnetic phenomena in a system moving with any velocity smaller than that of light*, *KNAW Proc.* **6** (1904) 809–831.

[5] T. Aoyama, M. Hayakawa, T. Kinoshita, and M. Nio, *Tenth-Order Electron Anomalous Magnetic Moment — Contribution of Diagrams without Closed Lepton Loops*, *Phys Rev* **D91** (2015), no. 3 033006, [arXiv:1412.8284].

[6] D. Hanneke, S. F. Hoogerheide, and G. Gabrielse, *Cavity Control of a Single-Electron Quantum Cyclotron: Measuring the Electron Magnetic Moment*, *Phys Rev* **A83** (2011) 052122, [arXiv:1009.4831].

[7] A. Zee, *Quantum Field Theory in a Nutshell*. Princeton University Press, 2nd ed., (2010).

[8] R. Percacci, *Asymptotic Safety*, *Oriti Ed Approaches Quantum Gravity* (2007) 111–128, [arXiv:0709.3851].

[9] S. Gonzalez-Martin, T. R. Morris, and Z. H. Slade, *Asymptotic solutions in*

asymptotic safety, *Phys Rev* **D95** (2017), no. 10 106010, [arXiv:1704.0887].

[10] D. Tong, "String Theory - University of Cambridge Part III Mathematical Tripos." 2009.

[11] P. LaBelle, *Supersymmetry DeMYSTiFied*. US: McCraw-Hill Professional, (2009).

[12] M. E. Peskin and D. V. Schroeder, *An Introduction to Quantum Field Theory*. Westview Press, (1995).

[13] The ATLAS Collaboration, *Search for high-mass dilepton resonances in pp collisions at $\sqrt{s}$ = 8 TeV with the ATLAS detector*, *Phys Rev* **D90** (2014), no. 5 052005, [arXiv:1405.4123].

[14] CMS collaboration, *Search for physics beyond the standard model in dilepton mass spectra in proton-proton collisions at $\sqrt{s}$ = 8 TeV*, *JHEP* **04** (2015) 025, [arXiv:1412.6302].

[15] The ATLAS Collaboration, *Search for high-mass new phenomena in the dilepton final state using proton–proton collisions at $\sqrt{s}$ = 13 TeV with the ATLAS detector*, *Phys Lett* **B761** (2016) 372 – 392, [arXiv:1607.3669].

[16] The ATLAS Collaboration, *Search for new high-mass resonances in the dilepton final state using proton-proton collisions at $\sqrt{s}$ = 13 TeV with the ATLAS detector*, *ATLAS-CONF-2016-045* (2016) [arXiv:1607.3669].

[17] CMS collaboration, *Search for a high-mass resonance decaying into a dilepton final state in 13 fb-1 of pp collisions at $\sqrt{s}$ = 13 TeV*, *CMS-PAS-EXO-16-031* (2016).

[18] The ATLAS Collaboration, *A search for ttbar resonances using lepton-plus-jets events in proton–proton collisions at $\sqrt{s}$ = 8 TeV with the ATLAS detector*, *JHEP* **08** (2015) 148, [arXiv:1505.7018].

[19] CMS collaboration, *Search for resonant ttbar production in proton-proton collisions at $\sqrt{s}$ = 8 TeV*, *Phys Rev* **D93** (2016), no. 1 012001, [arXiv:1506.3062].

[20] C. Dib and F. J. Gilman, *Extra neutral gauge bosons in electron-positron collisions at resonance*, *Phys Rev* **D36** (1987) 1337.

[21] E. Accomando, A. Belyaev, L. Fedeli, S. F. King, and C. Shepherd-Themistocleous, *Z' physics with early LHC data*, *Phys Rev* **D83** (2011), no. 7 075012, [arXiv:1010.6058].

[22] E. Accomando, K. Mimasu, and S. Moretti, *Uncovering quasi-degenerate Kaluza-Klein Electro-Weak gauge bosons with top asymmetries at the LHC*, *JHEP*

07 (2013) 154, [arXiv:1304.4494].

[23] P. Langacker, *The physics of heavy Z' gauge bosons*, *Rev. Mod. Phys.* **81** (2009), no. 3 1199–1228, [arXiv:0801.1345].

[24] T. G. Rizzo, *Gauge kinetic mixing and leptophobic Z in E(6) and SO(10)*, *Phys Rev* **D59** (1998) 015020, [hep-ph/9806397].

[25] H. Georgi and S. L. Glashow, *Unity of All Elementary-Particle Forces*, *Phys. Rev. Lett.* **32** (1974), no. 8 438.

[26] H. Fritzsch and P. Minkowski, *Unified Interactions of Leptons and Hadrons*, *Ann. Phys* **93** (1975) 193–266.

[27] F. Gursey, P. Ramond, and P. Sikivie, *A Universal Gauge Theory Model Based on E6*, *Phys Lett* **B60** (1976) 177–180.

[28] A. J. Buras, J. R. Ellis, M. K. Gaillard, and D. V. Nanopoulos, *Aspects of the Grand Unification of Strong, Weak and Electromagnetic Interactions*, *Nucl Phys* **B135** (1978) 66–92.

[29] L. Di Luzio, *Aspects of Symmetry Breaking in Grand Unified Theories*, PhD thesis, SISSA, (2011), [arXiv:1110.3210].

[30] M. Cvetic and P. Langacker, *Z' Physics and Supersymmetry*, *Adv Ser Direct High Energy Phys* **18** (1998) 312–331, [hep-ph/9707451].

[31] J. L. Feng, *Naturalness and the Status of Supersymmetry*, *Ann Rev Nucl Part Sci* **63** (2013) 351–382, [arXiv:1302.6587].

[32] E. Witten, *Dimensional Reduction of Superstring Models*, *Phys Lett* **B155** (1985) 151.

[33] J. Erler, P. Langacker, and T. J. Li, *The Z - Z' mass hierarchy in a supersymmetric model with a secluded U(1) -prime breaking sector*, *Phys Rev* **D66** (2002) 015002, [hep-ph/0205001].

[34] R. W. Robinett, *Neutral currents in E6*, *Phys Rev D* **26** (1982), no. 9 2388–2395.

[35] S. F. King, S. Moretti, and R. Nevzorov, *Theory and phenomenology of an exceptional supersymmetric standard model*, *Phys Rev* **D73** (2006) 035009, [hep-ph/0510419v2].

[36] L. Susskind, *Dynamics of spontaneous symmetry breaking in the Weinberg-Salam theory*, *Phys Rev D* **20** (1979-11), no. 10 2619–2625.

[37] S. F. King, *Dynamical electroweak symmetry breaking*, *Rept Prog Phys* **58** (1995) 263–310, [hep-ph/9406401].

[38] N. Arkani-Hamed, A. G. Cohen, and H. Georgi, *Electroweak symmetry breaking from dimensional deconstruction*, *Phys Lett* **B513** (2001) 232–240, [hep-ph/0105239].

[39] G. F. Giudice, C. Grojean, A. Pomarol, and R. Rattazzi, *The Strongly-Interacting Light Higgs*, *JHEP* **06** (2007) 045, [hep-ph/0703164].

[40] S. De Curtis, M. Redi, and A. Tesi, *The 4D composite Higgs*, *J. High Energy Phys.* **2012** (2012), no. 4 1–29, [arXiv:1110.1613].

[41] D. Barducci, S. De Curtis, K. Mimasu, and S. Moretti, *Multiple Z'->tt signals in a 4D Composite Higgs Model*, *Phys Rev* **D88** (2012) 074024, [arXiv:1212.5948].

[42] A. Belyaev, M. Brown, S. D. Curtis, and S. Moretti, *The 4-Dimensional Composite Higgs Model (4DCHM) and the 125 GeV Higgs-like signals at the LHC*, *JHEP* **09** (2013) 047, [arXiv:1302.2371].

[43] Wolfram Research Inc., *Mathematica, Version 11.3*, Champaign, IL, (2018).

[44] T. H. West, *FeynmanParameter and trace - programs for expressing Feynman amplitudes as integrals over Feynman parameters*, *Comput. Phys. Commun.* **77** (1993), no. 2 286–298.

[45] M. Arai, N. Okada, K. Smolek, and V. Simak, *Influence of Z' boson on top quark spin correlations at the LHC*, *Acta Phys Pol.* **B40** (2009) 93–110, [arXiv:0804.3740].

[46] M. Tanabashi, et al, and (Particle Data Group), *The Review of Particle Physics*, *Phys Rev* **D 98** (2018), no. 030001.

[47] K. A. V. Mimasu, *Z' Phenomenology in Ttbar and Its Asymmetries at the LHC*, PhD thesis, University of Southampton, (2014).

[48] L. Basso, K. Mimasu, and S. Moretti, *Z' signals in polarised top-antitop final states*, *JHEP* **09** (2012) 024, [arXiv:1203.2542].

[49] W. Bernreuther, M. Fuecker, and Z. G. Si, *Weak interaction corrections to hadronic top quark pair production*, *Phys Rev* **D74** (2006) 113005, [hep-ph/0610334].

[50] S. Moretti, M. R. Nolten, and D. A. Ross, *Weak corrections to gluon-induced top-antitop hadro-production*, *Phys Lett* **B639** (2006) 513–519, [hep-ph/0603083v3]. [Erratum: Phys. Lett.B660,607(2008)].

[51] K. Hagiwara, J. Kanzaki, H. Murayama, and I. Watanabe, *HELAS: HELicity Amplitude Subtroutines for Feynman diagram evaluations*, *KEK-91-11* (1992).

[52] T. Stelzer and W. F. Long, *Automatic generation of tree level helicity amplitudes*, *Comput. Phys. Commun.* **81** (1994), no. 3 357–371, [hep-ph/9401258v1].

[53] T. Ohl, *Vegas revisited: Adaptive Monte Carlo integration beyond factorization*, *Comput Phys Commun* **120** (1999) 13–19, [hep-ph/9806432].

[54] G. P. Lepage, *A new algorithm for adaptive multidimensional integration*, *J Comput Phys* **27** (1978) 192–203.

[55] J. Gao, M. Guzzi, J. Huston, H.-L. Lai, Z. Li, P. Nadolsky, J. Pumplin, D. Stump, and C. P. Yuan, *CT10 next-to-next-to-leading order global analysis of QCD*, *Phys Rev* **D89** (2014), no. 3 033009, [arXiv:1302.6246].

[56] H. L. Lai, M. Guzzi, J. Huston, Z. Li, P. M. Nadolsky, J. Pumplin, and C. P. Yuan, *New parton distributions for collider physics*, *Phys Rev* **D82** (2010) 074024, [arXiv:1007.2241].

[57] J. Pumplin, D. R. Stump, J. Huston, H. L. Lai, P. M. Nadolsky, and W. K. Tung, *New generation of parton distributions with uncertainties from global QCD analysis*, *JHEP* **07** (2002) 012, [hep-ph/0201195v3].

[58] S. Dulat, T. J. Hou, J. Gao, M. Guzzi, J. Huston, P. Nadolsky, J. Pumplin, C. Schmidt, D. Stump, and C. P. Yuan, *New parton distribution functions from a global analysis of quantum chromodynamics*, *Phys Rev* **D93** (2016), no. 3 033006, [arXiv:1506.0744].

[59] J. Alwall and others, *A Standard format for Les Houches event files*, *Comput. Phys. Commun.* **176** (2007) 300–304, [hep-ph/0609017].

[60] E. Accomando, A. Belyaev, J. Fiaschi, S. Moretti, K. Mimasu, and C. Shepherd-Themistocleous, *Forward-Backward Asymmetry as a Discovery Tool for Z' Bosons at the LHC*, *JHEP* **01** (2016), no. 1 127, [arXiv:1503.2672].

[61] T. Sjöstrand, S. Mrenna, and P. Z. Skands, *PYTHIA 6.4 Physics and Manual*, *JHEP* **05** (2006) 026, [hep-ph/0603175].

[62] T. Sjöstrand, S. Mrenna, and P. Skands, *A Brief Introduction to PYTHIA 8.1*, *Comput. Phys. Commun.* (2008) 1–27, [arXiv:0710.3820].

[63] T. Sjöstrand, S. Ask, J. R. Christiansen, R. Corke, N. Desai, P. Ilten, S. Mrenna, S. Prestel, C. O. Rasmussen, and P. Z. Skands, *An Introduction to PYTHIA 8.2*, *Comput Phys Commun* **191** (2015) 159–177, [arXiv:1410.3012].

[64] J. de Favereau, C. Delaere, P. Demin, A. Giammanco, V. Lemaître, A. Mertens, and M. Selvaggi, *DELPHES 3: A modular framework for fast simulation of a generic collider experiment*, *J. High Energy Phys.* **2014** (2014), no. 2 57, [arXiv:1307.6346].

[65] M. Selvaggi, *DELPHES 3: A modular framework for fast-simulation of generic collider experiments*, *J. Phys. Conf. Ser.* **523** (2014) 012033.

[66] A. Mertens, *New features in Delphes 3*, *J. Phys. Conf. Ser.* **608** (2015), no. 1 012045.

[67] P. Nason, S. Dawson, and R. K. Ellis, *The One Particle Inclusive Differential Cross-Section for Heavy Quark Production in Hadronic Collisions*, *Nucl Phys* **B327** (1989) 49–92. [Erratum: Nucl. Phys.B335,260(1990)].

[68] W. Beenakker, W. L. van Neerven, R. Meng, G. A. Schuler, and J. Smith, *QCD corrections to heavy quark production in hadron hadron collisions*, *Nucl Phys* **B351** (1991) 507–560.

[69] M. L. Mangano, P. Nason, and G. Ridolfi, *Heavy quark correlations in hadron collisions at next-to-leading order*, *Nucl Phys* **B373** (1992) 295–345.

[70] S. Frixione, M. L. Mangano, P. Nason, and G. Ridolfi, *Top quark distributions in hadronic collisions*, *Phys Lett* **B351** (1995) 555–561, [hep-ph/9503213].

[71] W. Bernreuther, A. Brandenburg, Z. G. Si, and P. Uwer, *Top quark pair production and decay at hadron colliders*, *Nucl Phys* **B690** (2004) 81–137, [hep-ph/0403035].

[72] K. Melnikov and M. Schulze, *NLO QCD corrections to top quark pair production and decay at hadron colliders*, *JHEP* **08** (2009) 049, [arXiv:0907.3090].

[73] W. Bernreuther and Z. G. Si, *Distributions and correlations for top quark pair production and decay at the Tevatron and LHC.*, *Nucl Phys* **B837** (2010) 90–121, [arXiv:1003.3926].

[74] A. Denner, S. Dittmaier, S. Kallweit, and S. Pozzorini, *NLO QCD corrections to WWbb production at hadron colliders*, *Phys Rev Lett* **106** (2011) 052001, [arXiv:1012.3975].

[75] A. Denner, S. Dittmaier, S. Kallweit, and S. Pozzorini, *NLO QCD corrections to off-shell ttbar production at hadron colliders*, *PoS* **LL2012** (2012) 015, [arXiv:1208.4053].

[76] A. Denner, S. Dittmaier, S. Kallweit, and S. Pozzorini, *NLO QCD corrections to off-shell top-antitop production with leptonic decays at hadron colliders*, *JHEP* **10** (2012) 110, [arXiv:1207.5018].

[77] G. Bevilacqua, M. Czakon, A. van Hameren, C. G. Papadopoulos, and M. Worek, *Complete off-shell effects in top quark pair hadroproduction with leptonic decay at next-to-leading order*, *JHEP* **02** (2011) 083, [arXiv:1012.4230].

[78] W. Beenakker, A. Denner, W. Hollik, R. Mertig, T. Sack, and D. Wackeroth, *Electroweak one loop contributions to top pair production in hadron colliders*, *Nucl Phys* **B411** (1994) 343–380.

[79] J. H. Kuhn, A. Scharf, and P. Uwer, *Electroweak effects in top-quark pair production at hadron colliders*, *Eur Phys J* **C51** (2007) 37–53, [hep-ph/0610335].

[80] W. Bernreuther, M. Fucker, and Z.-G. Si, *Electroweak corrections to t anti-t production at hadron colliders*, *Nuovo Cim.* **B123** (2008) 1036–1044, [arXiv:0808.1142].

[81] P. Bärnreuther, M. Czakon, and A. Mitov, *Percent Level Precision Physics at the Tevatron: First Genuine NNLO QCD Corrections to q q tot t + X*, *Phys Rev Lett* **109** (2012) 132001, [arXiv:1204.5201].

[82] M. Czakon, P. Fiedler, and A. Mitov, *Resolving the Tevatron Top Quark Forward-Backward Asymmetry Puzzle: Fully Differential Next-to-Next-to-Leading-Order Calculation*, *Phys Rev Lett* **115** (2015), no. 5 052001, [arXiv:1411.3007].

[83] M. Czakon, P. Fiedler, D. Heymes, and A. Mitov, *NNLO QCD predictions for fully-differential top-quark pair production at the Tevatron*, *JHEP* **05** (2016) 034, [arXiv:1601.5375].

[84] M. Czakon and A. Mitov, *On the Soft-Gluon Resummation in Top Quark Pair Production at Hadron Colliders*, *Phys Lett* **B680** (2009) 154–158, [arXiv:0812.0353].

[85] M. Czakon, A. Mitov, and G. F. Sterman, *Threshold Resummation for Top-Pair Hadroproduction to Next-to-Next-to-Leading Log*, *Phys Rev* **D80** (2009) 074017, [arXiv:0907.1790].

[86] M. Beneke, P. Falgari, and C. Schwinn, *Soft radiation in heavy-particle pair production: All-order colour structure and two-loop anomalous dimension*, *Nucl Phys* **B828** (2010) 69–101, [arXiv:0907.1443].

[87] J. Gao, C. S. Li, B. H. Li, C. P. Yuan, and H. X. Zhu, *Next-to-leading order QCD corrections to the heavy resonance production and decay into top quark pair at the LHC*, *Phys Rev* **D82** (2010) 014020, [arXiv:1004.0876].

[88] R. Bonciani, T. Jezo, M. Klasen, F. Lyonnet, and I. Schienbein, *Electroweak top-quark pair production at the LHC with Z' bosons to NLO QCD in POWHEG*, *JHEP* **02** (2016) 141, [arXiv:1511.8185].

[89] D0 Collaboration, *Measurement of the forward-backward asymmetry in top quark-antiquark production in ppbar collisions using the lepton+jets channel*, *Phys Rev* **D90** (2014) 072011, [arXiv:1405.0421].

[90] CMS collaboration, *Measurement of the charge asymmetry in top quark pair production in pp collisions at $\sqrt{s}$ = 8 TeV using a template method*, *Phys Rev* **D93** (2016), no. 3 034014, [arXiv:1508.0386].

[91] The ATLAS Collaboration, *Measurement of the charge asymmetry in highly boosted top-quark pair production in $\sqrt{s}$ = 8 TeV pp collision data collected by the ATLAS experiment*, *Phys Lett* **B756** (2015) 52–71, [arXiv:1512.0609].

[92] The ATLAS Collaboration, *Measurements of the charge asymmetry in top-quark pair production in the dilepton final state at s=8 TeV with the ATLAS detector*, *Phys Rev* **D94** (2016), no. 3 032006, [arXiv:1604.0553].

[93] The ATLAS Collaboration, *Measurement of the charge asymmetry in top-quark pair production in the lepton-plus-jets final state in pp collision data at 8 TeV with the ATLAS detector*, *Eur Phys J* **C76** (2016), no. 2 87, [arXiv:1509.0235].

[94] The ATLAS Collaboration, *Measurement of Top Quark Polarization in Top-Antitop Events from Proton-Proton Collisions at s = 7 TeV Using the ATLAS Detector*, *Phys Rev Lett* **111** (2013), no. 23 232002, [arXiv:1307.6511].

[95] G. T. Bodwin, *Factorization of the Drell-Yan cross section in perturbation theory*, *Phys Rev D* **31** (1985), no. 10 2616–2642.

[96] R. Kleiss and W. J. Stirling, *Spinor Techniques for Calculating p anti-p —> W+- / Z0 + Jets*, *Nucl Phys* **B262** (1985) 235–262.

[97] L. J. Dixon, *A brief introduction to modern amplitude methods*, *Proc. ESHEP 2012* (2014) 31–67, [arXiv:1310.5353].

[98] R. Kleiss, *The Cross-section for e+e- -> e+e- e+e-*, *Nucl Phys* **B241** (1984) 61.

[99] J. C. Romao and A. Barroso, *Higgs Production With Polarized e+e- Beams*, *Phys Lett* **B185** (1987) 195–199.

[100] G. Cacciapaglia, A. Deandrea, and S. De Curtis, *Nearby resonances beyond the Breit–Wigner approximation*, *Phys Lett* **B682** (2009) 43–49, [arXiv:0906.3417].

[101] C. F. Uhlemann and N. Kauer, *Narrow-width approximation accuracy*, *Nucl Phys* **B814** (2009) 195–211, [arXiv:0807.4112].

[102] D. Berdine, N. Kauer, and D. Rainwater, *Breakdown of the Narrow Width Approximation for New Physics*, *Phys Rev Lett* **99** (2007) 111601, [hep-ph/0703058].

[103] L. Basso, K. Mimasu, and S. Moretti, *The role of charge and spin asymmetries in profiling Z'-> tt events*, *J Phys Conf Ser* **452** (2013) 012002, [arXiv:1211.5599].

[104] V. N. Gribov and L. N. Lipatov, *Deep inelastic e p scattering in perturbation theory*, *Sov J Nucl Phys* **15** (1972) 438–450.

[105] Y. L. Dokshitzer, *Calculation of the Structure Functions for Deep Inelastic Scattering and e+ e- Annihilation by Perturbation Theory in Quantum Chromodynamics.*, *Sov Phys JETP* **46** (1977) 641–653.

[106] G. Altarelli, R. K. Ellis, and G. Martinelli, *Large Perturbative Corrections to the Drell-Yan Process in QCD*, *Nucl Phys* **B157** (1979) 461–497.

[107] J. Bellm and others, *Herwig 7.0/Herwig++ 3.0 release note*, *Eur Phys J* **C76** (2016), no. 4 196, [arXiv:1512.0117].

[108] A. Jeff, A. Boccardi, E. Bravin, A. S. S. Fisher, T. Lefevre, A. Rabiller, F. Roncarolo, and C. P. P. Welsch, *First results of the LHC longitudinal density monitor*, *Nucl. Instrum. Methods Phys. Res. Sect. Accel. Spectrometers Detect. Assoc. Equip.* **659** (2011), no. 1 549–556.

[109] L. Evans and P. Bryant, *LHC machine*, *JINST* **3** (2008) S08001.

[110] The ATLAS Collaboration, *The ATLAS Experiment at the CERN Large Hadron Collider*, *J. Instrum.* **3** (2008), no. 08 S08003.

[111] A. Abdesselam, P. P. Allport, B. Anderson, and L. Andricek, *Engineering for the ATLAS SemiConductor Tracker (SCT) end-cap*, *J. Instrum.* **3** (2008).

[112] ATLAS Pixel Collaboration, *ATLAS pixel detector electronics and sensors*, *J. Instrum.* **3** (2008), no. 07 P07007.

[113] M. Capeans, G. Darbo, K. Einsweiler, M. Elsing, T. Flick, M. Garcia-Sciveres, C. Gemme, H. Pernegger, O. Rohne, and R. Vuillermet, *ATLAS Insertable B-Layer Technical Design Report*, *CERN-LHCC-2010-013 ATLAS-TDR-19* (2010).

[114] B. Dolgoshein, *Transition Radiation Detectors*, *Nucl. Instrum. Methods Phys. Res. Sect. Accel. Spectrometers Detect. Assoc. Equip.* **326** (1993), no. 3 434–469.

[115] J. H. Hubbell, *Electron–positron pair production by photons: A historical overview*, *Radiat. Phys. Chem.* **75** (2006), no. 6 614 – 623.

[116] S. Eidelman, H. Bichsel, D. E. Groom, and S. R. Klein, *Passage of Particles Through Matter*, *Phys. Lett.* **1** (2006), no. B592.

[117] The ATLAS Collaboration, *Electron efficiency measurements with the ATLAS detector using the 2015 LHC proton-proton collision data*, *ATLAS-CONF-2016-024* (2016).

[118] J. G. Panduro Vazquez, *The ATLAS Data Acquisition System: From Run 1 to Run 2*, *ATL-DAQ-PROC-2014-035* (2014).

[119] The ATLAS Collaboration, *Technical Design Report for the Phase-I Upgrade of the ATLAS TDAQ System*, *CERN-LHCC-2013-018 ATLAS-TDR-023* (2013).

[120] F. Seifert, *Upgrade plans for the ATLAS calorimeters*, *Nucl. Instrum. Methods Phys. Res. Sect. Accel. Spectrometers Detect. Assoc. Equip.* **718** (2013) 16–20.

[121] T. G. Cornelissen, M. Elsing, I. Gavrilenko, J. F. Laporte, W. Liebig, M. Limper, K. Nikolopoulos, A. Poppleton, and A Salzburger, *The global $x2$ track fitter in ATLAS*, *J. Phys. Conf. Ser.* **119** (2008), no. 3 032013.

[122] The ATLAS Collaboration, *Improved electron reconstruction in ATLAS using the Gaussian Sum Filter-based model for bremsstrahlung*, *ATLAS-CONF-2012-047* (2012).

[123] The ATLAS Collaboration, *Electron and photon energy calibration with the ATLAS detector using LHC Run 1 data*, *Eur Phys J* **C74** (2014), no. 10 3071, [arXiv:1407.5063].

[124] The ATLAS Collaboration, *Topological cell clustering in the ATLAS calorimeters and its performance in LHC Run 1*, *Eur Phys J* **C77** (2017) 490, [arXiv:1603.0293].

[125] R. Achenbach and others, *The ATLAS level-1 calorimeter trigger*, *JINST* **3** (2008) P03001.

[126] The ATLAS Collaboration, *Electron efficiency measurements with the ATLAS detector using the 2012 LHC proton-proton collision data*, *Eur Phys J* **C77** (2017), no. 3 195, [arXiv:1612.0145].

[127] The ATLAS Collaboration, *Performance of the ATLAS Electron and Photon Triggers in p-p Collisions at $\sqrt{s}$ = 7 TeV and $\sqrt{s}$ = 8 TeV in Run-1*, *ATL-COM-DAQ-2014-107* (2014).

[128] R. M. Godbole, K. Rao, S. D. Rindani, and R. K. Singh, *On measurement of top polarization as a probe of t bart production mechanisms at the LHC*, *JHEP* **11** (2010) 144, [arXiv:1010.1458].

[129] R. M. Godbole, S. D. Rindani, K. Rao, and R. K. Singh, *Top polarization as a probe of new physics*, *AIP Conf. Proc.* **1200** (2010) 682–685, [arXiv:0911.3622].

[130] S. Fajfer, J. F. Kamenik, and B. Melic, *Discerning New Physics in Top-Antitop Production using Top Spin Observables at Hadron Colliders*, *JHEP* **08** (2012) 114, [arXiv:1205.0264].

[131] R. M. Godbole, G. Mendiratta, and S. Rindani, *Looking for bSM physics using top-quark polarization and decay-lepton kinematic asymmetries*, *Phys Rev* **D92** (2015), no. 9 094013, [arXiv:1506.7486].

[132] F. Hubaut, E. Monnier, P. Pralavorio, K. Smolek, and V. Simak, *ATLAS sensitivity to top quark and W boson polarization in ttbar events*, *Eur Phys J* **C44S2** (2005) 13–33, [hep-ex/0508061].

[133] E. L. Berger, Q. H. Cao, C. R. Chen, and H. Zhang, *Top Quark Polarization As A Probe of Models with Extra Gauge Bosons*, *Phys Rev* **D83** (2011) 114026, [arXiv:1103.3274].

[134] M. Baumgart and B. Tweedie, *Transverse Top Quark Polarization and the ttbar Forward-Backward Asymmetry*, *JHEP* **08** (2013) 072, [arXiv:1303.1200].

[135] M. Baumgart and B. Tweedie, *Discriminating Top-Antitop Resonances using Azimuthal Decay Correlations*, *JHEP* **09** (2011) 049, [arXiv:1104.2043].

[136] B. Tweedie, *Better Hadronic Top Quark Polarimetry*, *Phys Rev* **D90** (2014), no. 9 094010, [arXiv:1401.3021].

[137] R. Brun and F. Rademakers, *ROOT: An object oriented data analysis framework*, *Nucl. Instrum. Meth.* **A389** (1997) 81–86.

[138] I. Antcheva and others, *ROOT: A C++ framework for petabyte data storage, statistical analysis and visualization*, *Comput Phys Commun* **180** (2009) 2499–2512, [arXiv:1508.7749].

[139] G. Cowan, K. Cranmer, E. Gross, and O. Vitells, *Asymptotic formulae for likelihood-based tests of new physics*, *Eur Phys J* **C71** (2011) 1554, [arXiv:1007.1727].

[140] L. Moneta, K. Belasco, K. S. Cranmer, S. Kreiss, A. Lazzaro, D. Piparo, G. Schott, W. Verkerke, and M. Wolf, *The RooStats project*, *PoS* **ACAT2010** (2010) 057,

[arXiv:1009.1003].

[141] K. Cranmer, G. Lewis, L. Moneta, A. Shibata, and W. Verkerke, *HistFactory: A tool for creating statistical models for use with RooFit and RooStats*, *CERN-OPEN-2012-016* (2012).

[142] A. Buckley, J. Ferrando, S. Lloyd, K. Nordström, B. Page, M. Rüfenacht, M. Schönherr, and G. Watt, *LHAPDF6: Parton density access in the LHC precision era*, *Eur Phys J* **C75** (2015) 132, [arXiv:1412.7420].

[143] The ATLAS Collaboration, *Measurement of the charge asymmetry in top quark pair production in pp collisions at $\sqrt{s}$ = 7 TeV using the ATLAS detector*, *Eur. Phys. J. C* **72** (2012), no. 6 16–16, [arXiv:1203.4211].

[144] The ATLAS Collaboration, *Measurements of top-quark pair differential cross-sections in the e\mu channel in pp collisions at $\sqrt{s}$ = 13 TeV using the ATLAS detector*, *Eur Phys J* **C77** (2017), no. 5 292, [arXiv:1612.0522].

[145] M. Cacciari, G. P. Salam, and G. Soyez, *The Anti-k(t) jet clustering algorithm*, *JHEP* **04** (2008) 063, [arXiv:0802.1189].

[146] The ATLAS Collaboration, *Study of the spin of the new boson with up to 25 fb-1 of ATLAS data*, *ATLAS-CONF-2013-040* (2013).

[147] The ATLAS Collaboration, *Measurements of top-quark pair differential cross-sections in the lepton+jets channel in pp collisions at $\sqrt{s}$ = 13 TeV using the ATLAS detector*, *JHEP* **11** (2017) 191, [arXiv:1708.0072].

[148] L. Sonnenschein, *Algebraic approach to solve ttbar dilepton equations*, *Phys. Rev. D* **72** (2005), no. 9 7–7, [hep-ph/0510100].

[149] D0 Collaboration, *Measurement of the top quark mass in the dilepton channel*, *Phys Rev D* **60** (1999), no. 5 052001, [hep-ex/9808029].

[150] D0 Collaboration, *Measurement of the Top Quark Mass in Final States with Two Leptons*, *Phys Rev* **D80** (2009) 092006, [arXiv:0904.3195].

[151] D0 Collaboration, *Precise measurement of the top quark mass in dilepton decays using optimized neutrino weighting*, *Phys Lett* **B752** (2016) 18–26, [arXiv:1508.0332].

[152] CDF Collaboration, *Measurement of the top quark mass using template methods on dilepton events in proton antiproton collisions at $\sqrt{s}$ = 1.96-TeV.*, *Phys Rev* **D73** (2006) 112006, [hep-ex/0602008].

[153] W. Bernreuther and Z. G. Si, *Top quark spin correlations and polarization at the LHC: Standard model predictions and effects of anomalous top chromo moments*, *Phys. Lett. Sect. B Nucl. Elem. Part. High-Energy Phys.* **725** (2013), no. 1-3 115–122, [arXiv:1305.2066].